The origin and diagenesis of the Mt. Simon storage complex: Illinois Basin, USA

Inauguraldissertation

zur

Erlangung des akademischen Grades eines

Doktors der Naturwissenschaften (Dr.rer. nat.)

der

Mathematisch-Naturwissenschaftlichen Fakultät

der

Universität Greifswald

Vorgelegt von Jared Thomas Freiburg

Greifswald, 14th of January, 2022

Dekan*in: Prof. Dr. Gerald Kerth.....

1. Gutachter*in: Prof. Dr. Laurence Warr.....

2. Gutachter*in: Prof. Dr. Guido Meinhold.....

Tag der Promotion: 23.06 2022.....

Table of Contents

Abstract

Anthropogenic greenhouse gases such as carbon dioxide ($C0_2$) must be mitigated and reduced to preserve a stable climate for future generations. One promising technology is carbon capture and storage (CCS) in geologic formations, which is currently being deployed in numerous pilot projects across the United States. One of these is the Illinois Basin–Decatur Project that has successfully stored 1 million metric tons of $C0_2$ in the Mt. Simon storage complex. The Mt. Simon Sandstone reservoir has been largely unexplored due to a previous lack of economic interest. Oil-bearing formations in the Illinois Basin are in younger successions and formation waters in the Mt. Simon are highly saline but with low levels of critical elements (i.e. lithium, magnesium). In the Illinois Basin, a limited number of drill holes penetrate the Mt. Simon formation with an even smaller number of core samples in these deep strata. This has left the earliest Paleozoic rocks in the Illinois Basin poorly understood. The stratigraphic test well at the IBDP revealed the lowest most section of the Mt. Simon to be a thick highly porous and permeable sandstone. With a near to complete lack of other wells penetrating this lower Mt. Simon unit, major questions arose such as 1) what is the origin of this deep porous sandstone; 2) what controls the distribution of this sandstone and where can more of it be found; 3) what controls porosity at this depth when overlying sandstones have largely poor reservoir properties; and 4) is it suitable for geologic carbon storage (i.e. are there high quality seals that provide secure storage and prevent vertical migration)?

This research examines the origin and diagenesis of the Mt. Simon storage complex by first resolving the age of the underlying Precambrian basement and investigating basement structures associated with sediment accommodation (chapter ii). Basement geochronology and a comprehensive investigation of the Mt. Simon provenance (chapter iii) suggests a largely local sediment supply depositing into a rift basin. Detrital zircon geochronology of the lower Mt. Simon yields a dominant Mesoproterozoic proximal source as confirmed in regional basement samples yielding Eastern Granite-Rhyolite, Southern Granite-Rhyolite, and Mazatzal Province rocks. A small peak of Early Cambrian zircons (527 to 541 Ma) in the lower Mt. Simon is indicative of rift volcanics as confirmed by the geochronology of a basalt sample recovered in a deep stratigraphic test hole along the rift axis in west-central Indiana. Failed rifting pre-dated the formation of the Illinois Basin with the earliest Paleozoic sediments deposited in a northward trending Cambrian aulacogen. Locally sourced arkose in the lower Mt. Simon is considered to present an anomalously high porosity that was preserved throughout its diagenetic history. Petrographic characterization shows the lower Mt. Simon contains abundant diagenetic grain coatings of illite that prevented pervasive nucleation of authigenic quartz found in the other overlying Mt. Simon units (chapter iv). These clay coating are considered the most significant feature that controlled porosity preservation in the Mt. Simon storage complex. Geochronology of these illite coatings reveals two major events of illitization both of which correspond with structural deformation and igneous activity in and around the basin in response to regional orogenic events (chapter v). The early illitization event (mostly Carboniferous) was associated with smectite illitization and potassium feldspar dissolution, which caused significant secondary porosity. The later illitization event (Triassic) is identified in non-reservoir units of the Mt. Simon where pore occluding kaolinite was partially illitized. Lastly, high-resolution pore space characterization of thick pervasive shale formations overlying the Mt. Simon indicates the Eau Claire shale,

directly overlying the Mt. Simon, provides the best seal to the Mt. Simon reservoir completing the Mt. Simon storage complex (chapter vi).

Chapter i

Introduction to the Mt. Simon storage complex, including publications and author contributions

Addressing anthropogenic carbon dioxide (CO_2) mitigation from power and industrial sources is imperative for maintaining the increasing demand for energy while limiting the effects of CO_2 on climate change during the shift to green energy. Geologic carbon capture and storage (CCS) has been identified as an important technology to address the challenges of climate change while future green technologies become available (Pacala and Socolow, 2004; Bachu et al., 2007; Gibbins and Chalmers, 2018; Rackley, S.A.; 2017; Linda and Singh, 2021). In order to demonstrate safe geologic storage of CO_2, a thorough assessment of the reservoir and seal must be completed prior to the deployment of large-scale CCS. This study aims to investigate the origin of a CCS reservoir while closely examining the reservoir seal system that will be subject to future industrial-scale CCS projects.

The Cambrian Mt. Simon Sandstone has been the recent subject of extensive study (Leetaru et al., 2009; Bowen et al., 2011; Medina et al., 2011; Freiburg et al., 2014; Ritzi et al., 2018; Reesink et al., 2020; Akono et al., 2021) concurrent with multiple industrial-scale CO_2 storage demonstrations in central Illinois, USA (Figure 1). The first major demonstration project in the Illinois Basin for CCS was the Illinois Basin–Decatur Project (IBDP) and is the seminal demonstration project of the ever-expanding carbon capture, utilization, and storage (CCUS) infrastructure in the Illinois Basin (Finley, 2014; Figure 2). At the IBDP, an extensive set of drill core was recovered in units of the Mt. Simon Sandstone that had previously never been cored, and thus, much of the geology was inferred based on regional geologic trends, geophysical well logs, and shallower Mt. Simon drill core where certain depositional facies are not present (Buschbach and Bond, 1974; Willman et al., 1975; Hoholick et al., 1984; Makowitz and Milliken, 2003; Lovell and Bowen, 2013). The drill core from the IBDP currently represents the most complete set of Mt. Simon samples including the Precambrian basement in and around the Mt. Simon depocenter (Freiburg et al., 2014) or what has previously been referred to as the proto-Illinois Basin (Treworgy, 1988; Kolata and Nelson, 1990). The studies presented herein focus on the Mt. Simon storage complex and were conducted with collaborators for their respective expertise and research input. Co-author contribution varied on each chapter with details of each author's contribution outlined in table 1. This study considers the following geologic units as what is herein referred to as the Mt. Simon storage complex: 1) the underlying Precambrian basement; 2) the entire Mt. Simon including reservoir and non-reservoir quality lithologies; and 3) the overlying caprocks (primarily shale-rich formations; Figure 3). Chapter ii focuses on the characterization of the Precambrian basement directly beneath the Mt. Simon Sandstone at the IBDP. Including the Precambrian basement may seem unconventional in a reservoir-seal system; however, characterization of the basement is critical for micro-seismic mitigation during CO_2 injection and storage (Bauer et al., 2016; Williams-Stroud et al., 2020) and for understanding the depositional controls on the reservoir (Leetaru and McBride, 2009).

Chapter iii investigates the provenance of the Mt. Simon Sandstone reservoir including shallower non-reservoir units in the Mt. Simon. This chapter highlights the importance of proximally sourced sediments

from the local Precambrian terrain and identifies the first Cambrian igneous rocks found within the Illinois basin and associated with basalt identified within a failed rift trending northwest-southeast across east-central Illinois and west central Indiana. Prior to this research, early Cambrian rifting was hypothesized with an overall lack of substantial geochronologic evidence (Marshak and Paulsen, 1996; Hildebrand and Ravat, 1997; Potter et al., 1997).

Chapter iv examines the major diagenetic controls (i.e. compaction, cementation) on all units within the Mt. Simon Sandstone. Clay mineral cements are identified as a major control on reservoir properties with past studies indicating a complex paragenetic history of detrital grain alteration and diagenetic cementation (Duffin et al., 1989; Fishman, 1997; Chen et al., 2001; Grathoff et al., 2001; Pollington et al., 2011). Illite clay coatings are identified as the most important control on reservoir porosity preservation within the Mt. Simon.

Chapter v investigates the timing of illitization throughout the Mt. Simon and overlying caprocks. Illite polytype quantification combined with potassium (K) – argon (Ar) dating allows the extrapolation to apparent detrital and diagenetic illite dates. These age dates coupled with paragenetic relationships are used to interpret illitization events, controls on reservoir properties, and major continental-scale tectonics controlling midcontinent deformation and fluid migration.

Lastly in chapter vi, caprock overlying the Mt. Simon reservoir are investigated through mineral and pore space characterization, sealing properties, and CO_2 sealing capacity. Together, this study investigates the origin and diagenesis of the Mt. Simon Sandstone in the Illinois Basin with much attention on the Mt. Simon storage complex and implications for CCS. The geologic background and a high-level synopsis of major contributions from each chapter herein are discussed below.

Figure 1 Map of the United States with the outline (blue) of the Illinois Basin and the location of the Illinois Basin—Decatur Project in Decatur, Illinois

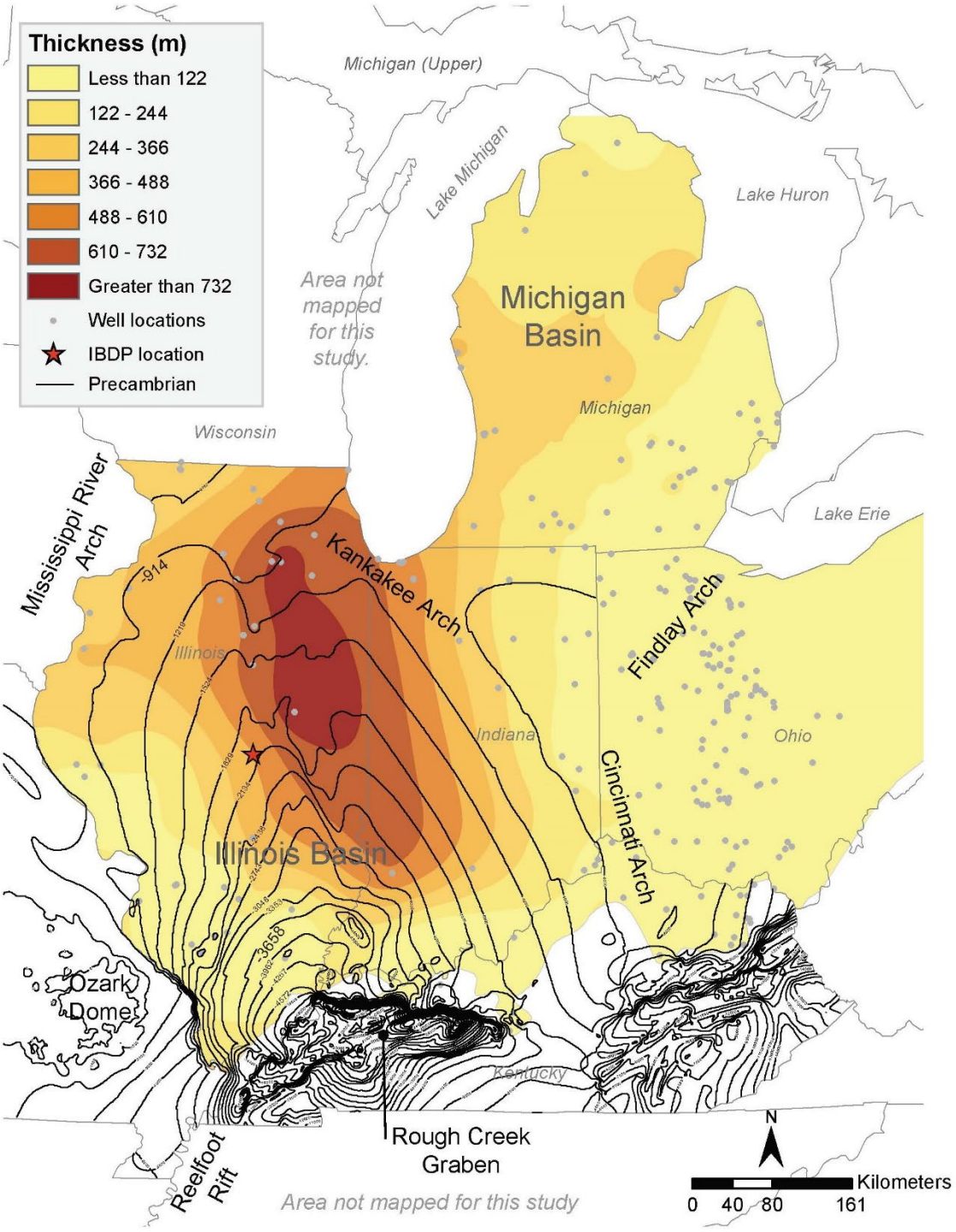

Figure 2 Isopach map displaying Mt. Simon Sandstone and Argenta Formation thickness and distribution, Precambrian Basement topography, the location of the Illinois Basin—Decatur Project (IBDP), and locations of wells penetrating the Mt. Simon Sandstone. The Precambrian topography defines the Illinois Basin depocenter in southeastern Illinois, shows offset from the Mt. Simon depocenter in east-central and north-east Illinois, and show the deformation along the Cambrian aulacogen or proto-Illinois Basin.

Author	Contribution									
	Text		Analysis						Interpretation	
	Primary	Secondary	Petrographic	Geochronology	Geophysics	Statistics	Mineralogy	FIB-SEM	Major	Minor
Freiburg	i, ii, iii, iv, v, vi		ii, iv, v, vi	ii, iii	ii, iv		ii, v, vi		i, ii, iii, iv, v, vi	
McBride		ii			ii				ii	
D. Malone		iii		iii					iii	ii
Leetaru					ii					ii
Holland		iii								iii
S. Malone		iii								iii
Ritzi		iv				iv				iv
Kehoe		iv	iv							
Grathoff							v, vi	vi	v	vi
Henkel							v			v
Wemmer				v						
Peltz								vi	vi	
Willette		vi				vi				vi

Table 1 Author and co-authors contributions to chapter manuscript contents and all publications summarized in Chapters ii, iii, iv, v and vi:

ii. Freiburg, J. T., McBride, J. H., Malone, D. H., & Leetaru, H. E. (2020). Petrology, geochronology, and geophysical characterization of Mesoproterozoic rocks in central Illinois, USA. Geoscience Frontiers.

iii. Freiburg, J.T., Holland, M.E., Malone, D.H., & Malone, S.J., (2020). Detrital zircon geochronology of basal Cambrian strata in the deep Illinois Basin, USA: Evidence for Paleoproterozoic-Cambrian tectonic and sedimentary evolution of Laurentia. Journal of Geology

iv. Freiburg, J. T., Ritzi, R. W., & Kehoe, K. S. (2016). Depositional and diagenetic controls on anomalously high porosity within a deeply buried CO2 storage reservoir—The Cambrian Mt. Simon Sandstone, Illinois Basin, USA. International Journal of Greenhouse Gas Control, 55, 42-54.

v. Freiburg, J.T. Grathoff, G.H., Henkel, K., Wemmer, K. (in press) The timing of illitization in Paleozoic Strata at the Illinois Basin—Decatur Project: Implications for CO2 Storage. to be published in Illinois Basin Decatur Final Report (2021) Sallie Greenberg (ed.) on United States Department of Energy OSTI.gov

vi Freiburg, J.T., Peltz, M., Grathoff, G.H. (in review) High-resolution pore network and mineralogical modeling of sealing shales at the Illinois Basin-Decatur Project, USA

Author: Jared T. Freiburg

Advisor: Prof. Laurence Warr

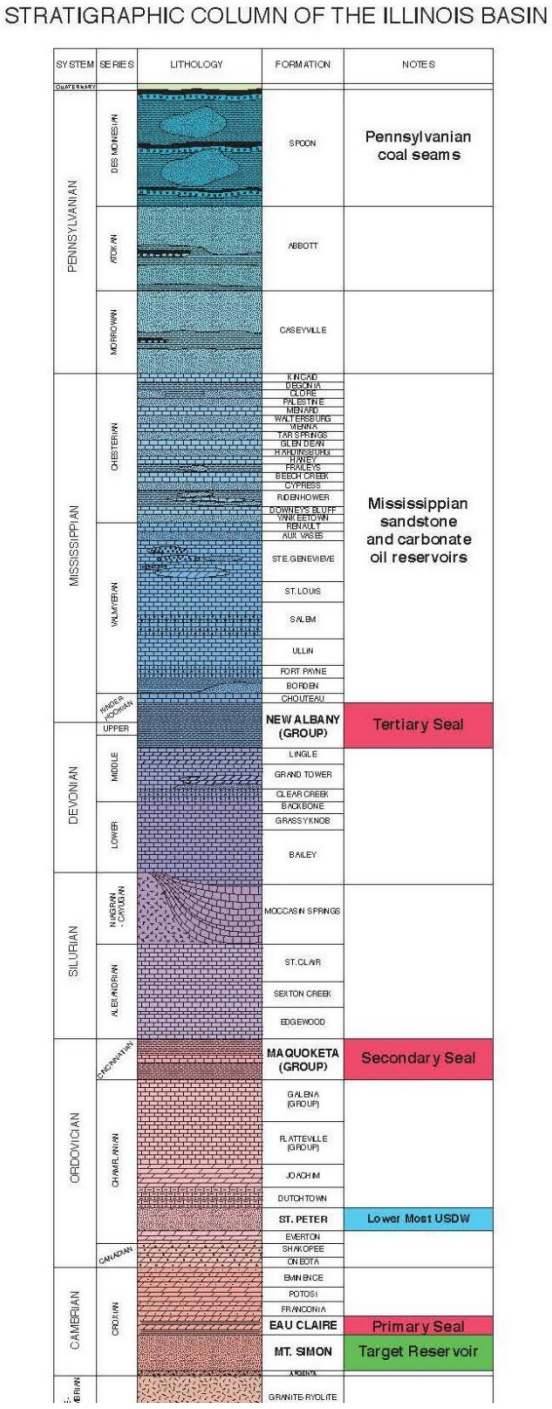

Figure 3 Stratigraphic column in the Illinois Basin with identified reservoirs and seals in the Mt. Simon storage complex.

The Mt. Simon storage complex: Precambrian basement and regional tectonics

The origin of the lower Mt. Simon is poorly understood. The current known distribution of the entire Mt. Simon relative to the structural depocenter of the Illinois Basin (Figure 2) suggests early Paleozoic tectonics played a key role in the deposition of these lower most Cambrian strata by causing subsidence and creating accommodation space for the proximally sourced sediments of the lower Mt. Simon Sandstone (chapters ii and iii). A greater understanding of the regional basement terrain, inherent structures, and sediment provenance assist with predicting the distribution of the lower Mt. Simon reservoir across the Illinois Basin.

The Mt. Simon depocenter is located in northern and east-central Illinois along the axis of a structural feature known as the Lasalle Anticlinorium (Nelson, 1990). This Mt. Simon basin or proto-Illinois Basin predates the Illinois Basin depocenter (located in southern Illinois) and is proposed to have formed as an early Cambrian aulacogen concurrent with the end of the breakup of Rodinia (chapter iii; Freiburg et al. 2020a;). Early Cambrian volcanism associated with this rift event occurred near areas of maximum extension (i.e. depocenter axis) where thinning of crust occurred, and mantle melts ascended. This hypothesis has been confirmed in drill core recovered from the recent CarbonSAFE Wabash #1 well in West Terre Haute, Indiana where a flood basalt approximately 9 meters thick was encountered below the Mt. Simon and overlying a Mt. Simon-like sandstone. A recent Ar-Ar date of the basalt yielded an age of 525 ± 1 Ma. Seismic reflection data over the well location reveals a series of three prominent reflectors that suggest multiple basalt layers. These rift-related volcanic occurrences are further supported by detrital zircons identified in the Argenta and lower Mt. Simon sandstones on the western flank of the rift recording dates from 540 to 525 Ma (Freiburg et al., 2020a). This suggests the deposition of the lower Mt. Simon and underlying

sedimentary rocks were likely penecontemporaneous with rift related volcanism associated with the final episodes of the break-up of Rodinia.

Other detrital components of the lower Mt. Simon Sandstone include Mesoproterozoic age rocks of the Granite-Rhyolite Province (GRP; both Southern Granite-Rhyolite Province (SGRP) and Eastern Granite-Rhyolite Province (EGRP)) and Paleoproterozoic age rocks of the Mazatzal Province (Freiburg et al., 2020a). These three major detrital zircon age peaks are proximally sourced as supported by the U-Pb geochronology age data of zircons extracted from Precambrian basement rhyolite core from three regional wells: 1371 ± 8 Ma at the T.R. McMillen #2 well in Christian Co., Illinois; 1467 ± 9 Ma at the Verification #1 well in Macon Co., Illinois (chapter ii; Freiburg et al., 2020b); and 1650 ± 13 Ma at the Futuregen Alliance #1 well in Morgan Co., Illinois. The younger ages are consistent with ages reported from the SGRP and the EGRP respectively (Van Schmus et al., 1996). This is the first report of SGRP age basement rocks in Illinois that have previously been reported from eastern Kansas and Missouri (Van Schmus et al., 1996) to west Texas (Barnes et al., 2002). The wells with SGRP and EGRP age basement cores are located in central Illinois and likely associated with a large isolated spherical magnetic anomaly (Freiburg et al., 2020b) observed on the Illinois statewide aeromagnetic map (Daniels et al., 2008). The SGRP rhyolite is particularly magnetic with a high magnetite content. The EGRP rhyolite is crosscut by magnetite-rich olivine gabbro that was recently dated yielding an Ar-Ar date of 1335 ± 19 Ma (hornblende) consistent with SGRP dates. A high resolution 2D seismic profile across the magnetic anomaly and to the west of the anomaly reveals a bowl-shaped Precambrian layered sequence (McBride et al., 2016) of younger crust emplaced onto older crust (chapter ii; Freiburg et al., 2020b). This layered sequence is comprised of SGRP and EGRP rocks as indicated by drill core. These rocks were emplaced onto older rocks that appear to have the same seismic reflection signature and structural affinity as basement rocks to the west dated as older Mazatzal Province (chapter ii). The boundaries of the emplaced EGRP and SGRP crust on Mazatzal Province are susceptible to faulting during continental-scale tectonic events (Freiburg et al., 2020b). For example, approximately 16 km (10 mi) west of the IBDP site, Mesoproterozoic crust of the SGRP and EGRP contacts the Mazatzal crust and appears as an angular unconformity. At this contact, a fault, presumably a detachment, is observed and can traced downward to the east. The discontinuity likely experienced failure during continental-scale break up or rifting events. Such phenomena are observed in other continental rifts (i.e. East African Rift System; Chorowicz, J., 1989). Detachment occurs along a ramp like feature that outlines the bowl-like structure (Mcbride et al., 2016) that host the SGRP and EGRP crust (Freiburg et al. 2020b). Extension appears to occur along this seismic-discontinuity and is further accommodated through a series of steep angle normal faults closer to the Precambrian surface of the bowl-like structure. Most of the extension within a continental rift is accommodated through displacement on a series of normal faults (Bosworth, 1985). Along this series of normal faults, localized accommodation on the hanging wall, provides areas of catchment for proximal sediment from footwall Precambrian highs via alluvial, fluvial, and eolian processes. These series of normal faults host some of the thickest sediment packages of lower Mt. Simon Sandstone and present exploration opportunities for new CCS reservoirs.

A major control on the maturity of a particular section of the Mt. Simon is the depositional environment and the location of the sediment source. In general, the further the sediment is transported, the more

mature it is (i.e. more sorted, rounded, and less feldspar and lithic detritus). Thus, more proximal sediments will generally be less mature than a sediment supplied from a distal source. Previous work has demonstrated that changes in detrital zircon U-Pb age distributions, which are interpreted as changes in sedimentary provenance, correspond to distinct changes in framework grain composition within the Mt. Simon Sandstone (Lovell and Bowen, 2013). Detrital zircon U-Pb age distributions change from the base of the Mt. Simon to the top and correspond to fluctuation in sedimentary provenance driven by eustatic changes (Runkel et al., 2007) and tectonic activity. A drop in the base-level results in more proximal, locally sourced sediments, whereas a rise in base-level or transgression would result in an influx of distally sourced sediments. The proximally sourced sediments contain more feldspar, polycrystalline quartz, and clay while distally sourced sediments are more mature with less detrital feldspar, more monocrystalline quartz, and less clay (Lovell, 2017). Conclusions by Lovell (2017) suggested that increased polycrystalline quartz in the lower Mt. Simon is more susceptible to dissolution than monocrystalline quartz leading to increased authigenic quartz in the lower Mt. Simon. Freiburg et al. (2016) found less authigenic quartz in the lower Mt. Simon than the monocrystalline quartz rich upper Mt. Simon. Based on detrital zircon work (chapter iii), the arkosic lower Mt. Simon is not present in the location of Lovell's study (2017) and lies outside of the lower Mt. Simon depocenter.

The Mt. Simon storage complex: the Cambrian Mt. Simon Sandstone and controls on reservoir properties

At the IBDP site, the Mt. Simon Sandstone is divided into three major lithostratigraphic sections: the lower, middle, and upper (Freiburg et al., 2014; Figure 4). The lower Mt. Simon is the IBDP reservoir due to its locally thick and continuous section of high porosity/permeability properties. The Mt. Simon divisions are controlled by changes in depositional environments and observed throughout much of the basin (Morse and Leetaru, 2005; Leeatru and McBride, 2009; Medina et al. 2012; Freiburg et al., 2014). A series of siltstones, sandstones and conglomerates, referred to as the Argenta, underlie the Mt. Simon. These are believed to be disconformable with the Mt. Simon (Freiburg et al., 2015) and marked a distinct change in depositional environment. The Argenta interval unconformably overlies the Precambrian basement. The lower, middle, and upper Mt. Simon sections can be further divided into units based on major depositional facies. These include fluvial braided river, floodplain, alluvial plain, eolian sand-sheet, dune, interdune, beach, lagoon, and shallow marine deposits. The best reservoir-quality rocks in the lower Mt. Simon and are predominantly eolian, beach, fluvial, and alluvial plain deposits (Reesink et al., 2020). Similar fluvial and eolian deposits in the middle Mt. Simon have poor reservoir properties due to higher diagenetic cementation (Freiburg et al., 2014) and differentiate the middle Mt. Simon from the lower Mt. Simon. The depositional cycle and resulting diagenetic differences likely reflect the evolution of the Proto-Illinois Basin in the early Cambrian aulacogen. The lower Mt. Simon Sandstone is commonly referred to as the "arkosic" section due to its increase in feldspar with depth nearing the Precambrian surface. Below the arkose, a previously unidentified sandstone unit is now referred to as the Argenta (Freiburg et al., 2015). Despite being partly arkosic, textural and mineralogical differences compared to the overlying lower Mt. Simon give it distinctly lower reservoir properties making it easily recognized on geophysical logs. Provenance has a direct impact on sandstone composition (Dickenson and Suzcek, 1979), specifically framework composition, and can thus impart controls (i.e. compaction, cementation, and dissolution) on the reservoir quality. Due to the lack of deep wells with core, much of this work focused on the entirety

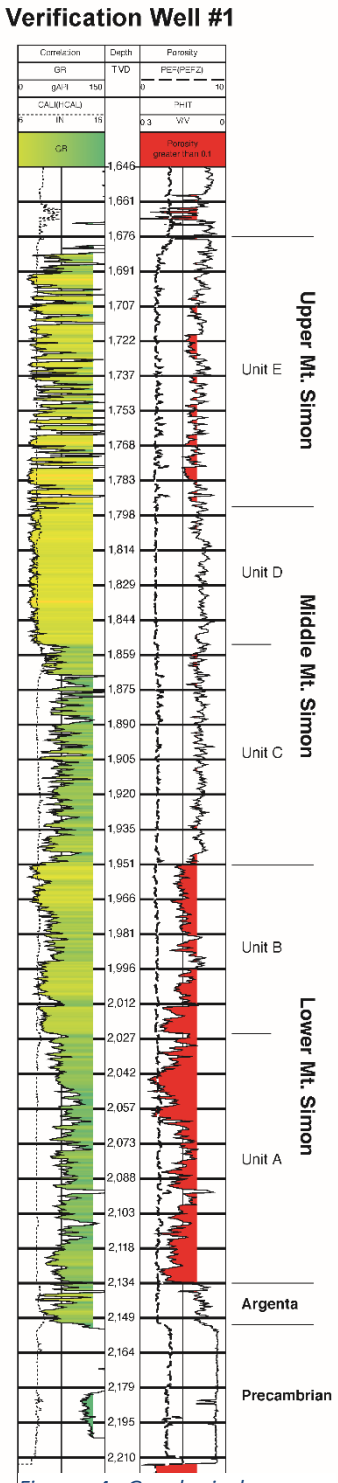

Figure 4 Geophysical gamma and neutron porosity logs from the IBDP Verfication #1 well displaying section through the Mt. Simon Sandstone showing units. Porosity greater than 10% is red.

of the Mt. Simon, but few studies were undertaken on the lower most Mt. Simon (Bowen et al. 2011), which hosts the best reservoir properties, at least in east-central Illinois.

Compaction of sediments is the most detrimental to reservoir properties followed closely by cementation (chapter iv; Freiburg et al., 2016). Sediments were compacted as burial depth increased and thus the degree of sediment compaction is observed to increase with depth. The controls on cementation were many (i.e. mineralogy, texture) but generally related to the depositional environment and perhaps were tectonically controlled sediment packages rather than a simple burial depth model. For example, cementation in the lower, middle, and upper Mt. Simon are significantly different from each other but similar throughout each individual section or depositional package. Mineralogy, controlled by sediment source or provenance, played a major role in diagenetic cementation. For example, a mature, fine to medium-grained quartz arenite such as that of the middle Mt. Simon Unit D, has more quartz cement than a less mature, medium to very coarse-grained sub-arkose such as those of the lower Mt. Simon units. Quartz surface area increases in the quartz arenite along with enhanced quartz cement growth. Diagenetic clay minerals also appear to have influenced sandstone cementation. Authigenic clay coats are abundant in the lower Mt. Simon and likely inhibited nucleation of authigenic quartz (Figure 5). This does not appear to have been the case in the middle Mt. Simon where authigenic illite coatings commonly coat detrital grains but did not deter authigenic quartz nucleation. Clay content is generally higher in the middle Mt. Simon compared to the lower Mt. Simon and likely originated as allogenic or detrital smectite and was diagenetically altered or illitized during the burial record. Pore occluding and likely allogenic clays in both the Argenta and middle Mt. Simon reflect higher sediment supply and likely correlate to regional tectonic events. Nearly all clay throughout the Mt. Simon is identified as illite. Since illite strongly influenced reservoir properties throughout the Mt. Simon, determining the timing and controls on illitization is important for modeling and predicting basin-scale reservoir properties. Based on K-Ar geochronology, the lower Mt. Simon experienced an early diagenetic event from 360 to 315 Ma (chapter iv). During illitization, tectonically driven brines passed through the lower and upper Mt. Simon, the most porous units of the Mt. Simon, illitizing all smectite. The tighter Argenta and middle Mt. Simon, both rich in allogenic and pore occluding clay, experienced illitization in a later tectonically driven event from 250 to 220 Ma (chapter iv). This late event of illitization may be contemporaneous with late stage feldspar dissolution and secondary porosity development in the lower Mt. Simon.

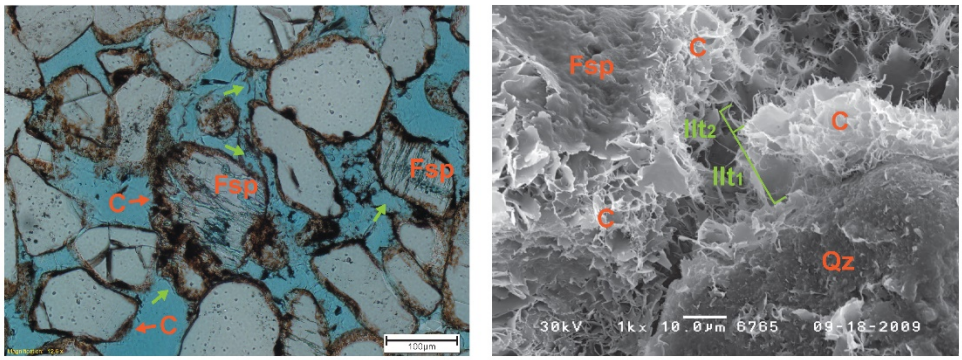

Figure 5(A) thin section photomicrograph from the lower Mt. Simon showing common clay coatings (C) on detrital quartz (Qz) and feldspar (Fsp) grains. Feldspar grains are partially to completely (green arrows) dissolved contributing secondary porosity. (B) Scanning Electron Microscope photomicrograph of lower Mt. Simon showing multiple illite cement generation (Ilt1, Ilt2) coatings over detrital quartz and feldspar grains.

The Mt. Simon storage complex: caprocks

The Cambrian-age Eau Claire Formation directly overlies the Mt. Simon Sandstone and is the caprock at the IBDP (Figure 3). Two other thick shale units, the Ordovician-age Maquoketa Group and the Devonian-age New Albany Shale Group, are considered secondary seals and lie in shallower Paleozoic horizons. The Eau Claire is laterally extensive, underlies all of Illinois, and is only found in the subsurface (Willman et al., 1975). The Eau Claire Formation is described as a heterolithic, shallow marine succession, dominated by interbedded shale, siltstone, sandstone, and dolomite (Yawar and Schieber, 2008; Neufelder et al., 2012; Lahann et al., 2014). Despite the Maquoketa and New Albany shales not directly overlying the reservoir, they are both thick, laterally extensive formations that occur throughout much of central and southern Illinois (Willman et al., 1975). The Maquoketa Group is comprised of four formations, three of which are described as shale (Kolata and Graese, 1983). The New Albany Shale Group is comprised of five distinct shale formations (Cluff et al., 1981).

Evaluation of the shales overlying the reservoir at the IBDP are necessary to securely store injected CO_2. A variety of studies have analyzed the lithology, mineralogy, petrophysics, pore size distribution and capillary entry pressure, fluid-fracture pressure, CO_2-brine-rock interaction, (Liu et al., 2012; Neufelder et al., 2012; Lahann et al., 2013; Lahann et al., 2014; Mastalerz et al., 2013; Mozley et al., 2016; Medina et al., 2020) throughout the Illinois Basin, but no study has evaluated the pore space and seal capacity of all major caprocks at a single CCS demonstration project in the Illinois Basin such as the IBDP. In chapter vi, the nanometer-scaled pore system and mineralogy of the three major caprocks including a mudstone within the Mt. Simon Sandstone at the IBDP are characterized. The nanometer-scale pore system of shales is an important control on fluid transmissivity (Chalmers et al., 2012) and vital for understanding the seal capacity (Ross and Bustin, 2009). The research presented in chapter vi does not propose to represent the entire formation with small, single samples, but instead attempts to provide awareness of the nature and variability in the pore structure and mineralogy in caprocks at the IBDP.

Chapter ii synopsis: Petrology, geochronology, and geophysical characterization of Mesoproterozoic rocks in central Illinois, USA

The Precambrian basement rocks of the Eastern Granite-Rhyolite Province (EGRP) in central Illinois (midcontinent region of North America), which are largely obscured by younger Phanerozoic strata, exhibit a complex history of early volcanism, granite emplacement, and shallow intrusion of deeper-seated mafic rocks. A comprehensive suite of dedicated petrographic analysis, geophysical-logs, and drill core from four basement-penetrating wells, two-dimensional and three-dimensional seismic reflection, and U-Pb age data from the IBDP site provide new constraints for interpreting the Precambrian basement of the Illinois Basin. These new data reveal the basement to be compositionally and structurally complex, having typical EGRP felsic volcanic rocks intruded by the first reported *in situ* gabbro in Illinois. Ample zircons (n=29) from rhyolite give a U-Pb weighted mean average age of 1467±9 Ma. Sparse zircons (n=3) from a gabbro dike that intrudes the rhyolite yields a concordia age of 1073±12 Ma which corresponds to the latest stage of Keweenawan rifting, and represents the first Keweenawan-age rock in Illinois and in the EGRP. A high-resolution three-dimensional seismic reflection volume, coincident with the four wells, provides a context for interpreting the petrological data and implies a high degree of heterogeneity for basement rocks at the IBDP site, as also shown by the drill cores. The occurrence of Keweenawan-age gabbro is related to a prominent bowl-like structure observed on local two-dimensional seismic reflection profiles and the three-dimensional volume that is interpreted as a deep-seated mafic-sill complex. Furthermore, heterogeneities such as brecciated EGRP rhyolite and later gabbro intrusion observed in the basement lithology at the IBDP may reflect previously unknown distal elements of the 1.1 Ga Keweenaw Rift in the EGRP.

This is the first work that has provided comprehensive mineralogy and geochronology of the Precambrian rocks at the IBDP. Before this research, there have been a total of four age-dates of Precambrian rocks throughout the entirety of Illinois (Bickford et al. 2015) with all rocks classified as EGRP. This research presents new evidence for late rifting, SGRP and EGRP volcanism, and suggests a much more heterogeneous Precambrian basement among the previous characterized EGRP.

Chapter ii supplemental geochronology data on the Precambrian Basement in central Illinois, USA

Introduction

In addition to the four wells that penetrate Precambrian basement at the IBDP, Precambrian core samples were acquired for two new wells that penetrate the Precambrian basement (Figure 6). The first well is the T.R. McMillen #2 well located approximately 29 km (18 mi) southwest of the IBDP wells. This well was drilled as part of the CarbonSAFE Macon County project; a carbon storage feasibility study. The well is located on the southwest flank of the positive magnetic anomaly identified in Freiburg et al. (2020). The second well is the FutureGen Alliance #1 well located approximately 160 km (100 mi) due west of the IBDP wells. It was drilled as part of the FutureGen 2.0 Project; a carbon storage demonstration project. The T.R. McMillen #2 well is located on the east side of the Nd-line (Figure 6; Van Schmus et al., 1996) and the FutureGen Alliance #1 is on the west side. The Precambrian rocks from both wells are described as meta-rhyolite; or altered rhyolites. One core sample from each well was selected for geochronology and zircons

were mechanically separated for U-Pb dating following the methods outlined in Freiburg et al. (2020). Also, for a more robust age date of the gabbro intruding the 1467±9 Ma rhyolite at the Verification #2 well at the IBDP site (Figure 6), $^{40}Ar/^{39}Ar$ geochronology was completed. Previous U-Pb zircon geochronology yielded a concordia age of 1073±12 Ma Freiburg et al. (2020).

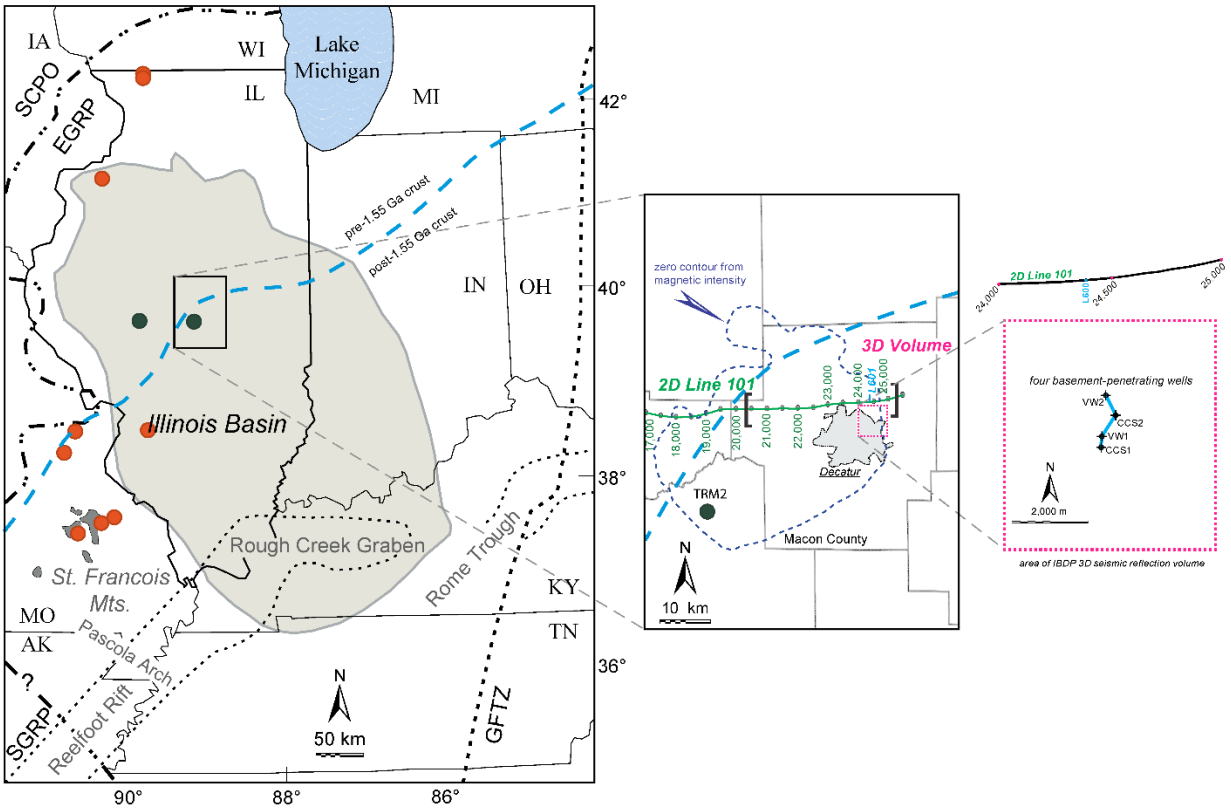

Figure 6 Modified from Freiburg et al. (2020) figure 1 to includetwo new wells that Precambrian core samples were acquired from (black circles). The map t the left shows the Futuregen Alliance #1 well furthest to the west and the T.R. McMillen #2 well to the east (in box). The center map shows the T.R. McMillen well and its proximity from the IBDP wells and location on the magnetic high. The map on the right shows the location of the IBDP wells with the gabbro sampled from Verification #2 well (VW#2).

Results

Zircons were separated from approximately 1 kg (TRM2) and 0.5 kg (FutureGen1) of rhyolite. The U-Pb geochronology results are provided in tables 2 and 3. Twenty-three zircons from T.R. McMillen #2 rhyolite where analyzed, and twelve zircons were used in the age calculation. Rejected zircons were either more than 20% discordant, 3% reverse discordant, had high internal error, or had more than 1000 ppm ^{204}Pb. Uranium concentrations are moderate to high and range from 63 ppm to 613 ppm. The U/Th ratio ranges from 0.8 to 3.8. Zircon ages range from 1352.2 Ma to 1468.5 Ma. The Concordia age is 1372 ± 13

Ma with an MSWD of 0.95 (2s; Figure 7A). The WMA of these same zircons is 1376.0 ± 8.9 Ma with a MSWD of 0.89 (Figure 7B). Twenty-two zircons were analyzed from the FutureGen Alliance #1 rhyolite. Ten passed the filters indicated above. Uranium concentrations are moderate to high and range from 58 ppm to 667 ppm. The U/Th ratio ranges from 1.5 to 2.0. Zircon ages range from 1350.7 Ma to 1730.8 Ma. Most zircons range from 1630.6 Ma to 1673.2 Ma with a Concordia age of 1653 ± 20 with an MSWD of 0.22 (2s; Figure 7C). The WMA of these zircons is 1649 ± 13 (95% confidence interval) with a MSWD of 1.17 (Figure 7D). The $^{40}Ar/^{39}Ar$ dating results (plateau ages with 2σ uncertainties) for the Verification #2 well gabbro is presented in table 4.

Well_analysis	Isotope ratio									
	U (ppm)	$^{206}Pb/^{204}Pb$	U/Th	$^{206}Pb/^{207}Pb$*	± (%)	$^{207}Pb/^{235}U$ *	± (%)	$^{206}Pb/^{238}U$	± (%)	Error correction
TRM2_1_25	112	37727	2.6	11.5387	0.7	2.8024	1.1	0.2346	0.9	0.79
TRM2_1_9	107	33890	1.8	11.5052	1.1	2.7348	1.6	0.2283	1.2	0.73
TRM2_1_17	396	30326	0.8	11.4215	0.6	2.3738	1.5	0.1967	1.4	0.91
TRM2_ 1_3	87	23550	3.2	11.4099	0.6	2.7782	1.2	0.2300	1.0	0.86
TRM2_1_10	69	21054	2.1	11.4033	0.8	2.7777	1.3	0.2298	1.0	0.77
TRM2_1_16	63	18955	2.8	11.3930	0.8	2.8009	1.3	0.2315	0.9	0.74
TRM2_1_11	97	40262	1.9	11.3387	0.6	2.7398	1.2	0.2254	1.0	0.86
TRM2_1_5	379	303209	1.0	11.3265	0.7	2.6687	1.1	0.2193	0.9	0.78
TRM2_1_23	613	20034	1.0	11.3027	0.7	2.5861	1.6	0.2121	1.4	0.90
TRM2_1_6	232	28986	2.8	10.9971	0.6	3.1612	1.2	0.2522	1.0	0.87
TRM2_1_19	261	300158	3.8	10.8585	0.7	3.0869	1.3	0.2432	1.1	0.82

	Apparent ages (Ma)								
	$^{206}Pb/^{238}U$	± (Ma)	$^{207}Pb/^{235}U$	± (Ma)	$^{206}Pb/^{207}Pb$	± (Ma)	Best age (Ma)	± (Ma)	Concordance (%)
TRM2_1_25	1358.7	10.8	1356.2	8.3	1352.2	13.1	1352.2	13.1	100.5
TRM2_1_9	1325.6	14.4	1338.0	12.1	1357.8	21.4	1357.8	21.4	97.6
TRM2_1_17	1157.7	14.7	1234.7	10.8	1371.9	11.8	1371.9	11.8	84.4
TRM2_ 1_3	1334.5	12.4	1349.7	9.0	1373.8	11.9	1373.8	11.9	97.1
TRM2_1_10	1333.6	12.1	1349.6	9.7	1374.9	15.9	1374.9	15.9	97.0
TRM2_1_16	1342.6	11.4	1355.8	9.4	1376.7	16.2	1376.7	16.2	97.5
TRM2_1_11	1310.4	12.0	1339.3	8.7	1385.9	11.4	1385.9	11.4	94.6
TRM2_1_5	1278.3	10.3	1319.8	8.4	1387.9	13.8	1387.9	13.8	92.1

TRM2_1_23	1239.9	16.2	1296.7	11.7	1392.0	13.5	1392.0	13.5	89.1
TRM2_1_6	1450.0	13.3	1447.7	9.0	1444.3	11.0	1444.3	11.0	100.4
TRM2_1_19	1403.4	13.4	1429.4	9.9	1468.5	14.0	1468.5	14.0	95.6

Table 2 U-Pb geochronological data for the basement rhyolite in the T.R. McMillen #2 well

Well, analysis	Isotope ratio									
	U (ppm)	$^{206}Pb/^{204}Pb$	U/Th	$^{206}Pb/^{207}Pb$*	± (%)	$^{207}Pb/^{235}U$ *	± (%)	$^{206}Pb/^{238}U$	± (%)	Error correction
FutureGen1_1	114	12382	2.2	11.5474	1.1	2.8181	2.9	0.2361	2.7	0.93
FutureGen1_9	333	58206	1.4	11.2250	0.8	2.8207	3.5	0.2297	3.5	0.98
FutureGen1_11	132	12618	2.0	10.9342	1.0	2.9270	3.1	0.2322	2.9	0.94
FutureGen1_20	69	21913	2.1	9.9612	1.0	4.1487	4.8	0.2999	4.7	0.98
FutureGen1_16	62	39870	1.6	9.9270	1.1	4.2675	4.5	0.3074	4.4	0.97
FutureGen1_3	162	46109	1.6	9.9110	0.9	4.0911	2.6	0.2942	2.5	0.94
FutureGen1_2	134	135054	2.0	9.9004	0.7	4.0717	2.5	0.2925	2.4	0.96
FutureGen1_18	667	41669	1.1	9.7525	0.9	4.0453	4.5	0.2863	4.4	0.98
FutureGen1_15	82	49802	1.8	9.7345	0.9	4.1529	5.2	0.2933	5.1	0.99
FutureGen1_22	58	8033	2.0	9.4346	1.3	4.1883	5.6	0.2867	5.4	0.97

	Apparent ages (Ma)								
	$^{206}Pb/^{238}U$	± (Ma)	$^{207}Pb/^{235}U$	± (Ma)	$^{206}Pb/^{207}Pb$	± (Ma)	Best age (Ma)	± (Ma)	Concordance (%)
FutureGen1_1	1366.5	33.5	1360.4	21.9	1350.7	20.9	1350.7	20.9	101.2
FutureGen1_9	1333.1	41.6	1361.1	26.5	1405.2	14.8	1405.2	14.8	94.9
FutureGen1_11	1346.1	34.9	1388.9	23.1	1455.3	19.6	1455.3	19.6	92.5
FutureGen1_20	1690.6	69.9	1663.9	39.3	1630.5	18.2	1630.5	18.2	103.7
FutureGen1_16	1727.8	66.2	1687.1	37.0	1636.9	20.0	1636.9	20.0	104.6
FutureGen1_3	1662.5	36.3	1652.5	21.4	1639.9	16.3	1639.9	16.3	101.4
FutureGen1_2	1654.0	35.6	1648.6	20.7	1641.9	12.8	1641.9	12.8	100.7
FutureGen1_18	1622.8	63.1	1643.4	36.5	1669.7	16.3	1669.7	16.3	97.2
FutureGen1_15	1658.1	75.3	1664.8	42.8	1673.2	16.2	1673.2	16.2	99.1
FutureGen1_22	1625.1	77.5	1671.7	45.6	1730.8	24.4	1730.8	24.4	93.9

Table 3 Geochronological data for the basement rhyolite in the FutureGen Alliance #1 well

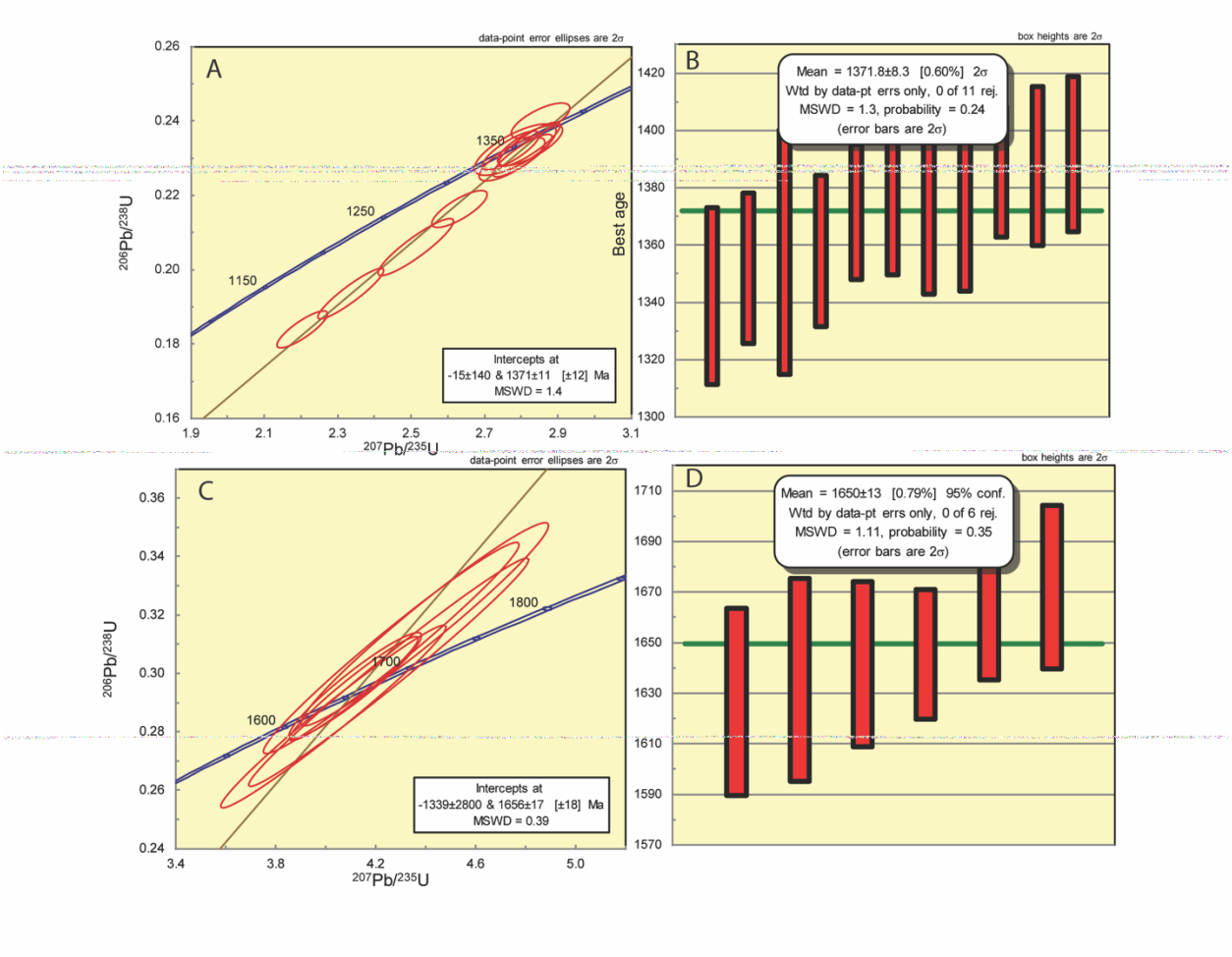

Figure 7 Concordia (A) and weighted mean age (B) determinations for the CarbonSAFE Macon Co., T.R. McMillen #1 well rhyolite. Concordia (C) and the weighted mean age (D) determinations for the FutureGen 2.0, FutureGen Alliance #1 well.

Sample			Results		
Sample Name	Location	Material	Age Type	Age Interpretation	**Age ± 2σ (i)**
VW2-7155	Decatur, Illinois	Plagioclase	Plateau	Crystallization Age	**725.26 ± 13.99 Ma**
VW2-7155	Decatur, Illinois	Biotite	Plateau	Crystallization Age	**1.332 ± 0.003 Ga**
VW2-7155	Decatur, Illinois	Hornblende	Plateau	Crystallization Age	**1.335 ± 0.019 Ga**
VW2-7155	Decatur, Illinois	Pyroxene	Plateau	Crystallization Age	**1.311 ± 0.003 Ga**

Table 4 Ar-Ar dating results for the Verification #2 well gabbro in Decatur, Illinois.

Discussion

This study provides an opportunity to compare geochronological data to a high resolution 2-D seismic profile across a major North American Precambrian terrane boundary beneath the Paleozoic in the Illinois Basin. This boundary separates the proposed Mazatzal province from the Granite-Rhyolite province which have different isotopic ages and tectono-magmatic origins (Whitmeyer and Karlstrom, 2007). The significant variation in the pattern of reflectivity for the upper Precambrian crust on the profile (McBride et al., 2020) supports previous geochemical arguments for a major suture corresponding to the terrane boundary (Van Schmus et al., 1996). Such a suture may present the convergence of a juvenile crustal block (with a model age younger than 1.55 Ga) against the older, south-east facing Laurentian continental margin (southeastern edge of the Mazatzal province) (Whitmeyer and Karlstrom, 2007; Freiburg et al., 2020b). New evidence provide here supports the emplacement or intrusion of Granite-Rhyolite province rock onto older Mazatzal-age province crust.

As discussed in Freiburg et al. (2020b), seismic reflection data suggest that the Decatur site wells including the T.R. McMillen #2 well are located on an upper Precambrian sequence that is defined by poor reflectivity and separated by a deeper, and likely older Precambrian sequence with strong reflectivity at the top (green line). The geochronology of rhyolite penetrated within this upper Precambrian sequence that forms a dish shape visible on 2-D seismic reflection (Figure 8), indicates that this sequence is comprised of Granite-Rhyolite province crust. Two events of magmatism are recorded in this sequence: (1) 1.46 Ga at the Illinois Basin Decatur Project Verification #1 well. This age correlates to the Eastern Granite-Rhyolite province (Bickford et al., 2015); (2) 1.37 Ga at the CarbonSAFE Macon County T.R. McMillen #2 well. This age correlates to the Southern Granite-Rhyolite province (Bickford et al., 2015) and is the first record of this age crust in Illinois as the most northern record of this province. This bimodal record of magmatism where early events of magmatism ~1.45 Ga have been re-intruded by later events of magmatism ~1.35 Ga has been observed in other locations, for example: (A) in Colorado the ca. 1.37 Ga San Isabel Batholith intrudes older crust consisting of ca. 1.65 and 1.44 Ga granitoids (Bickford et al., 1989); and (B) in the St. Francois Mountains of SE Missouri, the ca. 1.36 Ga Graniteville granite intrudes ca. 1.48 Ga rhyolites (Bickford and Mose, 1975). Below this magmatic intrusion of Granite-Rhyolite age rock, marked by strong reflectivity in the 2D seismic (green line), is likely older crust of which the Granite-Rhyolite intruded through. This older crust appears to be the top of the Precambrian west of the Granite-Rhyolite intrusion. On this surface, approximately 160 Km (100 mi) west of the IBDP site is the FutureGen Alliance #1 well. The seismic reflection signal near FutureGen appears similar to the deep seismic reflection signal beneath the dish-shaped structure filled with Granite-Rhyolite province rocks. In addition to the seismic reflective evidence for this is isotopic ages of rhyolite penetrated in the top of the Precambrian in the FutureGen well. Isotopic ages for zircons yielded two general age groups (table 6: (1) 1350.7 Ma to 1455.3 Ma; and (2) 1630.5 Ma to 1730.8 Ma. Three points yielded Granite-Rhyolite ages in the 1350.7 Ma to 1455.3 Ma range. These dates may be the true age of the rhyolite and it is possible that the older age group are all xenocrysts. This older age group comprises the bulk of the zircons dated and thus a Concordia age was assigned to this group of 1653 ± 20 Ma and a WMA of these zircons of 1649 ± 13 Ma, which can be classified as Mazatzal province age. The complete lack of Mazatzal-age zircons in the T.R. McMillen #2 and IBDP rhyolites imply Mazatzal-age crust is shallower and closer to the Precambrian

surface west of the major Granite-Rhyolite province intrusion viewed on seismic (Figure 8). Based on zircon data from the FutureGen rhyolite, it is most likely part of the Granite-Rhyolite province occurring as a thin intrusion of magmatic layer over a thick Mazatzal province age juvenile crust.

In addition to the significance of the evolution of the Midcontinent and the greater Laurentia unraveling the framework of the Precambrian basement is critical for mapping sediment source rock for the overlying Mt. Simon Sandstone. The lower Mt. Simon Sandstone, the storage reservoir for the IBDP, is made up of detrital sediment from five major sources, respectively: (1) Southern Granite-Rhyolite Province (ca. 1377 Ma); (2) Eastern Granite-Rhyolite Province (ca. 1460 Ma); (3) Mazatzal Province (ca. 1650 Ma); (4) Grenville Province (ca. 1129 Ma); and (5) Cambrian Rift Intrusives (ca. 533 Ma). 1, 2, and 3 can be accounted for proximally. 4 and 5 are likely more prominent towards the rift or along the Mt. Simon depocenter. Out on the far northern flanks of the Illinois Basin and Mt. Simon depocenter, the Mt. Simon detritus shows a nearly complete distal source comprised of Archaean -age sediments (Lovell and Bowen, 2013). The porous lower Mt. Simon is partly attributed to this proximal source comprised dominantly of Granite-Rhyolite province sediments particularly Southern Granite-Rhyolite province. It is proposed here that a zone of long-lived weakness in which magmatic rocks were emplaced onto older juvenile crust act as a zone of reactivation (failed rifting) and the development of a series of normal faults or localized depocenters. Along these zones of magmatism and reactivation, arkose accumulates, and the thickest lower Mt. Simon occurs.

The gabbro from the Verification #2 well in Decatur Illinois was included in this study as it was initially suspected to have an MCR age based on minimal zircon data (Freiburg et al, 2020b). The gabbro located on the western flank of this Reelfoot Rift arm has an $^{40}Ar/^{39}Ar$ plateau age date of approximately 1.33 Ga with slight variations in pyroxene, hornblende, and biotite likely a result of argon variation. This age is consistent (though slightly younger) with the pervasive GRP basement in the region and particularly the younger SGRP (Bickford and Van Schmus et al., 1987) volcanism. This highly magnetic gabbro is thought to be associated with the magnetic high observed in Decatur (Freiburg et al. 2020b) and may be related to volcanism associated with the rhyolite basement penetrated on the southwest flank of this anomaly that is also highly magnetic with zircons yielding a U/Pb age of approximately 1.37 Ga. These anomalies are common throughout the GRP as a result of the common magnetite-series granite and rhyolite (Zietz and Godson, 1982; Yarger, 1985). Despite the gabbro not showing a genetic relationship to the Wabash #1 gabbro, it does show a potential thermal reset stage in the plagioclase with a $^{40}Ar/^{39}Ar$ plateau age date of 725.26 +/- 13.99 Ma. This date is consistent with and may relate to the early event of rifting along the continental margin as proposed by the many synrift igneous rocks along the Laurentian margin (references within Thomas, 2014) and implies an earlier origin to the development of the proto-Illinois rift basin.

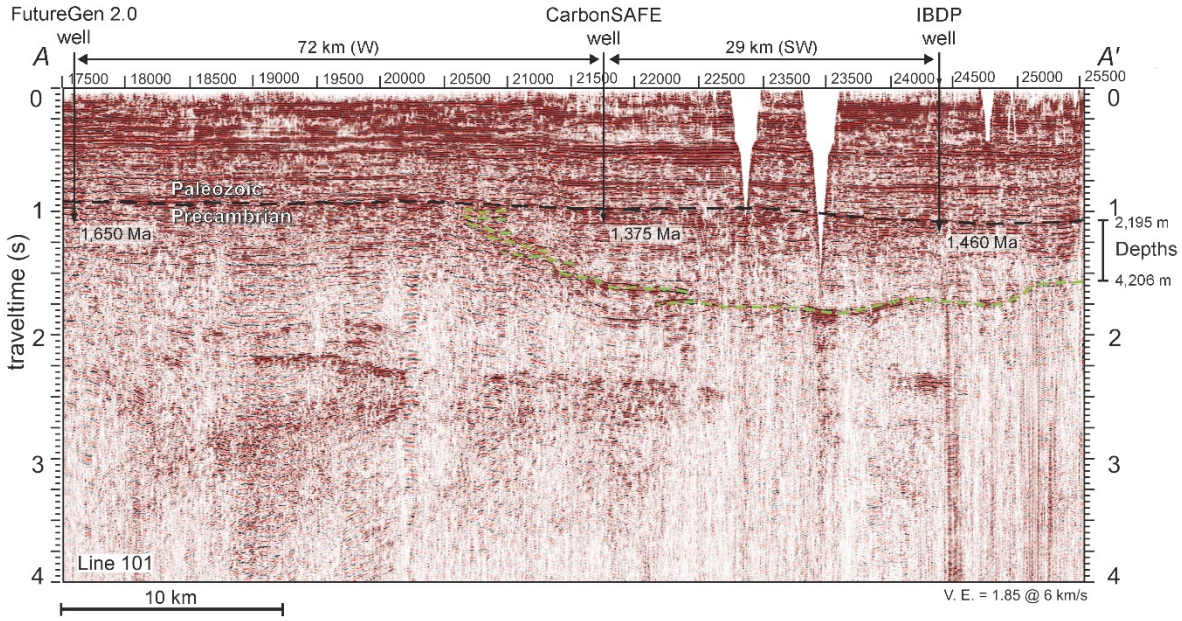

Figure 8Section of the L101 2D seismic profile A–A0 (Figure 6) through Macon Co., Illinois. The location of the IBDP wells are accurately located on the profile. The T.R. McMillen #2 (TRM #2) and FutureGen Alliance #1 (FutureGen Well #1) wells are added to the suspected locations in relationship to the observed dish-shape structure outlined by the green line. The locations of these two wells are not to scale on the profile. The mean best age (Ma) are from the Precambrian rhyolite sampled in each well.

Chapter iii synopsis: Detrital zircon geochronology of basal Cambrian strata in the deep Illinois Basin, USA: evidence for the Paleoproterozoic-Cambrian Tectonic and sedimentary evolution of central Laurentia

In this chapter, 960 new detrital zircon ages from three new, deep boreholes from the Illinois Basin, USA. These zircon age spectra reveal new details of the late Paleoproterozoic through early Cambrian tectonic history of the Illinois Basin, including evidence of the timing of the development of the Reelfoot Rift and break-up of Rodinia. The oldest detrital zircon population is ~1650 Ma, older than any known age for crystalline rocks from other deep drill cores in the basin, and conspicuously absent in other Cambrian strata in the region. This population is interpreted to have been derived from late Paleoproterozoic crust that exists beneath the Illinois Basin and was exposed during the deposition of Cambrian strata. The principle age peak is ~1375 Ma, characteristic of igneous rocks of the Southern Granite-Rhyolite province (SGRP), but also present in the St. Francois Mountains of the Eastern Granite-Rhyolite province (EGRP). A secondary peak of ~1460 Ma detrital zircon reflects the known ages of crystalline rocks that characterize EGRP determined from the along the periphery of the Illinois Basin. This population of detrital zircon in Cambrian strata may reflect a greater abundance of ~1370 Ma crust beneath the Illinois Basin than presently recognized. These data reveal basal Cambrian sandstones in the Illinois Basin have a detrital zircon provenance that is distinct from the overlying late Cambrian arenites, and that a previously unknown northern arm of the Reelfoot Rift extends into central Illinois, which is more than 300 km further north than currently mapped. The opening of the Reelfoot Rift, which was part of the broader rifting of Rodinia during the Neoproterozoic and early Cambrian, is marked by zircons, probably from Reelfoot Rift igneous rocks, that range from 540-525 Ma.

Major discoveries include:

- Detrital zircon U-b geochronology indicate that the lower Mt. Simon has a maximum depositional age range from 527 to 541 Ma.
- Zircon geochronology indicates the lower Mt. Simon has a unique provenance distinct from the overlying middle and upper Mt. Simon. Data indicates a proximal detrital source. These proximal sediment sources were critical in supplying feldspar to the lower Mt. Simon arkose.
- A population of 540-525 Ma detrital zircons is present in the lower Mt. Simon and are the first indication of Cambrian igneous rocks discovered in the Illinois Basin. A Cambrian igneous source is proposed to be associated with volcanism along a northern extensional arm of the failed Reelfoot Rift marking the end of the breakup of the supercontinent Rodinia. Sediments were sourced from proximal Precambrian highs (see chapter vi) along the flanks of this rift basin.

Supplemental geochronology of the late Mt. Simon Archean sediments and Rodinia rift basalt

Since publication of this manuscript, zircons from the middle Mt. Simon (unit C depth 1942 m (6373 ft) and unit D depth 1825 m (5989 ft)) and upper Mt. Simon (depth 1676 m (5500 ft)) have been dated. Compared to the Argenta and lower Mt. Simon, the middle Mt. Simon unit C shows a similar detrital zircon provenance with a dominant age peak of ~1375 Ma (SGRP), followed by populations of 1460 Ma and 1650 Ma zircons. The middle shows a minor population of early Cambrian zircons, similar to those observed in the Argenta and lower but less pronounced. Of particular note is the introduction of Superior province zircons with a principal age peak of 2692 Ma. Moving up section into the middle Mt. Simon unit D, the Superior province signature increases with a larger zircon population. A minor Archean zircon age signature is introduced in the middle Mt. Simon unit D. In the upper Mt. Simon, the peak zircon age has shifted to a dominant Superior province source at ~2690 Ma. A minor Archean and Mazatzal peak are observed with a departure of nearly all Granite-Rhyolite province zircons. This indicates the upper Mt. Simon has a separate sediment source than the middle and lower Mt. Simon as well as the Argenta below. The lower Mt. Simon and Argenta are solely sourced from proximal sediments with the assumption that the Cambrian zircons are related to local rift volcanism. The middle Mt. Simon represents the final stage of proximal Precambrian burial and localized sedimentation with the minor influx of distal sediments; likely carried by wind from an encroaching shoreline. During deposition of the upper Mt. Simon, all local Precambrian rock has been buried, and all sediment is distal with the exception of minor re-working and input of underlying sediments.

Recent drilling along the proposed Reelfoot Rift penetrated a basalt layer below the Mt. Simon Sandstone before passing back into sandstones. The recovered basalt has recently been dated via Ar/Ar geochronology with an $^{40}Ar/^{39}Ar$ plateau age date of 525.79 ± 1.10 Ma (Table 5). This date is consistent with late events of rifting along the Laurentian margin and similar to other synrift igneous rocks reported along the margin (Badger and Sinha, 1988; Aleinikoff et al., 1995; Thomas et al., 2012; Hanson et al., 2013; Thomas, 2014) and marks the end of the break-up of Rodinia (Li et al., 2008). The basalt or perhaps underlying basalts are likely the source of early Cambrian zircons observed in the lower Mt. Simon and Argenta on the rift margins reported in Freiburg et al. (2020a). Seismic reflection over the well site suggests at least two more layers of basalt below the first layer penetrated (J. McBride, pers. Comm) and dated here.

Sample			**Results**		
Sample Name	Location	Material	Age Type	Age Interpretation	**Age ± 2σ (i)**
Wabash-8530	Terre Haute, Indiana	Groundmass	Plateau	Crystallization Age	**525.79 ± 1.10 Ma**

Table 5 $^{40}Ar/^{39}Ar$ dating results fort eh Wabash #1 well basalt in Terre Haute, Indiana

Chapter iv synopsis: Depositional and diagenetic controls on anomalously high porosity within a deeply buried CO_2 storage reservoir—The Cambrian Mt. Simon Sandstone, Illinois Basin, USA

Current diagenetic models predict that sandstone porosity and reservoir quality decrease with burial depth and formation age (Leetaru et al., 2009). However, the opposite trend is true for the lower most section of the Cambrian Mt. Simon Sandstone. The lower Mt. Simon is highly porous—it has an average log-derived effective porosity of 17%. To understand the possible reason(s) for this anomaly, the amount of porosity reduction due to compaction porosity loss (COPL) and cementation porosity loss (CEPL) was analyzed. The COPL and CEPL were coupled with sedimentary characteristics in order to ascertain which factors control porosity and reservoir quality in the Mt. Simon. The underlying Argenta sedimentary unit disconformably underlies the Mt. Simon and is included for diagenetic and depositional comparison.

Like trends from other deep basin sandstone units (Leetaru et al., 2009), the COPL generally increases with depth in the Mt. Simon. The CEPL is significantly lower in the lower half of the Mt. Simon compared to the upper half of the Mt. Simon, indicating that higher porosity corresponds to having a lower volume of intergranular cement. Early episodes of diagenesis within the arkosic lower Mt. Simon, such as clay infiltration and feldspar alteration, produced diagenetic grain-coating clays, which inhibited the development of quartz cements. These grain coatings assisted in porosity preservation within the lower Mt. Simon by reducing CEPL. The upper half of the Mt. Simon is more heavily cemented as a result of changes in the depositional setting and thus changes in the mineralogy and lithology. Later, largely post-compaction feldspar dissolution further increased porosity in the lower Mt. Simon Sandstone.

New findings include:

- The Mt. Simon Sandstone exhibits normal compaction trends (i.e. compaction generally increased with depth).
- The lower Mt. Simon and underlying Argenta exhibit similar porosity loss as a result of cementation and compaction. One major difference in porosity resulted from differences in the initial porosities due to sorting and mineralogical differences. The lower Mt. Simon is more mature and exhibits better sorting than the Argenta. Controls on this are inferred to reflect differences in the tectonic setting discussed in chapter v and vi. Another major difference in porosity reflects secondary porosity development in the lower Mt. Simon, which resulted from grain dissolution.
- Compared to other units, the lower Mt. Simon contains abundant grain coating illite that prevented pervasive nucleation of authigenic quartz found in other units. The origin of this authigenic illite is discussed in chapter iv.
- Mineralogical, diagenetic, and depositional data resulting from this study suggest the lower Mt. Simon and Argenta were deposited in a rift basin. Geochronologic evidence strengthening this hypothesis is presented in chapter V.

Chapter v synopsis: The timing of illitization in Paleozoic Strata at the Illinois Basin—Decatur Project: Implications for CO_2 Storage

The timing of diagenetic illite precipitation in the Cambrian-age Mt. Simon Sandstone is used to evaluate the history of diagenesis and the overall controls on reservoir properties. Overlying major shale units are included in the investigation as comparative units subjected to basin diagenesis and to provide context regarding the integrity of a reservoir-seal system.

In this chapter, the depositional history and reservoir properties of the Mt. Simon are summarized, and the origin of illite in the Mt. Simon is investigated. Illitization of the Argenta, Eau Claire, and Maquoketa Formations and the New Albany Shale are analyzed for comparison with the Mt. Simon to better understand the diagenetic history and major regional controls on the diagenesis observed in key formations important to the IBDP reservoir and seal system and, more broadly, the Illinois Basin geologic history.

Major discoveries include:

- Potassium-argon dates of illite indicating two major events of illitization were identified in the Cambrian-age Mt. Simon Sandstone in central Illinois: (1) the early event formed illite from 360 to 315 Ma (mostly Carboniferous), predominantly in the porous lower and upper Mt. Simon sections, and (2) the late event formed illite from 250 to 220 Ma (Triassic), predominantly in the tight Argenta and middle Mt. Simon.
- Tectonic activity during the Mt. Simon deposition resulted in depositional variation, changes in the detrital source, and heterogeneity in detrital mineralogy; all of which exerted controls on the diagenetic products observed throughout the Mt. Simon storage complex. For example, the Argenta was partly deposited in a near-shore, high energy environment and contains abundant detrital aluminosolicate minerals such as feldspars, mica, and igneous rock fragments. A regression that separated the Argenta from the overlying lower Mt. Simon, led to subaerial exposure, meteoric recharge, and unstable detritus replacement by kaolinite. Kaolinite is absent in the largely fluvial deposits of the overlying lower Mt. Simon. Instead, pervasive illite coatings are common in the lower Mt. Simon that may have partly originated from early smectite coatings.
- The early and most dominant illitization event formed illite in the lower and upper Mt. Simon and likely resulted in major K-feldspar dissolution contributing secondary porosity enhancement and potassium for illite growth in the lower Mt. Simon. Illitization occurred in response to tectonically driven, low-temperature hydrothermal brines during the Late Devonian to Late Carboniferous and correlates to widespread folding, faulting, and igneous activity in and around the Illinois Basin. These deformation driven brines likely associated with the end of the Acadian and predominantly the Alleghenian and Ouachita Orogenies.
- During early illitization, these tectonically driven brines followed the most porous pathways, illitizing all smectite, including pore-lining terrestrial smectite in the lower Mt. Simon and smectite-rich tidal shale and terrestrial mudstone in the upper Mt. Simon. K-feldspar was a major reactant during illitization, leading to K-feldspar dissolution and an excess source of K and resulting in the authigenic feldspar precipitation observed in the Mt. Simon, especially the upper Mt. Simon.

- With the consumption and illitization of all smectite in the lower and upper Mt. Simon during the early event, pore-filling kaolinite, common in the Argenta and middle Mt. Simon, reacted to form illite during the late event.
- The late illitization event occurred primarily within the Late Triassic and likely in response to compressional stresses during the formation of Pangea and later an episode of extension and reactivation of faults during the breakup of Pangea. This illitization event post-dates Mississippi Valley type lead-zinc and fluorite deposits associated with Permian-age (circa 270 Ma) basin brine migration.

Chapter vi synopsis: High-resolution pore space imaging, mineralogical characterization, and sealing capacity estimates of caprock at the Illinois Basin—Decatur Project

Shales and mudstones act as seals and baffles for reservoirs. Their low permeability and high capillary entry pressure are critical for the retention and vertical migration of fluids in sedimentary basins. At the IBDP, three overlying and laterally continuous shale formations (the Eau Claire, Maquoketa, and New Albany; Figure 3) are considered caprock. Mudstones internal to the reservoir may also hinder vertical migration of the CO_2. Understanding sealing properties of caprocks and reservoir baffles is vital to the project and future commercialization of geologic carbon storage. To characterize the controls on the seal integrity of the rocks, nanoscale-resolution focused ion beam (FIB) scanning electron microscopy (SEM), mercury injection capillary pressure (MICP), X-ray diffraction (XRD) spectroscopy, and quantitative evaluation of minerals by scanning electron microscopy (QEMSCAN) were used.

Results show that porosity and pore size generally decrease with depth, except for the carbonate-rich Maquoketa shale. The Maquoketa sample is ranked as the poorest seal out of the three major caprocks. The Maquoketa has the highest volume of pore space and a predominant intracrystalline dolomite component compared with the other mudstone and shale samples, which are clay-rich. It has the highest effective porosity, the lowest fluid/gas entry pressure, and the second largest pore throat size and the highest median pore diameter. Also, the Maquoketa has the highest pore volume out of all samples analyzed (FIB-SEM). The shallowest sample and secondary seal to the reservoir, the organic-rich New Albany shale, has the highest frequency of the smallest pore throat size and is most comparable, with respect to pore sizes and entry pressures, to the deepest black shale and primary reservoir seal, the Eau Claire shale. Results indicate that the Eau Claire provides the overall best seal. The Eau Claire is dominated by an illite clay matrix and has the lowest effective porosity despite the higher median pore throat and lower fluid/gas entry pressure compared to the New Albany Shale. The Eau Claire sample exhibits the smallest median pore throat compared to other shale samples. The mudstone internal to the Mt. Simon reservoir exhibits the best sealing properties relative to all samples analyzed. However, this mudstone is not considered a caprock due to its lack of lateral continuity. It has the lowest porosity, smallest pore sizes, and highest entry pressures of all the samples investigated. This mudstone has abundant hematite cement and a matrix that is predominantly composed of and has the highest percentage of illite (mica) compared with the other shales and mudstones. The dense layering, abundant hematite and illite, and lack of mineral heterogeneity in this mudstone make it a quintessential sealing lithology.

Porosity data from MIP and FIB-SEM methods show good correlation across all samples. Although FIB-SEM underestimates pores sizes below its resolution (> 50nm), it obtains the characteristics of pores that

are ineffectively identified and evaluated by MIP. Data shows that mudstone baffles in the Mt. Simon reservoir lack a pore network and offers the greatest immediate sealing capability. However, the three shales at IBDP are regionally laterally continuous, much thicker, and therefore better seals for long-term impervious storage. Although all three shales have negligible permeability (<0.01 mD), data indicates that the pore size, distribution, and connectivity within the shales are highly variable and indicate that the secondary seal (Maquoketa) has the poorest sealing quality. With low pore connectivity, the primary (Eau Claire) and tertiary (New Albany) reservoir seals are the highest quality.

Point specific MICP threshold pressure results, theoretical calculations based upon a range of permeabilities, and column height calculations indicate that the Mt. Simon mudstones and Eau Claire Shale are effective seals to super critical (sc) CO_2 in the Mt. Simon reservoir. As the mudstones are laterally discontinuous, they should be considered as baffles (where present) to scCO2 migration. The Maquoketa Shale and New Albany Shale caprocks are considered non-primary seals and will provide additional sealing capacity. However, column height calculations are considered approximations since a porous reservoir for $_{CO2}$ migration is absent beneath the formations.

Main findings include:

- The Eau Claire sample provides the overall best seal. The Eau Claire has the lowest effective porosity despite the higher median pore throat and lower fluid/gas entry pressure than the New Albany. This slightly lower entry pressure may be the result of more abundant pore volume than the New Albany. The Eau Claire exhibits the smallest median pore size despite the largest pore throat reported from MICP analyses.
- The New Albany sample is the second-best seal. It has the second highest effective porosity and the highest fluid/gas entry pressure. It has the smallest reported median pore throat size (MICP), the second smallest median pore according to FIB-SEM analysis, and the smallest overall pore volume.
- The Maquoketa sample is ranked last out of the three sample. It has the highest effective porosity and the lowest fluid/gas entry pressure. The Maquoketa has the second largest pore throat size and the highest median pore diameter. Analyses indicate that the Maquoketa has the highest pore volume out of all samples analyzed (FIB-SEM).
- The mudstone internal to the Mt. Simon reservoir exhibits the best sealing properties relative to all samples analyzed. However, the interval is not ranked or considered a major seal due to its lack of lateral continuity. Despite this, the mudstone is an excellent baffle and should prevent any localized vertical CO_2/fluid migration. The mudstone has an exponentially lower effective porosity (MICP) as well as entry pressure relative to the other samples. Although the median pore size is similar to the Eau Claire and New Albany, the median pore range is smaller than all samples. The mudstone also exhibits the smallest pore volume out of all samples analyzed.
- Point specific MICP threshold pressure results, theoretical calculations based upon a range of permeabilities, and column height calculations indicate that the Mt. Simon mudstones and Eau Claire Shale are effective seals to scCO_2 in the Mt. Simon reservoir. As the mudstones are laterally

discontinuous, they should be considered as baffles (where present) to scCO2 migration. The Maquoketa Shale and New Albany Shale caprocks are considered non-primary seals and will provide additional sealing capacity. However, column height calculations are considered approximations since a porous reservoir for $_{CO2}$ migration is absent beneath the formations.

Summary and implications of work

The unique depositional setting controlled by continental-scale tectonic processes followed by a diagenetic history favoring illitization and primary porosity preservation resulted in the development of the thick and porous lower Mt. Simon Sandstone in central Illinois. Subsequent sedimentary cover of widespread marine shale sequences created a reservoir-seal system ideal for storage of unconventional resources in the Illinois Basin. Future work may focus on the newly discovered diverse Precambrian landscape across the basin, early Cambrian tectonics and volcanism, and developing data driven models on reservoir distribution, development, and diagenetic history (i.e. burial). To curb the effects of man-made greenhouse gases on the planet and perhaps develop and store greener fuel sources, a storage corridor must be identified for infrastructure to develop across the Illinois Basin. This will require new wells to be drilled in order to explore for and exploit the lower Mt. Simon Sandstone. The research presented here has identified some guidelines or exploration notes that may aid in site planning and development.

- The thickness of the lower Mt. Simon is structurally controlled. The lower Mt. Simon occurs along the rift axis (LaSalle Anticlinorium) with the thickest lower Mt. Simon found west of the rift along localized normal fault controlled depocenters.
- Precambrian boundaries west of the rift are ideal targets for extensional faulting and thicker sections of the lower Mt. Simon. Precambrian boundaries such as the Mazatzal-GRP identified herein via 2D seismic and aeromagnetic surveys (Freiburg et al. 2020b) or the Central Sequence identified via 2D seismic reflection (Pratt et al., 1992) should be explored further and considered prime targets for structurally controlled accommodation space and a thick proximally sourced lower Mt. Simon.
- Careful attention should be given to how far west the site of exploration is in proximity to the rift-controlled Mt. Simon-Argenta depocenter and the Precambrian surface to avoid a thin lower Mt. Simon (i.e. Futuregen Alliance #1 Well, Morgan Co., Illinois). East of the rift, deep Mt. Simon sediments are largely unexplored, especially below early Cambrian basalts (CarbonSAFE Wabash #1 Well, West Terre Haute, Indiana) and projects should proceed with caution.
- Careful attention should be given to the depth and controls on porosity in the lower Mt. Simon. The lower Mt. Simon does not follow a depth/porosity trend like the overlying upper Mt. Simon (Leetaru et al., 2009). This appears to be the result of primary porosity preservation from diagenetic illite or perhaps early smectite coatings governing authigenic quartz nucleation and secondary porosity development in late diagenetic cement and detrital feldspar dissolution minimizing porosity loss from burial controlled compaction. Well data in the lower Mt. Simon

below 2500 meters is limited and thus the controls on porosity preservation and generation is poorly understood and would benefit from future basin-scale reservoir quality models.

References

Akono, A.T., Werth, C., Shi, Z., Jessen, K. and Tsotsis, T.T., 2021. Advanced Geomechanical Model to Predict the Impact of CO2-Induced Microstructural Alterations on the Cohesive-Frictional Behavior of Mt. Simon Sandstone. *Minerals*, *11*(1), p.38.

Aleinikoff, J.N., Zartman, R.E., Walters, M., Rankin, D.W., Lyttle, P.T. and Burton, W.C., 1995. U-Pb ages of metarhyolites of the Catoctin and Mount Rogers Formations, central and southern Appalachians: Evidence for two pulses of Iapetan rifting. *American Journal of Science*, *295*(4), pp.428-454.

Bachu, S., Bonijoly, D., Bradshaw, J., Burruss, R., Holloway, S., Christensen, N.P. and Mathiassen, O.M., 2007. CO2 storage capacity estimation: Methodology and gaps. *International journal of greenhouse gas control*, *1*(4), pp.430-443.

Badger, R. and Sinha, A.K., 1988. Age and Sr isotopic signature of the Catoctin volcanic province: Implications for subcrustal mantle evolution. *Geology*, *16*(8), pp.692-695.

Barnes, M.A., Anthony, E.Y., Williams, I. and Asquith, G.B., 2002. Architecture of a 1.38–1.34 Ga granite–rhyolite complex as revealed by geochronology and isotopic and elemental geochemistry of subsurface samples from west Texas, USA. *Precambrian Research*, *119*(1-4), pp.9-43.

Bickford, M.E. and Mose, D.G., 1975. *Geochronology of Precambrian rocks in the St. Francois Mountains, southeastern Missouri* (Vol. 165). Geological Society of America.

Bickford, M.E., Cullers, R.L., Shuster, R.D., Premo, W.R. and Van Schmus, W.R., 1989. U-Pb geochronology of Proterozoic and Cambrian plutons in the Wet Mountains and southem Front Range, Colorado. *Grarnbling, JA, and Tewksbury, BJ, Proterozoic geology of the southem Rocky Mountains: Boulder, Colorado. Geological Society of America Special Paper*, *235*.

Bickford, M.E., Van Schmus, W.R., Karlstrom, K.E., Mueller, P.A. and Kamenov, G.D., 2015. Mesoproterozoic-trans-Laurentian magmatism: A synthesis of continent-wide age distributions, new SIMS U–Pb ages, zircon saturation temperatures, and Hf and Nd isotopic compositions. *Precambrian Research*, *265*, pp.286-312.

Bowen, B.B., Ochoa, R.I., Wilkens, N.D., Brophy, J., Lovell, T.R., Fischietto, N., Medina, C.R. and Rupp, J.A., 2011. Depositional and diagenetic variability within the Cambrian Mount Simon Sandstone: Implications for carbon dioxide sequestration. *Environmental Geosciences*, *18*(2), pp.69-89.

Bosworth, W., 1985. Geometry of propagating continental rifts. *Nature*, *316*(6029), pp.625-627.

Buschbach, T.C. and Bond, D.C., 1974. Underground storage of natural gas in Illinois, 1973. *Illinois petroleum no. 101*.

Chalmers, G.R., Bustin, R.M. and Power, I.M., 2012. Characterization of gas shale pore systems by porosimetry, pycnometry, surface area, and field emission scanning electron microscopy/transmission

electron microscopy image analyses: Examples from the Barnett, Woodford, Haynesville, Marcellus, and Doig units. *AAPG bulletin*, *96*(6), pp.1099-1119.

Chen, Z., Riciputi, L.R., Mora, C.I. and Fishman, N.S., 2001. Regional fluid migration in the Illinois basin: Evidence from in situ oxygen isotope analysis of authigenic K-feldspar and quartz from the Mount Simon Sandstone. *Geology*, *29*(12), pp.1067-1070.

Chorowicz, J., 1989. Transfer and transform fault zones in continental rifts: examples in the Afro-Arabian rift system. Implications of crust breaking. *Journal of African Earth Sciences (and the Middle East)*, *8*(2-4), pp.203-214.

Cluff, R.M., Reinbold, M.L. and Lineback, J.A., 1981. New Albany shale group of Illinois. *Ill. State Geol. Surv., Circ.;(United States)*, *518*.

Daniels, D.L., Kucks, R.P. and Hill, P.L., 2008. *Illinois, Indiana, and Ohio Magnetic and Gravity Maps and Data: A Website for Distribution of Data* (No. 321). Geological Survey (US).

Duffin, M.E., Lee, M., Klein, G.D. and Hay, R.L., 1989. Potassic diagenesis of Cambrian sandstones and Precambrian granitic basement in UPH-3 deep hole, Upper Mississippi Valley, USA. *Journal of Sedimentary Research*, *59*(5), pp.848-861.

Finley, R.J., 2014. An overview of the Illinois Basin–Decatur project. *Greenhouse Gases: Science and Technology*, *4*(5), pp.571-579.

Fishman, N.S., 1997. Basin-wide fluid movement in a Cambrian paleoaquifer: evidence from the Mt. Simon sandstone, Illinois and Indiana.in Montan˜ez, I.P., Gregg, J.M., and Shelton, K.L., eds., Basin-wide diagenetic patterns: SEPM (Society for Sedimentary Geology) Special Publication 57, p. 221–234.

Freiburg, J.T., Morse, D.G., Leetaru, H.E., Hoss, R.P. and Yan, Q., 2014. A depositional and diagenetic characterization of the Mt. Simon Sandstone at the Illinois Basin-Decatur Project carbon capture and storage site, Decatur, Illinois, USA.

Freiburg, J.T., Ritzi, R.W. and Kehoe, K.S., 2016. Depositional and diagenetic controls on anomalously high porosity within a deeply buried CO2 storage reservoir—The Cambrian Mt. Simon Sandstone, Illinois Basin, USA. *International Journal of Greenhouse Gas Control*, *55*, pp.42-54.

Freiburg, J.T., Holland, M.E., Malone, D.H. and Malone, S.J., 2020. Detrital zircon geochronology of basal Cambrian strata in the deep Illinois Basin, USA: evidence for the Paleoproterozoic-Cambrian tectonic and sedimentary evolution of central Laurentia. *The Journal of Geology*, *128*(3), pp.303-317.

Freiburg, J.T., McBride, J.H., Malone, D.H. and Leetaru, H.E., 2020. Petrology, geochronology, and geophysical characterization of Mesoproterozoic rocks in central Illinois, USA. *Geoscience Frontiers*, *11*(2), pp.581-596.

Gibbins, J. and Chalmers, H., 2008. Carbon capture and storage. *Energy policy*, *36*(12), pp.4317-4322.

Grathoff, G.H., Moore, D.M., Hay, R.L. and Wemmer, K., 2001. Origin of illite in the lower Paleozoic of the Illinois basin: evidence for brine migrations. *Geological Society of America Bulletin*, *113*(8), pp.1092-1104.

Hanson, R.E., Puckett Jr, R.E., Keller, G.R., Brueseke, M.E., Bulen, C.L., Mertzman, S.A., Finegan, S.A. and McCleery, D.A., 2013. Intraplate magmatism related to opening of the southern Iapetus Ocean: Cambrian Wichita igneous province in the Southern Oklahoma rift zone. *Lithos*, *174*, pp.57-70.

Hildenbrand, T.G. and Ravat, D., 1997. Geophysical setting of the Wabash Valley fault system. *Seismological Research Letters*, *68*(4), pp.567-585.

Hoholick, J.D., Metarko, T. and Potter, P.E., 1984. Regional variations of porosity and cement: St. Peter and Mount Simon sandstones in Illinois Basin. *AAPG bulletin*, *68*(6), pp.753-764.

Kolata, D.R. and Graese, A.M., 1983. *Lithostratigraphy and depositional environments of the Maquoketa Group (Ordovician) in northern Illinois*. Champaign, Ill.: Illinois State Geological Survey, Prairie Research Institute.

Kolata, D.R. and Nelson, W.J., 1990. Tectonic History of the Illinois Basin: Chapter 18: Part I. Illinois Basin: Evolution.

Lahann, R., Mastalerz, M., Rupp, J.A. and Drobniak, A., 2013. Influence of CO2 on New Albany Shale composition and pore structure. *International Journal of Coal Geology*, *108*, pp.2-9.

Lahann, R., Rupp, J. and Medina, C., 2014. An evaluation of the seal capacity and CO2 retention properties of the Eau Claire Formation (Cambrian). *Environmental Geosciences*, *21*(3), pp.83-106.

Li, Z.X., Bogdanova, S., Collins, A.S., Davidson, A., De Waele, B., Ernst, R.E., Fitzsimons, I.C.W., Fuck, R.A., Gladkochub, D.P., Jacobs, J. and Karlstrom, K.E., 2008. Assembly, configuration, and break-up history of Rodinia: a synthesis. *Precambrian research*, *160*(1-2), pp.179-210.

Linda, A. and Singh, H.P., 2021. Geological Carbon Capture and Storage as a Climate-Change Mitigation Technology. In *Advances in Carbon Capture and Utilization* (pp. 33-55). Springer, Singapore.

Leetaru, H.E., Frailey, S., Morse, D., Finley, R.J., Rupp, J.A., Drahozval, J.A. and McBride, J.H., 2009. Carbon sequestration in the Mt. Simon Sandstone saline reservoir.

Leetaru, H.E. and McBride, J.H., 2009. Reservoir uncertainty, Precambrian topography, and carbon sequestration in the Mt. Simon Sandstone, Illinois Basin. *Environmental Geosciences*, *16*(4), pp.235-243.

Lovell, T.R. and Bowen, B.B., 2013. Fluctuations in sedimentary provenance of the Upper Cambrian Mount Simon Sandstone, Illinois Basin, United States. *The Journal of Geology*, *121*(2), pp.129-154.

Mastalerz, M., Schimmelmann, A., Drobniak, A. and Chen, Y., 2013. Porosity of Devonian and Mississippian New Albany Shale across a maturation gradient: Insights from organic petrology, gas adsorption, and mercury intrusionGeohorizon. *AAPG bulletin*, *97*(10), pp.1621-1643.

Medina, C.R., Mastalerz, M., Lahann, R.W. and Rupp, J.A., 2020. A novel multi-technique approach used in the petrophysical characterization of the Maquoketa Group (Ordovician) in the southeastern portion of the Illinois Basin: Implications for seal efficiency for the geologic sequestration of CO2. *International Journal of Greenhouse Gas Control*, *93*, p.102883.

Marshak, S. and Paulsen, T., 1996. Midcontinent US fault and fold zones: A legacy of Proterozoic intracratonic extensional tectonism. *Geology*, *24*(2), pp.151-154.

McBride, J.H., Leetaru, H.E., Keach, R.W. and McBride, E.I., 2016. Fine-scale structure of the Precambrian beneath the Illinois Basin. *Geosphere*, *12*(2), pp.585-606.

McBride, J.H., Leetaru, H.E., Freiburg, J.T., and Whittaker, S.G., 2020. Variations in Precambrian structure revealed by CCS seismic profiles from the Illinois Basin, Society for Economic Geophysics

Makowitz, A. and Milliken, K.L., 2003. Quantification of brittle deformation in burial compaction, Frio and Mount Simon Formation sandstones. *Journal of Sedimentary Research*, *73*(6), pp.1007-1021.

Medina, C.R., Rupp, J.A. and Barnes, D.A., 2011. Effects of reduction in porosity and permeability with depth on storage capacity and injectivity in deep saline aquifers: A case study from the Mount Simon Sandstone aquifer. *International journal of greenhouse gas control*, *5*(1), pp.146-156.

Medina, C.R., Mastalerz, M., Lahann, R.W. and Rupp, J.A., 2020. A novel multi-technique approach used in the petrophysical characterization of the Maquoketa Group (Ordovician) in the southeastern portion of the Illinois Basin: Implications for seal efficiency for the geologic sequestration of CO2. *International Journal of Greenhouse Gas Control*, *93*, p.102883.

Morse, D.G. and Leetaru, H.E., 2005. *Reservoir characterization and three-dimensional models of Mt. Simon gas storage fields in the Illinois Basin*. Illinois State Geological Survey, Department of Natural Resources.

Mozley, P.S., Heath, J.E., Dewers, T.A. and Bauer, S.J., 2016. Origin and heterogeneity of pore sizes in the Mount Simon Sandstone and Eau Claire Formation: Implications for multiphase fluid flow. *Geosphere*, *12*(4), pp.1341-1361.

Nelson, W.J., 1990. Structural Styles of the Illinois Basin: Chapter 16: Part I. Illinois Basin: Structural Geology.

Neufelder, R.J., Bowen, B.B., Lahann, R.W. and Rupp, J.A., 2012. Lithologic, mineralogical, and petrophysical characteristics of the Eau Claire Formation: Complexities of a carbon storage system seal. *Environmental Geosciences*, *19*(3), pp.81-104.

Pacala, S. and Socolow, R., 2004. Stabilization wedges: solving the climate problem for the next 50 years with current technologies. *science*, *305*(5686), pp.968-972.

Pollington, A.D., Kozdon, R. and Valley, J.W., 2011. Evolution of quartz cementation during burial of the Cambrian Mount Simon Sandstone, Illinois Basin: In situ microanalysis of δ18O. *Geology*, *39*(12), pp.1119-1122.

Potter, C.J., Drahovzal, J.A., Sargent, M.L. and McBride, J.H., 1997. Proterozoic structure, Cambrian rifting, and younger faulting as revealed by a regional seismic reflection network in the southern Illinois Basin. *Seismological Research Letters*, *68*(4), pp.537-552.

Pratt, T.L., Hauser, E.C. and Nelson, K.D., 1992. Widespread buried Precambrian layered sequences in the US mid-continent: Evidence for large Proterozoic depositional basins. *AAPG bulletin*, *76*(9), pp.1384-1401.

Rackley, S.A., 2017. *Carbon capture and storage*. Butterworth-Heinemann.

Reesink, A.J.H., Best, J., Freiburg, J.T., Webb, N.D., Monson, C.C. and Ritzi, R.W., 2020. Interpreting pre-vegetation landscape dynamics: The Cambrian Lower Mount Simon Sandstone, Illinois, USA. *Journal of Sedimentary Research*, *90*(11), pp.1614-1641.

Ritzi, R.W., Ghose, R., Bottomley, M., Reesink, A.J., Best, J., Freiburg, J.T. and Webb, N.D., 2018. Linking the local vertical variability of permeability and porosity to newly-interpreted lithofacies in the lower Mt. Simon CO2 reservoir. *International Journal of Greenhouse Gas Control*, *68*, pp.26-41.

Ross, D.J. and Bustin, R.M., 2009. The importance of shale composition and pore structure upon gas storage potential of shale gas reservoirs. *Marine and petroleum Geology*, *26*(6), pp.916-927.

Thomas, W.A., Tucker, R.D., Astini, R.A. and Denison, R.E., 2012. Ages of pre-rift basement and synrift rocks along the conjugate rift and transform margins of the Argentine Precordillera and Laurentia. *Geosphere*, *8*(6), pp.1366-1383.

Thomas, W.A., 2014. A mechanism for tectonic inheritance at transform faults of the Iapetan margin of Laurentia. *Geoscience Canada*, pp.321-344

Treworgy, J.D., 1988. The Illinois Basin, a tidally and tectonically influenced ramp during mid-Chesterian time. *Circular no. 544*.

Van Schmus, W.R., Bickford, M.E., Turek, A., Van der Pluijm, B.A. and Catacosinos, P.A., 1996. Proterozoic geology of the east-central Midcontinent basement. *SPECIAL PAPERS-GEOLOGICAL SOCIETY OF AMERICA*, pp.7-32.

Whitmeyer, S.J. and Karlstrom, K.E., 2007. Tectonic model for the Proterozoic growth of North America. *Geosphere*, *3*(4), pp.220-259.

Williams-Stroud, S., Bauer, R., Leetaru, H., Oye, V., Stanek, F., Greenberg, S. and Langet, N., 2020. Analysis of Microseismicity and Reactivated Fault Size to Assess the Potential for Felt Events by CO 2 Injection in the Illinois Basin. *Bulletin of the Seismological Society of America*, *110*(5), pp.2188-2204.

Willman, H.B., Atherton, E., Buschbach, T.C., Collinson, C.W., Frye, J.C., Hopkins, M.E., Lineback, J.A. and Simon, J.A., 1975. Handbook of Illinois stratigraphy. *Bulletin no. 095*.

Yawar, Z. and Schieber, J., 2008, October. Facies and depositional setting of Eau Claire Formation (Cambrian) mudstones in northwestern Indiana. In *Geological Society of America Abstracts with Programs* (Vol. 40, p. A433).

Chapter ii Manuscript

Petrology, geochronology, and geophysical characterization of Mesoproterozoic rock in central Illinois, USA

Geoscience Frontiers 11 (2020) 581–596

Contents lists available at ScienceDirect

Geoscience Frontiers

journal homepage: www.elsevier.com/locate/gsf

Research Paper

Petrology, geochronology, and geophysical characterization of Mesoproterozoic rocks in central Illinois, USA

Jared T. Freiburg [a,b,*], John H. McBride [c], David H. Malone [d], Hannes E. Leetaru [a]

[a] Illinois State Geological Survey, Prairie Research Institute, University of Illinois at Urbana-Champaign, 615 E. Peabody Drive, Champaign, IL 61820, USA
[b] University of Greifswald, Institute of Geography and Geology, Friedrich-Ludwig-Jahn Str. 17a, D-17489 Greifswald, Germany
[c] Department of Geological Sciences, Brigham Young University, Provo, UT, 84602, USA
[d] Department of Geography, Geology, and the Environment, Campus Box 4400, Illinois State University, Normal, IL, 61790-4400, USA

ARTICLE INFO

Handling Editor: Damian Nance

Keywords:
Eastern granite-rhyolite province
Mesoproterozoic
Carbon storage
Reflection seismology
Zircon U-Pb geochronology
Illinois

ABSTRACT

The Precambrian basement rocks of the Eastern Granite-Rhyolite Province (EGRP) in central Illinois (mid-continent region of North America) exhibit a complex history of early volcanism, granite emplacement, and intrusion of mafic rocks. A comprehensive suite of dedicated petrographic analyses, geophysical logs, and drill core from four basement-penetrating wells, two-dimensional and three-dimensional seismic reflection data, and U-Pb age data from the Illinois Basin–Decatur Project (IBDP) and Illinois Carbon Capture Storage (ICCS) Project site provide new constraints for interpreting the Precambrian basement of the Illinois Basin. These new data reveal the basement to be compositionally and structurally complex, having typical EGRP felsic volcanic rocks intruded by the first reported gabbro in the Precambrian basement in Illinois. Zircons ($n = 29$) from rhyolite give a U-Pb weighted mean average age of 1467 ± 9 Ma. Zircons ($n = 3$) from a gabbro dike that intrudes the rhyolite yield a concordia age of 1073 ± 12 Ma, which corresponds to Grenville-age extension and represents the first Grenville-age rock in Illinois and in the EGRP. A high-resolution three-dimensional seismic reflection volume, coincident with the four wells, provides a context for interpreting the petrological data and implies a high degree of heterogeneity for basement rocks at the IBDP–ICCS site, as also shown by the drill cores. The occurrence of Grenville-age gabbro is related to a prominent bowl-like structure observed on local two-dimensional seismic reflection profiles and the three-dimensional volume that is interpreted as a deep-seated mafic sill complex. Furthermore, heterogeneities such as the brecciated EGRP rhyolite and later gabbro intrusion observed in the basement lithology at the IBDP–ICCS may reflect previously unknown distal elements of the 1.1 Ga Midcontinent Rift in the EGRP and more likely Grenville-age extension.

1. Introduction

The Precambrian basement of the Illinois Basin has recently gained the attention of both researchers and industry members as a result of the Illinois Basin–Decatur Project (IBDP) and the Illinois Carbon Capture and Storage (ICCS) Project (Fig. 1). These demonstration projects were designed to successfully capture, inject, and store industrially sourced carbon dioxide (CO_2) in the Cambrian Mt. Simon Sandstone, the basal Paleozoic unit overlying the Precambrian basement. During injection of approximately 1 million tonnes (1.1 million tons) of CO_2 into the base of the Mt. Simon at the IBDP, microseismicity (magnitude ≤1.17) was detected in the Precambrian basement (Bauer et al., 2016). At the ICCS Project, 0.9 million tonnes (1 million tons) of CO_2 is currently being injected annually into a shallower section of the Mt. Simon with minimal microseismicity detected. Thus, interest in the basement heterogeneity is particularly focused on the basement structure, lithology, and origin.

Abbreviations: 2D, two-dimensional; 3D, three-dimensional; CCS1, Carbon Capture and Storage 1 well; CCS2, Carbon Capture and Storage 2 well; EGRP, Eastern Granite-Rhyolite Province; FMI log, fullbore microimager log; FWR, Fort Wayne Rift; IBDP, Illinois Basin–Decatur Project; ICCS, Illinois Carbon Capture and Storage Project; LA-ICPMS, laser ablation–inductively coupled plasma mass spectrometry; MCR, Midcontinent Rift; MSWD, mean square weighted deviation; VW1, Verification Well 1; VW2, Verification Well 2; WMA, weighted mean age.

* Corresponding author. Illinois State Geological Survey, Prairie Research Institute, University of Illinois at Urbana-Champaign, 615 E. Peabody Drive, Champaign, IL 61820, USA.
E-mail address: freiburg@illinois.edu (J.T. Freiburg).

Peer-review under responsibility of China University of Geosciences (Beijing).

https://doi.org/10.1016/j.gsf.2019.07.004
Received 21 January 2019; Received in revised form 20 May 2019; Accepted 8 July 2019
Available online 22 July 2019

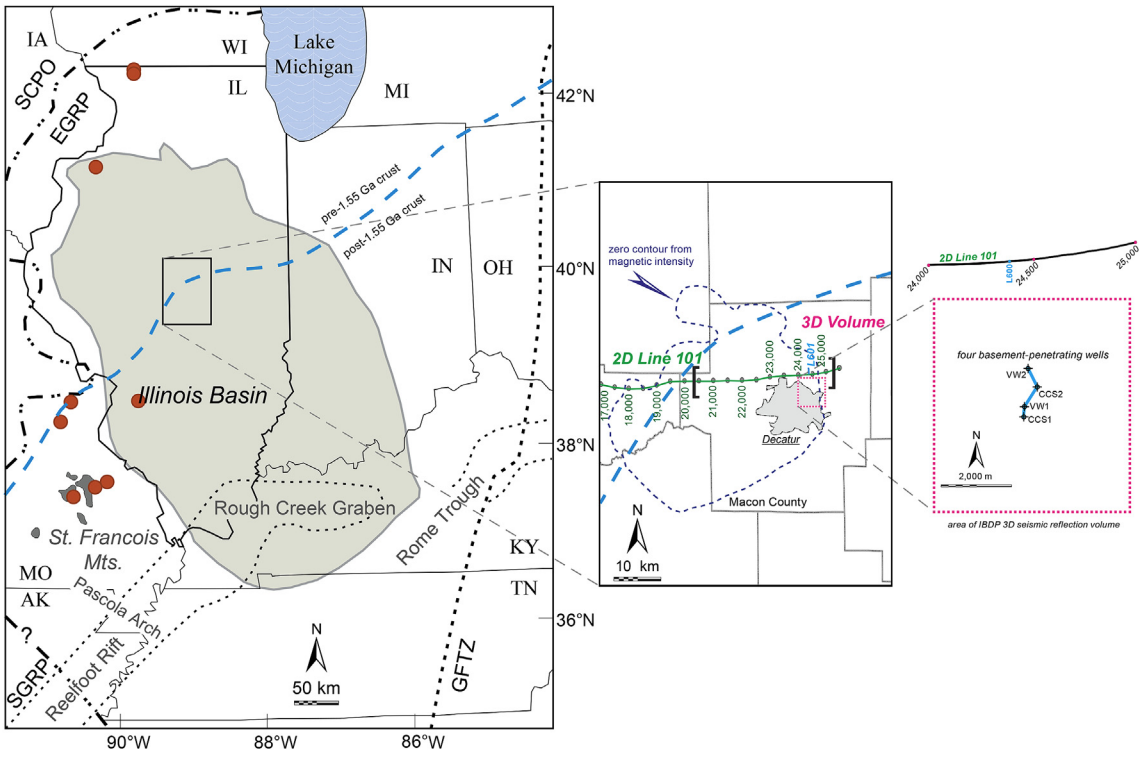

Fig. 1. (Left to right) Location map showing the outline of the extent of Pennsylvanian strata in the Illinois Basin and selected tectonic elements and boundaries. The dashed blue line is the geochemically defined boundary delineating ages for the Precambrian basement crust (modified from Van Schmus et al., 1996). Eastern Granite-Rhyolite Province (EGRP) rocks with approximately 1.47 Ga ages in Missouri and Illinois are marked with red circles (from Bickford et al., 2015). Detailed map of the L101 2D seismic reflection profile and 3D IBDP–ICCS seismic data volume, along with the zero-contour outline for a positive magnetic anomaly. The black brackets delineate limits of the high-amplitude reflection on the L101 seismic profile. Detailed map showing the locations of four drill holes within the area of the 3D seismic volume. SCPO, Southern Central Plains Orogen; SGRP, Southern Granite-Rhyolite Province; GFTZ, Grenville Front Tectonic Zone.

The Illinois Basin is centered between prominent geologic features expressed on magnetic and gravity maps: the Midcontinent Rift (MCR) and the Fort Wayne Rift (Van Schmus and Hinze, 1985; Hinze et al., 1997; Fig. 2). The MCR formed from 1109 Ma to 1087 Ma (Davis and Sutcliffe, 1985; Davis and Paces, 1990) by extensional and volcanic processes during the Grenville orogeny, where extensional forces continued into the Neoproterozoic on the ancient Laurentian craton (Whitmeyer and Karlstrom, 2007). Mafic sills are common in rift basins (Ruppel, 1996). Studies of basement igneous intrusions on the Laurentian craton are limited because of the lack of deep well data and, in basins such as Illinois, the lack of good-quality seismic reflection data.

This paper presents the results of multiple data sources from the IBDP and ICCS Project wells: petrographic analysis and U-Pb geochronology on zircon from drill cores, downhole geophysical logs, and three-dimensional (3D) seismic reflection surveys. Together, they provide the most detailed set of information to date on the Precambrian basement beneath the Illinois Basin. These data indicate early volcanism within the Laurentian EGRP, with later intrusion of Grenville-age gabbro.

2. Geologic background

The Proterozoic tectonic evolution of Laurentia is complicated and represents more than 800 million years of deformation, crustal formation, southward growth, and metamorphism (Whitmeyer and Karlstrom, 2007). These Proterozoic orogenic belts extend thousands of kilometers from Arizona to Labrador. This southward growth began with two cycles of accretionary orogenesis, beginning with the Yavapai Orogeny ca. 1800–1700 Ma and concluding with the Mazatzal Orogeny from 1700 Ma to 1600 Ma (Karlstrom and Bowring, 1988; Bowring and Karlstrom, 1990; Whitmeyer and Karlstrom, 2007). These two belts are collectively as much as 1000 km (621 mi) wide and are composed largely of juvenile crust (Hill and Bickford, 2001; Whitmeyer and Karlstrom, 2007). The Yavapai and Mazatzal events were followed by widespread, obscure, and enigmatic felsic volcanism and granitic magmatism from 1480 Ma to 1360 Ma, which is collectively referred to as the Midcontinent Granite-Rhyolite (MCGR) province (Lidiak et al., 1966; Van Schmus et al., 1975, 1996; Hoppe et al., 1983; Bickford et al., 1986, 2015; Bowring et al., 1992; Dewane and Van Schmus, 2007). The development of the Laurentian basement culminated with the Grenville Orogeny and the assembly of Rodina from 1300 Ma to 1000 Ma (Dalziel, 1991; Moores, 1991; Craddock et al., 2017a).

The Precambrian basement of most of the Illinois Basin is referred to as the Eastern Granite-Rhyolite Province (EGRP), which occurs from western Ohio and Kentucky westward to Missouri, Kansas, and Oklahoma (Denison et al., 1987). Zircon U-Pb ages for the EGRP range from 1.35 Ga to 1.55 Ga (Hoppe et al., 1983; Bickford et al., 1986; Hoffman, 1989; Van Schmus et al., 1996). The EGRP belt stretches SW–NE across the southern and eastern parts of the United States and is interpreted as a juvenile terrane accreted to the margin of the Laurentian continent (Whitmeyer and Karlstrom, 2007). A proposed crustal terrane boundary has been identified by using Nd model ages with protolith ages older than 1.55 Ga on the northwestern side and younger than 1.55 Ga to the southeast (Van Schmus et al., 1996). This Nd boundary runs SW–NE through central Illinois, near the IBDP–ICCS site (Figs. 1 and 2).

The EGRP is characterized by undeformed and mostly unmetamorphosed rhyolite to dacite with granite of extensional or intraplate (i.e., anorogenic) tectonic origin (Bickford et al., 1986). A-type granites were intruded within the EGRP between 1.48 Ga and 1.35 Ga and occur (Van Schmus et al., 1996) in older Paleo- and Mesoproterozoic crust to the north and west (Karlstrom and Humphreys, 1998; Van Schmus et al., 1996; Whitmeyer and Karlstrom, 2007). Juvenile EGRP volcanic and intrusive rocks crop out in southeastern Canada (Dickin and Higgins,

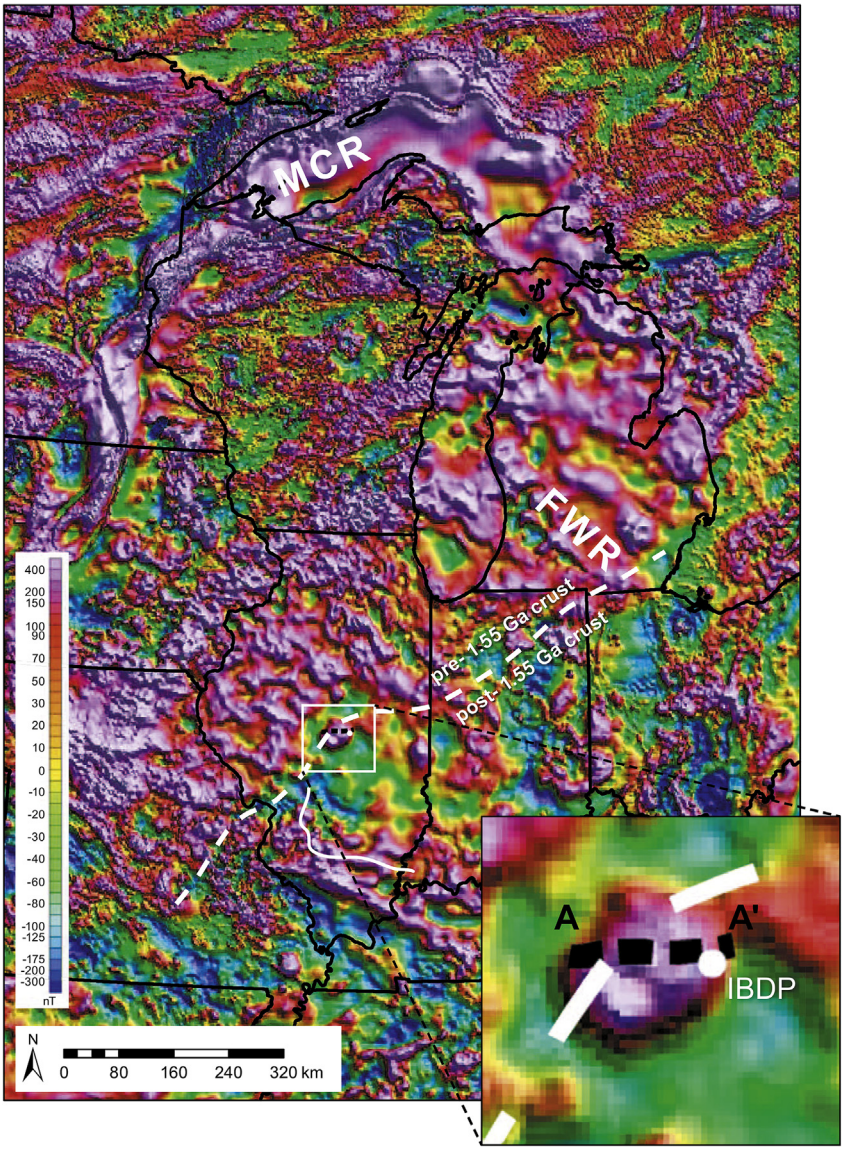

Fig. 2. Magnetic anomaly (nanoteslas) base map (modified from Daniels et al., 2008) showing the location of the IBDP and the portion of the 2D seismic profile (dashed black line) used in this study (Fig. 2). The dashed white line is the geochemically defined boundary delineating ages for the Precambrian basement crust (modified from Van Schmus et al., 1996; McBride et al., 2016). The curved solid white line outlines the southern boundary of the known Precambrian Centralia sequence (modified from McBride et al., 2003). Notable structural features surrounding the IBDP include the Mid-continent Rift (MCR) and the Fort Wayne Rift (FWR).

1992; Gower and Tucker, 1994; Rivers, 1997), the St. Francois Mountains of Missouri (Bowring et al., 1992; Van Schmus et al., 1996), northwestern Texas (Patchett, 1989; Mosher, 1998; Barnes et al., 1999), southern New Mexico (Barnes et al., 1999), and parts of northern Mexico (Patchett and Ruiz, 1989).

Approximately 275 ages are available for MCGR rocks from 16 states and Ontario, Canada (Bickford et al., 2015). Of these, only four basement rock ages are available for Illinois (Hoppe et al., 1983; Bickford et al., 2015; Fig. 1). Each penetrates undeformed granite that ranges in age from 1.50 Ga to 1.46 Ga. Two wells are located in Stephenson County in northern Illinois (UPH1 and UPH3), one is in Henry County in western Illinois (R.E. Davis, South-1), and one is in Madison County in southern Illinois (Klein S-2). About a dozen other wells have penetrated basement rock, but cores were not taken from these wells.

Bickford et al. (2015) reported the ages of four mafic rocks in the EGRP (out of the 275 ages total). All are gabbroic intrusions in the St. Francis Mountains that range in age from 1470 Ma to 1450 Ma. Younger mafic rocks are suspected in the EGRP in geophysically delineated rift structures (Keller et al., 1983; Lidiak et al., 1985). The lack of significant mafic volcanic rocks within the EGRP has been attributed to shallow extensional tectonics (Bickford et al., 1986; Drahovzal et al., 1992).

The Grenville Orogeny was historically believed to cause intracratonic extension, resulting in major tectonic features such as the MCR (Van Schmus and Hinze, 1985; Fig. 2). More recent interpretations of MCR genesis propose that the failed Precambrian intercontinental rift formed separately from the Grenville Orogeny, during the rifting of Amazonia (Precambrian northeast South America) from Laurentia (Precambrian North America) and failed because of the establishment of seafloor spreading (Stein et al., 2014; Malone et al., 2016). During the formation of the MCR, voluminous mafic rocks intruded and extruded along the axis of the rift between 1109 Ma and 1087 Ma (e.g., Swanson-Hysell et al., 2014, 2019; Stein et al., 2015; and references therein).

Seismic reflection data reveal the EGRP as being structurally complex in Illinois (Pratt et al., 1989). Before the Paleozoic Illinois Basin formed, a similar structural depression, referred to as the proto-Illinois Basin, formed between 1.48 Ga and 500 Ma (Kolata and Nelson, 2010) and may be evidence of rifting in central Illinois (Marshak and Paulsen, 1996). Despite the lack of drill holes penetrating Precambrian rocks perceived to be part of the proto-Illinois Basin, evidence for the early basin is two-fold:

(1) A prominent layered sequence of subhorizontal seismic reflectors appears to sag into a depression that lies north of the Illinois Basin depocenter (McBride et al., 2003). This layered succession is referred to as the Centralia sequence (Pratt et al., 1989, 1992) and

exhibits a geometry that strongly suggests a succession of layered rocks that have been postulated as sedimentary or volcanic in origin (McBride and Kolata, 1999).

(2) The Centralia sequence is overlain by the Mt. Simon Sandstone, which has a depocenter in east-central Illinois approximately 300 km (186 mi) north of the post-Mt. Simon Paleozoic sediment depocenter (the Illinois Basin in southern Illinois; Freiburg et al., 2014). The thickness trends of the Mt. Simon roughly coincide with that of the underlying Centralia succession, suggesting a similar subsidence event that accommodates both units (McBride et al., 2003). Prominent pinch-out boundaries of the Centralia sequence are observed on seismic profiles in west-central and south-central Illinois (Pratt et al., 1989; McBride and Kolata, 1999; McBride et al., 2003) and may correspond to a rift boundary, as marked by the Nd line of Van Schmus et al. (1996) and McBride et al. (2016) (Figs. 1 and 2).

3. Methodology

The study area is located in Decatur, Illinois, on the property of the Archer Daniels Midland Company. Using dedicated drill holes (Fig. 4), the IBDP and ICCS Project involved intensive testing of CO_2 injection and monitoring of the reservoir (Cambrian Mt. Simon Sandstone) as well as the overlying and underlying sealing formations, including the Precambrian basement (Table 1 and Fig. 5). To provide a broad regional context for the Precambrian in relation to the IBDP basement, high-resolution intersecting two-dimensional (2D) seismic profiles totaling 200 km (124.3 mi) were acquired just north of the three-dimensional (3D) seismic volume (Figs. 1 and 3), which had 10.36 km^2 (4 mi^2) of surface coverage and was centered over the four wells (Fig. 1). Specific information on both the 2D and 3D seismic data are provided in McBride et al. (2016), including detailed information on data processing. Seismic data processing included refraction statics using a tomographic solution, followed by multiple passes of surface-consistent residual static corrections. The careful application of static corrections reduces the risk of lateral breaks in coherence (Fig. 8) being misinterpreted as static shifts caused by unaccounted-for lateral variations in seismic velocity in the shallow subsurface. Results from a vertical seismic profile were used to accurately correlate the top of the Precambrian basement with the 3D reflection data (Figs. 4–8) and to guide the conversion of the seismic 3D data from time to depth (Couëslan et al., 2013). A short section (~50 km (31.1 mi)) of the longest E–W 2D profile (L101, ~150 km (93.2 mi)), located just north of the 3D seismic volume and coincident deep drill holes, was used in this study (Fig. 3).

Extensive data from the four drill holes that penetrated Precambrian basement at the site were used for this study (Figs. 1 and 4). A full suite of petrophysical logs were acquired through each borehole, including full-bore microimager (FMI) logs (Fig. 9). Each well penetrated variable depths of basement (Table 1 and Fig. 6), with whole core (10 cm (3.9 inch) in diameter), rotary sidewall core (2.5 cm (1 inch) in diameter), and cuttings. Cores and cuttings were compared with FMI logs to identify all basement lithologies encountered in the wells (Table 1 and Fig. 9). Forty-six thin sections were prepared from the cores and cuttings and described. Because of the limited access to samples for sufficient mineralogical analysis, six thin sections were selected for nondestructive quantitative electron mineralogy analysis by QEMSCAN (quantitative evaluation of minerals by scanning electron microscopy). Analyses were completed by the SGS Laboratory in Vancouver, Canada, and the Automated Mineralogy Laboratory at the Colorado School of Mines in Golden, Colorado.

Because of the limited availability of samples, only two basement samples were U-Pb age dated, including the rhyolite and gabbro. Zircon crystals were extracted from samples by traditional methods of crushing and grinding, followed by panning, heavy liquids, and a Frantz magnetic separator. Zircons were mounted with Sri Lanka, FC-1, and R33 zircon crystals, which were used as primary standards. The mounts were sanded down to a depth of ~20 μm, polished, imaged, and cleaned before isotopic analysis.

The U-Pb geochronology of zircons was conducted by laser ablation inductively coupled plasma mass spectrometry (LA-ICPMS) at the Arizona LaserChron Center (Gehrels et al., 2006, 2008; Gehrels and Pecha, 2014). The analyses involved ablation of zircon with a Photon Machines Analyte G2 excimer laser equipped with a HelEx ablation cell using a spot diameter of 20 μm. The ablated material is carried in He into the plasma source of an Element2 HR ICPMS, which sequences rapidly through U, Th, and Pb isotopes. Signal intensities were measured with a scanning electron microscope that operates in pulse-counting mode for signals less than 50K counts per second (cps), in both pulse-counting and analog mode for signals between 50K cps and 5M cps, and in analog mode above

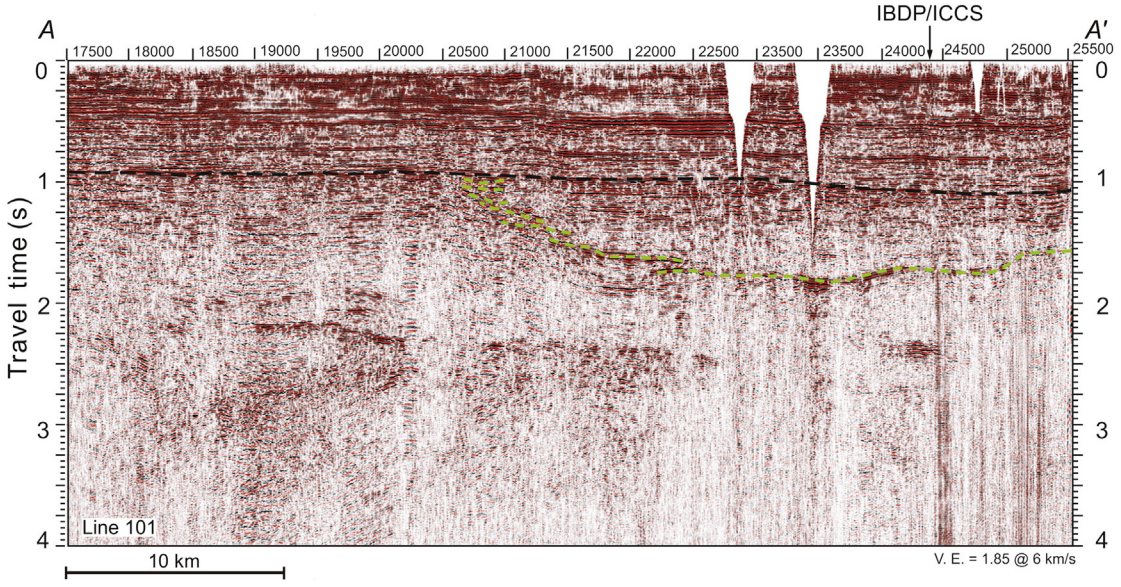

Fig. 3. Section of the L101 2D seismic profile A–A′ (Fig. 2) through Macon County, Illinois (Fig. 1B). The well locations from the IBDP–ICCS project area are located to the south of the 24000 and 24500 profile line markers. The top of the Precambrian surface is labeled with a black dashed line. The western flank of the bowl-shaped structure and the eastern edge of the presumably older Precambrian crust is labeled with a green dashed line. The western edge of the green dashed line is uneven where suspected faults are observed.

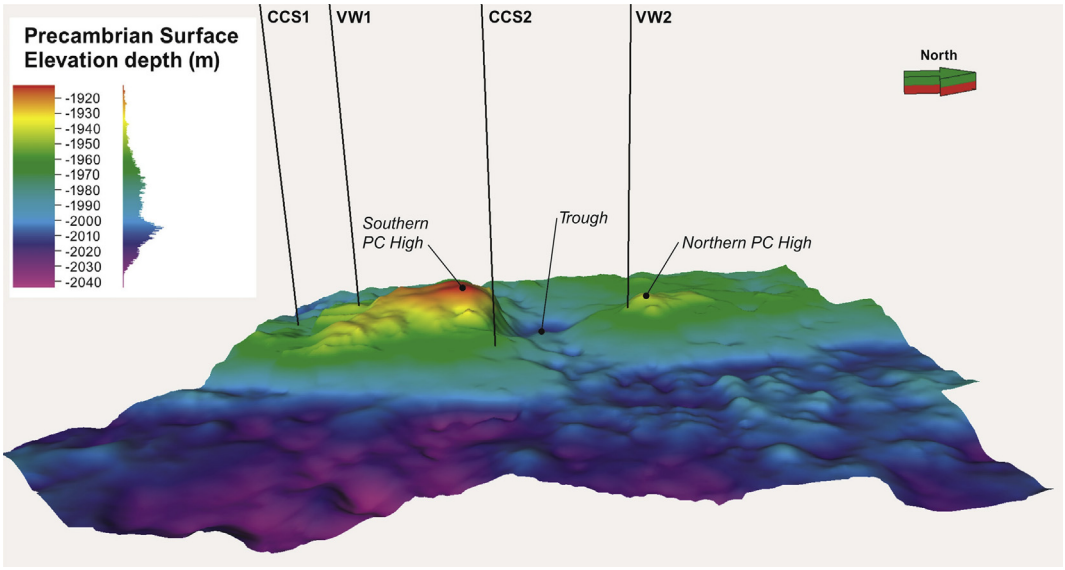

Fig. 4. Precambrian basement topography with locations of the four wells with petrologic observations. The Carbon Capture and Storage 1 well (CCS1) and Verification Well 1 (VW1) are approximately 305 m (1000 ft) apart. Two Precambrian (PC) highs are separated by an E–W-trending trough. The basement topographic elevation is based on the 3D seismic reflection volume from the IBDP–ICCS site and is shown with 10× exaggeration. View looking west (north arrow on bottom right of figure). The area represents 8.6 km^2 (3.3 mi^2). For distance between wells, refer to Fig. 5.

Table 1
Top depths (m) of basement lithologies encountered in the IBDP and ICCS wells.

Well name	Lithology					Well base	Drilled depth into basement
	Rhyolite	Volcaniclastic/breccia	Layered gabbro	Trachyte	Granite		
VW1	2151	2178/2214	-	2209	-	2222	71
CCS1	2185	2195	-	-	-	2206	21
CCS2	2183	-	-	-	-	2192	9
VW2	2167		2174		2192	2202	35

5M cps. The calibration between pulse-counting and analog signals was determined line by line for signals between 50K cps and 5M cps, and was applied to signals >5M cps. Four intensities were determined and averaged for each isotope, with dwell times of 0.0052 s for ^{202}Hg, 0.0075 s for ^{204}Pb, 0.0202 s for ^{206}Pb, 0.0284 s for ^{207}Pb, 0.0026 s for ^{208}Pb, 0.0026 s for ^{232}Th, and 0.0104 s for ^{238}U.

With the laser set at an energy density of ~5 J/cm^2, a repetition rate of 8 Hz, and an ablation time of 10 s, ablation pits were ~12 μm in depth. Sensitivity with these settings was ~5000 cps/ppm. Each analysis consisted of 5 s on peaks with the laser off (for backgrounds), 10 s with the laser firing (for peak intensities), and a 20 s delay to purge the previous sample and save files.

After analysis, data reduction was performed with an in-house Python decoding routine and an Excel spreadsheet (E2agecalc). The routines in Isoplot were used to show the ages on Pb*/U concordia and weighted mean diagrams (Ludwig, 2008). The weighted mean diagrams used weighting according to the square of the internal uncertainties, the uncertainty of the weighted mean, the external (systematic) uncertainty that corresponded to the ages used, the final uncertainty of the age (determined by quadratic addition of the weighted mean and external uncertainties), and the mean square weighted deviation (MSWD) of the data set.

4. Results

4.1. Geophysics

4.1.1. Seismic reflection

The degree of coverage by 2D and 3D seismic reflection data at the IBDP–ICCS site is unprecedented in the Illinois Basin for a study of the Precambrian basement (McBride et al., 2016). A 2D reflection profile (Fig. 3), located just north of the site and the 3D seismic volume (Figs. 1 and 4), provides a regional geophysical context for the basement lithologic interpretations. The seismic profile (Fig. 3) shows a prominent series of high-amplitude reflections, including a deep intrabasement bowl-shaped structure. This reflector, which appears on both the 2D seismic profile and the 3D seismic volume (Fig. 6), is interpreted to be part of a layered mafic sill sequence and may be related to a poorly documented episode of Precambrian lithospheric extension and igneous intrusion (McBride et al., 2016). The area of intrabasement reflectivity appears to correspond to a prominent closed-contour positive magnetic intensity anomaly (Fig. 2).

To establish a context for interpreting the petrologic data from the four deep wells (Fig. 4), vertical depth profiles were extracted from the 3D seismic volume along a line connecting the wells (Fig. 6). This included a high-resolution, close-up view of Verification Well 2 (VW2; Fig. 7) and depth slices through the volume that provided plan views through the basal Cambrian and the top of the Precambrian basement (Fig. 8). As shown in Fig. 4, the four holes are located on the flanks of two prominent basement structural highs expressed by a fence diagram crossing the structural highs. The southern three holes (Carbon Capture and Storage 1 well (CCS1), Verification Well 1 (VW1), and Carbon Capture and Storage 2 well (CCS2); Fig. 4) are located on the southern basement high (Fig. 4). The northernmost hole, VW2 (Fig. 4), is located on the northern basement high (Fig. 4), just over a small oval area of anomalous reflectivity (1965 m (6447 ft) depth slice; Fig. 8). The top of the Precambrian basement between CCS1 and VW1 is a continuous reflection associated with a strong positive-amplitude excursion (orange;

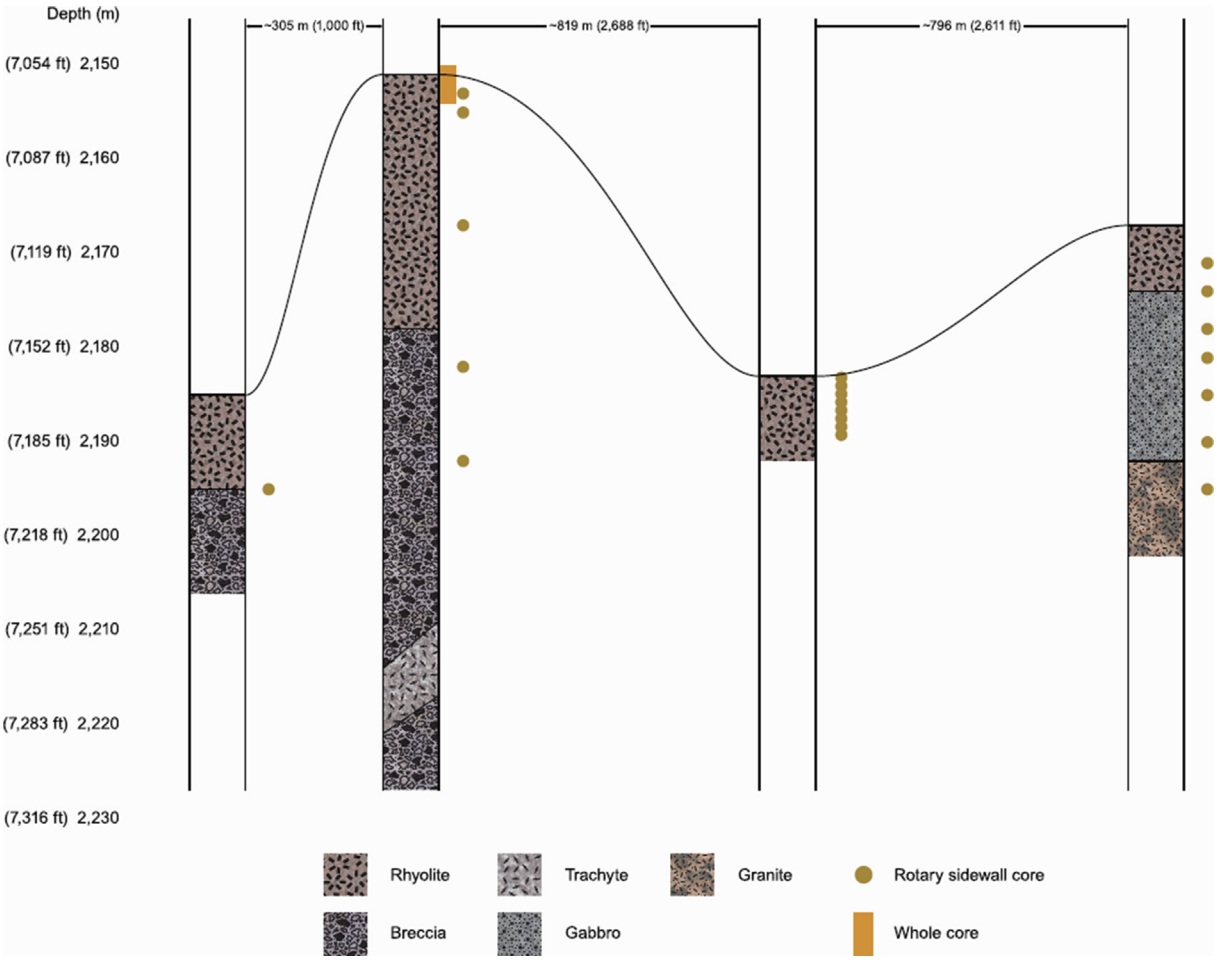

Fig. 5. Cross section of the four wells showing basement horizon, lithologies (Table 1), and samples. Well cuttings were obtained through the entire section of each well. True vertical depths from the top of well.

warm colors indicate positive amplitudes), implying a contrast from lower to higher seismic velocity with depth. The CCS2 and VW2 display a more complex top-basement interface and are separated in map view by a structurally low area between the basement highs (Fig. 4). Fig. 6 reveals a lenticular body (in a N–S cross section) with an additional reflection cycle that includes two inward-facing pinch-outs, which define the edges of the trough between the two holes (Fig. 4). This lenticular body also appears in a vertical view through the VW2 hole in an east–west cross section (Fig. 7). The vertical seismic views reveal a zone of strong reflectors ~150 m (~492 ft) thick and 150 m (~192 ft) below the depth of well penetration (Figs. 6–7). The gabbro penetrated in VW2 may relate to the layering observed in the seismic data (Fig. 7).

We computed seismic-attribute depth slices beginning at the approximate depth of the basement and continuing deeper (Fig. 8). These results suggest vertical and lateral variations in basement seismic properties. A semblance attribute shows the degree of similarity between adjacent seismic traces and thus delineates discontinuities when displayed as a horizontal depth slice through a seismic volume (Marfurt et al., 1998). For example, the depth slice from near the top of the basement shows a clear rectilinear trend in semblance for the N–NW and E–NE directions (white arrows in Fig. 8). At 1965 m (6447 ft) below mean sea level, a N–NW linear trend in the semblance begins to emerge and becomes more prominent with increasing depth. This semblance pattern indicates a set of parallel discontinuities. These discontinuities are spaced at intervals of ~50–100 m (~164–328 ft) and traverse much of the north-to-south length of the seismic volume. Beginning at a depth of ~2014 m (~6608 ft), an opposing trend, northeast, appears in the semblance, indicating possible discontinuities in this direction. Together, the two trends define a rectilinear pattern, possibly fractures or faults of small displacement that persist down into the Precambrian basement, corresponding to the levels from which the petrographic observations were made. The interpreted fault or fracture pattern suggests a lateral compartmentalization or heterogeneity of basement rocks. The lithologic variation observed from the holes could be explained by structural discontinuities separating zones of different crystalline rocks.

We can see examples of possible compartmentalization of basement lithologic properties marked by interpreted discontinuities. The closely spaced (305 m (1001 ft)) VW1 and CCS1 wells are both located along the edge of a rectilinear semblance pattern (2064 m (6772 ft) depth slice; Fig. 8) and have basement rocks that show similar characteristics (e.g., a concentration of volcanic breccia and granite). Note also that the semblance around these holes is low, suggesting a more structurally complex volume of rock. In contrast, the more widely spaced CCS2 and VW2 holes are separated by a northeast-trending discontinuity, but each is in a zone of more consistent, higher semblance (2047 m (6716 ft) depth slice; Fig. 8). The basement rocks from each of these two wells are granite but also may be intruded by gabbro (VW2 has the only gabbro of the four wells). The variation in basement lithology between the CCS2 and VW2 wells is broadly consistent with the variation in basement acoustic structure as defined by the semblance.

In summary, the 3D seismic reflection volume indicates top-basement topography expressed as two structural highs (Fig. 4) and strong heterogeneity within the uppermost part of the basement rocks penetrated by the holes (Fig. 8). The closely spaced wells CCS1 and VW1, located over the southern flank of the southern basement high (Fig. 3), show a similar top-basement reflectivity (Fig. 6), whereas wells CCS2 and VW2

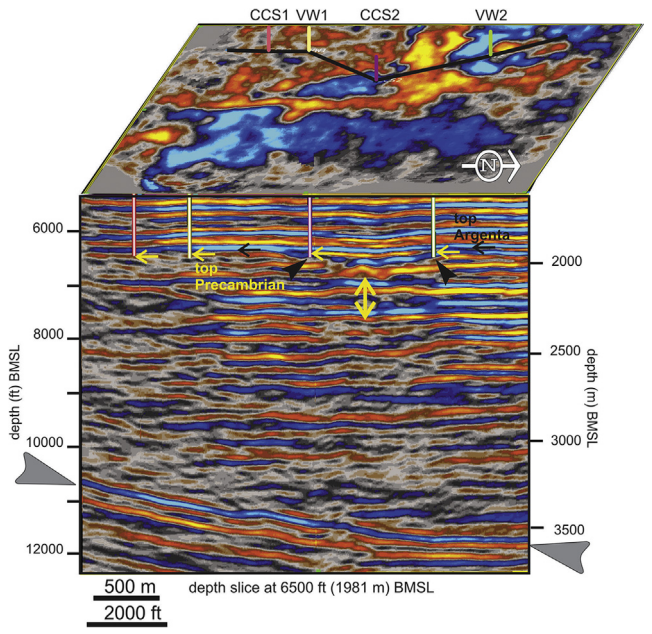

Fig. 6. Cross section vertical view excerpted from the depth-converted 3D seismic volume from the IBDP–ICCS site. The section follows the black line through the four holes shown on the horizontal depth slice (at 1981 m (6500 ft)). The top of the Precambrian is shown by yellow horizontal arrows. The vertical double-headed yellow arrow indicates a zone of anomalous reflectivity just below the total depths of the wells. The tilted black arrows indicate pinch-out of reflectors and the lozenge-shaped body referred to in the text. The large gray arrows refer to the deep bowl-shaped reflector shown regionally in Fig. 2, which has been interpreted as a mafic igneous sill. All depths are referenced to mean sea level.

penetrate the northern and southern margins of a trough (Fig. 6) separating the two basement highs (Fig. 4). The location of the latter two holes in areas of variable seismic character and separated by a discontinuity are consistent with the variable basement lithology observed in them. The reflectivity structure at the top basement interface for the VW2 and CCS2 holes consists of a more multicyclic character compared with the southern two holes (VW1 and CCS1; Fig. 6). The multicyclic character is especially evident on the higher resolution vertical view through VW2 (Fig. 7). Although the vertical resolution of the seismic data obviously cannot match that in the drill hole, the variations in the seismic reflectivity and in the semblance attribute are consistent with the variations independently observed in basement petrology.

4.1.2. *Fullbore microimager logs*

Basement lithologic and structural variability is evident in microresistivity formation images in the FMI logs from all four wells (Table 1 and Fig. 9). In all wells, the Cambrian–Precambrian contact is sharp, and the top of the Precambrian is composed of a weathered rhyolite (Fig. 9A). Five lithologies are identified in core samples and cuttings, namely rhyolite (Fig. 10A), volcaniclastic breccia (Fig. 10B), granite (Fig. 10C), gabbro (Fig. 10D), and trachyte. The FMI characteristics of these lithologies are listed below.

4.1.2.1. Verification Well 1. In VW1, the top of the basement is at a depth of 2151 m (~7058 ft) below ground surface and is a weathered rhyolite that becomes more porphyritic and less altered with depth. The upper 2 m (6.6 ft) shows evidence of flow banding in the core that is not easily discernible in the FMI logs. However, differential resistivity intensities in the images appear to show partially spheroidal discontinuous layers in the upper section (Fig. 9A). These resistivity discontinuities become less apparent with depth, and the rock is more layered, porphyritic, and fractured. A volcanic breccia is penetrated at 2177 m (~7144 ft) and extends to the bottom of the well (Fig. 9B–C). The breccia contains abundant subangular, angular, and subrounded clasts that are highly resistive in a more conductive matrix. At ~2209 m (~7249 ft), a fractured 5-m (~16-ft)-thick trachyte layer crosscuts the breccia (Fig. 9C).

4.1.2.2. Verification Well 2. In VW2, the top of the basement is penetrated at a depth of 2167 m (7111 ft). Rhyolite occurs for 7 m (23 ft) before encountering gabbro (Fig. 9D–F). The contact of the rhyolite and gabbro is sharp and possibly chilled. Fracturing is more common in the gabbro than in the overlying rhyolite. The gabbro includes thin layers of more conductive rock and thicker layers of mottled and coarser grained material (e.g., CCS1). At ~2192 m (~7191 ft), the fracture density increases, and a granite is encountered. The occurrence of granite was confirmed by using cuttings and rotary sidewall core.

4.1.2.3. Carbon Capture and Storage 1 well. In CCS1, the top of the basement is at 2185 m (7168 ft). The rhyolite is mottled and is coarser grained than what is present in the other wells. Breccia begins at ~2195 m (~7203 ft), and the contact with the overlying rhyolite is subtle. The most notable difference between CCS1 and all other wells is the paucity of fractures.

4.1.2.4. Carbon Capture and Storage 2 well. The CCS2 well is the shallowest well, with a depth of 2183 m (7162 ft). The FMI log reveals 15 m (50 ft) of fine-grained, homogeneous rhyolite with subtle layering.

4.2. *Petrography*

The texture and mineralogy of basement lithologies identified at the IBDP–ICCS site show rock types typical of the EGRP and rock types

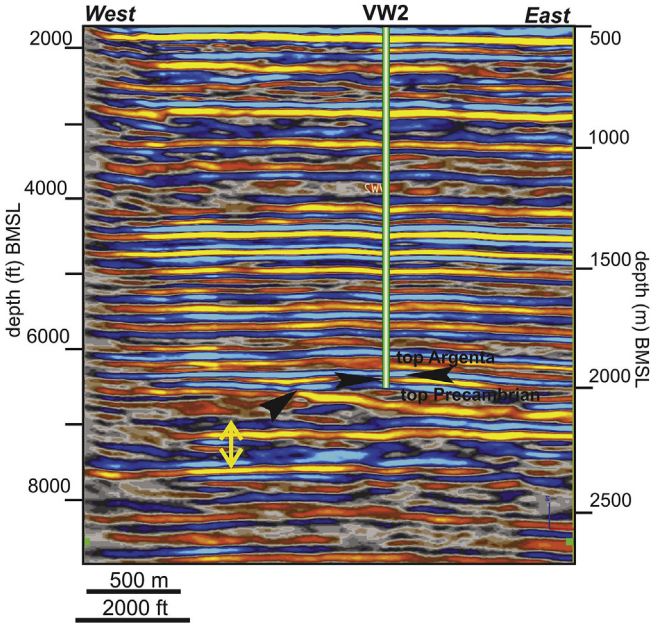

Fig. 7. Cross section excerpt from the depth-converted 3D seismic volume from the IBDP–ICCS site along a profile intersecting Verification Well 2 (VW2; see location in Fig. 3). The vertical cylinder is a representation of the VW2 well bore. The interpreted top of the Precambrian is shown by a horizontal black arrow. The vertical double-headed yellow arrow indicates a zone of anomalous reflectivity just below the total depth of the wells. The tilted black arrow indicates pinch-out of reflectors and the western flank of the lenticular body referred to in the text and denoted in Fig. 4. All depths are referenced to mean sea level.

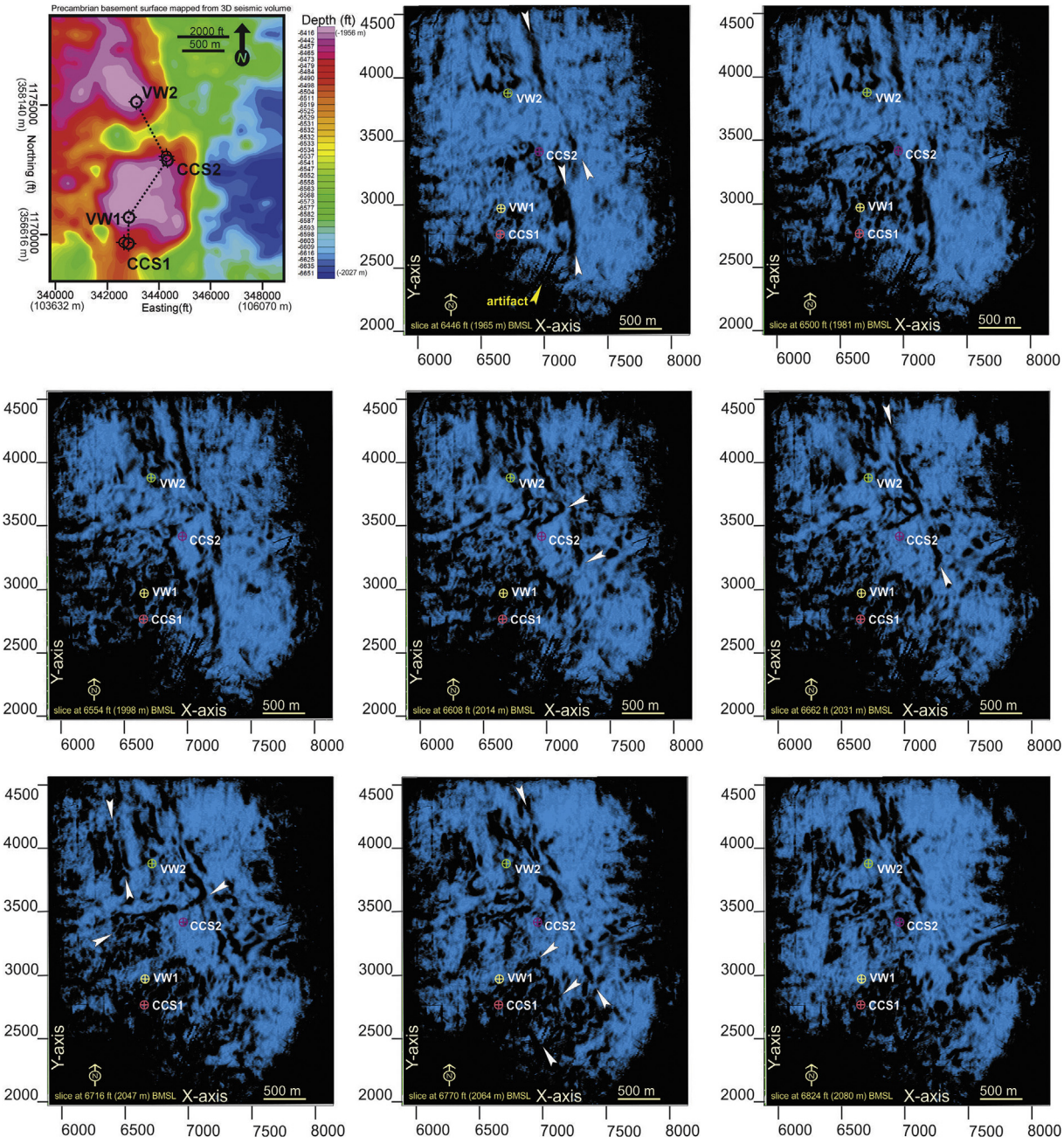

Fig. 8. Horizontal depth slices through the depth-converted 3D seismic volume from the IBDP–ICCS site, starting at 1965 m (6446 ft) below mean sea level just above the top of the Precambrian basement and ending at 2080 m (6824 ft) below mean sea level well below it. The top of the basement is approximately 1960 m (6430 ft) below mean sea level in VW2. Note that the seismic time-to-depth conversion was performed by using the dedicated vertical seismic profile. The interval between the depth slices is ~16 m (54 ft), which is approaching the quarter wavelength (Rayleigh) criterion for vertical resolution for high-seismic-velocity Precambrian rocks. We interpret the uncertainty in relative depths on the slices to be within this limit. Well locations are shown (Fig. 3). Slices show a nine-trace semblance seismic volume attribute computed for the depths indicated. The white arrows show selected north-northwest and southeast discontinuity (expressed as black) trends. The map in the upper left-hand corner is the gridded depth (below mean sea level) of the top of the Precambrian basement as mapped from the seismic volume.

atypical of this province. The variable mineralogy and textures of these rocks are described below (Figs. 11 and 12 and Table 2).

4.2.1. Rhyolite

The most abundant basement lithology at the IBDP–ICCS site is rhyolite. Rhyolite is present in all wells (Table 1). Most rhyolite (Figs. 11A,B and 12A) consists of phenocrysts of K-feldspar and quartz in a dark purple aphanitic groundmass that is likely devitrified glass. The top of the rhyolite is weathered with abundant feldspar and volcanic glass alteration products, including kaolinite, chlorite, and illite. A fabric, as manifested by flattened chlorite lenses that may represent altered volcanic fiamme clasts, is present in the rhyolite core. Spherulites are common and occur in association with a devitrified glass matrix (Fig. 12B) that is characterized by randomly oriented needlelike crystals.

4.2.2. Volcaniclastic breccia

The breccia consists of sand- and gravel-sized, angular to subrounded fragments of altered aphanitic volcanic clasts that are composed of

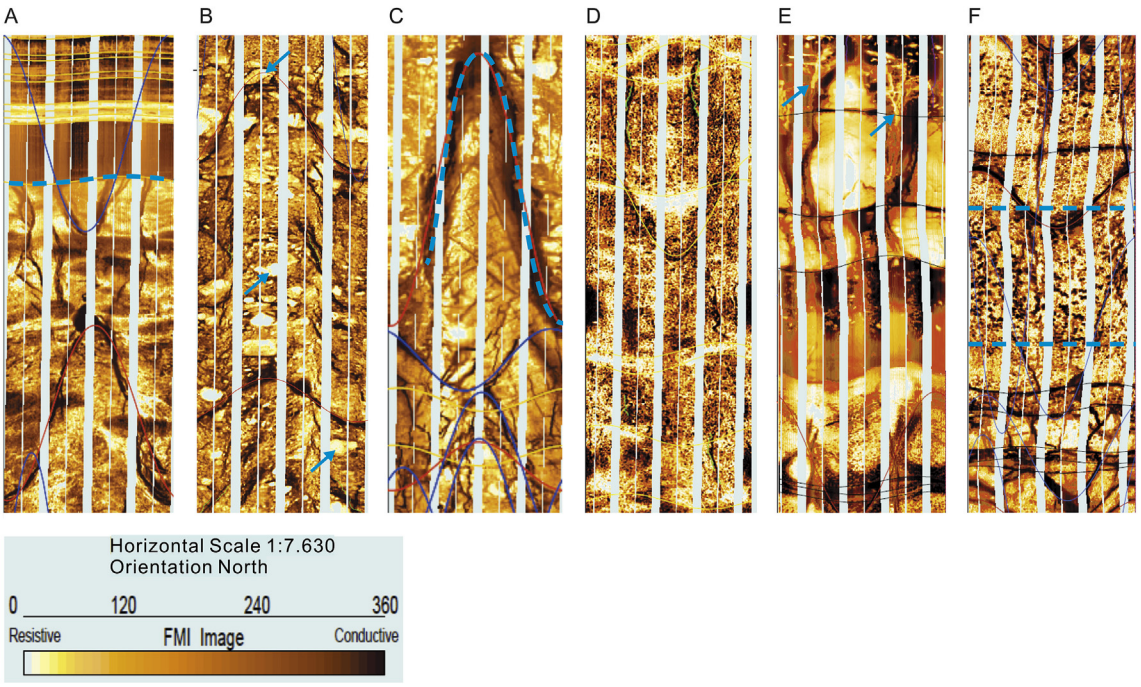

Fig. 9. Fullbore microimager log images (FMI) within the Precambrian basement in the IBDP–ICCS wells. Each image (A–F) is a composite of 90° images of the borehole stitched together to create a 2D 0° to 360° view of the borehole. (A) The VW1 2151–2153 m (7056–7064 ft) at depth shows the contact (dashed line) of the Cambrian (Argenta) and Precambrian basement. Note the sedimentary layering in the Cambrian rocks and abundant fractures in the Precambrian basement rocks. (B) The VW1 2198–2200 m (7210–7218 ft) at depth shows a breccia with large clasts (arrows) in a fine-grained matrix. (C) The VW1 2209–2212 m (7249–7257 ft) at depth shows a trachyte intrusive (outlined with a dashed line) crosscutting the breccia. Note the difference in fracture patterns in the trachyte, which are highly systematic and conchoidal in appearance, compared with fractures in the rhyolite (A) and breccia (B), which are singular and high angle. Note the (D) VW2 2170–2172 m (7118–7127 ft) at depth showing typical porphyritic rhyolite. (E) The VW2 2175–2178 m (7136–7145 ft) at depth shows layering and possible mineralized fractures near the basal rhyolite and top of gabbro contact. (F) The VW2 2184–2186 m (7164–7172 ft) at depth shows coarse-grained gabbro.

plagioclase and quartz (Figs. 11C and 12C,D). In the two thin sections examined, clasts constituted approximately 75% and 15% of the samples. Quartz and plagioclase are common, with rarer pyroxene and K-feldspar present in the breccia matrix. Accessory minerals include mica, iron and titanium oxides, and apatite.

4.2.3. Granite

Granite occurs in VW2. The granite is coarse grained with nearly equal parts of quartz, K-feldspar, and plagioclase and is classified as a monzogranite. It contains minor pyroxene, mica, chlorite, and trace accessory minerals, such as iron oxides, titanium oxides, apatite, fluorite, pyrite, and chalcopyrite (Figs. 11D and 12E). Albite is the most abundant feldspar and commonly has intergrowths of quartz and orthoclase that exhibit a micrographic texture. Chlorite is present as an alteration product of pyroxene.

4.2.4. Gabbro

Gabbro occurs in VW2 and consists of anorthite, clinopyroxene, orthopyroxene, olivine, and mica with minor quartz, biotite, chlorite, and trace accessories, including iron oxides (dominantly magnetite), titanium oxides, and apatite (Figs. 11E, 12F). The opaque minerals (likely magnetite) commonly occur as a symplecite, often near boundaries of olivine and plagioclase (Fig. 12G). Mica occurs throughout and appears as inclusions or intergrowths within anorthite. Minor quartz appears to be associated with altered albite cores. Accessory minerals are most commonly associated with altered albite.

4.2.5. Trachyte

At the base of VW1, a trachyte dike is crosscutting the volcaniclastic breccia (Fig. 9C). It is composed of a groundmass with plagioclase laths that appear to have preferential orientation (Figs. 11E, 12F). Chlorite, pyroxene, and opaque minerals are common. Opaque minerals most

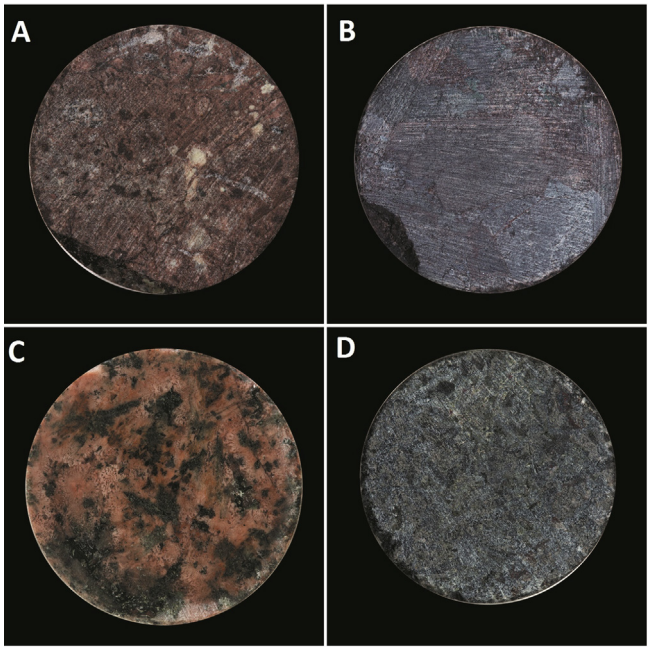

Fig. 10. Photographs of 2.5-cm (1 inch)-diameter rotary sidewall core. (A) Porphyritic rhyolite from CCS2, 2185 m (7170 ft) well depth. White feldspar phenocrysts are scattered in a fine-grained reddish-gray colored matrix. (B) Igneous breccia composed of rhyolite and subangular to subrounded aphanitic igneous clasts from VW1, 2192 m (7193 ft) well depth. (C) Granite from VW2, 2195 m (7201 ft) well depth. Coarse grains of quartz and feldspar are ingrown with medium to coarse grains of plagioclase, pyroxene, and olivine. (D) Gabbro from VW2, 2185 m (7168 ft) well depth.

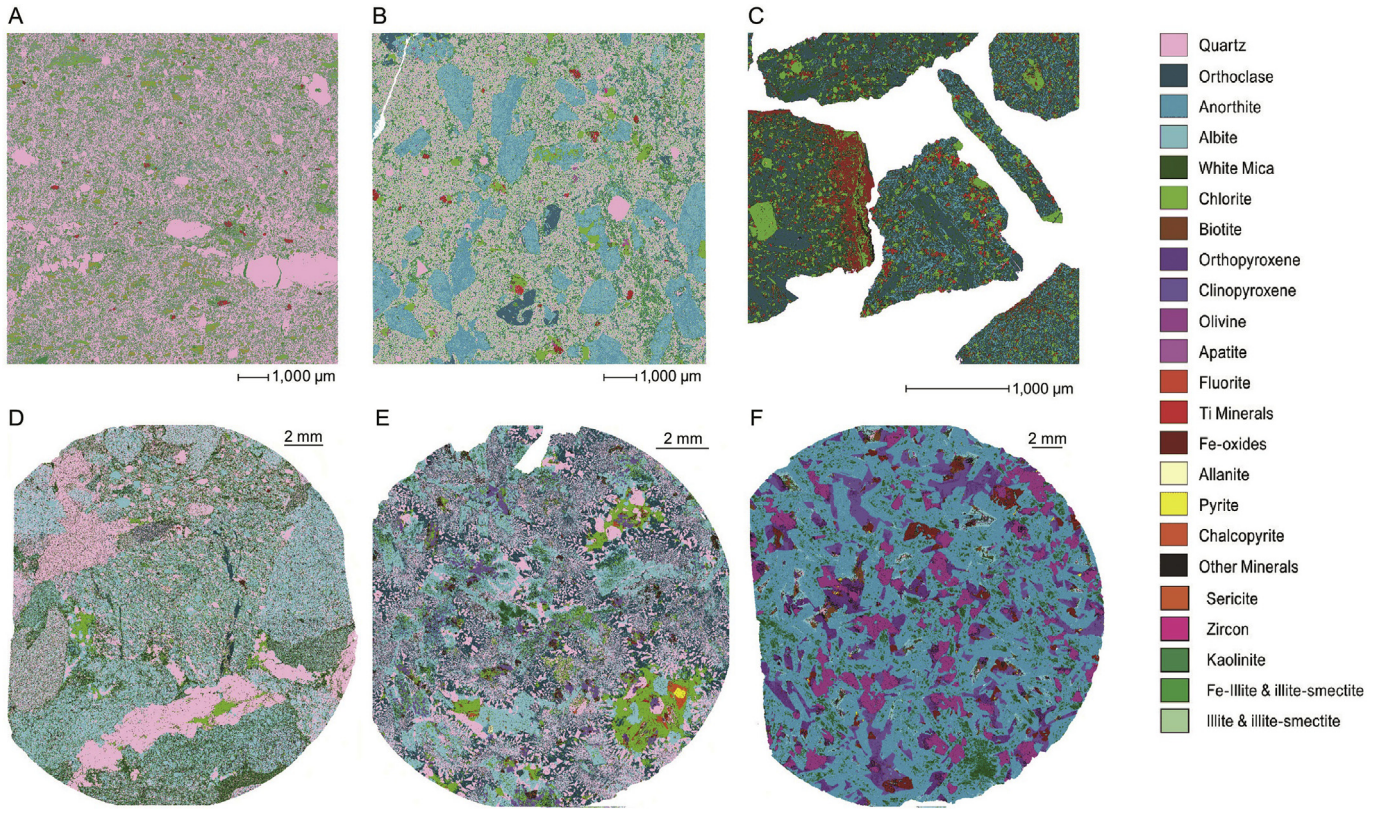

Fig. 11. Quantitative evaluation of minerals by scanning electron microscopy (QEMSCAN) images of the Precambrian basement from the IBDP–ICCS site. (A) The VW1 core at a 2149.5 m (7052.3 ft) at depth is a rhyolite composed of quartz, kaolinite, and chlorite with minor plagioclase and illite. Note the abundance of quartz phenocrysts and quartz-rich matrix shown in pink. (B) The VW1 core at a 2154.5 m (7068.8 ft) at depth is porphyritic rhyolite that has a quartz and illite matrix with abundant plagioclase phenocrysts and minor K-feldspar, chlorite, and titanium minerals. Note the abundance of plagioclase phenocrysts in blue and the increase of clay minerals in the matrix show in green. (C) The VW1 cuttings at a 2210–2214 m (7250–7264 ft) at depth are a trachyte with a plagioclase- and clay-rich matrix with abundant K-feldspar phenocrysts and common titanium minerals and iron oxides. Note the dominance of feldspar shown in blue throughout the sample and the concentration of titanium minerals in the sample shown in red. (D) The VW1 core at 2192 m (7193 ft) at depth is a breccia composed of quartz-, albite-, mica-, and chlorite-rich clasts and minor orthoclase and iron oxides. Note the aphanitic clasts rich in plagioclase shown in blue and the abundance of quartz as both cements and phenocrysts shown in pink. All clasts have variable concentrations of quartz shown in pink. (E) The VW2 core at a 2195 m (7201 ft) at depth is a granite or granophyre with a strong micrographic texture of K-feldspar and quartz intergrowth and common plagioclase and chlorite. (F) The VW2 core at a 2189.9 m (7184.9 ft) at depth is a gabbro composed of plagioclase, pyroxene, and olivine with minor mica, iron oxides, and titanium minerals. Note the abundance of olivine and pyroxene shown in purple throughout the sample in a matrix dominated by plagioclase shown in blue.

commonly appear as symplecites that dominate the boundaries of plagioclase and pyroxene. The trachyte has a variable grain size, ranging from very fine to medium grained. Textural variations imply a slowly cooled center and a rapidly cooled margin of the dike.

4.3. U-Pb geochronology

Zircons were separated from about 1 kg (2.2 lb) of the rhyolite core (VW1) and <0.04 kg (0.09 lb) of the gabbro sidewall core. Of note, the processed gabbro contained 11.75 g of magnetite separately, nearly 30% of the sample. The U-Pb geochronology results are provided in Table 3. The concordia and weighted mean ages (WMA) are presented in Fig. 13.

Twenty-nine spots were analyzed on 26 rhyolite zircons. Uranium concentrations are moderate and range from 59 ppm to 264 ppm. The U/Th ratio ranges from 1.5 to 3.0. Zircon ages range from 1407 Ma to 1522 Ma, and the three zircons for which both cores and rims were analyzed showed no difference in age when the error was considered. The concordia age, based on 27 analyses, is 1467 ± 10 Ma with an MSWD of 0.70 (2σ; Fig. 13A). The WMA of these same zircons is 1467.4 ± 9.3 Ma (95% confidence interval) with an MSWD of 0.68 (Fig. 13B).

The zircon yield for the gabbro is low because of the mafic composition and limited sample size. Ten zircons were analyzed and eight produced concordant dates. The age range for these zircons is astonishing, ranging from 1039 Ma to 2860 Ma. Three zircons at the younger end of the age distribution reveal a concordia age of 1073 ± 12 Ma and an MSWD of 0.026 (2σ; Fig. 13C). The WMA of these three zircons is 1073.7 ± 9.3 Ma (2σ; Fig. 13D) with an MSWD of 0.013. The oldest four zircons are 1303 Ma (earliest Grenville), 1723 Ma (Yavapai), 2853 Ma, and 2860 (Archean) Ma.

5. Discussion

Seismic reflection data suggest that the Decatur site is located on the far northwestern edge of the layered Precambrian Centralia succession (McBride et al., 2003, 2016) and on the southeastern side of a northeast-trending geochemically defined boundary that separates pre-1.55 Ga model-age crust (north) from post-1.55 Ga model-age crust (south; Van Schmus et al., 1996, Figs. 1 and 2). The Decatur site lies on the eastern flank of a closed-contour, high-amplitude magnetic anomaly that corresponds to the Precambrian crust on the south or east side of the geochemically defined boundary along a seismically defined bowl-shaped feature (Fig. 3). It is unclear whether the bowl-shaped feature observed at the Decatur site can be exactly correlated to the previously proposed Centralia sequence-equivalent rocks (Pratt et al.,

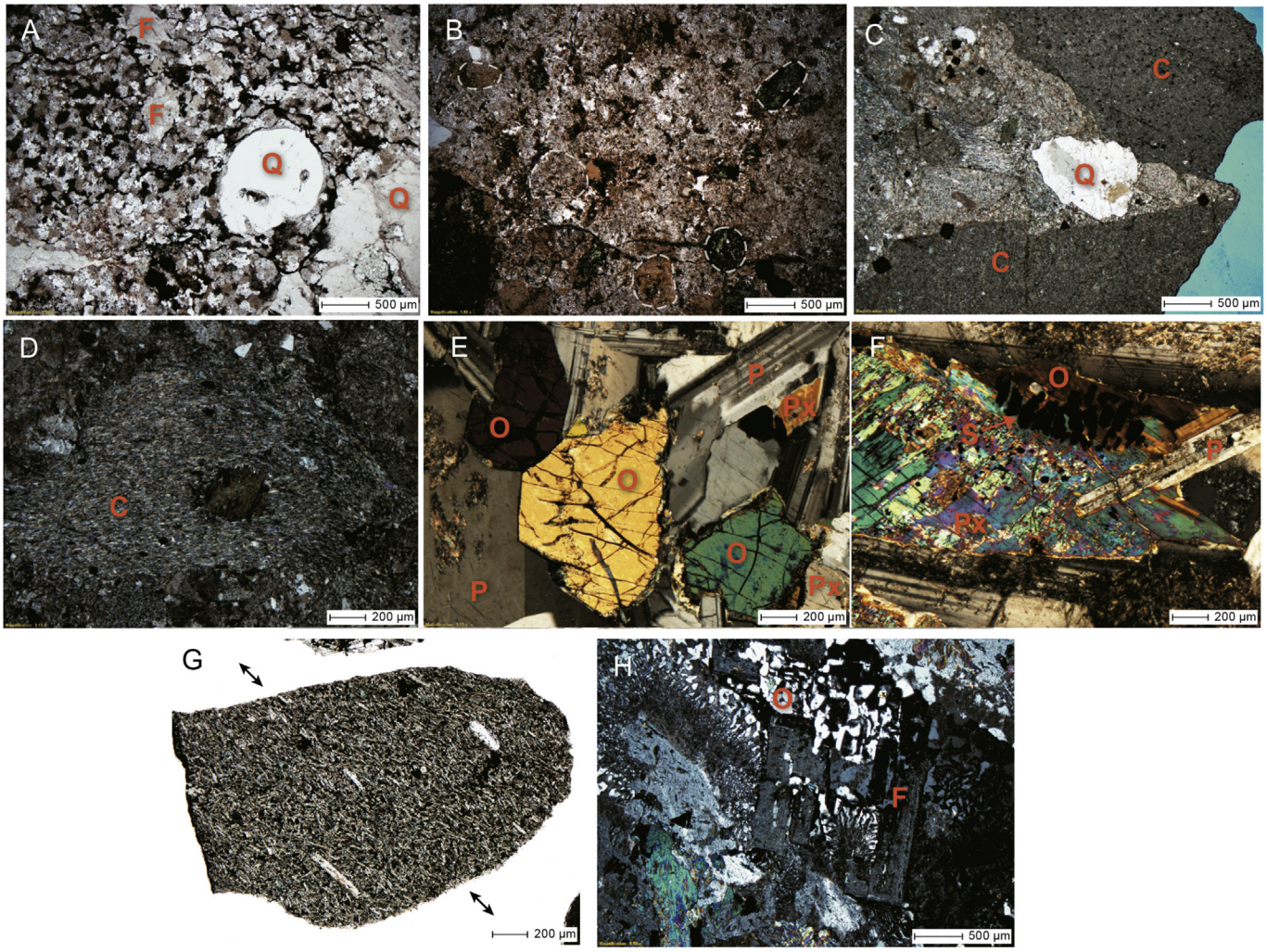

Fig. 12. Thin section photomicrographs (all cross-polarized light) of Precambrian basement from the IBDP–ICCS site. (A) VW1 at a 2151.5 m (7058.9 ft) depth shows a porphyritic rhyolite with a spherulitic texture, strong compaction and foliation, feldspar , and embayed quartz phenocrysts. (B) CCS2 at a 2187 m (7174 ft) depth shows a porphyritic rhyolite with a spherulitic (white dashed line) texture, highly altered felsitic matrix, and quartz and feldspar phenocrysts. Note the devitrified matrix with needlelike crystals of randomly arranged tridymite. (C) VW1 at a 2182 m (7159 ft) depth shows a breccia predominantly composed of aphanitic volcanic clasts. Phenocrysts of quartz and iron oxides are common. (D) The VW1 at a 2182 m (7159 ft) depth shows a possible andesite clast composed of plagioclase with a hornblende phenocryst in the center and trace iron oxides throughout. (E) VW2 at a 2189.9 m (7184.9 ft) depth shows a gabbro with common olivine and pyroxene in a plagioclase matrix. (F) The VW2 at a 2185 m (7168 ft) depth is a gabbro with plagioclase, pyroxene, olivine, and opaques such as iron oxides and titanium minerals. Symplecites of opaque oxides formed at the grain boundary between olivine and pyroxene. (G) VW1 at a 2210–2214 m (7250–7264 ft) depth is a trachyte with a fine-grained trachytic to intergranular texture. Preferentially aligned phenocrysts of K-feldspar (alignment denoted by arrows) are in a matrix of more randomly aligned crystals. (H) VW2 at a 2195 m (7201 ft) depth shows a granite or granophyre composed of quartz and feldspar exhibiting a strong micrographic texture. Abbreviatons: F–feldspar, Q–quartz, C–clasts, O–olivine, Px–pyroxene, P–plagioclase, S–symplecites.

1989; McBride and Kolata, 1999; McBride et al., 2003). We propose that the bowl-shaped feature, internal layering, and correlating magnetic anomaly correspond to an intrusive complex crosscutting the EGRP basement.

Previous interpretations of seismic profiles in southern Illinois described a stacked series of seismic stratigraphic sequences of volcanoclastic origin, including the Centralia succession (McBride et al., 2003). According to the northernmost regional seismic profile available for the Illinois Basin (Figs. 1 and 3), well-developed layering within the Precambrian basement is not observed, but rather a reflection pattern that is defined by a broad, bowl-shaped basal surface that extends directly beneath the four wells (McBride et al., 2016; Fig. 6). Fine-scale layering is observed in shallow basement on the higher resolution 3D seismic volume; however, it is possible that only some of the layering is apparent and may be multiple reflections. Layering of rhyolite, gabbro, volcaniclastic breccia, and trachyte is clearly observed in the Decatur wells drilled into the shallow basement (Table 1 and Fig. 6), although obviously not at the same scale as observed in the seismic data (Fig. 7).

The new drill hole petrologic and FMI log data allow fine-scale observations of layered Precambrian rocks that have remained poorly understood regionally. The rhyolite dated at 1467 Ma represents the top of the Precambrian in all wells at the Decatur site. Similar interlayered volcanic rocks and possible volcaniclastic rocks occur in the southern Ozark Dome of Missouri and are related to a rift-margin setting (Lowell et al., 2010). The brecciated volcaniclastic deposits at the IBDP–ICCS site may be similar to those in the Ozark Domes where localized areas of brecciation include foreign volcanic fragments and are interpreted as volcanic vents (Lowell et al., 2010). The rhyolites of Shut-In Mountain in the Ozark Domes are dated at 1.47 Ga (Harrison et al., 2000; Fig. 1), similar to that of the EGRP rhyolite at Decatur. The felsic composition of the volcaniclastic breccia and the conformable appearance of the overlying rhyolite suggest the breccia is at least as old as the 1467 Ma

Table 2
Bulk mineralogy (%) from QEMSCAN.

Well	VW1	VW1	VW1	VW2	VW2	VW2	VW2	VW1
Depth (m)	2149.5	2153.9	2192.4	2171.6	2184.8	2189.9	2194.8	2209–2214
Type	Rhyolite	Rhyolite	Breccia	Sandstone	Gabbro	Gabbro	Granite	Trachyte
Quartz	59.08	30.82	41.03	28.8	1.65	0.21	30.7	0.03
K-feldspar	0	11.81	1.59	35.32	0.14	0.09	23.18	22.84
Anorthite	0	12.37	0.35	0.01	48.21	56.58	2.35	10.94
Orthopyroxene	0	0	0	0	5.22	7.39	0.06	0
Clinopyroxene	0	0	0.02	0	18.54	8.2	3.73	0.84
Olivine	0	0	0	0	4.51	10.16	0	0.14
Chlorite	16.42	4.31	3.06	0.06	0.32	0.12	6.94	15.56
Illitesmectite	2.11	29.12	0	0	0	0	0	0
White mica	0.08	0.02	10.43	27.15	3.78	6.82	2.53	24.95
Biotite	0	0.37	0.08	1.38	1.35	0.82	0.05	1.14
Kaolinite	16.34	0.01	0	0	0	0	0	0
Sericite	0.17	0.11	0	0	0	0	0	0
Iron oxide	0.1	0.1	0.24	0.7	2.62	1.7	0.11	6.56
Ti-oxides	0.57	0.65	0.06	0.22	0.85	0.53	0.77	0
Apatite	0	0.36	0.08	0	0.26	0.22	0.27	0
Zircon	0.03	0.06	0	0	0	0	0	0
Calcite	0	0.4	0	0	0	0	0	0
Pyrite	0	0	0.01	0	00.01	0.02	0.21	0.05
Chalcopyrite	0	0	0	0	0.16	0.11	0.08	0
Stilpnomelane	0	0	0	0	0.01	0.01	0.19	0.3
Unclassified	0	0	8.5	5.18	3.88	2.82	5.17	
Total	100	100	100	100	100	100	100	100

rhyolite. The age of the rhyolite is identical to that of the granites that were penetrated in the four other cores analyzed elsewhere in Illinois and is similar to the most commonly reported age for the EGRP.

The gabbro, dated at 1073 Ma, is either Grenville or late MCR in age. Similar mafic rocks are present in Missouri, but these rocks are all older and fall within the EGRP age group. Moreover, the gabbro at the Decatur site includes xenocrystic zircons of Yavapai and Archean age. Not only are inherited zircon cores virtually nonexistent everywhere in the MCGR province, but also no evidence for crust of this age this far south has ever been reported. If these inherited zircons prove to be reliable, the tectonic models of the genesis of the MCGR province will need to be reconsidered. Using high-resolution imaging techniques from geophysical data, Yang et al. (2017) observed highly localized crustal thinning and shallow Moho depths west of the La Salle Anticlinal Belt and along the Sangamon Arch (on the southwestern edge of the Decatur site). The gabbro is most likely related to the crustal thinning observed by Yang et al. (2017) and associated with the end of the MCR or more generally Grenville-age tectonism and associated extension. Tabular mafic intrusions are associated with continental rifting (e.g., ~1.1 Ga Duluth Complex, Mellen Complex, and Logan Sills; Paces and Miller, 1993; Craddock et al., 2017b). Within the Duluth Complex, layered gabbro intruded into volcanic rocks because of the upwelling of magma associated with the MCR. Gabbro at the Decatur site is at the younger end of the 1109–1087 Ma duration of MCR magmatism (Paces and Miller, 1993; Craddock et al., 2013; Malone et al., 2016). Younger documented mafic intrusives associated with Grenville tectonics include 1057 Ma olivine gabbros in the Adirondack Highlands terrane (McLelland et al., 1990) and a 1050 Ma mafic dike swarm in the central Grenville Province (Hervet et al., 1994; Rivers, 1997).

As shown by the FMI log for VW1, the volcaniclastic breccia is intruded by trachyte (Fig. 6F). The contact between the volcaniclastic breccia and the trachyte is sharp and discordant. The trachyte crosscuts the breccia at a steep angle that makes a cone-like appearance on the FMI log. This is an effect from stitching approximately 90° images of the borehole together to create a 2D 0° to 360° view of the borehole in the FMI log. The trachyte must be younger than the volcaniclastic breccia that it crosscuts and the associated EGRP rhyolite. The trachyte may be associated with the gabbro and may have derived from the suspected deeper mafic complex observed in seismic reflection data (McBride et al., 2016).

Granite underlies the rhyolite and layered gabbro in VW2 and is typical of granite found in the EGRP, having coarse-grained, micrographic textures (Fig. 12H). Recent interpretations show the convergence of an island arc with proto-Laurentia resulting from destabilization and crustal melting of a wide back-arc region of older crust, possibly attributable to delamination processes and back-arc extension (Okure and McBride, 2006; Bickford et al., 2015). Delamination and the resulting rise of hot asthenosphere and consequent crustal melting could have formed A-type granites. The granite at IBDP–ICCS is likely A-type that formed in an intracratonic setting along the interpreted long-lived convergent margin of eastern Laurentia (Bickford et al., 2015).

Whether any of the basement rocks penetrated at the IBDP–ICCS site represent or relate to the layered Centralia succession in a regional sense is unclear. The Centralia as a whole does not correspond to high-magnetic or high-gravity values, as might be expected for large bodies of mafic igneous rocks such as those found in the MCR System (Lidiak et al., 1985). Instead, the margins of the Centralia succession in map view are marked by small, closed-contour anomalies, much like the large, approximately circular anomaly at the IBDP–ICCS site (McBride et al., 2003; Fig. 2). McBride et al. (2003) showed that the southern and western boundaries of this sequence are marked by concentric, curved alignments of small magnetic anomaly highs (Fig. 2). Some of these anomalies are matched by a less well defined alignment of small gravity anomaly highs. The positive magnetic anomalies composing the outer rings partly correspond to the center of the gravity highs, which suggests a mafic igneous source (Lidiak et al., 1985). Northeastward along the proposed Centralia boundary and the Nd line, the magnetic highs become sparser and more isolated, such as the high at Decatur. Why these highs are isolated in an extensional setting is unclear, but they appear to be discreet and focused intrusive bodies.

Although the seismic reflection data do not show distinct, discernable layering within the Precambrian at IBDP–ICCS, as has been observed further south for the Centralia sequence (McBride et al., 2003), a high magnetic anomaly matched by a less well defined Bouguer anomaly gravity high appears to partially correlate with the bowl-shaped feature identified in Fig. 3 (McBride et al., 2016). This anomaly is likely a result of deeper mafic igneous components in the Precambrian basement. The gabbro identified in the Precambrian basement at the IBDP–ICCS site likely represents sills that intruded lower density, less magnetic crust, likely the source of these anomalies. The

Table 3
U-Pb geochronological data for the basement rhyolite and gabbro at the IBDP-ICCS site.

Analysis, well lithology	Isotope ratio									
	U (ppm)	$^{206}Pb/^{204}Pb$	U/Th	$^{206}Pb/^{207}Pb$	± (%)	$^{207}Pb/^{235}U$	± (%)	$^{206}Pb/^{238}U$	± (%)	Error correction
VER1-Rhyolite-6R	91	21884	2.4	11.2153	3.5	3.1560	5.4	0.2567	4.2	0.77
VER1-Rhyolite-27R	101	8606	2.3	11.0789	4.0	3.2203	4.6	0.2588	2.2	0.48
VER1-Rhyolite-2R	95	27707	2.4	11.0572	3.6	3.2267	4.2	0.2588	2.0	0.49
VER1-Rhyolite-18R-1	59	27229	2.4	11.0064	6.0	3.1828	6.7	0.2541	2.8	0.42
VER1-Rhyolite-21C	119	56083	1.7	10.9895	2.2	3.1884	3.8	0.2541	3.1	0.81
VER1-Rhyolite-13R	103	41406	2.2	10.9830	4.2	3.1702	4.5	0.2525	1.8	0.39
VER1-Rhyolite-18R	118	27964	2.3	10.9791	2.1	3.1473	5.1	0.2506	4.6	0.91
VER1-Rhyolite-12R	99	42953	2.3	10.9517	2.9	3.1653	3.1	0.2514	1.1	0.35
VER1-Rhyolite-9C	170	37262	1.6	10.9516	1.8	3.2516	3.3	0.2583	2.8	0.84
VER1-Rhyolite-11R	130	96437	1.9	10.9490	3.4	3.2184	3.6	0.2556	1.3	0.36
VER1-Rhyolite-9R	66	12974	2.8	10.9482	5.1	3.2034	5.6	0.2544	2.3	0.41
VER1-Rhyolite-15R	110	23140	2.1	10.9406	3.0	3.1140	3.5	0.2471	1.9	0.54
VER1-Rhyolite-17R	77	42168	1.5	10.9367	4.0	3.1626	4.9	0.2509	2.7	0.56
VER1-Rhyolite-5R	116	35894	2.1	10.9201	2.4	3.3370	10.0	0.2643	9.7	0.97
VER1-Rhyolite-3R	83	18895	3.0	10.9071	4.4	3.2642	4.6	0.2582	1.5	0.32
VER1-Rhyolite-16R	99	24443	1.9	10.8586	3.8	3.1836	4.5	0.2507	2.5	0.55
VER1-Rhyolite-19R	77	17918	2.3	10.8465	5.1	3.2377	5.3	0.2547	1.3	0.25
VER1-Rhyolite-14R	113	31249	2.5	10.8377	2.0	3.2951	3.1	0.2590	2.4	0.76
VER1-Rhyolite-4R	77	31050	2.6	10.8373	3.8	3.2846	4.7	0.2582	2.7	0.58
VER1-Rhyolite-29R	100	21472	2.2	10.8354	2.5	3.3953	3.4	0.2668	2.3	0.68
VER1-Rhyolite-24R	264	67096	1.9	10.8256	1.3	3.2506	2.4	0.2552	2.0	0.85
VER1-Rhyolite-20R	123	19897	1.9	10.8096	2.7	3.0373	5.2	0.2381	4.4	0.85
VER1-Rhyolite-21R	211	47482	2.3	10.8082	1.5	3.2341	2.4	0.2535	1.9	0.78
VER1-Rhyolite-25R	137	59270	2.2	10.7890	2.9	3.1276	3.2	0.2447	1.3	0.40
VER1-Rhyolite-26R	89	31051	2.3	10.6801	4.3	3.3411	4.6	0.2588	1.5	0.33
VER1-Rhyolite-28R	79	25502	2.3	10.6363	3.1	3.3744	3.6	0.2603	1.8	0.51
VER1-Rhyolite-22R	77	12986	2.6	10.6239	4.2	3.2661	5.4	0.2517	3.5	0.64
VER1-Rhyolite-14C	95	17689	2.2	10.6193	2.4	3.3985	5.3	0.2618	4.7	0.89
VER2-Gabbro-10	293	468879	3.0	13.5277	1.2	1.6945	2.6	0.1663	2.4	0.90
VER2-Gabbro-5	604	1374780	1.7	13.2995	0.7	1.7765	2.2	0.1714	2.1	0.95
VER2-Gabbro-1	210	262180	1.0	13.2917	0.9	1.8561	2.8	0.1790	2.7	0.95
VER2-Gabbro-6	460	92581	1.1	11.8412	1.3	2.6000	2.5	0.2234	2.1	0.85
VER2-Gabbro-7	691	499764	2.6	9.4783	1.2	4.4440	2.6	0.3056	2.4	0.90
VER2-Gabbro-4	214	319351	2.7	4.9188	0.8	15.1450	2.4	0.5405	2.2	0.94
VER2-Gabbro-3	157	51938	3.0	4.8962	1.1	14.6791	3.0	0.5215	2.8	0.93

	Apparent ages (Ma)								
	$^{206}Pb/^{238}U$	± (Ma)	$^{207}Pb/^{235}U$	± (Ma)	$^{206}Pb/^{207}Pb$	± (Ma)	Best age (Ma)	± (Ma)	Concordance (%)
VER1-Rhyolite-6R	1473.0	55.3	1446.5	41.9	1407.7	66.1	1407.7	66.1	104.6
VER1-Rhyolite-27R	1483.5	29.4	1462.1	35.7	1431.1	77.2	1431.1	77.2	103.7
VER1-Rhyolite-2R	1483.5	27.1	1463.6	32.2	1434.8	69.0	1434.8	69.0	103.4
VER1-Rhyolite-18R-1	1459.4	36.3	1453.0	51.5	1443.6	115.3	1443.6	115.3	101.1
VER1-Rhyolite-21C	1459.7	40.2	1454.3	29.4	1446.5	42.6	1446.5	42.6	100.9
VER1-Rhyolite-13R	1451.5	22.9	1449.9	35.1	1447.6	79.8	1447.6	79.8	100.3
VER1-Rhyolite-18R	1441.7	59.5	1444.4	38.9	1448.3	39.7	1448.3	39.7	99.5
VER1-Rhyolite-12R	1445.8	13.8	1448.7	23.9	1453.1	55.2	1453.1	55.2	99.5
VER1-Rhyolite-9C	1481.0	36.4	1469.6	25.5	1453.1	33.9	1453.1	33.9	101.9
VER1-Rhyolite-11R	1467.1	17.2	1461.6	27.9	1453.5	63.9	1453.5	63.9	100.9
VER1-Rhyolite-9R	1460.9	30.1	1458.0	43.1	1453.7	96.4	1453.7	96.4	100.5
VER1-Rhyolite-15R	1423.5	24.4	1436.2	27.0	1455.0	56.2	1455.0	56.2	97.8
VER1-Rhyolite-17R	1442.9	34.8	1448.1	37.4	1455.7	76.8	1455.7	76.8	99.1
VER1-Rhyolite-5R	1511.8	130.8	1489.8	78.3	1458.5	45.8	1458.5	45.8	103.6
VER1-Rhyolite-3R	1480.7	19.6	1472.6	35.9	1460.8	83.2	1460.8	83.2	101.4
VER1-Rhyolite-16R	1442.2	31.7	1453.2	34.7	1469.3	71.5	1469.3	71.5	98.2
VER1-Rhyolite-19R	1462.7	17.1	1466.2	41.1	1471.4	97.3	1471.4	97.3	99.4
VER1-Rhyolite-14R	1484.7	31.3	1479.9	24.1	1472.9	37.8	1472.9	37.8	100.8
VER1-Rhyolite-4R	1480.5	36.3	1477.4	36.7	1473.0	72.7	1473.0	72.7	100.5
VER1-Rhyolite-29R	1524.7	31.2	1503.3	26.5	1473.3	46.9	1473.3	46.9	103.5
VER1-Rhyolite-24R	1465.3	26.6	1469.3	18.6	1475.1	24.2	1475.1	24.2	99.3
VER1-Rhyolite-20R	1376.9	54.5	1417.0	39.6	1477.9	52.0	1477.9	52.0	93.2
VER1-Rhyolite-21R	1456.6	24.5	1465.4	18.8	1478.1	29.0	1478.1	29.0	98.5
VER1-Rhyolite-25R	1411.2	16.1	1439.5	24.4	1481.5	55.1	1481.5	55.1	95.3
VER1-Rhyolite-26R	1483.7	20.1	1490.7	35.6	1500.7	81.3	1500.7	81.3	98.9
VER1-Rhyolite-28R	1491.4	24.2	1498.5	28.0	1508.4	58.2	1508.4	58.2	98.9
VER1-Rhyolite-22R	1447.0	45.5	1473.0	42.3	1510.7	78.6	1510.7	78.6	95.8
VER1-Rhyolite-14C	1498.8	62.8	1504.1	41.4	1511.5	44.9	1511.5	44.9	99.2
VER2-Gabbro-10	991.8	21.8	1006.4	16.9	1039.3	23.3	1039.3	23.3	95.4
VER2-Gabbro-5	1020.0	19.8	1036.9	14.4	1073.6	14.0	1073.6	14.0	95.0
VER2-Gabbro-1	1061.6	26.2	1065.6	18.6	1074.8	17.5	1074.8	17.5	98.8
VER2-Gabbro-6	1299.7	24.8	1300.6	18.1	1302.9	25.0	1302.9	25.0	99.8
VER2-Gabbro-7	1719.2	35.7	1720.6	21.9	1723.1	21.6	1723.1	21.6	99.8
VER2-Gabbro-4	2785.7	50.1	2824.4	22.6	2852.9	13.6	2852.9	13.6	97.6
VER2-Gabbro-3	2705.5	62.0	2794.7	28.7	2860.4	18.2	2860.4	18.2	94.6

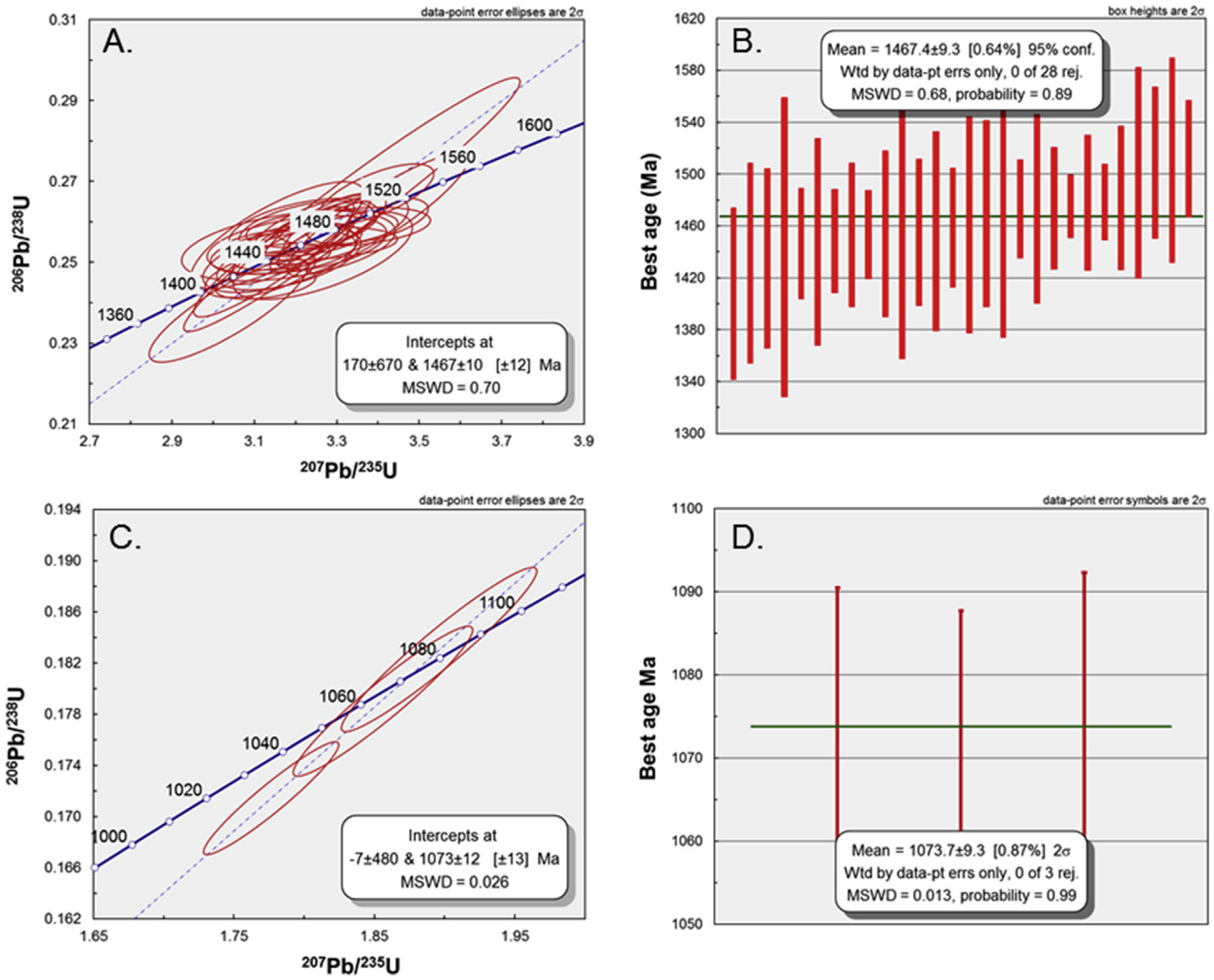

Fig. 13. Concordia (A) and weighted mean age (B) determinations for the Decatur rhyolite. Concordia (C) and weighted mean age (D) determinations for the Decatur gabbro.

anomalously high magnetite content of the gabbro (approximately 30% in the age-dated sample) may contribute the magnetic anomaly if similar rocks constitute a much larger iron-rich plutonic complex. A geochemical comparison could be made between the magnetite-rich gabbro at IBDP and geologically similar iron deposits in the EGRP, such as the pilot knob magnetite deposit in the St. Francois Mountains in Missouri (Nold et al., 2013), although these deposits are dated similarly to their EGRP host rocks.

The 3D seismic volume shows limited and localized multicyclic reflections near the wells for the uppermost part of Precambrian basement (Figs. 6 and 7). Although the resolving power of the seismic data cannot match that of the well logs or core observations, the reflection layering near the basement surface may be a long-wavelength expression of the finer scale igneous layering. McBride et al. (2016) concluded that the deep Precambrian reflectivity in the IBDP–ICCS study area represents mafic igneous sills that intruded into the granitic-rhyolite host rock. Although this reflectivity is much deeper than the depths logged in the four wells at IBDP–ICCS, mafic igneous rocks, such as the olivine gabbro encountered in the IBDP–ICCS site, are consistent with such an interpretation. Mafic igneous rocks observed in the wells may be derived from, or share a common source with, the deep sills interpreted from the reflection data.

6. Conclusions

A comprehensive suite of dedicated petrographic analyses, geophysical logs, drill core from four basement-penetrating wells, 2D and 3D seismic reflection data, and isotopic age data from the IBDP–ICCS site offer an unprecedented view of the Precambrian basement buried deep beneath the Illinois Basin. Our study shows that the Precambrian basement of central Illinois is compositionally and structurally complex. These results offer a glimpse into the origin of the EGRP and the influence of a broad Precambrian extensional setting in the crust.

At 1467 Ma, the age of the EGRP rhyolite at the IBDP–ICCS site is remarkably consistent with that of other Mesoproterozoic EGRP rocks dated in Illinois and southeastern Missouri. These widespread and consistent ages for the EGRP rocks imply that they are related to anorogenic volcanism and plutonic events and are unlikely directly related to the closed-contour positive magnetic anomaly and the bowl-shaped structure observed on seismic data. Instead, the anomaly is

likely related to highly magnetic intrusive rocks, such as the gabbro dated at 1073 Ma, which corresponds to the Grenville orogeny or late-stage volcanism along the MCR. This result suggests that the effects of major far-field extensional events can be observed in central Illinois. This paper documents the first late Mesoproterozoic rocks in Illinois, providing new constraints on the Precambrian evolution in the stable continental interior.

Acknowledgments

We gratefully acknowledge the assistance of R.W. Keach II with visualization and interpretation of the 3D seismic volume. We thank ISGS staff for critical reviews, edits, and graphical assistance. We also appreciate the thorough reviews of four anonymous reviewers. This research was supported by the Midwest Geological Sequestration Consortium (MGSC), which is funded by the U.S. Department of Energy through the National Energy Technology Laboratory (NETL) via the Regional Carbon Sequestration Partnership Program (contract number DE-FC26-05NT42588) and by a cost share agreement with the Illinois Department of Commerce and Economic Opportunity, Office of Coal Development through the Illinois Clean Coal Institute. Data processing and visualization were made possible by a software grant from the Landmark (Halliburton) University Grant Program to Brigham Young University and by a grant from the Schlumberger Worldwide University Software Program to the University of Illinois at Urbana-Champaign.

Appendix A. Supplementary data

Supplementary data to this article can be found online at https://doi.org/10.1016/j.gsf.2019.07.004.

References

Barnes, M.A., Rohs, C.R., Anthony, E.Y., Van Schmus, W.R., Denison, R.E., 1999. Isotopic and elemental chemistry of subsurface Precambrian igneous rocks, west Texas and eastern New Mexico. Rocky Mt. Geol. 34, 245–262.

Bauer, R.A., Carney, M., Finley, R.J., 2016. Overview of microseismic response to CO_2 injection into the Mt. Simon saline reservoir at the Illinois Basin – Decatur Project. Int. J. Greenh. Gas Contr. 54, 378–388.

Bickford, M.E., Van, W.R., Zietz, I., 1986. Proterozoic history of the midcontinent region of North America. Geology 14, 492–496.

Bickford, M.E., Van Schmus, W.R., Karlstrom, K.E., Mueller, P.A., Kamenov, G.D., 2015. Mesoproterozoic–trans-Laurentian magmatism: a synthesis of continent-wide age distributions, new SIMS U-Pb ages, zircon saturation temperatures, and Hf and Nd isotopic compositions. Precambrian Res. 265, 286–312.

Bowring, S.A., Karlstrom, K.E., 1990. Growth, stabilization, and reactivation of Proterozoic lithosphere in the southwestern United States. Geology 18, 1203–1206.

Bowring, S.A., Housh, T.B., Van Schmus, W.R., Podosek, F.A., 1992. A major Nd isotopic boundary along the southern margin of Laurentia. Eos 73, 333.

Couëslan, M.L., Ali, S., Campbell, A., Nutt, W.L., Leaney, W.S., Finley, R.J., Greenberg, S.E., 2013. Monitoring CO_2 injection for carbon capture and storage using time-lapse 3D VSPs. Lead. Edge 32, 1268–1276.

Craddock, J.P., Konstantinou, A., Vervoort, J.D., Wirth, K.R., Davidson, C., Finley-Blasi, L., Juda, N.A., Walker, E., 2013. Detrital zircon provenance of the Proterozoic midcontinent rift, USA. J. Geol. 121, 57–73.

Craddock, J.P., Craddock, S.D., Konstantinou, A., Kylander-Clark, A.R., Malone, D.H., 2017a. Calcite twinning strain variations across the Proterozoic Grenville orogen and Keweenaw-Kapuskasing inverted foreland, USA and Canada. Geosci. Front. 8, 1357–1384.

Craddock, J.P., Malone, D.H., Porter, R., Compton, J., Luczaj, J., Konstantinou, A., Day, J.E., Johnston, S.T., 2017b. Paleozoic reactivation structures in the Appalachian-Ouachita-Marathon foreland: far-field deformation across Pangea. Earth Sci. Rev. 169, 1–34.

Dalziel, I.W., 1991. Pacific margins of Laurentia and East Antarctica–Australia as a conjugate rift pair: evidence and implications for an Eocambrian supercontinent. Geology 19, 598–601.

Daniels, D.L., Kucks, R.P., Hill, P.L., 2008. Illinois, Indiana, and Ohio Magnetic and Gravity Maps and Data—A Website for Distribution of Data. U.S. Geological Survey, Reston, Virginia. Data Series 321.

Davis, D., Sutcliffe, R.H., 1985. U-Pb ages from the Nipigon plate and northern Lake Superior. Geol. Soc. Am. 96 (12) (1985): 1572-179.

Davis, D., Paces, J., 1990. Time resolution of geologic events on the Keweenaw Peninsula and applications for development of the Midcontinent Rift system. Earth Planet. Sci. Lett. 97, 54–64. https://doi.org/10.1016/0012-821X(90)90098-I.

Denison, R.E., Bickford, M.E., Lidiak, E.G., Kisvarsanyi, E.B., 1987. Geology and Geochronology of Precambrian Rocks in the Central Interior Region of the United States. U.S. Geological Survey, Reston, Virginia. Professional Paper 1241-C.

Dewane, T.J., Van Schmus, W.R., 2007. U–Pb geochronology of the Wolf River batholith, north-central Wisconsin: evidence for successive magmatism between 1484 Ma and 1468 Ma. Precambrian Res. 157, 215–234.

Dickin, A.P., Higgins, M.D., 1992. Sm/Nd evidence for a major 1.5 Ga crust-forming event in the central Grenville province. Geology 20, 137–140.

Drahovzal, J.A., Harris, D.C., Wickstrom, L.H., Walker, D., Baranoski, M.T., Keith, B., Furer, I.C., 1992. The East Continent Rift Basin—A New Discovery, vol. 18. Kentucky Geological Survey, Lexington, pp. 1–25. Special Publication.

Freiburg, J.T., Morse, D.G., Leetaru, H.E., Hoss, R.P., Yan, Q., 2014. A Depositional and Diagenetic Characterization of the Mt. Simon Sandstone at the Illinois Basin – Decatur Project Carbon Capture and Storage Site, Decatur, Illinois, USA. Circular 583. Illinois State Geological Survey, Champaign.

Gehrels, G., Pecha, M., 2014. Detrital zircon U-Pb geochronology and Hf isotope geochemistry of Paleozoic and Triassic passive margin strata of western North America. Geosphere 1, 49–65.

Gehrels, G.E., Valencia, V., Pullen, A., 2006. Detrital zircon geochronology by laser-ablation multicollector ICPMS at the Arizona LaserChron Center. In: Loszewski, T., Huff, W. (Eds.), Geochronology: Emerging Opportunities, Paleontology Society Short Course: Paleontology Society Paper, vol. 11, pp. 1–10.

Gehrels, G.E., Valencia, V., Ruiz, J., 2008. Enhanced precision, accuracy, efficiency, and spatial resolution of U-Pb ages by laser ablation–multicollector–inductively coupled plasma–mass spectrometry. Geochem. Geophys. Geosyst. 9, Q03017. https://doi.org/10.1029/2007GC001805.

Gower, C.F., Tucker, R.D., 1994. Distribution of pre-1400 Ma crust in the Grenville province: implications for rifting in Laurentia-Baltica during geon 14. Geology 22, 827–830.

Harrison, R.W., Lowell, G.R., Unruh, D.M., 2000. Geology, geochemistry, and age of Mesoproterozoic igneous rocks in the Eminence–Van Buren area: a major structural outlier of the St. Francois terrane, south-central Missouri. Geol. Soc. Am. Abstr. Progr. 32 (3), A–14.

Hervet, M., van Breemen, O., Higgins, M.D., 1994. U-Pb igneous crystallization ages of intrusive rocks near the southeastern margin of the lac-St-jean anorthosite complex, Grenville province, quebec. In: Radiogenic Age and Isotopic Studies, Report 8. Geological Survey of Canada, Ottawa, pp. 115–124.

Hill, B.M., Bickford, M.E., 2001. Paleoproterozoic rocks of central Colorado: accreted arcs or extended older crust? Geology 29, 1015–1018.

Hinze, W.J., Allen, D.J., Braile, L.W., 1997. The Midcontinent rift system: a major Proterozoic continental rift. Geol. Soc. Am. Spec. Pap. 312, 7–35.

Hoffman, P.F., 1989. Precambrian geology and tectonic history of North America. In: Bally, A.W., Palmer, A.R. (Eds.), The Geology of North America—An Overview. Decade of North American Geology, Volume A. Geological Society of America, Boulder, Colorado, pp. 447–512.

Hoppe, W.J., Montgomery, C.W., Van Schmus, W.R., 1983. Age and significance of Precambrian basement samples from northern Illinois and adjacent states. J. Geophys. Res.: Solid Earth 88, 7276–7286.

Karlstrom, K.E., Bowring, S.A., 1988. Early Proterozoic assembly of tectonostratigraphic terranes in southwestern North America. J. Geol. 96, 561–576.

Karlstrom, K.E., Humphreys, E.D., 1998. Persistent influence of Proterozoic accretionary boundaries in the tectonic evolution of southwestern North America. Rocky Mt. Geol. 33, 161–179.

Keller, G.R., Lidiak, E.G., Hinze, W.J., Braile, L.W., 1983. The role of rifting in the tectonic development of the midcontinent, USA. Tectonophysics 94, 391–412.

Kolata, D.R., Nelson, W.J., 2010. Tectonic history. In: Kolata, D.R., Nimz, C.K. (Eds.), Geology of Illinois. Illinois State Geological Survey, Champaign, pp. 77–89.

Lidiak, E.G., Marvin, R.F., Thomas, H.H., Bass, M.N., 1966. Geochronology of the mid-continent region of the United States: 4. Eastern area. J. Geophys. Res. 71, 5427–5438.

Lidiak, E.G., Hinze, W.J., Keller, G.R., Reed, J.E., Braile, L.W., Johnson, R.W., 1985. Geologic significance of regional gravity and magnetic anomalies in the east-central midcontinent. In: Hinze, W.J. (Ed.), The Utility of Regional Gravity and Magnetic Anomaly Maps. Society of Exploration Geophysicists, Tulsa, Oklahoma, pp. 287–307.

Ludwig, K.R., 2008. Isoplot 3.60. Special Publication 4. Berkeley Geochronology Center, Berkeley, California, p. 77.

Lowell, G.R., Harrison, R.W., Weary, D.J., Orndorff, R.C., Repetski, J.E., Pierce, H.A., 2010. Rift-related volcanism and karst geohydrology of the southern Ozark Dome. In: Field Guide, vol. 17. Geological Society of America, Boulder, Colorado, pp. 99–158.

Malone, D.H., Stein, C.A., Craddock, J.P., Kley, J., Stein, S., Malone, J.E., 2016. Maximum depositional age of the Neoproterozoic Jacobsville Sandstone, Michigan: implications for the evolution of the Midcontinent Rift. Geosphere 12, 1271–1282.

Marfurt, K.J., Kirlin, R.L., Farmer, S.L., Bahorich, M.S., 1998. 3-D seismic attributes using a semblance-based coherency algorithm. Geophysics 63, 1150–1165.

Marshak, S., Paulsen, T., 1996. Midcontinent US fault and fold zones: a legacy of Proterozoic intracratonic extensional tectonism? Geology 24 (2), 151–154.

McBride, J.H., Kolata, D.R., 1999. Upper crust beneath the central Illinois basin, United States. Geol. Soc. Am. Bull. 111, 375–394.

McBride, J.H., Kolata, D.R., Hildenbrand, T.G., 2003. Geophysical constraints on understanding the origin of the Illinois basin and its underlying crust. Tectonophysics 363, 45–78.

McBride, J.H., Leetaru, H.E., Keach, R.W., McBride, E.I., 2016. Fine-scale structure of the Precambrian beneath the Illinois basin. Geosphere 12, 585–606.

McLelland, J.M., Chiarenzelli, J.R., Gower, C., Rivers, T., Ryan, A.B., 1990. Geochronological studies in the Adirondack Mountains and the implications of a middle proterozoic tonalitic suite. In: Mid-Proterozoic Laurentia-Baltica. Special

Paper 38. Geological Association of Canada, St. John's, Newfoundland, Canada, pp. 175–194.
Moores, E.M., 1991. Southwest US-East Antarctic (SWEAT) connection: a hypothesis. Geology 19, 425–428.
Mosher, S., 1998. Tectonic evolution of the southern Laurentian Grenville orogenic belt. Geol. Soc. Am. Bull. 110, 1357–1375.
Nold, J.L., Davidson, P., Dudley, M.A., 2013. The pilot knob magnetite deposit in the Proterozoic St. Francois Mountains Terrane, southeast Missouri, USA: a magmatic and hydrothermal replacement iron deposit. Ore Geol. Rev. 53, 446–469.
Okure, M.S., McBride, J.H., 2006. Deep seismic reflectivity beneath an intracratonic basin: insights into the behavior of the uppermost mantle beneath the Illinois Basin. Precambrian Res. 149, 99–125.
Paces, J.B., Miller, J.D., 1993. Precise U-Pb ages of Duluth complex and related mafic intrusions, northeastern Minnesota: geochronological insights to physical, petrogenetic, paleomagnetic, and tectonomagmatic processes associated with the 1.1 Ga midcontinent rift system. J. Geophys. Res.: Solid Earth 98, 13997–14013.
Patchett, P.J., 1989. Radiogenic isotope geochemistry of rare earth elements. Rev. Mineral. Geochem. 21, 25–44.
Patchett, P.J., Ruiz, J., 1989. Nd isotopes and the origin of Grenville-age rocks in Texas: implications for Proterozoic evolution of the United States mid-continent region. J. Geol. 97, 685–695.
Pratt, T., Culotta, R., Hauser, E., Nelson, D., Brown, L., Kaufman, S., Hinze, W., 1989. Major Proterozoic basement features of the eastern midcontinent of North America revealed by recent COCORP profiling. Geology 17, 505–509.
Pratt, T.L., Hauser, E.C., Nelson, K.D., 1992. Widespread buried Precambrian layered sequences in the US Mid-Continent: evidence for large Proterozoic depositional basins. AAPG Am. Assoc. Pet. Geol. Bull. 76, 1384–1401.
Rivers, T., 1997. Lithotectonic elements of the Grenville province: review and tectonic implications. Precambrian Res. 86, 117–154.
Ruppel, C., 1996. Extensional processes in continental lithosphere. J. Geophys. Res. 100, 24187–24215.
Stein, C.A., Stein, S., Merino, M., Keller, G.R., Flesch, L.M., Jurdy, D.M., 2014. Was the Midcontinent Rift part of a successful seafloor-spreading episode? Geophys. Res. Lett. 41, 1465–1470.
Stein, C.A., Kley, J., Stein, S., Hindle, D., Keller, G.R., 2015. North America's Midcontinent Rift: when rift met LIP. Geosphere 11, 1607–1616. https://doi.org/10.1130/GES01183.1.
Swanson-Hysell, N.L., Burgess, S.D., Maloof, A.C., Bowring, S.A., 2014. Magmatic activity and plate motion during the latent stage of Midcontinent Rift development. Geology 42, 475–478. https://doi.org/10.1130/G35271.1.
Swanson-Hysell, N.L., Ramezani, J., Fairchild, L.M., Rose, I.R., 2019. Failed rifting and fast drifting: midcontinent Rift development, Laurentia's rapid motion and the driver of Grenvillian orogenesis. Geol. Soc. Am. Bull. 131, 913–940. https://doi.org/10.1130/B31944.1.
Van Schmus, W.R., Hinze, W.J., 1985. The midcontinent rift system. Annu. Rev. Earth Planet Sci. 13, 345–383.
Van Schmus, W.R., Medaris Jr., L.G., Banks, P.O., 1975. Geology and age of the wolf river batholith, Wisconsin. Geol. Soc. Am. Bull. 86, 907–914.
Van Schmus, W.R., Bickford, M.E., Turek, A., 1996. Proterozoic geology of the east-central midcontinent basement. In: Geological Society of America Special Paper, vol. 308, pp. 7–32.
Whitmeyer, S.J., Karlstrom, K.E., 2007. Tectonic model for the proterozoic growth of north America. Geosphere 3, 220–259.
Yang, X., Pavlis, G.L., Hamburger, M.W., Marshak, S., Gilbert, H., Rupp, J., Larson, T.H., Chen, C., Carpenter, N.S., 2017. Detailed crustal thickness variations beneath the Illinois Basin area: implications for crustal evolution of the midcontinent. J. Geophys. Res.: Solid Earth 122, 6323–6345.

Chapter iii Manuscript

Detrital zircon geochronology of basal Cambrian strata in the deep Illinois Basin, USA: Evidence for the Paleoproterozoic-Cambrian tectonic and sedimentary evolution of central Laurentia

Detrital Zircon Geochronology of Basal Cambrian Strata in the Deep Illinois Basin, USA: Evidence for the Paleoproterozoic-Cambrian Tectonic and Sedimentary Evolution of Central Laurentia

Jared T. Freiburg,[1,*] *Mark E. Holland,*[2] *David H. Malone,*[3] *and Shawn J. Malone*[4]

1. Illinois State Geological Survey, Prairie Research Institute, University of Illinois at Urbana-Champaign, 615 East Peabody Drive, Champaign, Illinois 61820, USA; and Institute of Geography and Geology, University of Greifswald, Friedrich-Ludwig-Jahn-Straße 17a, D-17489 Greifswald, Germany; 2. Department of Life, Earth and Environmental Science, West Texas A&M University, 2403 Russell Long Boulevard, Canyon, Texas 79015, USA; 3. Department of Geography, Geology, and the Environment, Campus Box 4400, Illinois State University, Normal, Illinois 61790-4400, USA; 4. Department of Environment, Geology, and Natural Resources, Fine Arts Building, Ball State University, Muncie, Indiana 47306, USA

ABSTRACT

We present 960 detrital zircon ages from three new, deep boreholes from the Illinois Basin, USA. These zircon age spectra reveal new details of the late Paleoproterozoic through early Cambrian tectonic history of the Illinois Basin, including evidence of the timing of the development of the Reelfoot Rift and breakup of Rodinia. The oldest detrital zircon population is ~1650 Ma, older than any known age for crystalline rocks from other deep drill cores in the basin and conspicuously absent in other Cambrian strata in the region. We interpret this population to have been derived from late Paleoproterozoic crust that exists beneath the Illinois Basin and was exposed during the deposition of Cambrian strata. The principal age peak is ~1375 Ma, characteristic of igneous rocks of the Southern Granite-Rhyolite Province but also present in the St. Francois Mountains of the Eastern Granite-Rhyolite Province (EGRP). A secondary peak of ~1460 Ma detrital zircon reflects the known ages of crystalline rocks that characterize EGRP determined from along the periphery of the Illinois Basin. This population of detrital zircon in Cambrian strata may reflect a greater abundance of ~1370 Ma crust beneath the Illinois Basin than presently recognized. These data reveal that basal Cambrian sandstones in the Illinois Basin have a detrital zircon provenance that is distinct from the overlying late Cambrian arenites and that a previously unknown northern arm of the Reelfoot Rift extends into central Illinois, which is more than 300 km further north than currently mapped. The opening of the Reelfoot Rift, which was part of the broader rifting of Rodinia during the Neoproterozoic and early Cambrian, is marked by zircons, probably from Reelfoot Rift igneous rocks, that range from 540 to 525 Ma.

Online enhancements: color figures, supplemental material.

Introduction

The Precambrian basement of the Illinois Basin has recently gained the attention of both researchers and industry as a result of investigations into geologic storage of CO_2 through CarbonSAFE, the Illinois Basin-Decatur Project, and the Illinois Carbon Capture and Storage Project (Freiburg et al. 2014). These projects were designed to evaluate and conduct CO_2 injection to store industrially sourced CO_2 in basal Cambrian strata.

In this article, we present 960 new detrital zircon ages from five lower Mt. Simon and Argenta sandstone samples extracted from three cores that were obtained as part of the greater CarbonSAFE efforts. These new data are compared with detrital zircon age spectra from younger Cambrian sandstones present to the north on the far flank of the Illinois Basin to provide an understanding of the evolution of sedimentary provenance during the Sauk transgression and the early development of the Illinois Basin. Our

Manuscript received October 17, 2019; accepted January 26, 2020; electronically published April 15, 2020.

* Author for correspondence; email: freiburg@illinois.edu.

[The Journal of Geology, 2020, volume 128, p. 303–317] 0022-1376/2020/12803-0003$15.00. DOI: 10.1086/708432

results show that the Mt. Simon and Argenta sandstones were derived from late Paleoproterozoic to early Cambrian crust. We interpret the 530, 1370, 1460, and 1650 Ma detrital zircon populations to be locally derived from Paleo- to Mesoproterozoic basement beneath the Illinois Basin and Cambrian igneous rocks associated with the development of a northern arm of the Reelfoot Rift.

Background

The Illinois Basin is an intracratonic basin that extends across most of Illinois and into parts of Kentucky and Indiana and contains more than 5 km of Paleozoic strata (Buschbach and Kolata 1990; Kolata and Nelson 1990; Kissock et al. 2018). Basement rocks of the Illinois Basin consist of a voluminous Mesoproterozoic magmatic province referred to as the Eastern Granite-Rhyolite Province (EGRP; Thomas et al. 1984; Bickford et al. 1986; Van Schmus et al. 1993). The EGRP is bisected by a southwest–northeast-trending isotopic discontinuity dubbed the "Nd line" (fig. 1; Van Schmus et al. 1996). The Nd line separates Mesoproterozoic igneous rocks with Nd model ages >1.55 Ga to the northwest from those with <1.55 Ga model ages to the southeast and is generally interpreted to be a continental-scale Proterozoic terrane boundary. Mesoproterozoic rocks to the southeast are thought to represent 1.55–1.4 Ga juvenile crust that accreted to Laurentia as part of a long-lived arc system, whereas rocks to the northwest were derived from melting of Paleoproterozoic crust during granite-rhyolite magmatism (Van Schmus et al. 1996; Whitmeyer and Karlstrom 2007; Bickford et al. 2015). Thus far, isotopic ages for Illinois basement granite and rhyolite are known from only five deep boreholes, four of which were drilled along the northern and western margins of the Illinois Basin (Bickford et al. 2015 and references therein). The fifth is from Verification Well 1 (Freiburg et al. 2019), from which we analyzed the overlying Cambrian sandstone as part of this study. All five published cores samples reveal rocks that are 1450–1500 Ma in age.

The Cambrian Mt. Simon sandstone unconformably overlies Precambrian basement rocks (fig. 2). Through seismic studies and deep drilling, Leetaru and Freiburg (2014) discovered an early Paleozoic depocenter located several hundred kilometers north of the late Paleozoic Illinois Basin depocenter (Freiburg et al. 2016). The axis of this early Paleozoic depocenter roughly corresponds to the north–south geometry of the La Salle anticlinal belt (Craddock et al. 2017 and references therein). Drilling also revealed a previously unknown sandstone unit referred to as the pre-Mt. Simon (Freiburg et al. 2014) and more recently as the Argenta sandstone (Freiburg et al. 2016). The lower Mt. Simon and Argenta sandstones overlie a layered Precambrian sedimentary or volcanic succession thus far known only on seismic reflection data and referred to as the Centralia Sequence (McBride et al. 2003).

The Cambrian Mt. Simon sandstone in central Illinois is divided into three informal lithostratigraphic units referred to as the upper, middle, and lower Mt. Simon (fig. 3; Freiburg et al. 2014). The Argenta sandstone is an informal basal Cambrian unit that nonconformably overlies the Precambrian basement and disconformably underlies the lower Mt. Simon sandstone. Together, the Argenta and Mt. Simon sandstones compose a thick (nearly 800-m) succession of sandstone and conglomerate that form the lowermost part of the Sauk sequence in the Illinois Basin (Sloss 1963; Collinson et al. 1988). This interval represents the thickest succession of Cambrian strata in the Laurentian midcontinent. The Argenta and lower Mt. Simon sandstones were deposited in a rift basin (Kolata and Nelson 1990) located in north-central Illinois, several hundred kilometers north of the Illinois Basin depocenter.

Deposition of the Argenta occurred in a rift basin setting where it is known to be as thick as 180 m near the depocenter and thins toward the margin of the basin. The depositional setting along the rift margin includes a transition from a fan-delta into a marine environment. Conglomeratic alluvial-fan facies occur along steeply dipping normal faults. Fluvial-deltaic fining-upward successions of coarse to fine-grained sandstone overlain by red mudstone occur above conglomerates. Fine-grained sandstone and mudstone are bioturbated with abundant *Skolithos*-, *Diplocraterion*-, and *Arencolites*-type burrows. The contact between the Argenta and the lower Mt. Simon sandstones is marked by a heavily bioturbated mudstone surface that includes pebble-sized, subangular, crystalline rock clasts. The Argenta sandstone is texturally immature with abundant pore-filling clays.

In its depocenter in east-central Illinois, the Mt. Simon sandstone is more than 700 m in thickness. The lower Mt. Simon sandstone comprises sandstone and conglomerate deposited in nearshore eolian and fluvial environments. Fine to coarse sandstone and conglomerate are tan to maroon in color and arkosic to subarkosic in composition. Some maroon mudstone and gray siltstone interbedded with fine lenticular-bedded and bioturbated sandstone is also present. These are interpreted as floodplain or lagoon deposits (Freiburg et al. 2014). Compared with the underlying Argenta, the lower Mt. Simon is texturally mature with minor pore-filling clays.

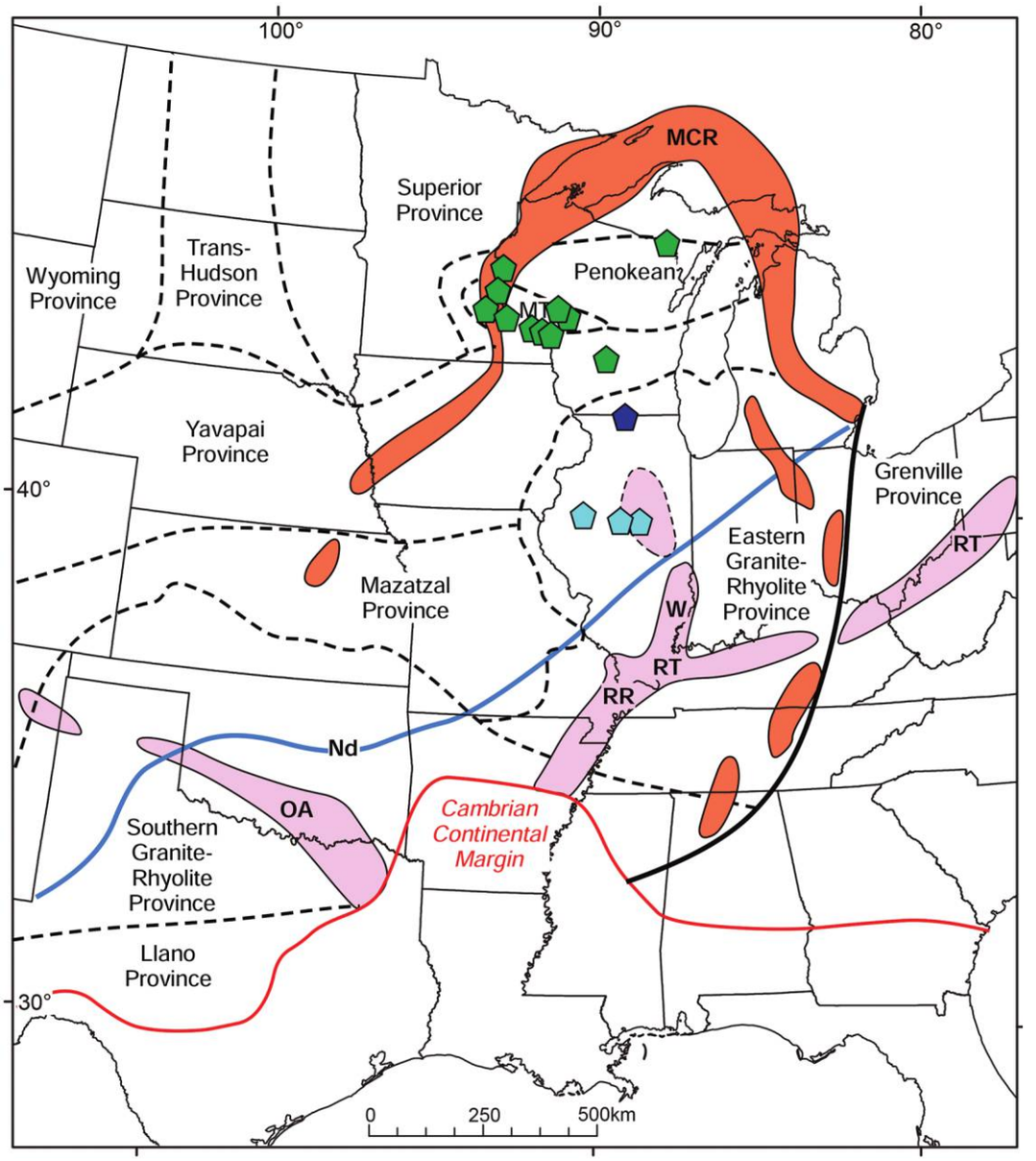

Figure 1. Map of basement terranes of the Laurentian midcontinent (modified from Bickford et al. 2015). The locations of the Oklahoma aulocogen (OA), Reelfoot Rift (RR), Rome Trough (RT), and Wabash (W) and LaSalle deformational belts are indicated in pink. The northern arm of the Reelfoot Rift (fig. 2) is indicated by the pink area enclosed by the dashed line. The 1.1 Ga Midcontinent Rift (MCR) is indicated in orange. Light blue pentagons = Illinois Basin sample locations for this study. Green pentagons = sampling sites for late Cambrian arenites reported in Konstantinou et al. (2014). Dark blue pentagons = Mt. Simon drill core sampling locality reported in Lovell and Bowen (2013). Blue line is the "Nd line" of Bickford et al. (2015), which separates crust yielding Nd model ages greater than 1.55 Ga to the north and less than 1.55 Ga to the south. Modified from Bickford et al. 2015 and Stein et al. 2018.

Detrital zircon provenance studies of Cambrian strata in Laurentia are numerous (e.g., Gaudette et al. 1981; Gehrels et al. 1995; Stewart et al. 2001; Amato et al. 2012; May et al. 2013; Link et al. 2017; Malone et al. 2017*a*; Matthews et al. 2017; Karlstrom et al. 2018). Studies of the late Cambrian arenites of the Laurentian midcontinent, which have well-established ages based on fossils (e.g., Berg 1952; Nelson 1956; Byers and Dott 1995), are dominated by zircons recycled from the Proterozoic Huron, Animike, and Midcontinent Rift Basins (Lovell and Bowen 2013; Konstantinou et al. 2014)

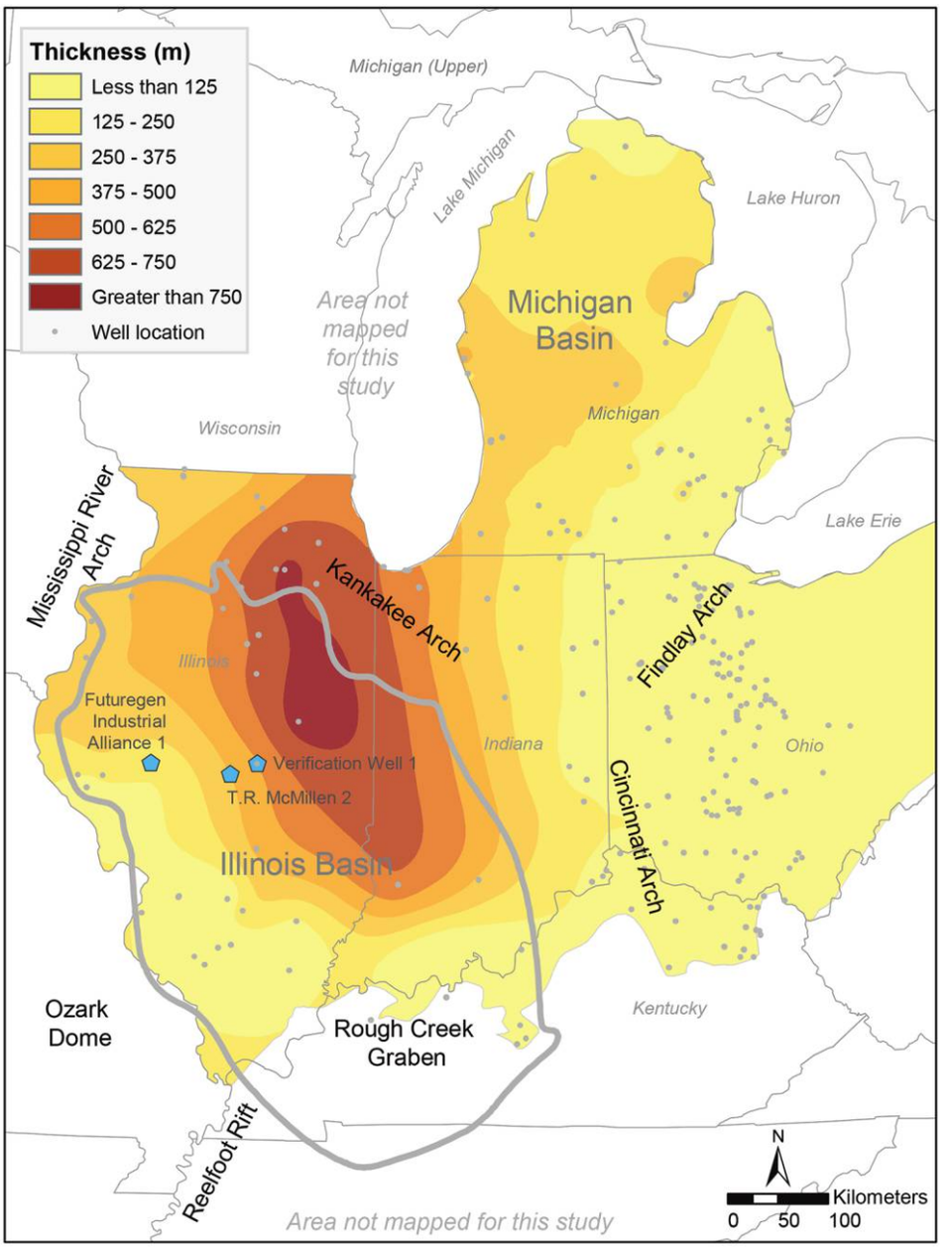

Figure 2. Isopach map of the combined Mt. Simon and Argenta sandstones indicating the depocenter in east-central Illinois. The locations of the well cores analyzed in this study are indicated.

and reflect greater sediment dispersal and sediment recycling as the Sauk Seas transgressed and local basement rocks were buried.

Methods

We sampled the lower Mt. Simon and the underlying Argenta sandstones from core from two deep wells ~30 km apart in central Illinois: the CarbonSAFE T. R. McMillen Well 2 (API 120212565000) located in Christian County and the Illinois Basin-Decatur Project Verification Well 1 (API 121152346000) located in Macon County (fig. 4). We also sampled the lower Mt. Simon from the Futuregen Industrial Alliance Well 1 (API 121372213100) in Morgan County, ~100 km to the west where the Argenta is absent and only a thin lower Mt. Simon sandstone is present. Zircon crystals were extracted from core samples by traditional methods of crushing and grinding, followed by separation by panning, heavy liquids,

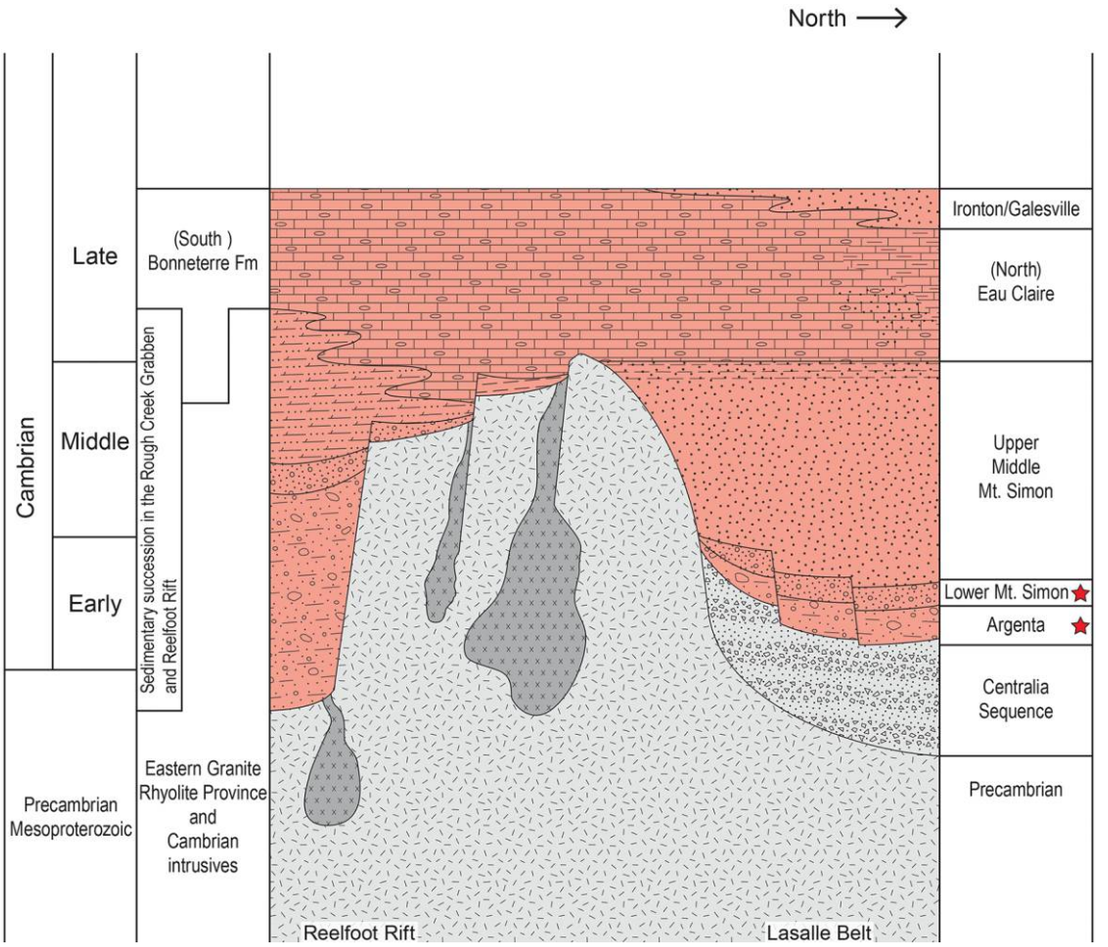

Figure 3. Correlation diagram of Cambrian strata and Proterozoic basement rocks present in the Illinois Basin. Our sampling localities are indicated by the stars.

and a Frantz magnetic separator. About 1 ft of drill core (~5 kg) was processed for each sample.

The mounts were sanded down to a depth of ~20 μm, polished, imaged, and cleaned before isotopic analysis. U-Pb geochronology of zircons was conducted by laser ablation-inductively coupled plasma mass spectrometry at the Arizona LaserChron Center (Gehrels et al. 2006, 2008; Gehrels and Pecha 2014). The analyses involved ablation of zircon with a Photon Machines Analyte G2 excimer laser equipped with HelEx ablation cell using a spot diameter of 20 μm. The ablated material was carried in helium into the plasma source of an Element2 HR inductively coupled plasma mass spectrometer, which sequences rapidly through U, Th, and Pb isotopes.

The ages are shown on relative age-probability diagrams using the routines in Isoplot (Ludwig 2012). The age-probability diagrams show each age and its uncertainty (for measurement error only) as a normal distribution and sum all ages from a sample into a single curve. Composite age probability plots were made from an in-house Excel program that normalizes each curve according to the number of constituent analyses, such that each curve contains the same area, and then stacks the probability curves. The maximum depositional age (MDA) for each sample was calculated by taking the weighted mean age of the youngest subset of grains (at least four) with overlapping age errors. The zircon data tables are provided in the supplementary data (available online).

Results

The probability density plots and the MDAs for each sample are provided in figures 5–9. The Argenta sandstone in Verification Well 1 was sampled from a depth of 2144.8–2145.1 m (7037–7038 ft), which is 6.4 m (21 ft) above the underlying basement (fig. 5). The basement here has a U-Pb age of

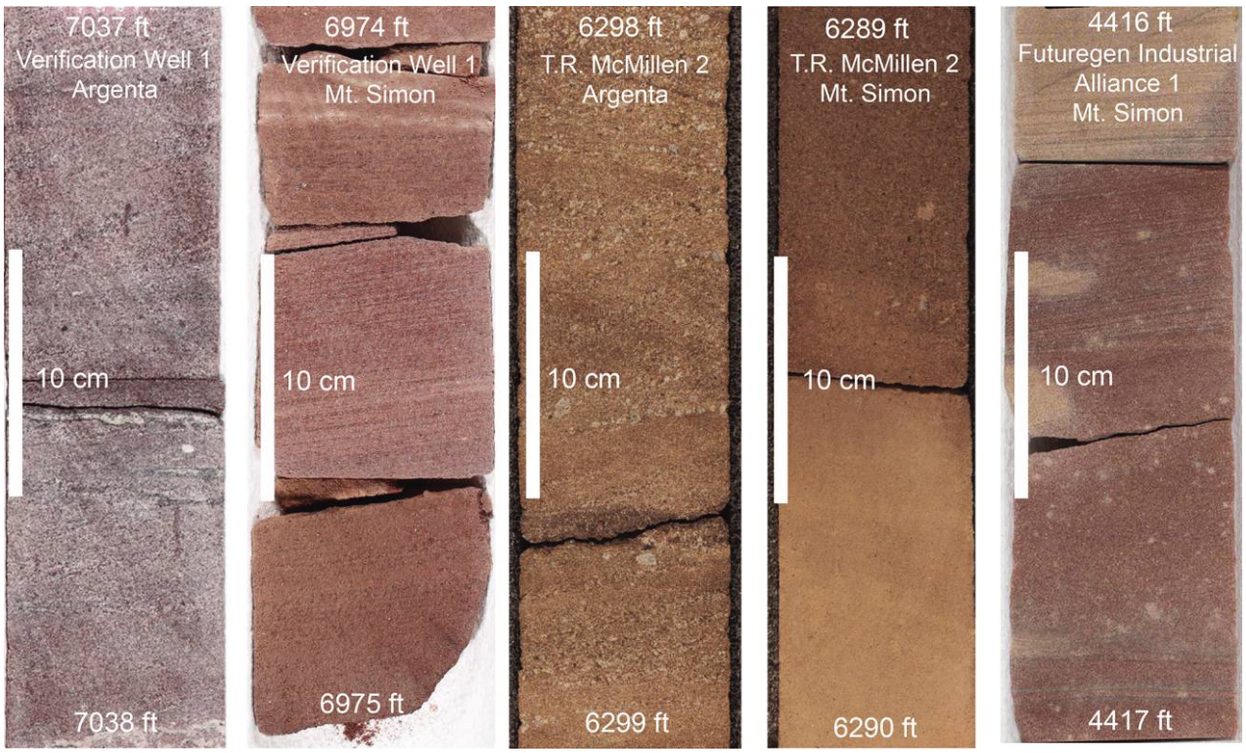

Figure 4. Photographs of core from five samples of the lower Mt. Simon and Argenta sandstones analyzed.

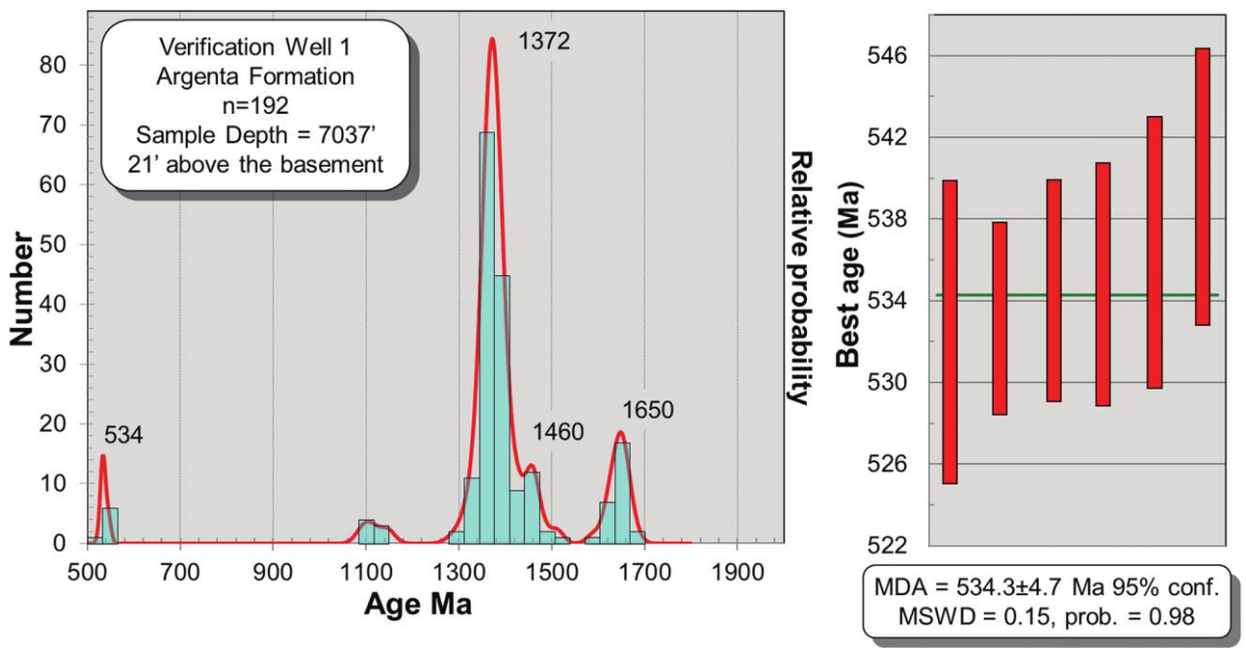

Figure 5. Probability density plot, histogram, and maximum depositional age (MDA [conf. = confidence]) of the Argenta sandstone in Verification Well 1.

1467 ± 10 Ma (Freiburg et al. 2019). A total of 192 detrital zircon ages are presented. The dominant age peak is ~1372 Ma, with lesser peaks at 1650, 534, and 1460 Ma. The MDA is 534 ± 4.7 Ma. The Argenta sandstone from the T. R. McMillen Well 2 was sampled at a depth of 1919.6–1919.9 m (6298–6299 ft), which is 20.1 m (66 ft) above the underlying basement (fig. 6). An isotopic age determination for basement rock here is in progress. The zircon age peaks are 1381, 1662, 541, and 1485 Ma, and the MDA is 541 ± 4.5.

The lower Mt. Simon sandstone in Verification Well 1 was sampled from a depth of 2125.6–2125.9 m (6974–6975 ft), which is 25.2 m (83 ft) above the underlying basement. A total of 180 detrital zircon ages are presented. The dominant age peak is ~1381 Ma, with lesser peaks at 1650, 530, and 1452 Ma. The MDA is 529 ± 5.6 Ma (fig. 7).

The lower Mt. Simon sandstone in T. R. McMillen Well 2 was sampled from a depth of 1916.8–1917.1 m (6289–6290 ft), which is 22.8 m (75 ft) above the underlying basement. A total of 183 detrital zircon ages are presented. The dominant age peak is ~1381 Ma, with lesser peaks at 527, 1653, and 1132 Ma. The MDA is 527 ± 4.1 Ma (fig. 8).

The lower Mt. Simon sandstone for the Futuregen Industrial Alliance Well 1 was sampled from a depth of 1406.6–1406.9 m (4615–4616 ft), which is 4.2 m (14 ft) above the underlying basement. This well was drilled ~100 km west of and more than 600 m (2000 ft) above the Argenta trough penetrated by the other two wells. An isotopic age determination for basement rock here is in progress. A total of 305 detrital zircon ages are presented. The dominant age peak is ~1380 Ma, with lesser peaks at 2600, 1652, 1453, 1652, and 1140 Ma. This sample is the only one of the five samples to have notable concentrations of Archean and Grenville grains. The MDA is 534 ± 4.6 Ma (fig. 9).

Kolmogorov-Smirnov analysis (supplementary data) indicates a statistical relationship between the lower samples in each well, between the upper sample in each well and each lower sample, but not between the two upper samples. When treated as a whole (i.e., all 960 grains; fig. 10), the youngest age group (~5% of the total) ranges in age from 524 to 547 Ma and has a peak age of 533 Ma. For the stratigraphically deeper Argenta sandstone, the respective age peaks are slightly older at 535 and 542 Ma. For the shallower lower Mt. Simon sample in each well, the respective peak ages are younger at 531 and 528 Ma. The largest age peak of 1375 Ma, with a secondary age peak of 1460 Ma, accounts for nearly 80% of the detrital zircon age spectrum. Paleoproterozoic zircons, with a peak age of 1655 Ma, account for ~10% of the zircon age spectrum. Grenville-age grains with a peak of 1130 Ma account for ~5% of the composite age spectrum.

Discussion

Age and Provenance of the Lower Mt. Simon and Argenta Sandstones. Cambrian strata in Wisconsin and Missouri are interpreted to be late Cambrian in age (Ojakangas 1963; Houseknecht and Ethridge 1978). Unfortunately, the cores that we analyzed do not provide biostratigraphic control for the age of the Mt. Simon and Argenta, although they are likely middle Cambrian in age. The middle Cambrian interpretation is supported by the presence of nearly 1000 m of demostrably late Cambrian strata that overlie the lower Mt. Simon and Argenta sandstones and by the range of MDAs from 527 to 541 Ma determined in this study.

Detrital zircon geochronologic data indicate that the Mt. Simon and Argenta sandstones sampled in this study have a provenance distinct from the overlying ubiquitous late Cambrian arenites present in the Laurentian midcontinent (fig. 11). Following is a summary of the major detrital zircon populations present in the Mt. Simon and Argenta sandstones and their possible sources, with important implications for the Paleoproterozoic to Cambrian evolution of the Laurentian midcontinent.

Paleoproterozoic Ages. The oldest detrital zircon population present in all samples is ~1650 Ma. This age is characteristic of the Mazatzal Province of Whitmeyer and Karlstrom (2007), known to be exposed in the southwestern United States and present in the subsurface in the midcontinent region. The 1650 Ma detritus in the Mt. Simon and Argenta sandstones could have been derived from the Mazatzal crustal province to the west of the Illinois Basin, where crust of that age is known to be present in the subsurface. Alternatively, 1650 Ma detrital zircons may have been locally derived. Proterozoic basement beneath the Illinois Basin is significantly undersampled compared with regions to the southwest and northeast (Bickford et al. 2015). Therefore, although the presence of >1.55 Ga Paleoproterozoic crust is inferred northwest of the Nd line, its true extent is unknown because of uncertainties about the location and tectonic significance of the Nd line itself (e.g., Petersson et al. 2015).

EGRP Basement Ages. All five samples of the Mt. Simon and Argenta sandstones display a prominent 1380–1370 Ma age peak and a subsidiary 1485–1450 Ma peak. These ages are consistent with the magmatic record of the EGRP. The EGRP is defined by rocks exposed in the St. Francois Mountains in

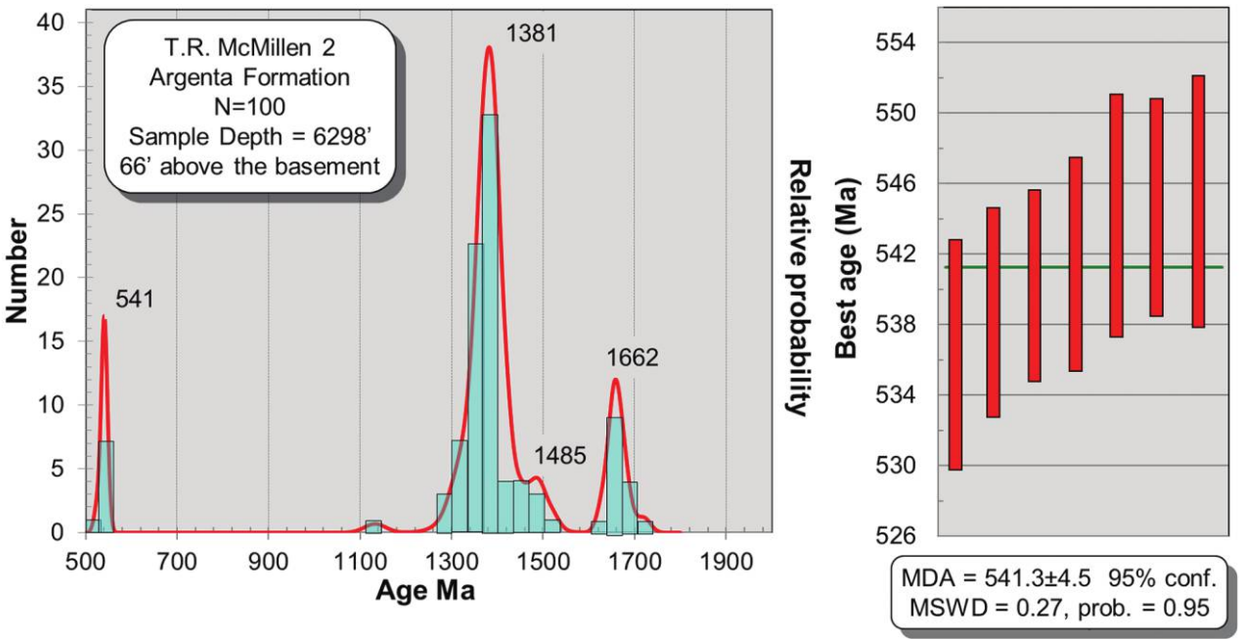

Figure 6. Probability density plot, histogram, and maximum depositional age (MDA [conf. = confidence]) of the Argenta sandstone in T. R. McMillen Well 2. Freiburg et al. (2019) report an age of 1467 Ma from the underlying rhyolite penetrated by this well.

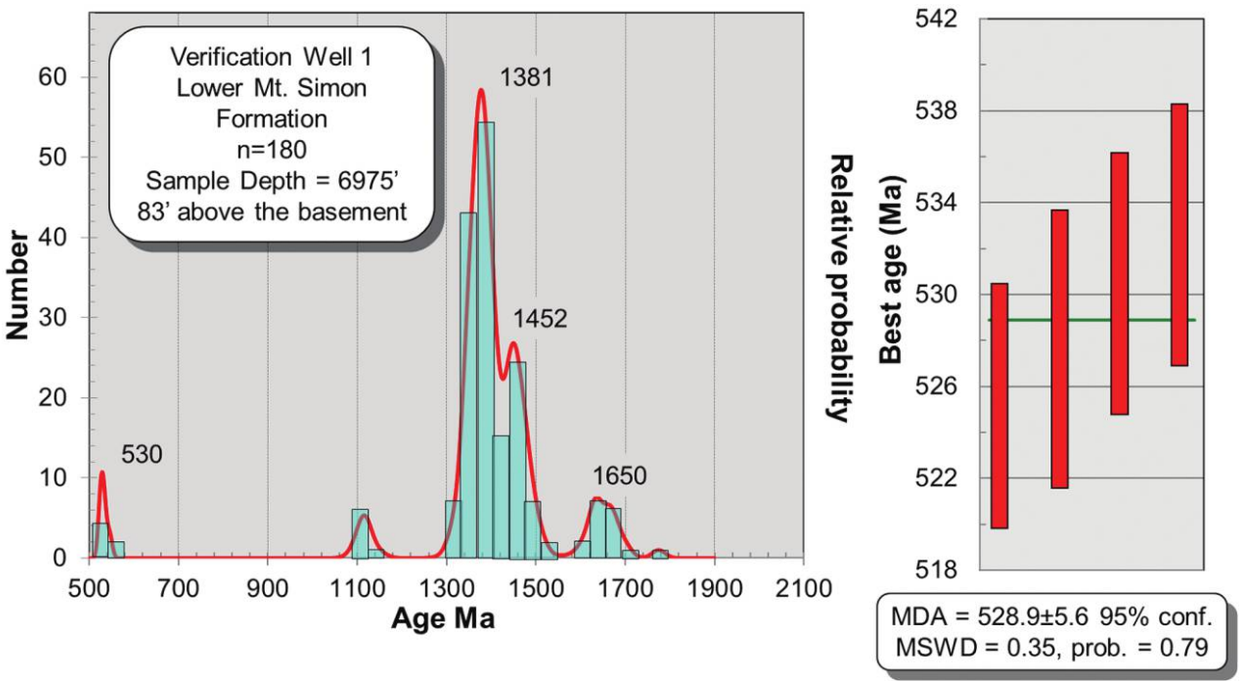

Figure 7. Probability density plot, histogram, and maximum depositional age (MDA [conf. = confidence]) of the lower Mt. Simon sandstone in Verification Well 1.

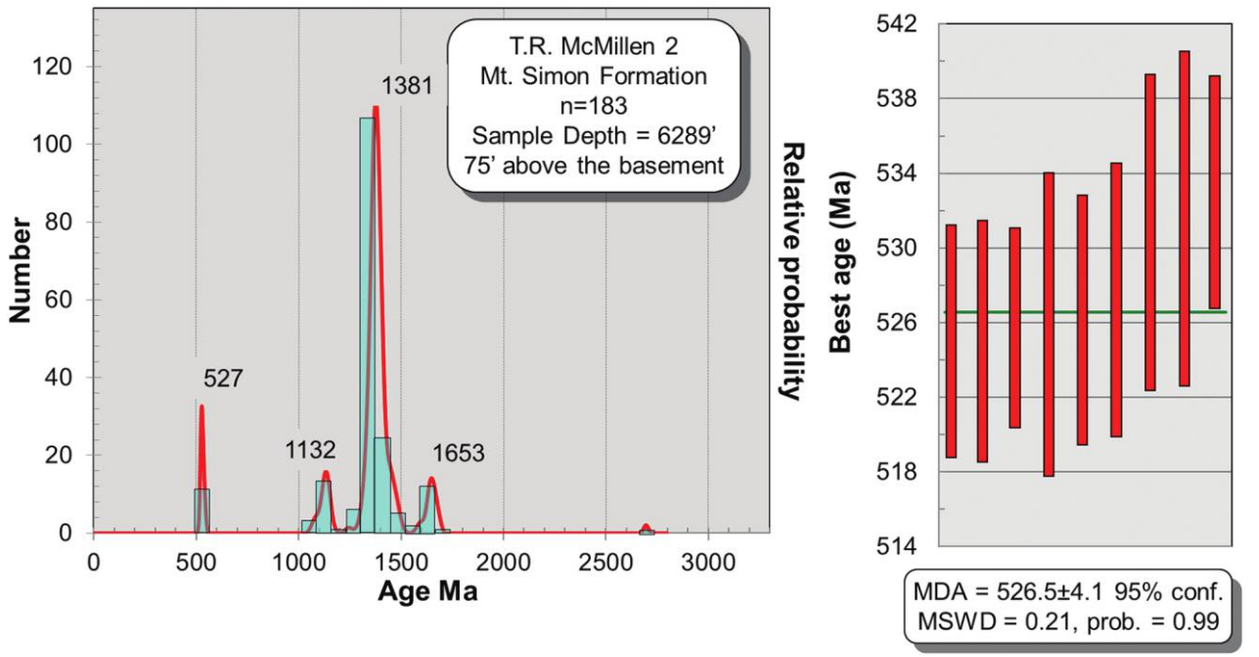

Figure 8. Probability density plot, histogram, and maximum depositional age (MDA [conf. = confidence]) of the lower Mt. Simon sandstone in T. R. McMillen Well 2.

eastern Missouri and data from deep drill cores in Missouri, Arkansas, Tennessee, Kentucky, Indiana, and Illinois, although the data set is heavily biased toward Missouri (Lidiak et al. 1993; Bickford et al. 2015). Rocks of the St. Francois Mountains record at least two episodes of magmatism: silicic volcanic rocks and epizonal granitic plutons have been interpreted as a caldera complex that was emplaced

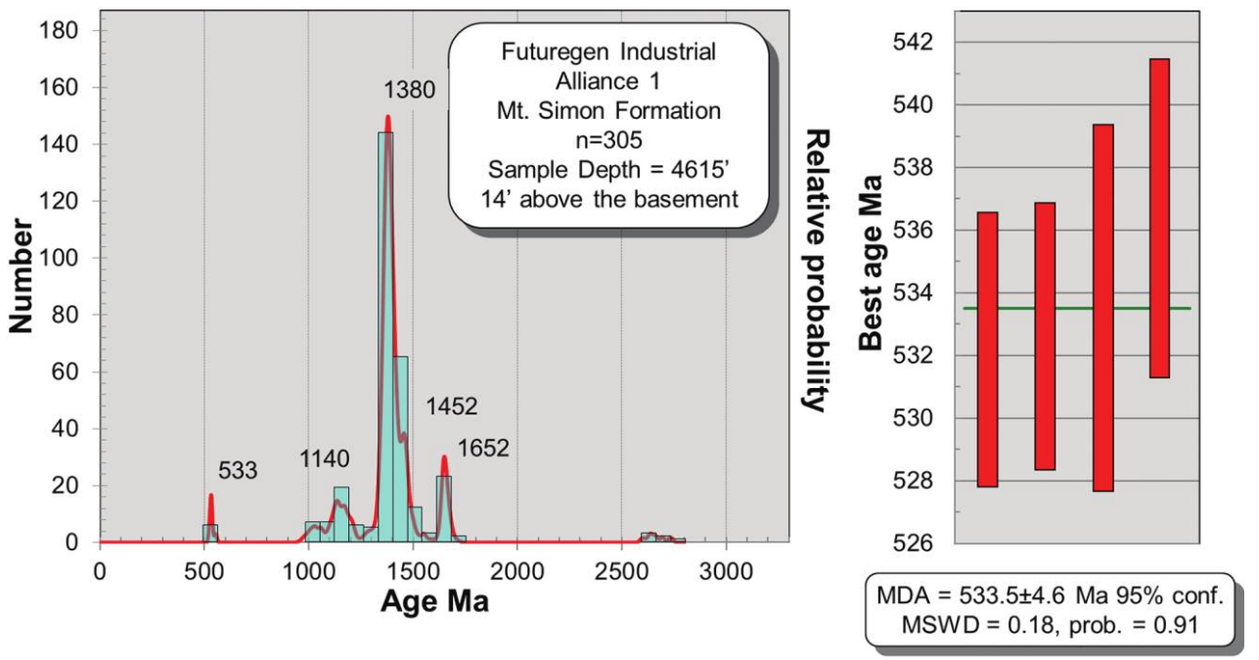

Figure 9. Probability density plot, histogram, and maximum depositional age (MDA [conf. = confidence]) of the lower Mt. Simon sandstone in Futuregen Industrial Alliance 1.

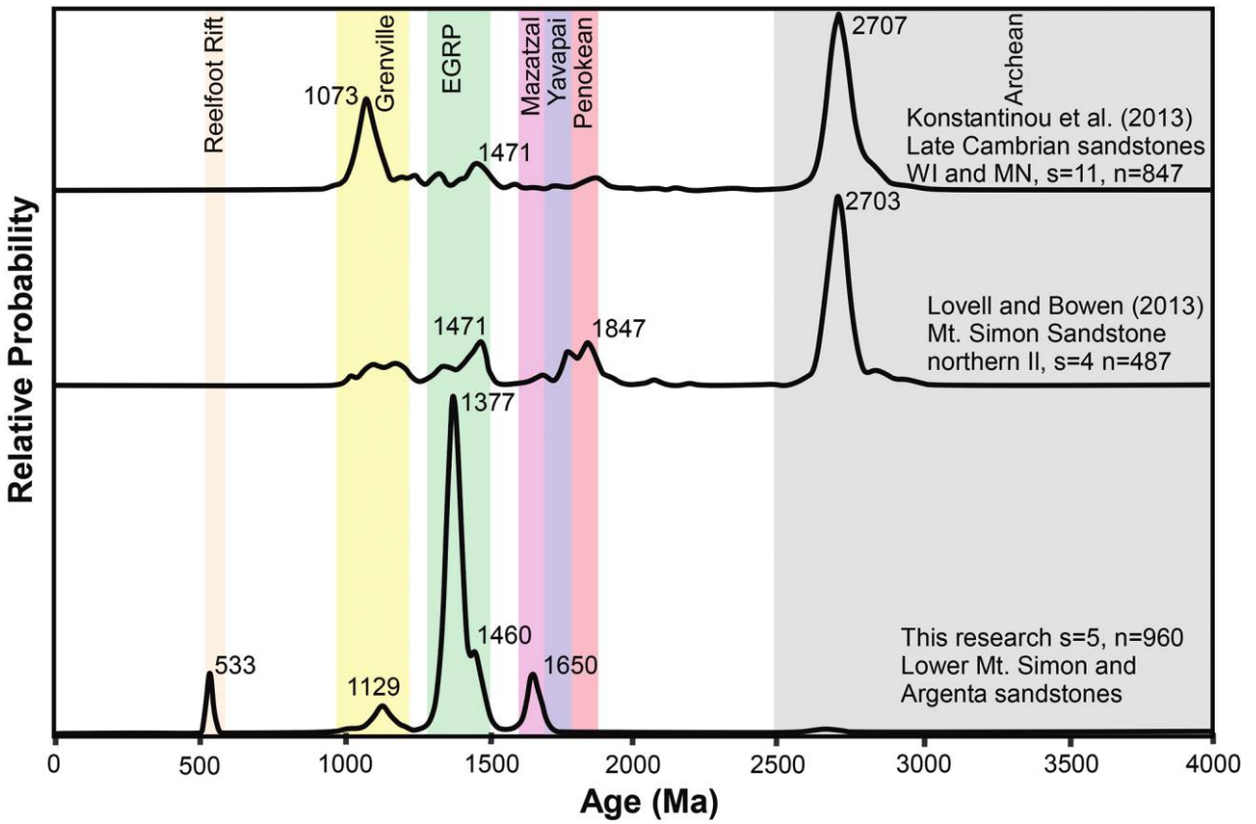

Figure 10. Stacked probability plots comparing the combined Mt. Simon and Argenta sandstones detrital zircon ages analyzed with the upper Mt. Simon core from northern Illinois (Lovell and Bowen 2013) and the Cambrian arenites in Minnesota and Wisconsin (Konstantinou et al. 2014). EGRP = Eastern Granite-Rhyolite Province.

at ~1.47 Ga (Sides et al. 1981; Van Schmus et al. 1996) and a relatively minor episode of granitic magmatism at ~1.37 Ga (Van Schmus et al. 1996). Both ages are represented in samples from drill cores throughout the EGRP, although the 1.47 Ga mode is more common, and 1.37 Ga magmatism is more typical of the Southern Granite-Rhyolite Province (SGRP; Van Schmus et al. 1996; Bickford et al. 2015). The only available basement data indicate that the Illinois Basin is underlain by 1500–1460 Ma crust (Hoppe et al. 1983; Van Schmus et al. 1987; Freiburg et al. 2019). Thus, the prominence of the 1380–1370 Ma age peak over the 1460 Ma peak may be interpreted to indicate either that rocks of this age are present throughout more of the EGRP than is currently recognized or that the Mt. Simon and Argenta sandstones received detritus from the SGRP.

Cambrian Ages. A population of 540–525 Ma detrital zircons is present in all five samples from the Argenta and lower Mt. Simon sandstones. This age range is characteristic of the Wichita igneous province exposed in the Wichita and Arbuckle mountains of southern Oklahoma (Hanson et al. 2013), and their presence could be interpreted to indicate that the lower Mt. Simon and Argenta sandstones were derived from sediment supplied from the southwest. A southwestern source would be consistent with the predominance of ~1370 Ma over 1460 Ma detrital zircons in the lower Mt. Simon and Argenta samples.

A Northern Arm of the Reelfoot Rift. Despite the apparent match between distal sources discussed above and the detrital zircon populations observed in our samples, we favor an alternative interpretation. We propose that the lower Mt. Simon and Argenta sandstones were deposited in a trough located north of (or perhaps a northern extension of) the Reelfoot Rift, an extensional arm of the New Madrid Rift system associated with the breakup of the supercontinent Rodinia. In our interpretation, the lower Mt. Simon and Argenta sandstones were deposited before and during rifting and were derived primarily from local Proterozoic basement rocks exposed along rift shoulders and Cambrian igneous rocks associated with the Reelfoot Rift itself.

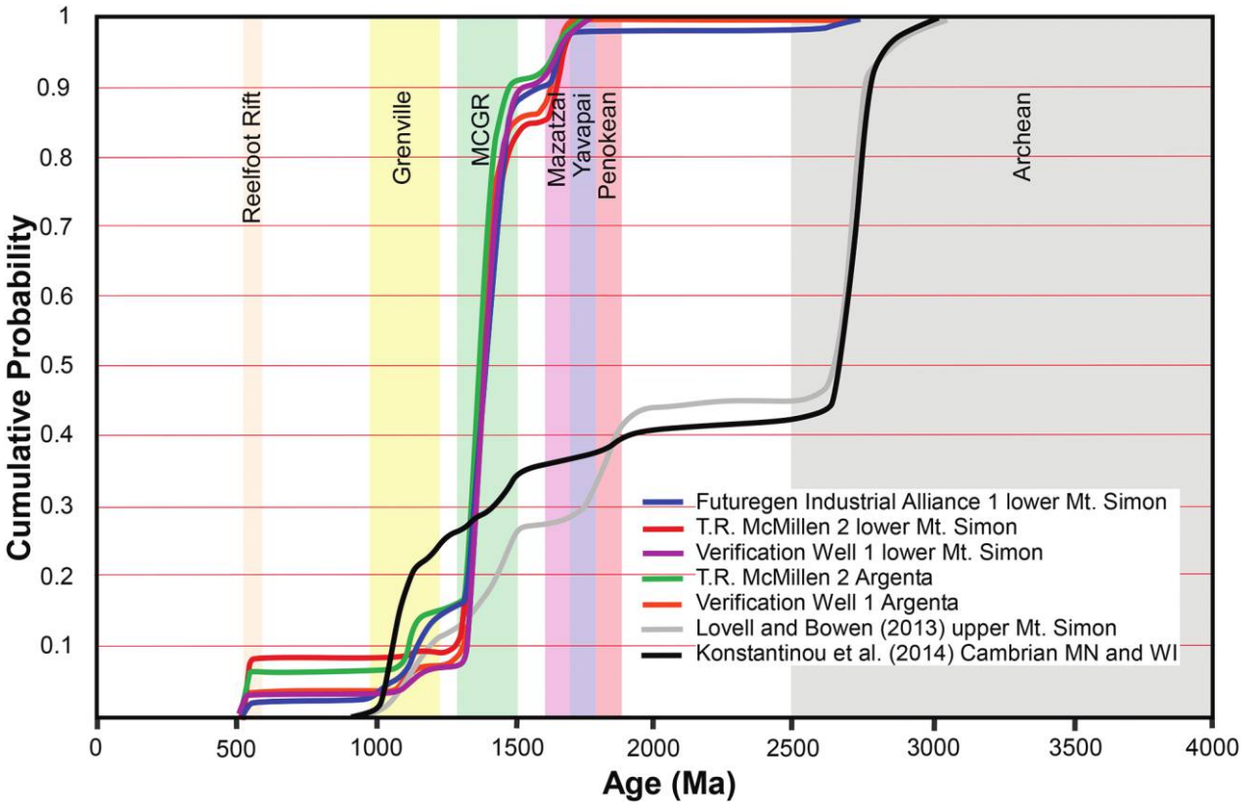

Figure 11. Cumulative probability plots comparing the combined Mt. Simon and Argenta sandstone detrital zircon ages analyzed with the upper Mt. Simon core from northern Illinois (Lovell and Bowen 2013) and the Cambrian arenites in Minnesota and Wisconsin (Konstantinou et al. 2014). MCGR = Midcontinent Granite-Rhyolite.

Ample geophysical evidence shows intrusive bodies along the margins of the Reelfoot Rift. Large igneous bodies have been interpreted from gravity and magnetic data (Ervin and McGinnis 1975; Hildenbrand 1982, 1985). Rift strata below the Paleozoic section are not observed at Verification Well 1, but seismic study reveals a bowl-shaped feature in the Precambrian rocks with apparent layering (McBride et al. 2016). A drill core in the basement is rhyolitic and yields an age of 1467 Ma, and a gabbro intrusion in the rhyolite yield an age of 1073 Ma (Freiburg et al. 2019). Freiburg et al. (2019) proposed that the bowl-shaped feature emplaced younger EGRP on older crust, herein, proposed as 1650 Ma crust (fig. 12). The margin of the Proterozoic basement appears faulted with a series of normal faults accommodating thicker sections of Argenta and lower Mt. Simon sandstones eastward.

Cawood et al. (2012) report that syndepositional sandstones in active rift basins tend to have the youngest subset of grains approximate the age of deposition. Most zircons present in sandstones deposited in rift-related successions such as this setting tend to be derived from proximal rather than distal source areas. This accounts for the disparity between detrital zircon populations of the lower Mt. Simon and Argenta and younger Cambrian sandstones regionally (fig. 10). Grenville zircons are rare in the Argenta and occur only in small numbers in the lower Mt. Simon, which indicates the first appearance of distal sediment that becomes dominant in late Cambrian sandstones to the north. Archean and Paleoproterozoic grains that dominate the late Cambrian succession to the north are not observed in the samples of this study (Lovell and Bowen 2013; Konstantinou et al. 2014). If these zircons were indeed far traveled, significant concentrations of the ubiquitous Superior and Grenville Province grains could also be expected in the lower Mt. Simon and Argenta sandstones, as they are in the overlying strata. The fertility bias for Grenville-age zircons is well known, and if such rocks were supplying sediment to the lower Mt. Simon and Argenta, zircons of this age would be present in quantity (Moecher and Samson 2006). Moreover, paleocurrent data for Cambrian strata to the north indicate that sediment was transported to the southwest (Michelson and Dott 1973). Westerly rather than easterly sediment transport of Laurentian sediment is evident for the

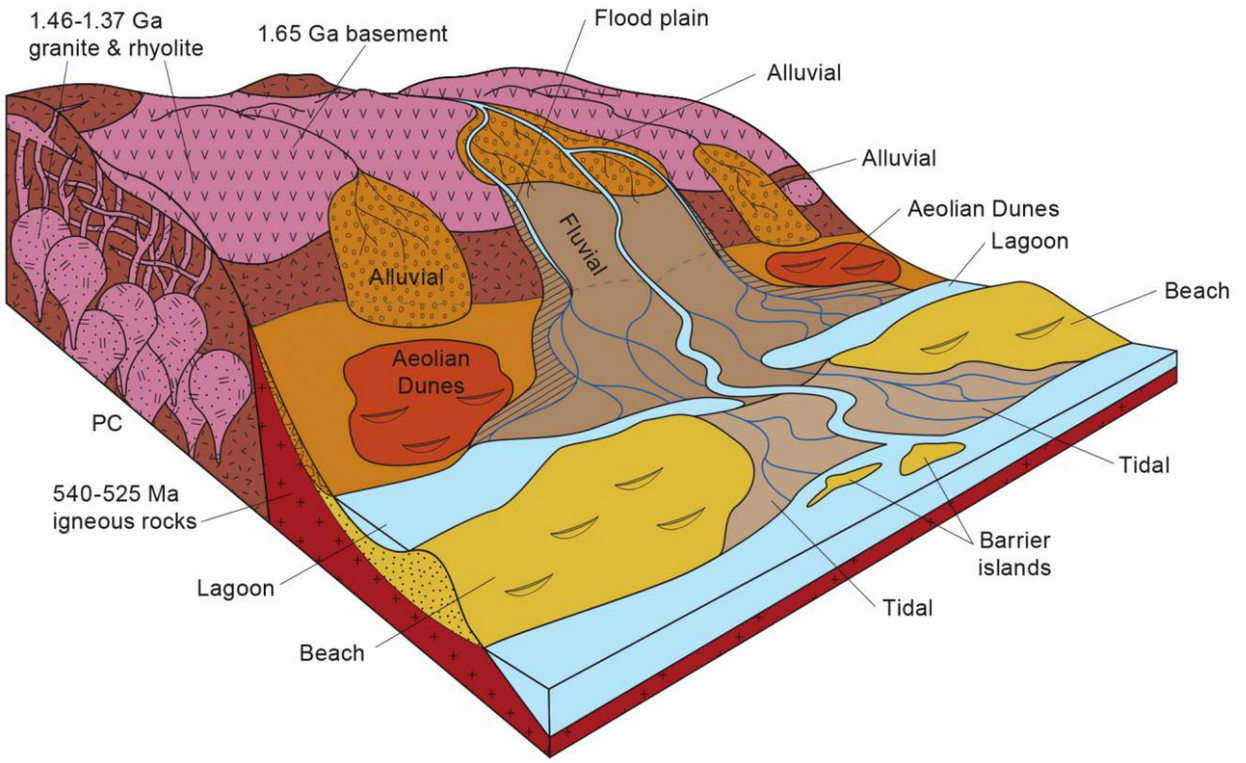

Figure 12. Depositional model for the Mt. Simon and Argenta sandstones in east-central Illinois. The Argenta and lower Mt. Simon sandstones were deposited in an isolated basin north of and perhaps an arm of the Reelfoot Rift. Sediment was derived from the rift shoulders, which includes Eastern Granite-Rhyolite Province and late Paleoproterozoic crust and from Cambrian rocks in the rift itself.

entire late Neoproterozoic-Cambrian strata deposited along the Cordilleran continental margin from California to Idaho (Yonkee et al. 2014; Malone et al. 2017*b*). Finally, the presence of ~1650 Ma basement beneath the Illinois Basin is supported by the presence of similarly aged (1660 Ma) detrital zircons in the Waterloo quartzite of Wisconsin, which records north-directed paleocurrent indicators (Medaris et al. 2019).

The Rifting of Rodinia. During the breakup of Rodinia (~780–530 Ma), major rift systems developed along the margins of Laurentia. The thickest, best exposed, and most studied occur along the Cordilleran continental margin (Yonkee et al. 2014), where almost 5 km of siliciclastic strata of the Uinta Mountain Group dated at 770–740 Ma are overlain by more than 1 km of the Pocatello Formation, representing the main phase of rifting from 680 to 720 Ma (Fanning and Link 2004). The Neoproterozoic-Cambrian Brigham Group consists of mature siliciclastic rocks that are as much as 4 km in thickness and were deposited along the Cordilleran continental margin following the earlier rifting. Late Neoproterozoic to Cambrian passive margin strata are also present along the Appalachian continental margin. The timing of rifting there ranged from ~770 to 570 Ma (Walsh and Aleinikoff 1999; Smoot and Southworth 2014). The Oklahoma aulocogen developed, and associated 530–540 Ma rift-related volcanic and plutonic rocks were also emplaced (Thomas 1991; Thomas et al. 2012; Hanson et al. 2013). Thomas et al. (2004) provide a detrital zircon age spectrum for the early-middle Cambrian Rome Formation in Alabama, but only long-transported cratonic rather than rift-related zircons are present.

The timing of the opening of the northern arm of the Reelfoot Rift in Illinois is now proposed to be 540–525 Ma based on the new detrital zircon ages. This age is identical to that of igneous rocks that occur in the Oklahoma aulocogen, which indicates that the timing of the rifting of the Iapetan rifted margin of southeast Laurentia occurred coevally rather than sequentially. Our data support the model of Thomas et al. (2004) showing that the Oklahoma aulacogen and Reelfoot Rift were failed arms of the fragmentation of the Argentine Precordillera. As rifting ceased and the transgression of the Sauk Seas commenced, the basement paleotopography was

buried, and the supply of local sediment to the Cambrian depositional systems waned. By late Cambrian time, much of the Reelfoot Rift, EGRP, and Paleo- to Mesoproterozoic basement crust of the Laurentian midcontinent were buried, and mature sediment recycled from older Proterozoic Basins in the Lake Superior area and the Grenville Province was deposited in the midcontinent (Konstantinou et al. 2014; Malone et al. 2016). It is evident that these Neoproterozoic-Cambrian Rift Basins in Illinois do not coincide with the presumed location of Proterozoic lithospheric boundaries (e.g., the Nd line).

Conclusions

The detrital zircon age spectra for the lower Mt. Simon and Argenta sandstones help constrain the age of Illinois basement rocks and early Cambrian rifting associated with the breakup of Rodinia (fig. 11). Both the Argenta and lower Mt. Simon were derived locally and eroded from Paleo- and Mesoproterozoic crust present on the northern extension of the Reelfoot Rift. Magmatic rocks associate with rifting from ~525 to 540 Ma also supplied sediment to the terrestrial and marginal marine depositional systems. As the Sauk Seas transgressed and sea level rose, the deeper troughs were filled and the sediment supply from local basement sources waned. By late Cambrian time, sediment was derived from more distal source areas in the Grenville and Superior Provinces. At this time, lower Mt. Simon and Argenta sandstones and underlying basement rocks were buried, and thus the availability of locally derived sediment into the late Cambrian arenites was not possible.

ACKNOWLEDGMENT

This research was funded by the US Department of Energy CarbonSAFE Illinois Macon County Project (DE-FE-0029381). We thank G. Medaris, R. Van Schmus, and P. Bickford for thoughtful reviews that improved this article and S. Whitmeyer for his comments on a previous version of this article.

REFERENCES CITED

Amato, J. M., and Mack, G. H. 2012. Detrital zircon geochronology from the Cambrian-Ordovician Bliss sandstone, New Mexico: evidence for contrasting Grenville-age and Cambrian sources on opposite sides of the Transcontinental Arch. Geol. Soc. Am. Bull. 124:1826–1840.

Berg, R. R. 1952. Feldspathized sandstone: Minnesota and Wisconsin. J. Sediment. Petrol. 22:221–223.

Bickford, M. E.; Van Schmus, W. R.; Karlstrom, K. E.; Mueller, P. A.; and Kamenov, G. D. 2015. Mesoproterozoic-trans-Laurentian magmatism: a synthesis of continent-wide age distributions, new SIMS U-Pb ages, zircon saturation temperatures, and Hf and Nd isotopic compositions. Precambrian Res. 265:286–312.

Bickford, M. E.; Van Schmus, W. R.; and Zietz, I. 1986. Proterozoic history of the midcontinent region of North America. Geology 14:492–496.

Buschbach, T. C., and Kolata, D. R. 1990. Regional setting of Illinois Basin. *In* Leighton, M. W.; Kolata, D. R.; Oltz, D. T.; and Eidel, J. J., eds. Interior cratonic basins. Am. Assoc. Pet. Geol. Bull. Mem. 51:29–55.

Byers, C. W., and Dott, R. H. 1995. Sedimentology and depositional sequences of the Jordan Formation (upper Cambrian), northern Mississippi Valley. J. Sediment. Res. 65:1073–1318.

Cawood, P. A.; Hawkesworth, C. J.; and Dhuime, B. 2012. Detrital zircon record and tectonic setting. Geology 40:875–878.

Collinson, C.; Sargent, M. L.; and Jennings, J. R. 1988. Illinois Basin region. *In* Sloss, L. L., ed. Sedimentary cover—North American Craton, US (Geology of North America, Vol. 2). Boulder, CO, Geol. Soc. Am., p. 383–426.

Craddock, J. P.; Malone, D. H.; Porter, R.; Compton, J.; Luczaj, J.; Konstantinou, A.; Day, J. E.; and Johnston, S. T. 2017. Paleozoic reactivation structures in the Appalachian-Ouachita-Marathon foreland: far-field deformation across Pangea. Earth-Sci. Rev. 169:1–34.

Ervin, C. P., and McGinnis, L. D. 1975. Reelfoot Rift: reactivated precursor to the Mississippi embayment. Geol. Soc. Am. Bull. 86:1287–1295.

Fanning, C. M., and Link, P. K. 2004. U-Pb SHRIMP ages of Neoproterozoic (Sturtian) glaciogenic Pocatello Formation, southeastern Idaho. Geology 32:881–884.

Freiburg, J. T.; McBride, J. H.; Malone, D. H.; and Leetaru, H. E. 2019. Petrology, geochronology, and geophysical characterization of Mesoproterozoic rocks in central Illinois, USA. Geosci. Front. https://doi.org/10.1016/j.gsf.2019.07.004.

Freiburg, J. T.; Morse, D. G.; Leetaru, H. E.; Hoss, R.P.; and Yan, Q. 2014. A depositional and diagenetic characterization of the Mt. Simon sandstone at the Illinois Basin–Decatur Project Carbon Capture and Storage Site, Decatur, Illinois, USA. Illinois State Geol. Surv. Circ. 583, 59 p.

Freiburg, J. T.; Ritzi, R. W.; and Kehoe, K. S. 2016. Depositional and diagenetic controls on anomalously high porosity within a deeply buried CO_2 storage reservoir—the Cambrian Mt. Simon sandstone, Illinois Basin, USA. Int. J. Greenhouse Gas Control 55:42–54.

Gaudette, H. E.; Vitrac-Michard, A.; and Allègre, C. J. 1981. North American Precambrian history recorded

in a single sample: high-resolution U-Pb systematics of the Potsdam sandstone detrital zircons, New York State. Earth. Planet. Sci. Lett. 54:248–260.
Gehrels, G., and Pecha, M. 2014. Detrital zircon U-Pb geochronology and Hf isotope geochemistry of Paleozoic and Triassic passive margin strata of western North America. Geosphere 10:49–65.
Gehrels, G. E.; Dickinson, W. R.; Ross, G. M.; Stewart, J. H.; and Howell, D. G. 1995. Detrital zircon reference for Cambrian to Triassic miogeoclinal strata of western North America. Geology 23:831–834.
Gehrels, G. E.; Valencia, V.; and Pullen, A. 2006. Detrital zircon geochronology by laser-ablation multicollector ICPMS at the Arizona LaserChron Center. *In* Loszewski, T., and Huff, W., eds. Geochronology: emerging opportunities. Paleontology Society short course. Paleontol. Soc. Pap. 11:1–10.
Gehrels, G. E.; Valencia, V.; and Ruiz, J. 2008. Enhanced precision, accuracy, efficiency, and spatial resolution of U-Pb ages by laser ablation-multicollector-inductively coupled plasma-mass spectrometry. Geochem. Geophys. Geosyst. 9:Q03017. https://doi.org/10.1029/2007GC001805.
Hanson, R. E.; Puckett, R. E., Jr.; Keller, G. R.; Brueseke, M. E.; Bulen, C. L.; Mertzman, S. A.; Finegan, S. A.; and McCleery, D. A. 2013. Intraplate magmatism related to opening of the southern Iapetus Ocean: Cambrian Wichita igneous province in the Southern Oklahoma rift zone. Lithos 174:57–70.
Hildenbrand, T. G. 1982. Model of the southeastern margin of the Mississippi Valley graben near Memphis, Tennessee, from interpretation of truck-magnetometer data. Geology 10:476–480.
———. 1985. Rift structure of the northern Mississippi embayment from the analysis of gravity and magnetic data. J. Geophys. Res. Solid Earth 90(B14):12,607–12,622.
Hoppe, W. J.; Montgomery, C. W.; and Van Schmus, W. R. 1983. Age and significance of Precambrian basement samples from northern Illinois and adjacent states. J. Geophys. Res. 88:7276–7286.
Houseknecht, D. W., and Ethridge, F. G. 1978. Depositional history of the Lamotte sandstone of southeastern Missouri. J. Sediment. Res. 48:575–586.
Karlstrom, K.; Hagadorn, J.; Gehrels, G.; Matthews, W.; Schmitz, M.; Madronich, L.; Mulder, J.; Pecha, M.; Giesler, D.; and Crossey, L. 2018. Cambrian Sauk transgression in the Grand Canyon region redefined by detrital zircons. Nat. Geosci. 11:438.
Kissock, J. K.; Finzel, E. S.; Malone, D. H.; and Craddock, J. P. 2018. Lower-Middle Pennsylvanian strata in the North American midcontinent record the interplay between erosional unroofing of the Appalachians and eustatic sea-level rise. Geosphere 15:1–21.
Kolata, D. R., and Nelson, W. J. 1990. Tectonic history of the Illinois Basin. *In* Leighton, M. W.; Kolata, D. R.; Oltz, D. E; and Eidel, J. J., eds. Interior cratonic basins. Am. Assoc. Pet. Geol. Mem. 51:263–285.
Konstantinou, A.; Wirth, K.; Craddock, J. P.; Malone, D. H.; Vervoort, J. D.; and Davidson, C. 2014. Provenance of early Paleozoic Quartz Arenites, midcontinent, USA. J. Geol. 122:201–216.
Leetaru, H. E., and Freiburg, J. T. 2014. Litho-facies and reservoir characterization of the Mt Simon sandstone at the Illinois Basin-Decatur Project. Greenhouse Gases Sci. Technol. 4:580–595.
Lidiak, E. G.; Bickford, M. E.; and Kisvarsanyi, E. B. 1993. Proterozoic geology of the eastern midcontinent basement. *In* Van Schmus, W. R., and Bickford, M. E., eds. Precambrian. Decade of North American Geology (DNAG). Geol. Soc. Am., p. 259–270.
Link, P. K.; Todt, M. K.; Pearson, D. M.; and Thomas, R. C. 2017. 500–490 Ma detrital zircons in upper Cambrian Worm Creek and correlative sandstones, Idaho, Montana, and Wyoming: magmatism and tectonism within the passive margin. Lithosphere 9:910–926.
Lovell, T. R., and Bowen, B. B. 2013. Fluctuations in sedimentary provenance of the upper Cambrian Mount Simon sandstone, Illinois Basin, United States. J. Geol. 121:129–154.
Ludwig, K. R. 2012. User's manual for ISOPLOT 3.75: a geochronological toolkit for Microsoft Excel. Spec. Publ. 5. Berkeley, CA, Berkeley Geochronology Center, 75 p.
Malone, D. H.; Craddock, J. P.; and Kenderes, S. 2017*a*. Detrital zircon geochronology of the Cambrian Flathead sandstone, Park County, WY. Mountain Geologist 54:86–103. doi:10.31582/rmag.mg.54.2.86.
Malone, D. H.; Craddock, J. P.; Link, P. K.; Foreman, B. Z.; Scroggins, M. A.; and Rappe, J. 2017*b*. Detrital zircon geochronology of quartzite clasts, northwest Wyoming: implications for Cordilleran Neoproterozoic stratigraphy and depositional patterns. Precambrian Res. 289:116–128.
Malone, D. H.; Stein, C.A.; Craddock, J. P.; Kley, J.; Stein, S.; and Malone, J. E. 2016. Maximum depositional age of the Neoproterozoic Jacobsville sandstone, Michigan: implications for the evolution of the Midcontinent Rift. Geosphere 12:1271–1282.
Matthews, W.; Guest, B.; and Madronich, L. 2017. Latest Neoproterozoic to Cambrian detrital zircon facies of western Laurentia. Geosphere 14:243–264.
May, S. R.; Gray, G. G.; Summa, L. L.; Stewart, N. R.; Gehrels, G. E.; and Pecha, M. E. 2013. Detrital zircon geochronology from the Bighorn Basin, Wyoming, USA: implications for tectonostratigraphic evolution and paleogeography. Geol. Soc. Am. Bull. 125:1403–1422.
McBride, J. H.; Kolata, D. R.; and Hildenbrand, T. G. 2003. Geophysical constraints on understanding the origin of the Illinois Basin and its underlying crust. Tectonophysics 363:45–78.
McBride, J. H.; Leetaru, H. E.; Keach, R. W.; and McBride, E. I. 2016. Fine-scale structure of the Precambrian beneath the Illinois Basin. Geosphere 12:585–606.
Medaris, L. G., Jr.; Singer, B. S.; Jicha, B. R.; Malone, D. H.; Schwartz, J. J.; Stewart, E. K.; Van Lankvelt, A.; Williams, M. L.; and Reiners, P. 2019. The geon 14 Wolf River tectonomagmatic event: a midcontinental link

between the Picuris and Pinwarian orogenies. Geol. Soc. Am. Abstr. Program 51(5). https://doi.org/10.1130/abs/2019AM-332516.

Michelson, P. C., and Dott, R. H., Jr. 1973. Orientation analysis of trough cross stratification in upper Cambrian sandstones of western Wisconsin. J. Sediment. Res. 43:784–794.

Moecher, D. P., and Samson, S. D. 2006. Differential zircon fertility of source terranes and natural bias in the detrital zircon record: implications for sedimentary provenance analysis. Earth Planet. Sci. Lett. 247:252–266.

Nelson, C. A. 1956. Upper Croixan stratigraphy, upper Mississippi Valley. Geol. Soc. Am. Bull. 67:165–183.

Ojakangas, R. W. 1963. Petrology and sedimentation of the upper Cambrian Lamotte sandstone in Missouri. J. Sediment. Res. 33:860–873.

Petersson, A.; Scherstén, A.; Andersson, J.; Whitehouse, M. J.; and Baranoski, M. T. 2015. Zircon U-Pb, Hf and O isotope constraints on growth versus reworking of continental crust in the subsurface Grenville orogen, Ohio, USA. Precambrian Res. 265:313–327.

Sides, J. R.; Bickford, M. E.; Shuster, R. D.; and Nusbaum, R. L. 1981. Calderas in the Precambrian terrane of the St. Francois Mountains, southeastern Missouri. J. Geophys. Res. 86:10,349–10,364.

Sloss, L. L. 1963. Sequences in the cratonic interior of North America. Geol. Soc. Am. Bull. 74:93–114.

Smoot, J. P., and Southworth, S. 2014. Volcanic rift margin model for the rift-to-drift setting of the late Neoproterozoic-early Cambrian eastern margin of Laurentia: Chilhowee Group of the Appalachian Blue Ridge. Geol. Soc. Am. Bull. 126:201–218.

Stein, C. A.; Stein, S.; Elling, R.; Keller, G. R.; and Kley, J. 2018. Is the "Grenville Front" in the central United States really the Midcontinent Rift? GSA Today 28:4–10.

Stewart, J. H.; Gehrels, G. E.; Barth, A. P.; Link, P. K.; Christie-Blick, N.; and Wrucke, C. T. 2001. Detrital zircon provenance of Mesoproterozoic to Cambrian arenites in the western United States and northwestern Mexico. Geol. Soc. Am. Bull. 113:1343–1356.

Thomas, J. J.; Shuster, R. D.; and Bickford, M. E. 1984. A terrane of 1,350- to 1,400-my-old silicic volcanic and plutonic rocks in the buried Proterozoic of the midcontinent and in the Wet Mountains, Colorado. Geol. Soc. Am. Bull. 95:1150–1157.

Thomas, W.A. 1991. The Appalachian-Ouachita rifted margin of southeastern North America. Geol. Am. Soc. Bull. 103:415–431.

Thomas, W. A.; Astini, R. A.; Mueller, P. A.; Gehrels, G. E.; and Wooden, J. L. 2004. Transfer of the Argentine Precordillera terrane from Laurentia: constraints from detrital-zircon geochronology. Geology 32:965–968.

Thomas, W. A.; Tucker, R. D.; Astini, R. A.; and Denison, R. E. 2012. Ages of pre-rift basement and synrift rocks along the conjugate rift and transform margins of the Argentine Precordillera and Laurentia. Geosphere 8:1366–1383.

Van Schmus, W. R.; Bickford, M. E.; Sims, P. K.; Anderson, R. R.; Shearer, C. K.; and Treves, S. B. 1993. Proterozoic geology of the western midcontinent basement. Precambrian: conterminous USA (Geology of North America, Vol. 2). Boulder, CO, Geol. Soc. Am., p. 239–258.

Van Schmus, W. R.; Bickford, M. E.; and Turek, A. 1996. Proterozoic geology of the east-central midcontinent basement. *In* van der Pluijm, B. A., and Catacosinos, P. A., eds. Basement and basins of eastern North America. Geol. Soc. Am. Spec. Pap. 308:7–32.

Van Schmus, W. R.; Bickford, M. E. and Zietz, I. 1987. Early and middle Proterozoic provinces in the central United States. *In* Kröner, A. ed., Proterozoic lithospheric evolution (Geophysical Series, Vol. 17). Washington, DC, American Geophys. Union, p. 43–68.

Walsh, G. J., and Aleinikoff, J. N. 1999. U-Pb zircon age of metafelsite from the Pinney Hollow Formation; implications for the development of the Vermont Appalachians. Am. J. Sci. 299:157–170.

Whitmeyer, S. J., and Karlstrom, K. E. 2007. Tectonic model for the Proterozoic growth of North America. Geosphere 3:220–259.

Yonkee, W. A.; Dehler, C. D.; Link, P. K.; Balgord, E. A.; Keeley, J. A.; Hayes, D. S.; Wells, M. L.; Fanning, C. M.; and Johnson, S. M. 2014. Tectono-stratigraphic framework of Neoproterozoic to Cambrian strata, west-central US: protracted rifting, glaciation, and evolution of the North American Cordilleran margin. Earth-Sci. Rev. 136:59–95.

Chapter iv Manuscript

Depositional and diagenetic controls on anomalously high porosity within a deeply buried CO_2 storage reservoir–The Cambrian Mt. Simon Sandstone, Illinois Basin, USA

International Journal of Greenhouse Gas Control 55 (2016) 42–54

Contents lists available at ScienceDirect

International Journal of Greenhouse Gas Control

journal homepage: www.elsevier.com/locate/ijggc

Depositional and diagenetic controls on anomalously high porosity within a deeply buried CO_2 storage reservoir—The Cambrian Mt. Simon Sandstone, Illinois Basin, USA

Jared T. Freiburg[a,b,*], Robert W. Ritzi[c], Kelsey S. Kehoe[a]

[a] Illinois State Geological Survey, Prairie Research Institute, University of Illinois at Urbana-Champaign, 615 E. Peabody Drive, Champaign, IL 61820, United States
[b] Ernst-Moritz-Arndt-University, Institute of Geography and Geology, Friedrich-Ludwig-Jahn Str. 17a, D-17489 Greifswald, Germany
[c] Department of Earth and Environmental Sciences, Wright State University, Dayton, OH 45435, United States

ARTICLE INFO

Article history:
Received 15 June 2016
Received in revised form 1 November 2016
Accepted 4 November 2016

Keywords:
CO_2 geo-sequestration
Anomalous porosity
Diagenesis
Compaction
Cementation
Illite clay coatings
Cambrian Mt. Simon Sandstone

ABSTRACT

Current diagenetic models predict that sandstone porosity and reservoir quality decrease with burial depth and formation age. However, the opposite trend is true for the Cambrian Mt. Simon Sandstone. The lowermost section of the Mt. Simon is highly porous—it has an average log-derived effective porosity of 17.0%. To understand the possible reason(s) for this anomaly, the amount of porosity reduction due to compaction porosity loss (COPL) and cementation porosity loss (CEPL) was analyzed. The COPL and CEPL were coupled with sedimentary characteristics in order to ascertain which factors controlled porosity and reservoir quality in the Mt. Simon. The underlying Argenta sedimentary unit disconformably underlies the Mt. Simon and is included for diagenetic and depositional comparison.

Similar to expected trends from other deep basin reservoirs, the COPL generally increases with depth in the Mt. Simon. The CEPL is significantly lower in the lower half of the Mt. Simon compared to the upper half of the Mt. Simon, indicating that higher porosity is attributed to having a lower volume of intergranular cement. Early episodes of diagenesis within the arkosic lower half of the Mt. Simon, such as clay infiltration and feldspar alteration, produced diagenetic grain-coating clays, which inhibited the development of quartz cements. Thus, these grain coatings assisted in porosity preservation within the Lower Mt. Simon by reducing CEPL. The upper half of the Mt. Simon is more heavily cemented as a result of changes in the depositional setting and thus changes in the lithology. Later, largely post-compaction feldspar dissolution further increased porosity in the Lower Mt. Simon Sandstone.

1. Introduction

Understanding the contributing factors behind highly porous reservoir rocks at depth remains a crucial aspect for the broader viability and implementation of geologic carbon storage projects. Identifying the properties that lead to heterogeneity in porosity within reservoirs has multiple applications, including improving conceptual models that aid in predicting carbon dioxide (CO_2) migration. Additionally, these properties can be used to characterize similar formations that may be suitable for storing CO_2. Properties from improved conceptual models are also important for maximizing petroleum production and improving enhanced oil recovery and liquid waste storage techniques.

The most important criteria of a CO_2 reservoir is injectivity. Most carbon capture and storage (CCS) projects require natural subsurface reservoirs with high values of porosity and permeability to achieve acceptable rates of injectivity. However, formations with high porosity and permeability at depths necessary to achieve high enough pressures for the injected CO_2 to maintain a supercritical state are relatively uncommon. Typically, intergranular volume and porosity decrease with increasing burial depth (Paxton et al., 2002). During burial, three primary diagenetic mechanisms act to reduce porosity: mechanical compaction, chemical compaction, and cementation (Houseknecht, 1984). Mechanical compaction reorients framework grains, resulting in a reduction of intergranular volume. Chemical compaction occurs as a result of lithostatic or tectonic stresses that act to dissolve framework grains, promoting consolidation (Houseknecht, 1987). The extent to which these

* Corresponding author at: Illinois State Geological Survey, Prairie Research Institute, University of Illinois at Urbana-Champaign, 615 E. Peabody Drive, Champaign, IL 61820, United States.
E-mail address: freiburg@illinois.edu (J.T. Freiburg).

http://dx.doi.org/10.1016/j.ijggc.2016.11.005
1750-5836/

mechanisms can reduce porosity relies heavily on the sedimentary properties (i.e., mineralogy and grain size) partly controlled by depositional processes in evolving basins and the subsequent diagenetic history of the target formation. Thus, understanding depositional processes is critical in deciphering diagenetic controls on reservoir properties.

This paper presents research analysis of porosity loss data due to compaction and cementation for the Cambrian Mt. Simon Sandstone. This formation includes the CO_2 storage reservoir for the Illinois Basin–Decatur Project (IBDP), a 1-million metric ton CCS demonstration project on the property of the Archer Daniels Midland Company corn processing facility in Decatur, Illinois. A large dataset acquired by the IBDP was used to determine the role that changing sedimentology plays in controlling the diagenetic processes that affect reservoir quality.

2. Geological background

The Mt. Simon Sandstone is a laterally extensive deposit throughout the Midwest (Fig. 1) and has been the focus of industrial development, specifically natural gas storage, as well as the focus of scientific research, for multiple decades. The majority of the research on the Mt. Simon has sought to characterize the formation sedimentology and stratigraphy and describe its diagenetic history, primarily utilizing small datasets from multiple wells located throughout the region. Freiburg et al. (2014) used a large dataset developed from newer IBDP wells and described all of the major depositional facies within the Mt. Simon from the Decatur site. This previous work is summarized here.

2.1. Mt. Simon units

The Cambrian Mt. Simon Sandstone is a transgressive terrestrial to shallow marine sequence deposited in the proto-Illinois and Illinois basins, as well as the Michigan and Appalachian basins (Kolata and Nelson, 1990). At the IBDP site it can be divided into five distinct units—A, B, C, D, and E (Fig. 2)—as determined by the changes in the depositional environment and sedimentology (Freiburg et al., 2014). Depositional environments in the Mt. Simon are highly variable; the numerous interpretations include shallow-marine, deltaic, fluvial, eolian, sabkha, and coastal (Driese et al., 1981; Hagadorn et al., 2002; Fischietto, 2009; Bowen et al., 2011; Freiburg et al., 2014). The Mt. Simon is unconformably underlain by the basal Cambrian Argenta Formation (formerly called the pre-Mt. Simon), a sedimentary unit that is composed of shallow marine (Freiburg et al., 2015) and fluvial clastic deposits and unconformably overlies Precambrian felsic rocks of the Granite-Rhyolite Province. The Upper Cambrian Eau Claire Formation, a tidally influenced marine deposit marked by a prominent shale unit, conformably overlies the Mt. Simon. In Illinois, the Mt. Simon varies in thickness from about 2600 ft (792.5 m) at its depocenter in east-central Illinois to less than 400 ft (122 m) thick in southern Illinois (Fig. 1). A postulated unconformity separates the Lower Mt. Simon (Units A and B) from the Middle Mt. Simon (Units C and D; Freiburg et al., 2014). The Middle Mt. Simon units and the Upper Mt. Simon (Unit E) appear to be transitional and represent the major Sauk transgression (Collinson et al., 1988). The Mt. Simon is predominantly a fine- to medium-grained quartz or subarkosic arenite with rare shales, wackes, and sublithic arenites. It is highly variable in sedimentary and diagenetic characteristics.

2.2. Unit depositional environments, bedding, texture, and classification

Mt. Simon Unit A includes mixed fluvial, eolian, and possible beach deposits and is dominantly composed of medium- to fine-grained cross-bedded to ripple-laminated subarkose arenite. To a lesser extent, it contains varying amounts of planar-bedded, ripple-laminated sandstone and conglomerate composed of subarkosic arenite, arkosic arenite, sublithic arenite, arkosic wacke, and mudstone (Freiburg et al., 2014).

Unit B contains mixed eolian and fluvial deposits, which are dominantly composed of fine- to medium-grained planar-bedded to fine-grained low-angle cross-bedded subarkosic and quartz arenites.

Unit C fluvial deposits are dominantly composed of medium- to coarse-grained cross-bedded subarkosic and quartz arenites with rare mudstones.

Unit D is composed of eolian deposits that are fine- to medium-grained planar-laminated and cross-bedded quartz arenites and quartz wackes.

Unit E of the Mt. Simon contains marine deposits of medium- to fine-grained bioturbated cross-bedded quartz to subarkosic arenites with thin interbedded black shales and red siltstones to mudstones.

In comparison to the Mt. Simon, the underlying Argenta contains mixed marine and fluvial deposits composed of fine- to medium-grained bioturbated cross-bedded to ripple-laminated sublithic and quartz arenites with common interbedded coarse-grained sandstones to conglomerates.

2.3. Porosity

Regionally, the Mt. Simon shows a trend of decreasing porosity with increasing depth (Hoholick et al., 1984; Medina et al., 2011), although there are few wells that penetrate the entire Mt. Simon with quality well data in the proto-Illinois or Illinois basins. For wells that only penetrate the Upper and Middle Mt. Simon Units C, D, and E, the observation of decreasing porosity with depth may stand true but is likely an oversimplification for the entirety of the Mt. Simon. There exists a range of porosities for any given depth within the Mt. Simon (Bowen et al., 2011); however, wells that penetrate the Lower Mt. Simon Units A and B, such as all the wells at the IBDP, generally show porosity increasing with depth from the Middle Units C and D to the Lower Units A and B (Bowen et al., 2011; Freiburg et al., 2014; Fig. 2). Out of the three Mt. Simon sections, the Lower Mt. Simon (Units A and B) contains the highest porosity, with an average whole core analysis porosity of 16.6% but may range as high as 27% (Freiburg et al., 2014). Porosity within the Mt. Simon is dominantly primary with the dissolution of feldspars contributing to moderate amounts of secondary porosity (Heald and Baker, 1977; Fishman, 1997; Bowen et al., 2011; Freiburg et al., 2014). Partial dissolution of framework grains commonly occurs in the Lower Mt. Simon (Units A and B).

2.4. Diagenesis

On average, the most dominant diagenetic cement in the Mt. Simon is quartz. The abundance of authigenic quartz is significantly lower in the Lower Mt. Simon Units A and B than the Middle and Upper Mt. Simon Units C, D, and E (Freiburg et al., 2014) and in the eastern extents of the formation (Heald and Baker, 1977). It forms thin or partial syntaxial overgrowths and pore-filling cements. Authigenic quartz formed during burial, where potential sources of silica may have originated from pressure solution, shale diagenesis, feldspar dissolution, or migrating paleofluids (Mississippi Valley-type; Pollington et al., 2011; Freiburg et al., 2014). Recent isotopic analysis of authigenic quartz cements suggests quartz precipitation occurred with increasing temperatures during burial and basin evolution rather than migrating warm paleofluids (Pollington et al., 2011).

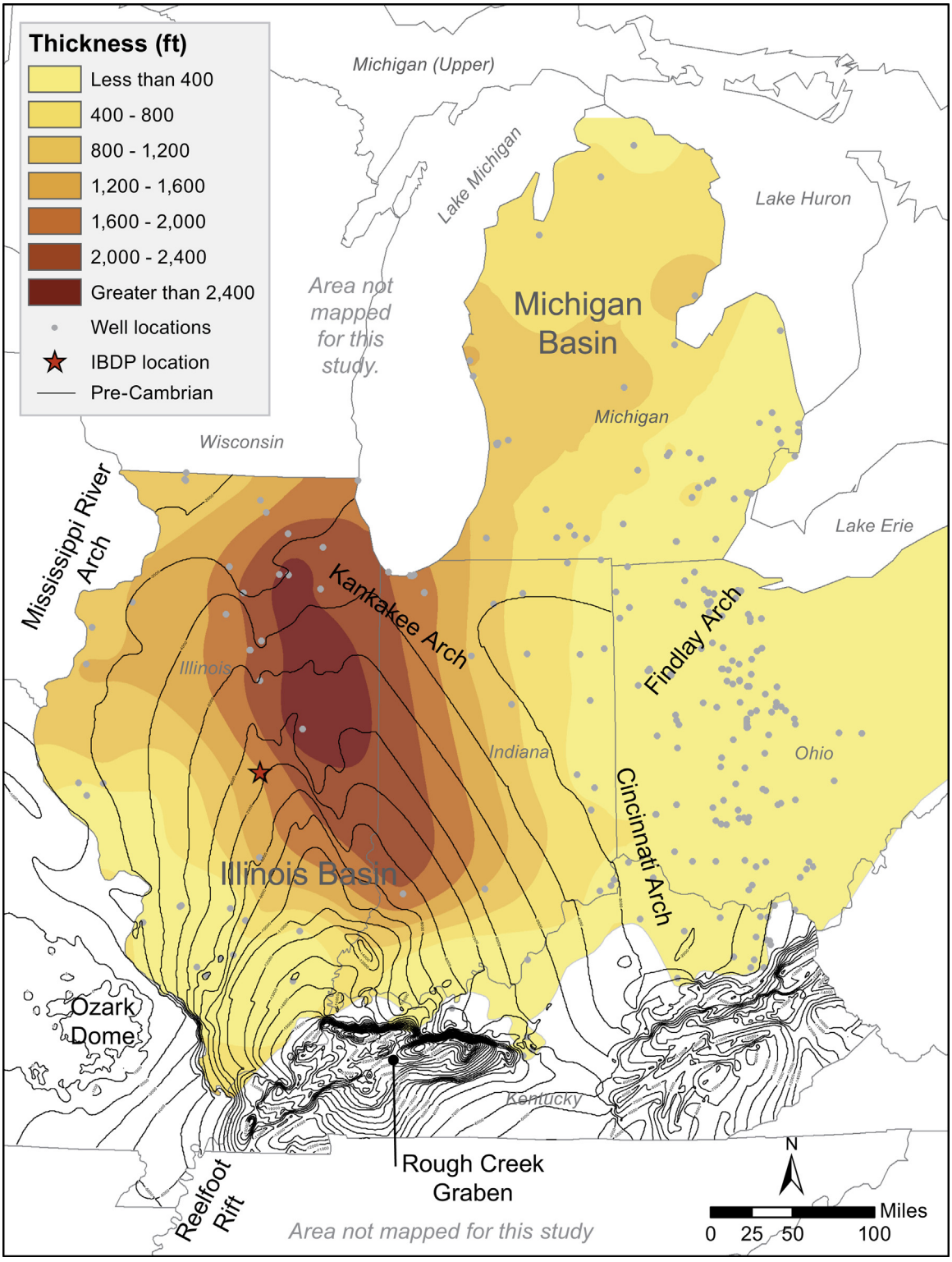

Fig. 1. Isopach map displaying Mt. Simon Sandstone and Argenta Formation thickness and distribution, Precambrian Basement topography, the location of the Illinois Basin–Decatur Project (IBDP), and locations of wells penetrating the Mt. Simon Sandstone.

Authigenic feldspar is abundant in the Upper Mt. Simon Unit E and Middle Mt. Simon Unit C with trace amounts in all other units, including the Argenta. In the Upper Mt. Simon Unit E, authigenic feldspar is most commonly found in arkosic sandstone beds beneath black shale beds, giving them a distinct pink color (Freiburg et al., 2014). The close spatial relationship between shale beds and abundant feldspar cements in the Upper Mt. Simon Unit E may support the idea that ions for authigenic feldspar cements originated in the shale beds and were expelled during compaction or pore-water-rock interaction (Freiburg et al., 2014). Petrographic evidence of authigenic feldspar forming both before and after quartz overgrowths (Duffin et al., 1989; Freiburg et al., 2014) implies that multiple episodes of cementation occurred during

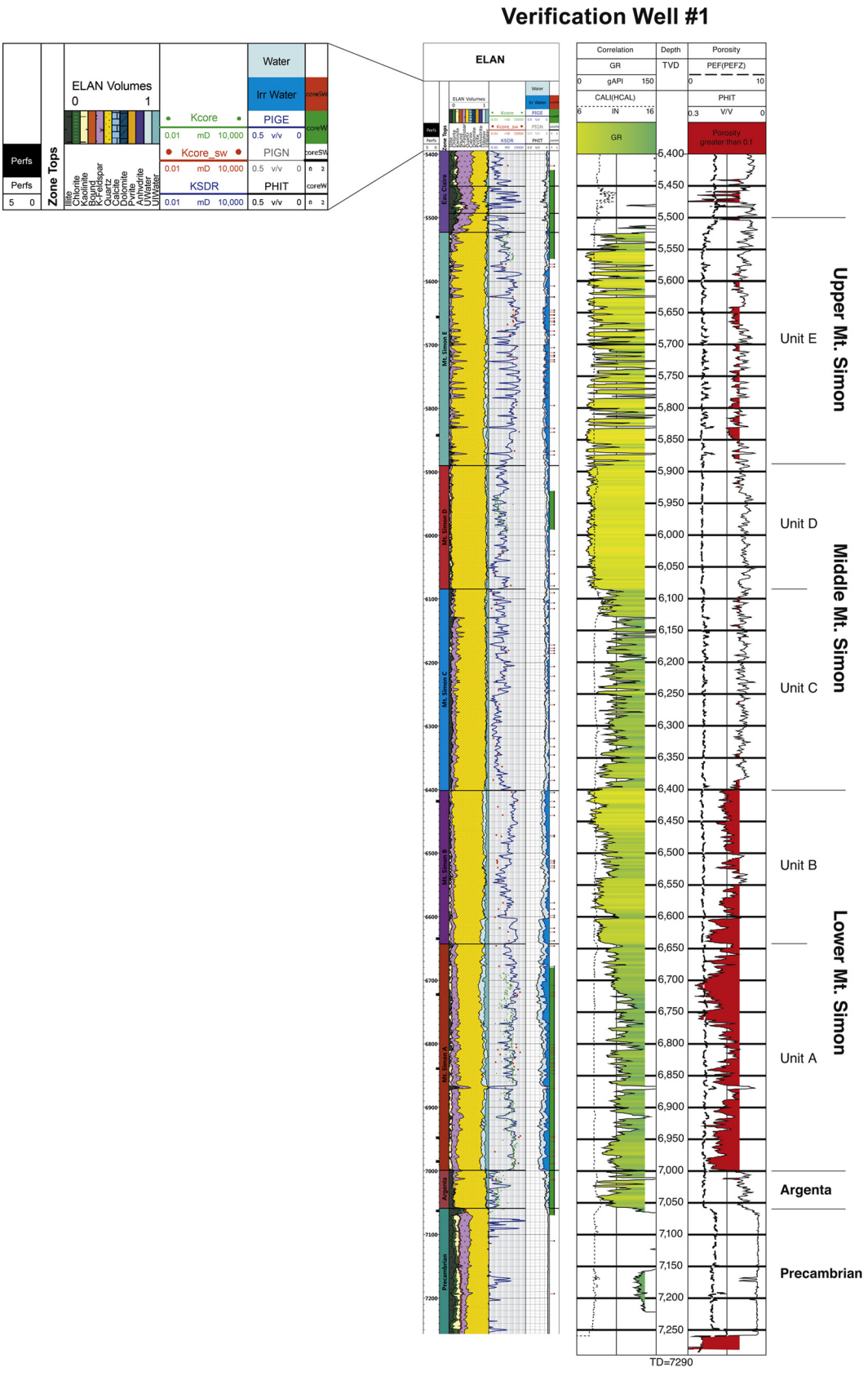

Fig. 2. Elemental analysis (ELAN) that includes permeability, gamma ray, and neutron-porosity logs through the Mt. Simon Sandstone and Argenta Formation from Verification Well #1 at the IBDP site. Whole core (green bar) and rotary sidewall core (tick marks) sample locations are located on the right side of the ELAN log. Units within the Upper, Middle, and Lower Mt. Simon Sandstone are labeled on the logs. (For interpretation of the references to colour in this figure legend, the reader is referred to the web version of this article.)

continued burial and compaction. It is also possible that different generations of feldspar cement originated from different sources.

2.5. Clay mineralogy and associations

Besides depositional facies rich in clay (i.e., mudstones and wackes), clays found in the Mt. Simon are thought to be of largely diagenetic origin (Freiburg et al., 2014). They form as grain coatings on detrital quartz and feldspar and as pore-filling cements. However, thin laminae of depositional clays associated with intertidal mud flats, eolian-playa adhesion ripples, and hiatal surfaces are common throughout the Mt. Simon. Authigenic clays appear most commonly near weathered feldspar grains and casts of dissolved feldspar grains, indicating that the feldspars may be one possible source of the authigenic clays (Bowen et al., 2011). The most common clays within the Mt. Simon are illite and mixed layered illite-smectite with small fractions of chlorite and kaolinite (Freiburg et al., 2014). The Lower Mt. Simon contains common friable sandstone intervals as a result of dominant clay cementation.

Iron oxides, primarily hematite and goethite, occur as grain coats, Liesegang bands, and as residues in stylolites within the Mt. Simon (Bowen et al., 2011; Freiburg et al., 2014), giving the Mt. Simon its red-maroon color. Most iron-oxide cements precipitated before other diagenetic alterations occurred (Fishman, 1997; Freiburg et al., 2014). In the Mt. Simon, high porosity values and small amounts of quartz cement were observed where illite (Freiburg et al., 2014) and low fractions of iron-oxide minerals (Bowen et al., 2011) form grain coatings.

To fully understand the intricate mechanisms that contribute to compaction and cementation porosity loss, quantification of these mechanisms is necessary in order to fully understand how reservoir quality develops. Houseknecht (1984) was the first paper to quantify the amount of porosity loss due to compaction and cementation, and subsequent research (Paxton et al., 2002) supports the conclusion that high porosity in reservoir rocks is achieved because of low volumes of cement and small to negligible amounts of pressure solution. As for the main cause of porosity loss, there is general agreement that compaction is the dominant mechanism (Lundegard, 1992; Makowitz and Milliken, 2003). Though there exists a large body of research on the chemical and physical conditions that occur during diagenesis and the resulting effect on reservoir quality, the role that changes in depositional facies play in determining reservoir quality is less studied.

3. Methods

Samples used in this research consist of whole core (4 in. [10 cm]) and rotary sidewall core (1 in. [2.5 cm]) samples from Verification Well #1 at the IBDP site (Fig. 2). Samples were collected from all five units of the Mt. Simon as well as the underlying Argenta.

Following Houseknecht (1987), variations in compaction and cementation have been quantified from modal analysis of thin sections in terms of intergranular volume while observing point-counting recommendations from Ehrenberg (1995). Cements (diagenetic and depositional matrix) were quantified by point-counting both plane polarizing light (PL) and cathodoluminescence (CL) thin section photomicrographs. Because of the difficulty in differentiating clay and hematite and the minute amounts of hematite identified in X-ray diffraction (XRD; Freiburg et al., 2014), hematite was included as a clay modal count. Each count consisted of 450 points per image, and CL was used in order to differentiate between detrital and authigenic quartz and feldspar. Plane polarizing light and CL photomicrographs were taken at 5× magnification. Using the Wentworth (1922) scale classification, median grain size was determined using measurements made on grains using point-counting methodologies. To deal with the complexities and problems associated with thin section grain-size measurements, the median grain size determined from the thin section measurements was compared to grain-size descriptions of the core sample in which each thin sections was made from. Macroporosity was quantified through thin section point-counting of PL photomicrographs and checked against whole core and rotary sidewall core helium (He) porosity analysis. Point-count-generated porosity values were always less than He-generated values because of errors associated with point-counting (Ehrenberg, 1995), inability to count microporosity tied up in the abundant intergranular clay, and the inherent differences between two-dimensional (2D) point-count analysis and three-dimensional (3D) He-porosity analysis. Ratios of monocrystalline to polycrystalline quartz were determined by point-counts of cross polarizing light (XP) photomicrographs for each sample.

The thin section modal point-count data was compared to elemental analysis (ELAN) log data (Fig. 2). The ELAN log reports quantitative formation evaluation based on log measurements of tools such as neutron porosity, gamma ray, and bulk density. The ELAN is processed every 0.5 ft (15 cm). Lithics are reported in point-count results. However, because of their compositions, they are reported among clay and feldspar values in the ELAN.

The thin section modal point-count data were used to establish amounts of porosity loss during diagenesis, using the formulas from Ehrenberg (1989), which are revisions of original equations from Houseknecht (1987). Because CL images of samples showed minimal intragranular fractures, and previous research had shown that individual grain crushing was not a factor in altering porosity in the Mt. Simon (Makowitz and Milliken, 2003), use of the modified porosity loss formulas from Makowitz and Milliken (2003) were deemed unnecessary. Porosity loss was calculated for each sample depth.

Compactional porosity loss (COPL) was calculated using the formula

$$COPL = P_i - \frac{(100 - P_i) \times IGV}{100 - IGV} \quad (1)$$

where P_i is an estimate of the initial, unconsolidated porosity, and IGV is the sum of the intergranular pore space of the rock sample, intergranular diagenetic cement (including quartz, feldspar, clay, and iron oxide), and matrix material (depositional clay), per total volume (Ehrenberg, 1989), and where $0 \leq \mathrm{COPL} \leq P_i$. Averages of input values can be found in Table 1. Cementation porosity loss (CEPL) was calculated using the formula

$$CEPL = (P_i - COPL) \times \frac{C}{IGV} \quad (2)$$

where C equals the volume of cement per total volume, with $0 \leq C \leq IGV$ and $0 \leq \mathrm{CEPL} \leq P_i$. The Index of Compaction (I_{comp}) is defined by Lundegard (1992) as

$$I_{comp} = COPL/(COPL + CEPL) \quad (3)$$

where $0 \leq I_{comp} \leq 1$. Compaction is the dominant mechanism behind porosity loss if I_{comp} is greater than 0.5, and cementation is the dominant mechanism if it is less than 0.5. Thus, this metric quantifies the relative amount of compaction vs. cementation that has occurred to the samples from the Mt. Simon, and it was used to compare the relative amount of cementation vs. compaction among samples and subunits of the Mt. Simon.

Because of the enormous variation of porosity in freshly deposited sands (Lundegard, 1992; Ehrenberg, 1995), P_i of the Mt. Simon and Argenta was determined using the Beard and Weyl (1973) thin section comparator of artificially mixed sand. Beard and Weyl (1973) have determined that grain size and sorting are

Table 1
Sample data and interpretations from thin section modal and lab analyses.

Averages	Unit E	Unit D	Unit C	Unit B	Unit A	Argenta
Samples (n)	30	20	17	21	81	11
COPL	13.71	18.84	14.33	25.29	21.32	21.21
CEPL	18.18	17.81	18.39	7.72	9.54	9.86
I_{comp}	0.43	0.51	0.43	0.76	0.69	0.66
Pi	36.46	38.18	35.08	37.13	36.84	33.05
IGV	25.83	23.26	24.13	15.72	19.51	14.55
Thin Section Porosity	5.79	1.88	2.61	5.48	7.51	2.36
Lab He porosity (%)	11.10	7.62	11.43	16.84	16.27	7.54
Total quartz (%)	82.15	91.72	85.11	80.87	65.99	82.73
Authigenic quartz (%)	11.38	15.97	6.23	3.08	3.25	4.54
Polycrystalline quartz (%)	n/a	1.25	13.24	1.98	8.93	15.07
Total Feldspar (%)	5.73	1.21	8.42	4.87	12.34	2.77
Authigenic Feldspar (%)	3.21	0.29	1.58	0.38	0.72	0.01
Lithics (%)	0.25	0.26	1.47	2.14	6.13	4.36
Clay (%)	6.08	4.93	6.62	6.79	8.02	7.64
Sorting Class	Moderate to well sorted	Well to moderately sorted	Moderate to poorly sorted	Well to moderately sorted	Well to moderately sorted	Moderate to poorly sorted
Grain Size Class	Medium lower to fine upper	Fine upper to lower medium	Medium lower to coarse lower	Fine upper to fine lower	Medium upper to fine upper	Fine upper to lower medium
Depositional Environment	Shallow Marine	Eolian	Fluvial	Eolian	Fluvial	Shallow Marine

the major controls on P_i of freshly deposited sands. They measured porosity using combinations of artificially mixed sand ranging from very fine to coarse grains with sorting from very poorly sorted to extremely well sorted. Mudstones and samples with detrital clay greater than 30% were excluded from the study presented here. The P_i values of wet-packed sand calculated by Beard and Weyl (1973) were used for the research presented here. It is important to note that if the estimated P_i is too high, COPL is overestimated, and if too low, COPL is underestimated. The CEPL will be affected the same way. Mold collapse of dissolved feldspars and intergranular pressure solution may also result in underestimation of COPL because of the reduction of total grain volume (Ehrenberg, 1995). Thus, the COPL may be a minimum value in well-sorted samples with an IGV value below 26% (Houseknecht, 1987; Ehrenberg, 1995). This situation is present in the vast majority of the Mt. Simon and Argenta intervals.

The grain size, initial porosity, cement, IGV, He porosity, and modal porosity were plotted (Fig. 3) as context to understand controls on porosity and input parameters in the calculation of COPL and CEPL. Therefore, they are reported as methods.

The mean grain size in Units B and C are lowest, and not significantly different (at the 0.05) level. The mean grain size is highest in Units C, A, and the Argenta, and the means in these units are not significantly different (Fig. 3A). The calculated P_i in the Argenta is distinctly lower than the units overlying it because of sorting (Fig. 3B). The mean P_i among Units A–E is not significantly different. The profiles of cement (Fig. 3C) and IGV (Fig. 3D) are quite similar. Both IGV and cement abundance are higher in Units C and above, and the means in these units are not significantly different (at the 0.05 level). Both IGV and cement abundance are lower in Unit B and below. The difference in the cementation index among Units B, A, and the Argenta is not statistically significan. The He-porosity measurements (Fig. 3E) and the modal porosity measurements (Fig. 3F) follow the same pattern with depth. The He-measured porosity is lowest in Unit D and the Argenta, and their means are not significantly different. The same is true for modal porosity in Units C, D, and the Argenta. Porosity by either measure generally decreases with depth from Unit E down to Unit D, then rises with depth and is highest in Units B and A (which are not statistically different), and lowers again in the Argenta.

4. Results

The profile of COPL with depth is somewhat complex (Fig. 4A). It is least in Units C, D, and E. The means for those units are not statistically different at the 0.05 level. The COPL is greatest in Units A, B, and the Argenta, and these means are not statistically different at the 0.05 level.

The CEPL with depth is less complicated (Fig. 4B). The mean CEPL is greatest in Units C–E, and the means in these units are not significantly different. The CEPL is least in Units A, B, and the Argenta, and the means are not statistically different from the Argenta. Thus, there is a marked change in CEPL between Units C–E and Units B, A, and the Argenta, with the decrease in CEPL appearing to start within the base of unit C, occurring rather abruptly right at the boundary.

The profile of I_{comp} is reversed from that of CEPL (Fig. 4C). It is lowest and less than 0.5 in Units C–E, and the means in these units are not statistically different. This indicates that porosity loss due to cementation is a larger factor than porosity loss due to compaction in Units C–E. The I_{comp} is highest and greater than 0.5 in Units A, B, and the Argenta, and the means in the units are not statistically different. As with CEPL, there is a marked change in I_{comp} between Units C–E, in which cementation loss dominates, and Units B, A, and the Argenta, in which compaction loss dominates. The increase in I_{comp} appears to start within the base of Unit C, occurring rather abruptly right at the boundary.

Because the mean I_{comp} for Units A, B, and the Argenta is not statistically different (Fig. 4C), they are reported together below and are further analyzed with respect to COPL and CEPL (Fig. 5A–C). The Argenta's average I_{comp} is 0.66 (Table 1), indicating that compaction is the dominant mechanism in destruction of reservoir porosity. Fig. 3A shows that only 3 samples had an I_{comp} below 0.5, indicating that compaction was the dominant mechanism is porosity loss in all but three samples. Two of those samples are located near the top of the Argenta unconformity within a residual facies dominated by clay buildup and thus slightly skewing the results for the Argenta. Without these two samples, the I_{comp} increases. For individual samples, Fig. 5A indicates that compaction has caused between 7%–33% porosity reduction while cementation has only resulted in a loss of porosity between 3%–19%. Thus, COPL values indicate that compaction is responsible for most of the porosity loss among the samples.

For samples from Unit A, the average I_{comp} = 0.69, indicating that compaction is the dominant mechanism contributing to porosity loss in the interval (Table 1). All but seven samples have an I_{comp} above 0.5, providing further evidence that compaction is the dominant mechanism for porosity loss (Fig. 5B). For individual samples, compaction has induced a loss of porosity within the interval, which ranges between 7%–33%, while cementation has produced a loss of porosity between 2%–24%. Thus, COPL is responsible for the most

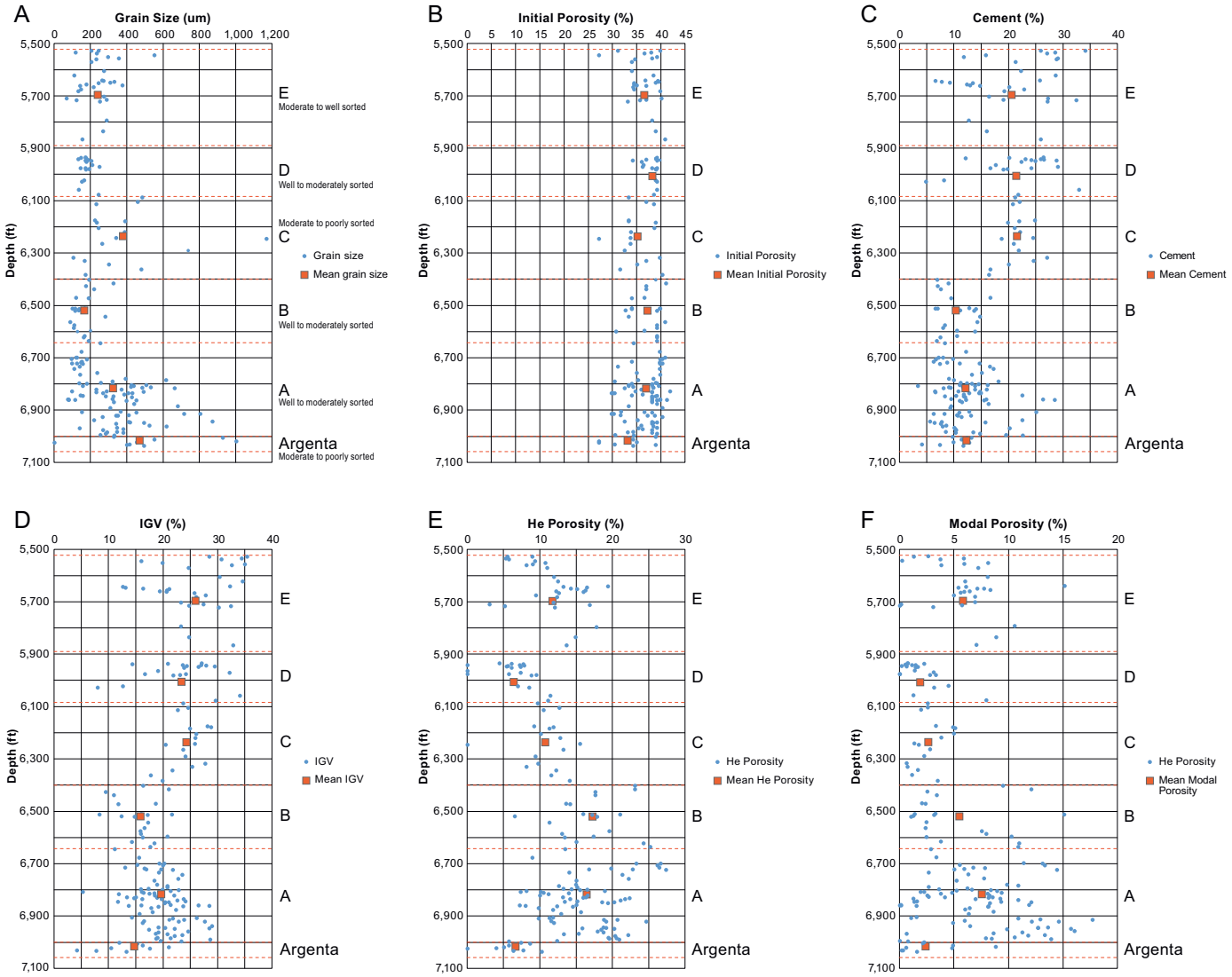

Fig. 3. Inputs of grain size (A), initial porosity (B), cement (C), IGV (D), He (helium) porosity (E), and modal porosity (F) vs. depth with an analysis of mean values (red box). (For interpretation of the references to colour in this figure legend, the reader is referred to the web version of this article.)

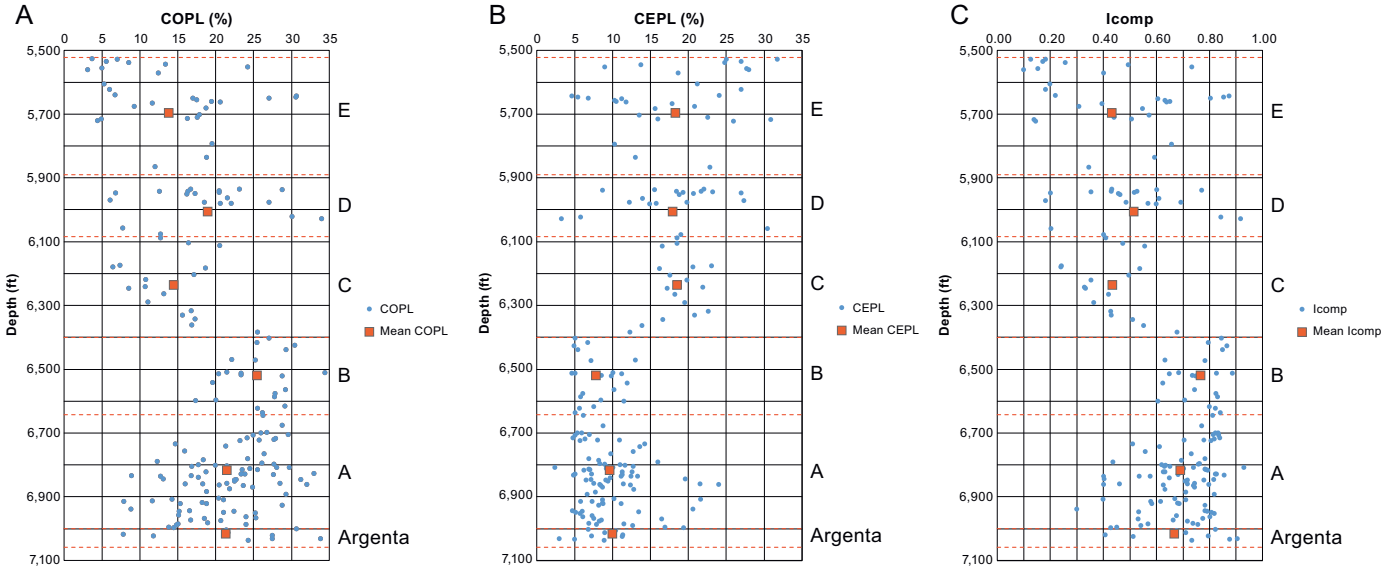

Fig. 4. Computed results of COPL (A), CEPL (B), and Icomp (C) vs. depth with analysis of mean values (red box). (For interpretation of the references to colour in this figure legend, the reader is referred to the web version of this article.)

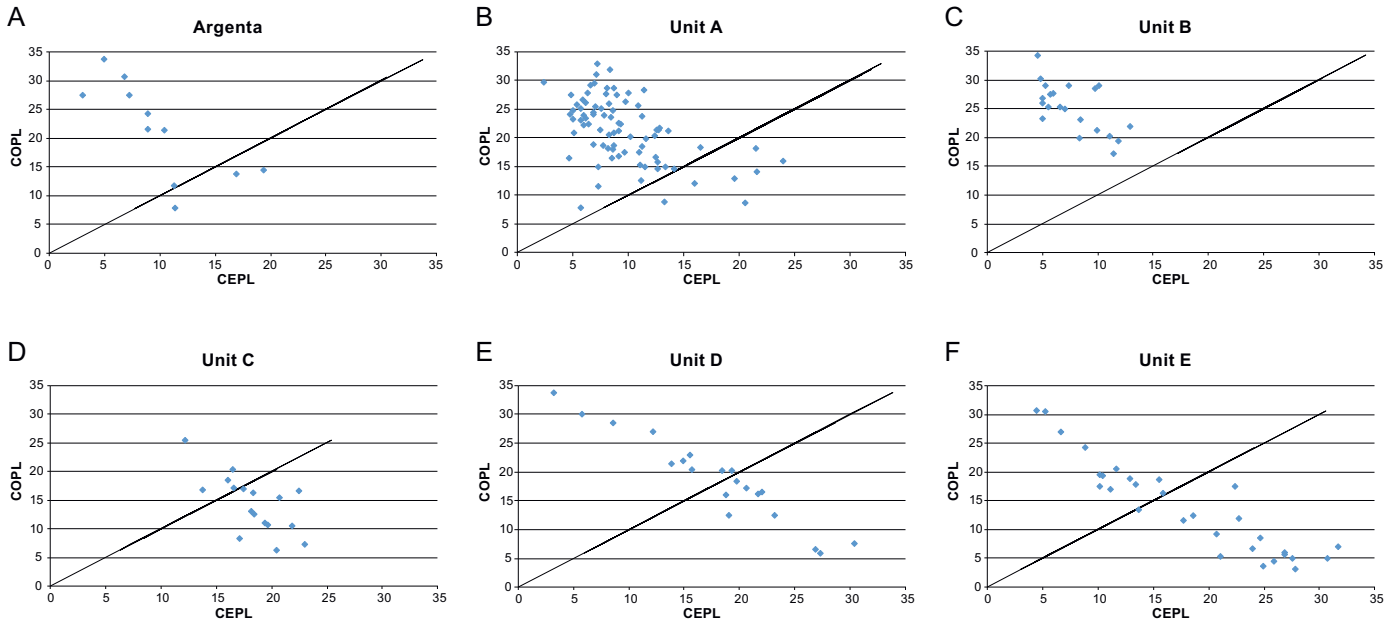

Fig. 5. Compaction porosity loss (COPL) and cementation porosity loss (CEPL) for the (A) Argenta Formation, (B) Mt. Simon Sandstone Unit A, (C) Unit B, (D) Unit C, (E) Unit D, and (F) Unit E.

porosity loss among the samples, with cementation having a significant effect on porosity loss on a much smaller subset of the samples.

Samples from Unit B have the highest average I_{comp} at 0.76, indicating that compaction is the dominant mechanism behind porosity loss in the interval (Table 1). All samples have an I_{comp} above 0.5, which indicates that compaction is the dominant mechanism for porosity loss (Fig. 5C). For individual samples, porosity loss due to compaction ranges between 17%–34% while porosity loss due to cementation in the samples has a much narrower range, between 4%–12%. Thus, compaction is responsible for the most of the reduction in porosity in this interval. The average P_i = 37.13%. The grain size averages between fine upper (177–250 μm) to fine lower (125–177 μm) and sorting averages between well to moderately sorted. The higher P_i value compared to Unit A is attributed to the finer grain size and better sorting of Unit B. The average IGV = 15.72%. The average thin section porosity is 5.48%.

Because the mean I_{comp} for Units C–E is not statistically different (Fig. 4C), they are reported together below and are separately analyzed (Fig. 5D–F). For samples from Unit C, the average I_{comp} = 0.43, indicating that porosity loss due to cementation is the dominant mechanism (Table 1). All but five samples have an I_{comp} below 0.5, identifying cementation as the dominant mechanism for porosity loss (Fig. 5D). Compaction induced porosity loss is between 6%–25%. The bulk of the samples indicate that cementation reduced porosity between 12%–23%. This is another indication that CEPL is responsible for the most porosity loss among the samples.

For samples from Unit D, the average I_{comp} = 0.51, indicating a nearly equal impact of compaction and cementation on porosity loss (Table 1). For individual samples, compaction has generated porosity loss between 5%–33% while cementation porosity loss ranges between 3%–30% (Fig. 5E).

For samples from Unit E, the average I_{comp} = 0.43, indicating that cementation is the dominant mechanism behind porosity loss (Table 1). For individual samples, compaction has generated porosity loss between 3%–30% while cementation porosity loss ranges between 4%–31% (Fig. 5F).

5. Discussion

When considering the diagenetic losses of porosity resulting from compaction and cementation through the stratigraphic section that includes the Upper, Middle, and Lower Mt. Simon and the Argenta Formation, there is a clear discontinuity across the contact between the Middle and the Lower Mt. Simon. The greatest porosity loss due to compaction occurs below this contact, in the deepest units, including the Lower Mt. Simon and the Argenta, as expected. The greatest porosity loss due to cementation occurs above this contact, in the Middle and the Upper Mt. Simon. Though the Lower Mt. Simon has more compaction loss of porosity relative to the overlying Middle and Upper sections of the Mt. Simon, it has a higher porosity. It has a higher porosity primarily because it has less porosity loss due to cementation relative to the overlying units. Furthermore, the Lower Mt. Simon appears to contain abundant secondary porosity that doesn't occur in the other sections of the Mt. Simon. The units overlying the Lower Mt. Simon contain abundant authigenic quartz and feldspar cement within their intergranular volume. There is relatively little of this authigenic quartz and feldspar cement in the Lower Mt. Simon, because diagenetic clay coatings on grains prevented nucleation of the cement, as discussed further below.

The porosity losses due to both compaction and cementation within the Lower Mt. Simon are similar to those of the underlying Argenta. The Lower Mt. Simon has a higher porosity than the Argenta because original porosity was higher in the Lower Mt. Simon, largely due to a better sorted grain fabric. Furthermore, the Argenta contains more pore-filling clays and lacks secondary porosity due to overall low feldspar content.

Thus, porosity loss by cementation is dominant above the contact between the Middle and Lower Mt. Simon, and porosity loss by compaction is dominant below the contact. The sections that follow elaborate more on the observed porosity loss by compaction and by cementation, and discuss how those observations support interpretations of the diagenesis and depositional history of the Mt. Simon and Argenta sections.

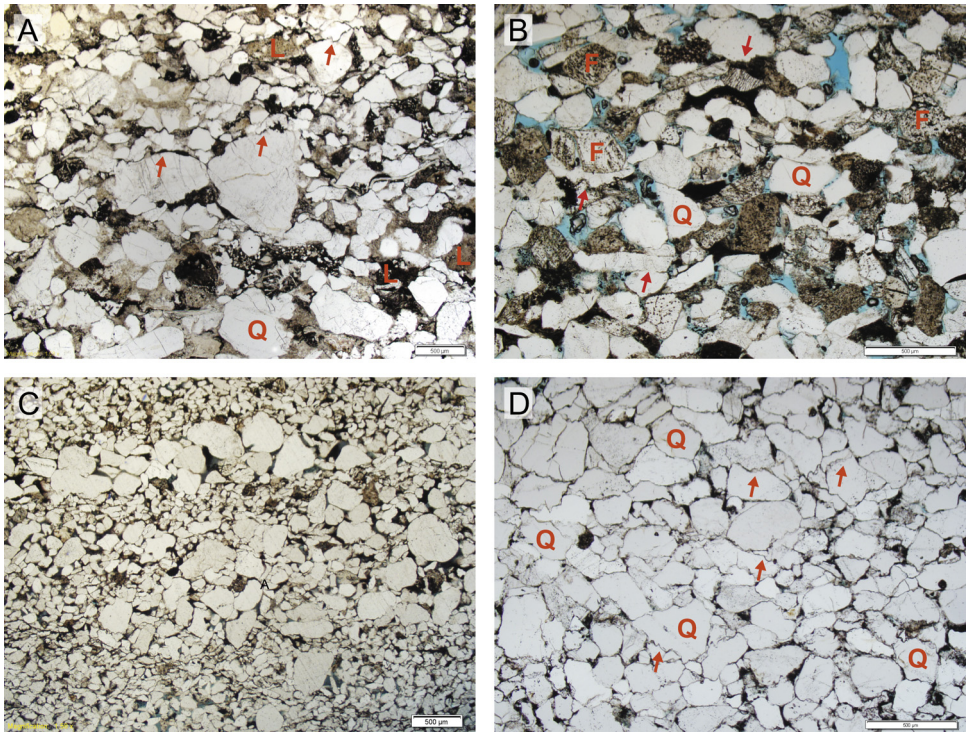

Fig. 6. Thin section photomicrographs illustrating COPL. Notice sutured grain boundaries (red arrows) and highly consolidated grains with labeled quartz (Q), feldspar (F), lithics (L), and porosity (blue). (A) Sample from the Argenta Formation at a depth of 7023.8 ft (2140.9 m). Notice abundant compacted detrital lithic and quartz grains; (B) Sample from the Lower Mt. Simon Unit A at a depth of 6928.4 ft (2111.8 m). Notice compaction with numerous elongated grains and sutured grain boundaries; (C) Sample from the Lower Mt. Simon Unit B at a depth of 6520 ft (1987 m). A well consolidated fine-grained sandstone with lenses of coarser grains; (D) Sample from the Middle Mt. Simon Unit D at a depth of 5943.7 ft (1811.6 m). Notice highly sutured quartz-grain boundaries. (For interpretation of the references to colour in this figure legend, the reader is referred to the web version of this article.)

5.1. Compaction

Compaction occurred to some extent within all units of the Mt. Simon and Argenta. Lower units, having larger overburdens, undergo more compaction than units higher up. This is common within many sandstone formations (Paxton et al., 2002). However, the wide range of porosities (log, laboratory, and thin sections) found throughout the Mt. Simon, and even within individual units (Fig. 2), indicates that nonuniform compaction occurred throughout the Mt. Simon. The presence of sutured grain contacts (Fig. 6) and deformation bands (Chentnik, 2012) throughout the Mt. Simon indicate that both chemical and mechanical compaction occurred. The extent of porosity loss due to mechanical compaction is dependent not only upon a formation's burial history (Lander and Walderhaug, 1999; Paxton et al., 2002), but also upon the size and shape of the grains (Pittman and Larese, 1991) and mineralogy. In the Argenta and Unit A, abundant lithic clasts (Table 1), which are prone to plastic deformation (Fig. 6A, B), contribute to the high degree of compaction. Mechanical compaction mechanisms, such as grain rotation and reorientation, are common throughout the Mt. Simon, especially in fine grained sandstones (Fig. 6C).

Grain size and pressure solution have been shown to have an inverse relationship; as grain size decreases, the amount of pressure solution increases (Heald, 1956; Houseknecht, 1984; Lander and Walderhaug, 1999). Additionally, previous research has observed that quartz-rich Mt. Simon sandstones are most likely to show evidence of pressure solution (Heald and Baker, 1977). This matches our observations that intervals with finer-grained sands, such as Units D and E, which are also the most quartz rich, have the highest volumes of cements (Fig. 7A, B) and show abundant suturing at grain contacts (Fig. 6D). The exception is Unit B that is comprised of fine-grained sediments but lacks cement.

5.2. Cementation

The greatest porosity loss due to cementation occurs in the Middle and Upper Mt. Simon. The cement responsible for this reduction in porosity is primarily authigenic quartz with minor authigenic feldspar. These cements are relatively lacking in the Lower Mt. Simon units and Argenta relative to the Middle and Upper Mt. Simon units. As suggested in the previous section, the high degree of chemical compaction may be a major contributor to the large volume of authigenic quartz observed in the Middle and Upper Mt. Simon units. However, to a lesser degree, sutured grain contacts throughout the Lower Mt. Simon Units A and B and Argenta indicate that pressure solution has occurred and may account for the minor authigenic quartz overgrowths observed.

It is also observed that areas of high clay volume cause higher CEPL in units, including the Argenta, A, and C (Fig. 7C). Although, the most common presence of clay in the Mt. Simon is in the form of clay coatings (Fig. 8A, B). The common presence of authigenic clay coatings and the lack of authigenic quartz cement in the Lower Mt. Simon suggests that cementation is most likely inhibited by clay coatings around quartz grains (Fig. 8A, B). Clay coatings have been shown to inhibit quartz overgrowths during burial (Heald and Larese, 1974; Surdam et al., 1989; Pittman et al., 1992; Bloch et al., 2002; Worden and Morad, 2003). The clays appear to have largely originated early, likely by means of infiltration; however, early alteration of feldspar to clay also appears likely (Fig. 8B). In addition, it is observed that clay coatings appear to pre-date feldspar dissolution as evidenced by common feldspar casts composed of illite (Fig. 8A, C). Early illite coatings are generally more laminar or sheet-like, suggesting an allogenic origin (Pittman et al., 1992) succeeded by a fibrous or hairy illite of likely authigenic origin (Fig. 8B). Samples missing the clay coatings (appear bleached in core) have

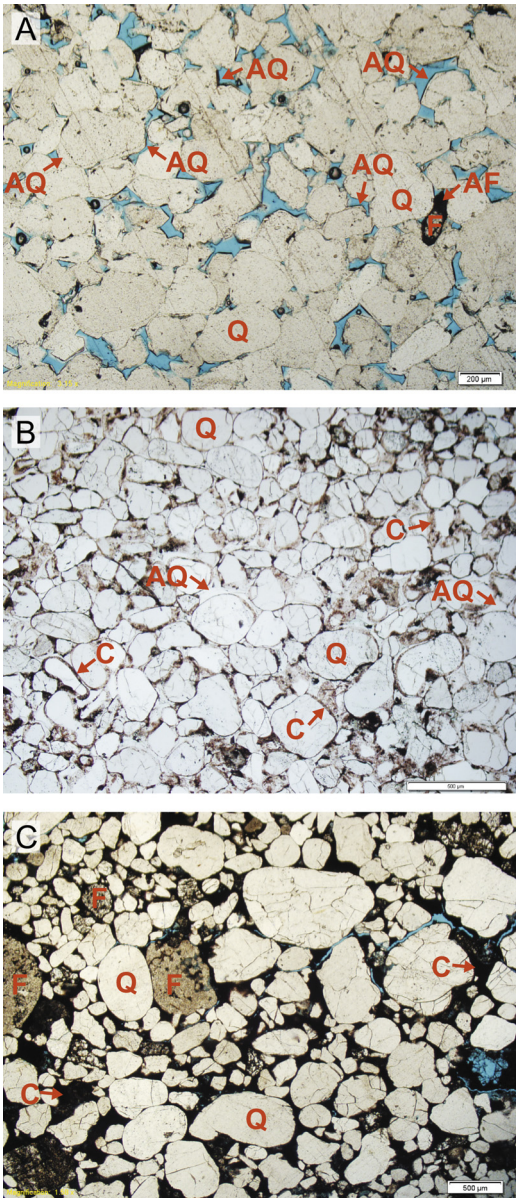

Fig. 7. Thin section photomicrographs illustrating CEPL with authigenic quartz overgrowths (AQ) on detrital quartz grains (Q), minor feldspar overgrowths (AF) on detrital feldspar grains (F), pore-filling clays (C), and porosity (blue). (A) Sample from the Upper Mt. Simon Unit E at a depth of 5684 ft. Notice the abundant authigenic quartz overgrowths and minor authigenic feldspar overgrowths. (B) Sample from the Middle Mt. Simon Unit D at a depth of 5947.2 ft. Notice the near to complete lack of pore space as a result of pore occluding authigenic quartz cement despite the miner clay coatings over quartz grains. (C) Sample from the Middle Mt. Simon Unit C at a depth of 6266 ft. Pore space is largely occluded by clay minerals. Porosity is more likely preserved in coarser-grained laminae compared to finer-grained laminae as a result of grain rotation and reorientation of finer grains. (For interpretation of the references to colour in this figure legend, the reader is referred to the web version of this article.)

lower porosity as shown in a detailed study of the Lower Mt. Simon by Ritzi et al. (2016).

5.3. Inferences on diagenetic history

Diagenetic differences between all the units of the Mt. Simon Sandstone and the Argenta Formation suggest complex paragenetic histories partly controlled by events of subaerial exposure and sediment burial. In the Lower Mt. Simon Units A and B, the majority of feldspar grains are partially to completely dissolved and altered to albite and clays, primarily illite, and mixed-layer illite/smectite (Fig. 8A, C; Freiburg et al., 2014). The sheer abundance of feldspar in the Lower Mt. Simon units, as well as the paragenetic relationship of early clay coatings followed by compaction, feldspar dissolution and alteration to clay, and later authigenic quartz cementation (Freiburg et al., 2014), suggests that the presence of early clay coatings is the most important reason for the preservation of primary porosity and secondly the later dissolution of feldspar generating abundant secondary porosity. The preservation of moldic porosity in clay casts of dissolved feldspars suggests feldspar dissolution largely occurred later in burial history when consolidation and compaction was largely complete (Fig. 8C). However, it should be mentioned that mold collapse may contribute to an underestimation of COPL, but this was not observed in the Lower Mt. Simon units. Hoholick et al. (1984) and Fishman (1997) reported that cement dissolution among detrital grain dissolution is a major contributor to secondary porosity. Dissolution of early cements such as gypsum, anhydrite (Mozley et al., 2016), and ferroan dolomite (Fishman, 1997) have been proposed. However, in the Lower Mt. Simon at the IBDP site, evidence for secondary porosity in the form of late-stage cement dissolution was not observed. The controls on later feldspar dissolution is poorly constrained. Labotka et al. (2015) found that the Mt. Simon brine geochemical and isotopic signature is distinct from other Illinois Basin brines and can't be explained by water-rock interaction suggesting that it has been influenced by an outside source. Narrowing the origins of the Mt. Simon brine may be key to constringing late feldspar dissolution.

It is unclear why early infiltration of clays in the form of grain coatings and late dissolution of feldspar occurred in the Lower Mt. Simon Units A and B and not the Middle Mt. Simon Units C and D, but there may be a relationship to an inferred unconformity separating the Lower and Middle Mt. Simon (Freiburg et al., 2014). An unconformity at the top of the Lower Mt. Simon Unit B may have allowed for increased infiltration of clay in the form of clay coatings. Minor clay coatings occur in the Middle Mt. Simon Units C and D but are commonly enclosed in with authigenic quartz and feldspar (Fig. 7B). It is possible that minor clay coatings in Unit C didn't coat the entire grains. Furthermore, feldspar dissolution is rare in Unit C compared to Units A and B. Unit E in the Upper Mt. Simon contains high authigenic cements like the Middle Mt. Simon Units C and D. These diagenetic differences indicate different paragenetic sequences between the Mt. Simon units.

The ELAN logs (Table 2; Fig. 2) suggest an increase of kaolinite in the Lower Mt. Simon Units A and B, which supports an unconformity on top of the Lower Mt. Simon. However, kaolinite above detection limits has not been identified in the Mt. Simon, but rather illite and mixed layered illite-smectite dominate (Freiburg et al., 2014). ELAN log values for quartz, feldspar, and bulk clay totals are relatively consistent with point count analysis and may be used as a reliable tool for mineral heterogeneity. However, ELAN results for clay mineralogy should be interpreted with caution.

Table 2
Argenta Formation and Mt. Simon Sandstone averages from ELAN and neutron-porosity logs (Fig. 2). Data is recorded every 0.5 ft (15 cm).

Averages (%)	Unit E	Unit D	Unit C	Unit B	Unit A	Argenta
Quartz	85.98	93.09	80.40	86.00	73.96	75.84
Feldspar	10.63	2.74	12.20	8.93	17.57	6.66
Clay Total	3.34	4.06	7.29	4.93	8.11	10.07
Chlorite	0.04	0	0	0.03	0.29	0
Illite	2.90	3.52	7.08	3.30	5.32	10.05
Kaolinite	0.40	0.54	0.21	1.61	2.50	0.02
Calcite/Dolomite	0	0	0	0.03	0.29	0
Pyrite	0.05	0.10	0.11	0.11	0.08	0.22
Porosity	10.15	8.21	9.09	15.08	17.65	8.89

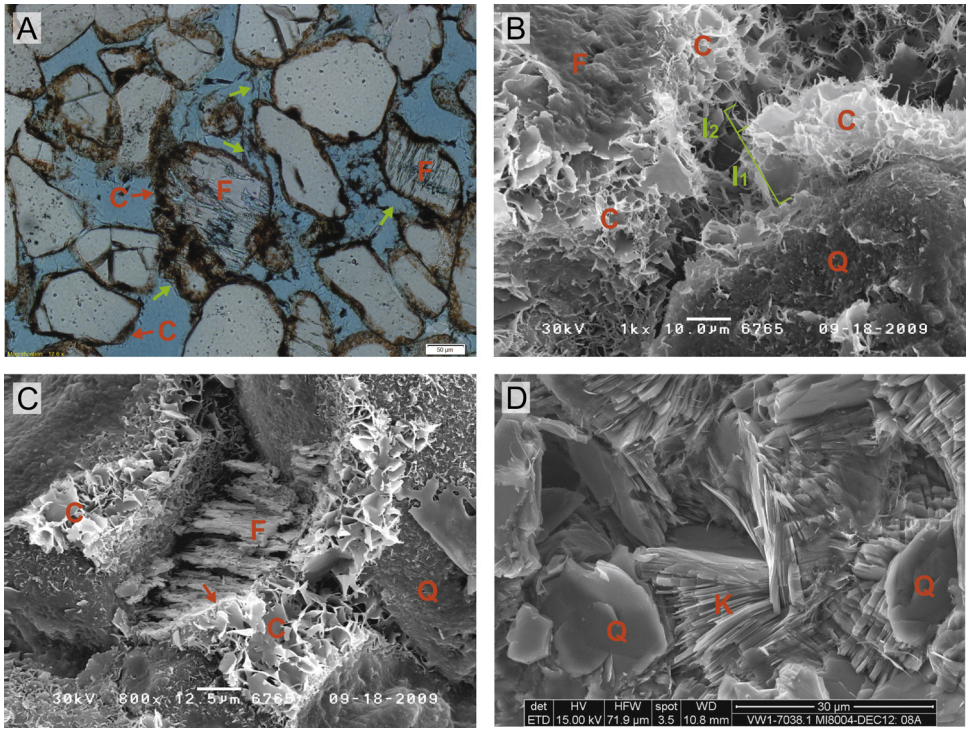

Fig. 8. (A) Thin section photomicrograph from the Lower Mt. Simon Unit A at a depth of 6765 ft (2062 m), showing common clay coatings on detrital quartz (Q) and feldspar grains (F). Notice partial dissolution and alteration of feldspar grains. Clay coating casts (green arrows) indicate feldspar grains that were completely dissolved out. (B) Scanning electron microscope (SEM) photograph of a sample from the Lower Mt. Simon Unit A at a depth of 6765 ft (2062 m), showing authigenic clay coatings (C) on detrital quartz (Q) and feldspar (F) grains. At least two different diagenetic clays are observed: (I1) an early grain-coating illite that is described as more laminar or sheet-like, and (I2) a later hairy illite growing on I1 illite. Feldspars appear to be altering to I1 illite. (C) Scanning electron microscope photograph of a sample from the Lower Mt. Simon Unit A at a depth of 6765 ft (2062 m), showing partial dissolved feldspar (F) altered to clay minerals (C). Arrow indicates clay cast of partially dissolved out feldspar grain. (D) Scanning electron microscope photograph of a sample from the Argenta Formation at a depth of 7038 ft (2145 m). Notice the abundant pore-filling kaolinite (K) among detrital quartz (Q) grains. (For interpretation of the references to colour in this figure legend, the reader is referred to the web version of this article.)

Kaolinite was observed in the Argenta (Fig. 8D; Freiburg et al., 2014). The discontinuities in clay mineralogy between the Argenta and Lower Mt. Simon units and the Lower and Middle Mt. Simon units may relate to differences in detrital mineralogy, such as the increased lithic content in the Lower compared to the Middle Mt. Simon. Lithics are largely composed of rhyolite and especially abundant in the Argenta (Freiburg et al., 2014). Water-mineral interaction in rocks abundant with iron- or magnesium-rich volcaniclastic fragments would produce different clay products than feldspar-rich rocks (Worden and Morad, 2003). Kaolinite forms under humid climatic conditions by the action of low-pH ground waters on detrital aluminosilicates (Emery et al., 1990). Plagioclase and albite tend to be more susceptible to kaolinitization than K-feldspar (Worden and Morad, 2003) and plagioclase is a common constituent of the rhyolitic basement directly underlying the Argenta (Freiburg et al., 2014; Labotka et al., 2015). A combination of increased subaerial exposure (unconformity) and humid conditions (increased meteoric recharge) would lead to increased amounts of kaolinite in the lithic-rich Argenta. This is demonstrated in a known unconformity within the Precambrian Basement in which increased kaolinite was observed (Freiburg et al., 2014).

5.4. Inferences on depositional history

The differences in sediment composition between the Lower Units A and B and Middle Units C and D is indicative of a change in sediment source, from a more proximal lithic-, feldspar-, and quartz-rich source to a more distal feldspar- and quartz-rich source. This aligns with the observations of increasing maturity and overall fining upwards throughout the Mt. Simon, indicating that the sediment source for the Middle and Upper Mt. Simon Units C–E was more distal and thus more mature than the source for the Lower Mt. Simon Units A and B (Lovell and Bowen, 2013). Overall compaction and cementation in the Mt. Simon and Argenta appear to be partially controlled by the observed changes in the lithology, which is ultimately caused by the depositional environment and the sediment source in relation to the location of the basin depositional center.

We propose that (1) the Lower Mt. Simon Units A and B and the underlying Argenta were deposited in a smaller catchment, the proto-Illinois Basin (Kolata and Nelson, 2010) or pre-Mt. Simon Basin (Freiburg et al., 2014); (2) the unconformity separating the Middle Units C and D and the Lower Units A and B marks the beginning of Illinois Basin subsidence; and (3) the Middle and Upper Mt. Simon Units C–E were later deposited in a slowly subsiding Illinois Basin. Considering the lithologies and immaturity of sediments of the Argenta and Lower Mt. Simon Units A and B, the proto-Illinois Basin likely had high relief and is postulated to be of failed-rift origin. The sediment source was likely more proximal, with nearby Precambrian highs as a major source. As the basin filled and relief lessened, the sediment source became more distal and thus more mature (finer grained, less feldspar and lithics, and less polycrystalline quartz). The Middle Mt. Simon Units C and D were deposited in a low-relief intracratonic sag structure (Illinois Basin) resulting in muddy, low-gradient braided river deposits in Unit C. In a perennially arid climate with a slowly subsiding basin, an eolian environment was pervasive, depositing the highly mature quartz arenites in Unit D. Rising sea level and the continued Illinois Basin subsidence resulted in the intertidal deposits of the Upper Mt. Simon Unit E. Similar to the proto-Illinois Basin sediments, Illinois Basin sediments become more mature upward until marine incursion in the Upper Mt. Simon Unit E.

6. Conclusion

Anomalously high porosity in the Lower Mt. Simon makes it favorable for CO_2 storage. This investigation examined the diagenetic characteristics of the entire Mt. Simon Sandstone (Upper, Middle, and Lower) and the underlying Argenta Formation, to identify the differences in those characteristics that explain the anomalously high porosity in the Lower Mt. Simon. The major conclusions of the investigation are as follows:

1.) Differential compaction occurs with depth through the stratigraphic section of the Upper Mt. Simon and Argenta Formation. The greatest porosity loss due to compaction occurs in the deepest units, including the Lower Mt. Simon and the Argenta, as expected. Though the Lower Mt. Simon units have more porosity loss due to compaction relative to the overlying Middle and Upper units of the Mt. Simon, they have a higher porosity. They have a higher porosity primarily because they has less porosity loss due to cementation relative to the overlying units. The porosity loss due to both compaction and cementation within the Lower Mt. Simon units is similar to that of the underlying Argenta. The Lower Mt. Simon has a higher porosity than the Argenta because its original porosity was higher, because of a better sorted grain fabric and abundant secondary porosity created by feldspar dissolution.
2.) The Lower Mt. Simon has less porosity loss due to cementation relative to the Middle and Upper Mt. Simon for the following main reason: the Lower Mt. Simon has abundant diagenetic clay coatings over detrital quartz grains, and the clay coatings inhibited authigenic quartz nucleation during later diagenesis. The origin of these early clays in the Lower Mt. Simon is unclear but there appears to be a relationship with an inferred unconformity separating the Lower and Middle Mt. Simon. The Middle and Upper Mt. Simon units lack the diagenetic clay coatings and as a result have an abundance of authigenic quartz cement occluding much of the original pore space. As the Mt. Simon experienced normal burial processes, sediments experienced compaction followed by cementation in the form of authigenic quartz and authigenic feldpspar. The abundant clay coatings in the Lower Mt. Simon inhibited cements while the Middle and Upper Mt. Simon experienced porosity loss by cementation. Later in burial, post-compaction, feldspars experienced dissolution, which further increased porosity in the form of secondary moldic porosity. Determining secondary porosity in the Mt. Simon is complicated by the abundant pore-bridging illite and should be further investigated along with understanding the origin of clays.
3.) Based on mineralogical, diagenetic, and depositional heterogeneities, it is proposed that the deposits composing the Lower Mt. Simon and Argenta Formation are associated with a failed rift basin referred to as the Proto-Illinois Basin, with a depocenter located in northeast-central Illinois. The Middle and Upper Mt. Simon reflect deposition in a slowly evolving Illinois Basin during the Sauk Transgression. Further studies of unit correlation, detrital source, and diagenesis are being completed to test this idea.

Acknowledgments

The authors would like to thank two anonymous reviewers along with Donna Willette, Hannes Leetaru, Sallie Greenberg, Daniel Byers, Daniel Klen, and Damon Garner for thoughtful comments and discussion.

Partial support (specifically calculations pertaining to COPL and CEPL) was provided as part of the Center for Geologic Storage of CO_2, an Energy Frontier Research Center funded by the U.S. Department of Energy, Office of Science, Basic Energy Sciences under Award # DE-SC0C12504. Petrographic analyses was supported by the Midwest Geological Sequestration Consortium (MGSC) which is funded by the U.S. Department of Energy through the National Energy Technology Laboratory (NETL) via the Regional Carbon Sequestration Partnership Program (contract number DE-FC26-05NT42588) and by a cost share agreement with the Illinois Department of Commerce and Economic Opportunity, Office of Coal Development through the Illinois Clean Coal Institute.

References

Beard, D.C., Weyl, P.K., 1973. Influence of texture on porosity and permeability of unconsolidated sand. AAPG Bull. 57, 349–369.
Bloch, S., Lander, R.H., Bonell, L., 2002. Anomalously high porosity and permeability in deeply buried sandstone reservoirs: origin and predictability. AAPG Bull. 86 (2), 301–328.
Bowen, B.B., Ochoa, R.I., Wilkens, N.D., Brophy, J., Lovell, T.R., Fischietto, N., Medina, C.R., Rupp, J.A., 2011. Depositional and diagenetic variability within the Cambrian Mount Simon Sandstone: implications for carbon dioxide sequestration. Environ. Geosci. 18, 69–89.
Chentnik, B.M., 2012. Characterizing fractures and deformation bands: implications for long-term CO_2 storage within the Cambrian Mount Simon Sandstone. J. Purdue Undergrad. Res. 2, 8–15.
Collinson, C., Sargent, M.L., Jennings, J.R., 1988. Illinois Basin region. In: Sloss, L.L. (Ed.), Sedimentary Cover—North American Craton: U.S., vol. D-2. Geological Society of America, The Geology of North America, Boulder, Colorado, pp. 383–426.
Driese, S.G., Byers, C.W., Dott Jr, R.H., 1981. Tidal deposition in the basal upper cambrian Mt. Simon formation in Wisconsin. J. Sediment. Res. 51, 0367–0381.
Duffin, M.E., Lee, M., deVries Klein, G., Hay, R.L., 1989. Potassic diagenesis of Cambrian sandstones and precambrian granitic basement in UPH-3 deep hole, Upper Mississippi Valley, U.S.A. J. Sediment. Petrol. 59, 848–861.
Ehrenberg, S.N., 1989. Assessing the relative importance of compaction processes and cementation to reduction of porosity in sandstones: discussion; compaction and porosity evolution of Pliocene sandstones, Ventura Basin, California: discussion. AAPG Bull. 73 (10), 1274–1276.
Ehrenberg, S.N., 1995. Measuring sandstone compaction from modal analysis of thin sections: how to do it and what the results mean. J. Sediment. Res. A65 (2), 369–379.
Emery, D., Myers, R.J., Young, R., 1990. Ancient subaerial exposure and freshwater leaching in sandstones. Geology 18, 1178–1181.
Fischietto, N.E., 2009. Lithofacies and Depositional Environments of the Cambrian Mount Simon Sandstone in the Northern Illinois Basin: Implications for CO_2 Sequestration. Master's Thesis. Purdue University, West Lafayette, Indiana, 114 p.
Fishman, N.S., 1997. Basinwide fluid movement in a Cambrian paleoaquifer: evidence from the Mt. Simon Sandstone, Illinois and Indiana. In: Montañez, I.P., Gregg, J.M., Shelton, K.L. (Eds.), Basinwide Diagenetic Patterns: Integrated Petrologic, Geochemical, and Hydrologic Considerations, vol. 57. Society for Sedimentary Geology (SEPM), Special Publication, pp. 221–234.
Freiburg, J.T., Morse, D.G., Leetaru, H.E., Hoss, R.P., Yan, Q., 2014. A Depositional and Diagenetic Characterization of the Mt. Simon Sandstone at the Illinois Basin–Decatur Project Carbon Capture and Storage Site, Decatur, Illinois, USA. Illinois State Geological Survey (Circular 583, 59 p. and 3 digital appendices).
Freiburg, J.T., Leetaru, H.E., Monson, C.C., 2015. The argenta formation: a newly recognized Cambrian stratigraphic unit in the Illinois Basin. Geol. Soc. Am. Abstr. Progr. 47 (5), 86.
Hagadorn, J.W., Dott, R.H., Damrow, D., 2002. Stranded on a late Cambrian shoreline: medusae from central Wisconsin. Geology 30 (2), 147–150.
Heald, M.T., Baker, G.F., 1977. Diagenesis of the Mt. Simon and rose run sandstones in western West Virginia and southern Ohio. J. Sediment. Res. 47 (1), 66–77.
Heald, M.T., Larese, R.E., 1974. Influence of coatings on quartz cementation. J. Sediment. Petrol. 44, 1269–1274.
Heald, M.T., 1956. Cementation of Simpson and St. Peter Sandstones in parts of Oklahoma, Arkansas, and Missouri. J. Geol. 64, 16–30.
Hoholick, J.D., Metarko, T., Potter, P.E., 1984. Regional variations of porosity and cement: St. Peter and Mount Simon Sandstones in Illinois Basin. AAPG Bull. 68 (6), 753–764.
Houseknecht, D.W., 1984. Influence of grain size and temperature on intergranular pressure solution, quartz cementation, and porosity in quartzose sandstone. J. Sediment. Petrol. 54, 348–361.
Houseknecht, D.W., 1987. Assessing the relative importance of compaction processes and cementation to reduction of porosity in sandstones. AAPG Bull. 71 (6), 633–642.
Kolata, D.R., Nelson, J.W., 1990. Tectonic history of the Illinois Basin. In: Leighton, M.W., Kolata, D.R., Oltz, D.F., Eidel, J.J. (Eds.), Interior Cratonic Basins, vol. 51. AAPG, Memoir, pp. 263–285.
Kolata, D.R., Nelson, J.W., 2010. Tectonic history. In: Kolata, D.R., Nimz, C.K. (Eds.), The Geology of Illinois. Illinois State Geological Survey, pp. 77–89.

Labotka, D.M., Panno, S.V., Locke, R.A., Freiburg, J.T., 2015. Isotopic and geochemical characterization of fossil brines of the Cambrian Mt. Simon Sandstone and Ironton-Galesville formation from the Illinois Basin, USA. Geochem. Cosmochim. Acta 165, 342–360.
Lander, R.H., Walderhaug, O., 1999. Predicting porosity through simulating sandstone compaction and quartz cementation. AAPG Bull. 83 (3), 433–449.
Lovell, T.R., Bowen, B.B., 2013. Fluctuations in sedimentary provenance of the Upper Cambrian Mount Simon Sandstone, Illinois Basin, United States. J. Geol. 121 (2), 129–154.
Lundegard, P.D., 1992. Sandstone porosity loss—a big picture view of the importance of compaction. J. Sediment. Petrol. 62 (2), 250–260.
Makowitz, A., Milliken, K.L., 2003. Quantification of brittle deformation in burial compaction, Frio and Mount Simon formation sandstones. J. Sediment. Res. 73 (6), 1007–1021.
Medina, C.R., Rupp, J.A., Barnes, D.A., 2011. Effects of reduction in porosity and permeability with depth on storage capacity and injectivity in deep saline aquifers: a case study from the Mt. Simon Sandstone aquifer. Int. J. Greenh. Gas Control 5 (1), 146–156.
Mozley, P.S., Heath, J.E., Dewers, T.A., Bauer, S.J., 2016. Origin of heterogeneity of pore sizes in the Mount Simon Sandstone and Eau Claire formation: implications for multiphase fluid flow. Geosphere 12 (4), 1341–1361.
Paxton, S.T., Szabo, J.O., Ajdukiewicz, J.M., Klimentidis, R.E., 2002. Construction of an intergranular volume compaction curve for evaluating and predicting compaction and porosity loss in rigid-grain sandstone reservoirs. AAPG Bull. 86 (12), 2047–2067.
Pittman, E.D., Larese, R.E., 1991. Compaction of lithic sands: experimental results and applications (1). AAPG Bull. 75 (8), 1279–1299.
Pittman, E.D., Larese, R.E., Heald, M.T., 1992. Clay Coats: Occurrence and Relevance to Preservation of Porosity in Sandstones. Society for Sedimentary Geology, pp. 242–255 (Special Publication No. 47).
Pollington, A.D., Kozdon, R., Valley, J.W., 2011. Evolution of quartz cementation in the Illinois Basin during burial of the Mt. Simon Sandstone: in situ microanalysis of $\delta^{18}O$. Geology 39, 1119–1122.
Ritzi, R.W., Freiburg, J.T., Webb, N.D., 2016. Understanding the (co) variance in petrophysical properties of CO_2 reservoirs comprising sedimentary architecture. Int. J. Greenh. Gas Control 51, 423–434.
Surdam, R.C., Dunn, T.L., MacGowan, D.B., Heasler, H.P., 1989. Conceptual models for the prediction of porosity evolution with an example from the Frontier Sandstone, Bighorn Basin, Wyoming. In: Coalson, E.B., Kaplan, S.S., Keighin, C.W., Oglesby, L.A., Robinson, J.W. (Eds.), Sandstone Reservoirs. Rocky Mountain Association of Geologists, pp. 7–21.
Wentworth, C.K., 1922. A scale of grade and class terms for clastic sediments. J. Geol. 30, 377–392.
Worden, R.H., Morad, S., 2003. Clay minerals in sandstones: controls on formation, distribution, and evolution. In: Worden, R.H., Morad, S. (Eds.), Clay Minerals in Sandstones. Blackwell Science, International Association of Sedimentologists, Oxford, UK, pp. 3–41 (Special Publication 34).

Chapter v Manuscript

The timing of illitization in Paleozoic strata at the Illinois Basin – Decatur Project: Implications for carbon dioxide storage

Illinois Basin – Decatur Project Report
Geology Report

The timing of Illitization in Paleozoic Strata at the Illinois Basin – Decatur Project: Implications for Carbon Dioxide Storage

Jared T. Freiburg,[1,2] Georg H. Grathoff,[2] Keven Henkel,[2] and Klaus Wemmer[3]

[1]*Illinois State Geological Survey, Prairie Research Institute, University of Illinois at Urbana-Champaign, 615 E. Peabody Dr., Champaign, IL 61820, USA*
[2]*Department of Geography and Geology, University of Greifswald, Greifswald, 17489, Germany*
[3]*Geoscience Center, University of Göttingen, Göttingen, Germany*

Summarize

The clay mineral illite is a common and abundant component in Paleozoic rocks of the Illinois Basin. Illite forms three polytypes: $2M_1$ of detrital origin, and $1M_d$ and 1M of diagenetic origin. Diagenetic illite forms as a cement in sandstones and as a replacement for smectite in shales. Illite polytype quantification combined with potassium (K)–argon (Ar) dating allowed extrapolation to apparent detrital and diagenetic illite dates. On the basis of these age data, diagenetic illite records a complex history of diagenesis, tectonics, and fluid migration in the Illinois Basin, as shown in distinct units of the Cambrian-age Mt. Simon Sandstone and overlying major shale formations, including the Cambrian-age Eau Claire Formation, the Ordovician-age Maquoketa Formation, and the Devonian-age New Albany Shale.

Introduction

Understanding the nature, origin, and age of illite helps researchers deduce the evolution of sedimentary basins and the depositional and diagenetic history of the sediments within. Here, we investigate the timing of diagenetic illite precipitation in the Cambrian-age Mt. Simon Sandstone to evaluate the history of diagenesis and the overall controls on reservoir properties. Overlying major shale units are included in the investigation as comparative units subjected to basin diagenesis and to provide context regarding the integrity of a reservoir-seal system.

The Cambrian-age Mt. Simon Sandstone is a laterally extensive deposit throughout the U.S. Midwest (Figure 1) and is the basal-most sedimentary rock in the Illinois Basin (Figure 2). It has long been the focus of industrial development, including natural gas storage and, more recently, carbon dioxide (CO_2) storage in an attempt to slow the release of anthropogenic CO_2 into the atmosphere. The Illinois Basin – Decatur Project (IBDP) has been the focus of much research on the Mt. Simon, and injection into and storage of CO_2 in the lowermost section of the Mt. Simon is ongoing. The Mt. Simon can be divided into three major sections on the basis of its depositional characteristics and petrophysical properties: the upper, middle, and lower (Figure 3). Additionally, a sandstone discovered at the IBDP that underlies the Mt. Simon and overlies the Precambrian basement has been named the Argenta (Freiburg et al. 2016). The primary seal for containment of CO_2 in the Mt. Simon is the Cambrian-age Eau Claire Formation, which directly overlies the upper Mt. Simon (Figure 2). The Ordovician-age Maquoketa Formation and the Devonian-age New Albany Shale are overlying shale units that are considered secondary sealing units (Figure 2).

In this report, the depositional history and reservoir properties of the Mt. Simon are summarized, and the origin of illite in the Mt. Simon is investigated. Illitization of the Argenta, Eau Claire, and Maquoketa Formations and the New Albany Shale are analyzed for comparison with the Mt. Simon to better understand the diagenetic history and major regional controls on the diagenesis observed in key formations important to the IBDP reservoir and seal system and, more broadly, the Illinois Basin geologic history.

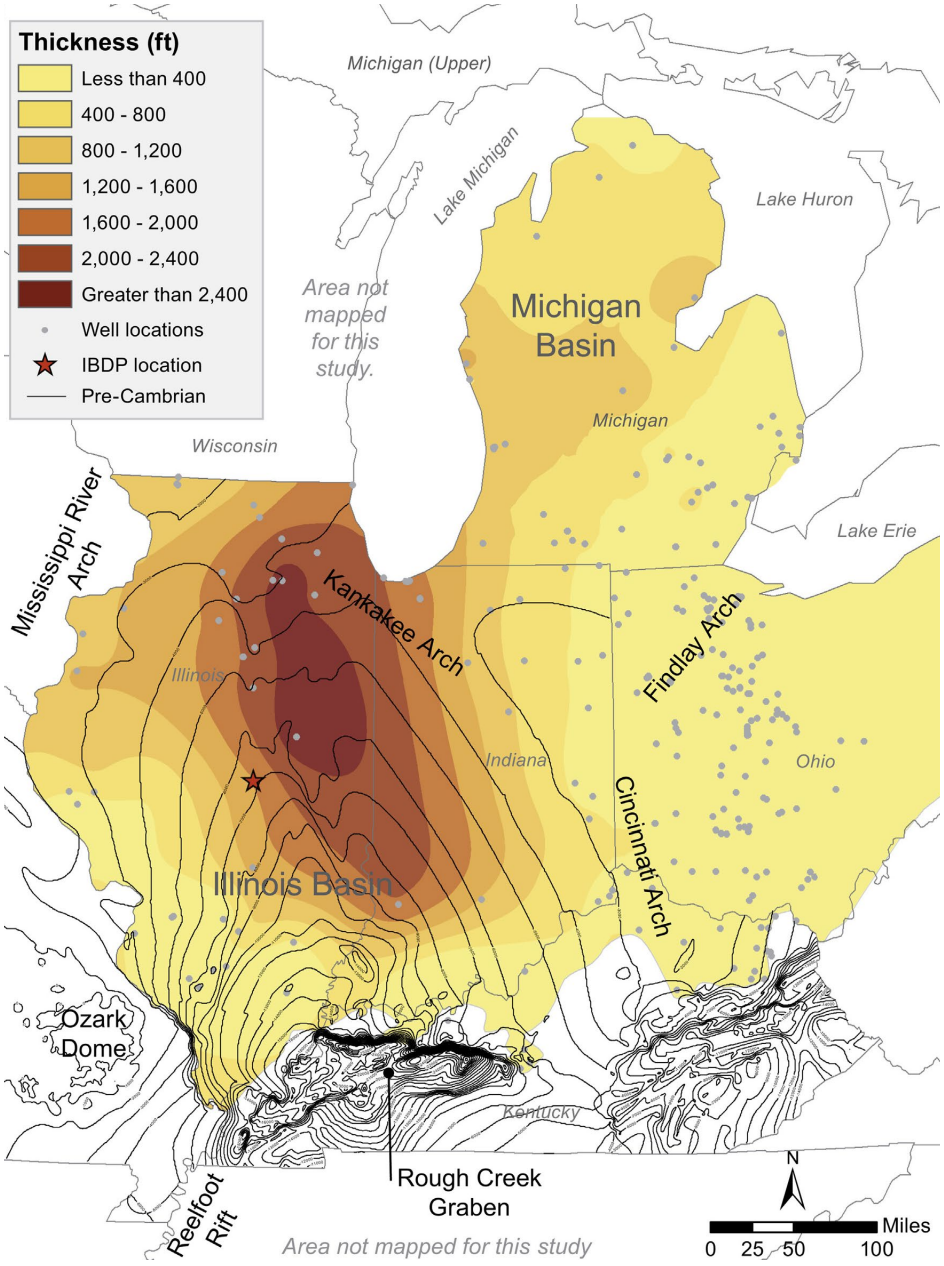

Figure 1. Thickness of the Mt. Simon Sandstone. Note that the Mt. Simon depocenter is north of the Illinois Basin, which follows the Precambrian topography (black contours) to the south. The location of the Illinois Basin – Decatur Project is marked by a red star. Modified from Freiburg et al. (2014). © University of Illinois Board of Trustees. Used with permission of the Illinois State Geological Survey.

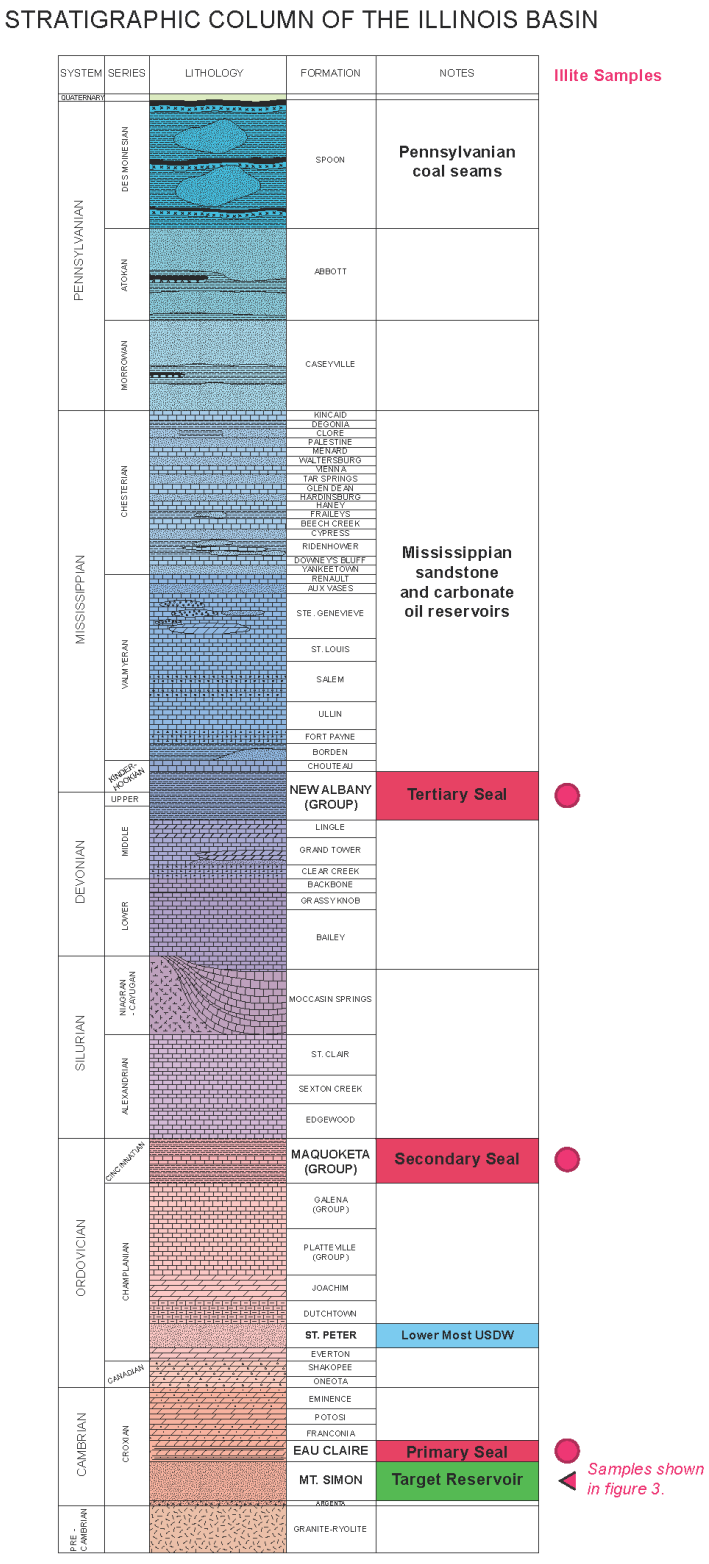

Figure 2. Generalized stratigraphic column in the Illinois Basin with the Mt. Simon shown as the target reservoir; the Eau Claire Formation, Maquoketa Formation, and New Albany Shale as sealing formations; and the St. Peter Sandstone as the lowest regional source for drinking water. Samples analyzed for illite in this study include the New Albany shale, Maquoketa shale, Eau Claire shale facies, and Mt. Simon sandstone.

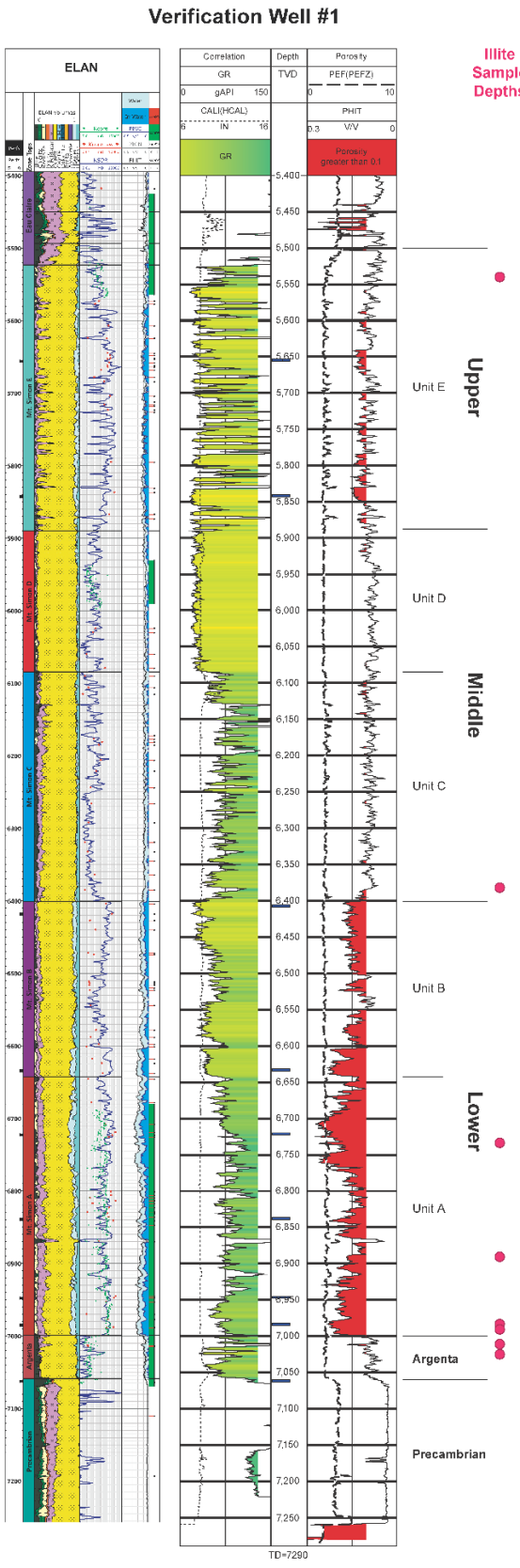

Figure 3. Representative geophysical logs through the Mt. Simon Sandstone and Argenta formation at the Illinois Basin – Decatur Project. Red on the neutron log represents porosity >10%. Samples for illite analysis were retrieved from 4-in. (10-cm) core in each major unit. Modified from Freiburg, J.T., R.W. Ritzi, and K.S. Kehoe, 2016, Depositional and diagenetic controls on anomalously high porosity within a deeply buried CO_2 storage reservoir—The Cambrian Mt. Simon Sandstone, Illinois Basin, USA: International Journal of Greenhouse Gas Control, v. 55, p. 42–54. Copyright © 2016 with permission from Elsevier.

Geological Background

The IBDP in east-central Illinois is located in the north-central section of the Illinois Basin in the midcontinental region of the United States (Figure 1). The Illinois Basin is a spoon-shaped structure predominantly filled with Paleozoic sedimentary rock ranging from the early or middle Cambrian to very early Permian (Collinson et al. 1988). This sedimentary rock unconformably overlies Precambrian basement rocks (Bickford et al. 1986) composed of granite or rhyolite of the Eastern Granite Rhyolite Province. Most Paleozoic sequences in the Illinois Basin thicken southward toward the region of the New Madrid Rift System (i.e., Reelfoot Rift and Rough Creek Graben in southern Illinois), suggesting that the processes operating there were linked to overall Illinois Basin subsidence (Kolata 2010). However, the Mt. Simon Sandstone and the underlying Argenta unit are thickest in northeastern Illinois and in east-central Illinois (Leetaru and McBride 2009; Figure 1), suggesting rifting extended into north-central Illinois (Figure 4).

Today, the Illinois Basin extends across central Illinois, southwestern Indiana, and western Kentucky and is, in part, coextensive with the rift system. The Illinois Basin is thought to have formed during the late Precambrian to early Cambrian time as the rift formed during the breakup of the supercontinent Rodinia (Braile et al. 1986; Kolata and Nelson 1990, 1997, 2010). However, Kolata and Nelson (2010) proposed that before the Illinois Basin was formed, a similar large depression (referred to as the proto-Illinois Basin) developed in the same general area (east-central Illinois and west-central Indiana) sometime between 1.48 billion years ago (Ga) and 500 million years ago (Ma). The axis of this proto-Illinois Basin and the thickness of the Argenta and Mt. Simon follow the general strike of the La Salle Anticlinorium. The La Salle appears to extend south into the Wabash Fault, both of which appear to be possible rift arms of the New Madrid (Figure 4). Rifting along the La Salle during the breakup of the supercontinent Rodinia led to significant accommodation space and an opening for incursion of the Neoproterozoic and early Cambrian Iapetus Ocean. Proximally sourced sediments of the Argenta and lower Mt. Simon largely filled in this accommodation space (Freiburg et al. 2020). Rift activity was largely dormant during deposition of the lower Mt. Simon, and by middle Mt. Simon deposition, the tectonic setting had changed from a rift basin to a broad embayment centered over but extending far beyond the rift (McBride and Kolata 1999). Marine incursion during the Sauk Sequence followed, with the upper Mt. Simon deposition. This varying environmental setting was a major control on the detrital source, maturity, and mineralogy (Lovell and Bowen 2013; Freiburg et al. 2016, 2020).

Previous research has examined the diagenesis of the Mt. Simon Sandstone in the Illinois Basin and the ages of respective events. Hoholick et al. (1984) identified the major cements in the Mt. Simon as quartz and potassium (K)-feldspar, whereas Duffin et al. (1989) and Fishman (1997) additionally identified illite as a major cement in the Mt. Simon. Most illite in the Mt. Simon is authigenic and was proposed to be derived from the breakdown of feldspar and by precipitation from paleo-fluids (Bowen et al. 2011). Fishman (1997) proposed that most of the porosity in the Mt. Simon is secondary, resulting from the dissolution of authigenic cements. Freiburg et al. (2016) proposed that much of the secondary porosity in the lower Mt. Simon is the result of partial to complete K-feldspar dissolution. Bowen et al. (2011) noted that iron oxide coatings on quartz grains in the Mt. Simon inhibit authigenic quartz precipitation and the preservation of pore space. Freiburg et al. (2014, 2016) attributed the inhibition of authigenic quartz cement to the abundance of authigenic illite coatings on detrital quartz grains and identified at least two episodes or generations of authigenic illite. Duffin et al. (1989) identified two major episodes of diagenetic cementation in the Mt. Simon: a K-feldspar episode at about 400 million years (My) and a sericite or illite episode that began in the early Permian (~275 Ma), with crystallization continuing over a time span of 40 to 60 My. Quartz cements in the Mt. Simon have been attributed to burial compaction processes, with quartz growth generations showing a general increase in the temperature of precipitation associated with the burial of the Illinois Basin (Pollington et al. 2011). This finding differs from the more punctuated event of the expulsion of northwestern-migrating metal-rich brines from deep sandstones in the depths of the Illinois Basin ca. 270 Ma (Sverjensky 1986; Duffin et al. 1989; Fishman 1997).

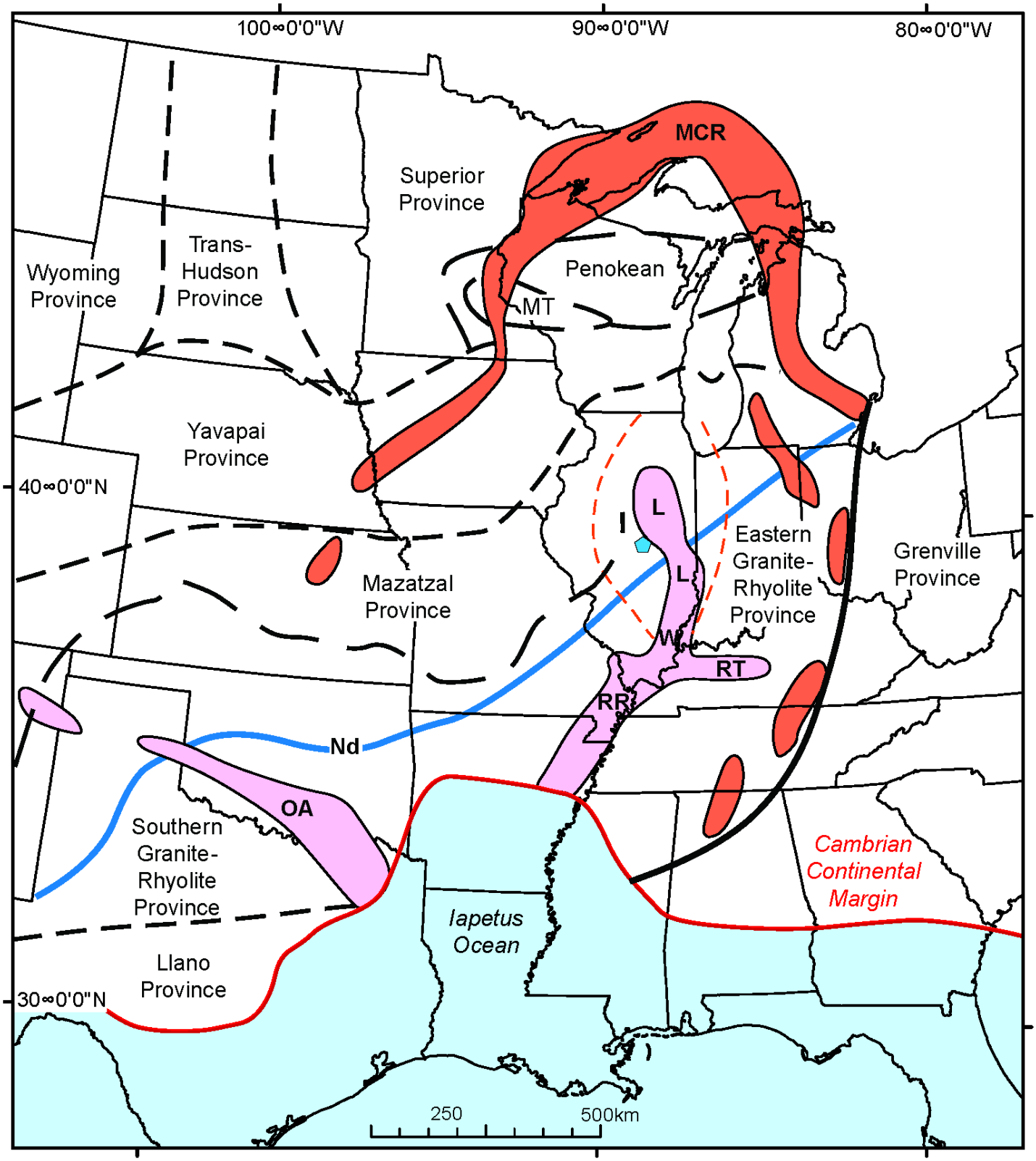

Figure 4. Generalized map of basement terranes of the Laurentian midcontinent (ca. 0.535 billion years ago [Ga]). The locations of the Oklahoma Aulacogen (OA), Reelfoot Rift (RR), Rome Trough (RT), and Wabash (W) and La Salle (L) deformational belts are indicated in pink, and the 1.1 Ga midcontinent rift (MCR) is indicated in orange. The red dashed line represents the estimated regional extent of the lower Mt. Simon and Argenta sandstones. The light blue pentagon indicates the Illinois Basin – Decatur Project sample location for this study. MT, Marshfield Terrane. Modified from Bickford et al. (2015).

Mt. Simon Environments of Deposition

The depositional environment of the Mt. Simon Sandstone at the IBDP has previously been described in detail (see Freiburg et al. 2014). New studies have detailed a more significant marine presence but still agree that the lower Mt. Simon reflects a largely drying-upward succession (Figure 5; Freiburg et al. 2016; Reesink et al. 2020). The Argenta formation and lower Mt. Simon Sandstone were deposited in a rift basin that likely formed within the Laurentian craton near the end of the breakup of the supercontinent Rodinia during the early Cambrian. This rift basin formed along the axis of the La Salle Fault Zone, a suspected area of failed rifting and the depocenter of the Argenta formation and Mt. Simon Sandstone (Freiburg et al. 2020). This basin, or proto-Illinois Basin, was open to the early Cambrian Iapetus Ocean, whose shoreline migrated up along the opening of the Reelfoot Rift and the Wabash and La Salle Fault Zones. Deposition of the Argenta occurred within an Iapetus shoreface environment, with localized alluvial fans being deposited off proximal Precambrian highs flanking the rift basin. Retreat of the Iapetus shoreline or sea level fall is marked by erosion and a brief hiatal surface on the top of the Argenta (Freiburg et al. 2014). Deposition of the overlying lower Mt. Simon began in a nearshore environment with fluctuating beach, alluvial, and fluvial deposits in the lowermost unit A (Figure 3) and transitioning to a more eolian environment in unit B (Figure 3). This drying-upward succession reflects the filling of the rift basin, the burial of proximal Precambrian highs, and the retreat of the Iapetus Ocean. The middle Mt. Simon marks a period of renewed subsidence, possibly the beginning of the major Illinois Basin subsidence coinciding with tectonic activity, and a renewal of alluvial and fluvial deposits carrying coarse sediments from basin peripheral highs in unit C (Figure 3). Similar to the lower Mt. Simon, the middle Mt. Simon repeats a drying-upward sequence with eolian fine-grained deposits in unit D (Figure 3). These middle Mt. Simon deposits are unique to the flanks of the basin, with deposits becoming more deltaic, similar to the upper Mt. Simon, toward the basin depocenter (Monson et al. 2020). The upper Mt. Simon (unit E) reflects a shallow marine-tidal flat, deltaic environment that marks the major Sauk Sequence transgression into the Illinois Basin. The overlying black shale facies of the Eau Claire marks a major sea level rise and the maximum sea level depth during Eau Claire deposition. The other two major seals investigated in this study (the Ordovician Maquoketa Formation and the Devonian New Albany Shale) represent the maximum seal level rise during their respective sequences of deposition.

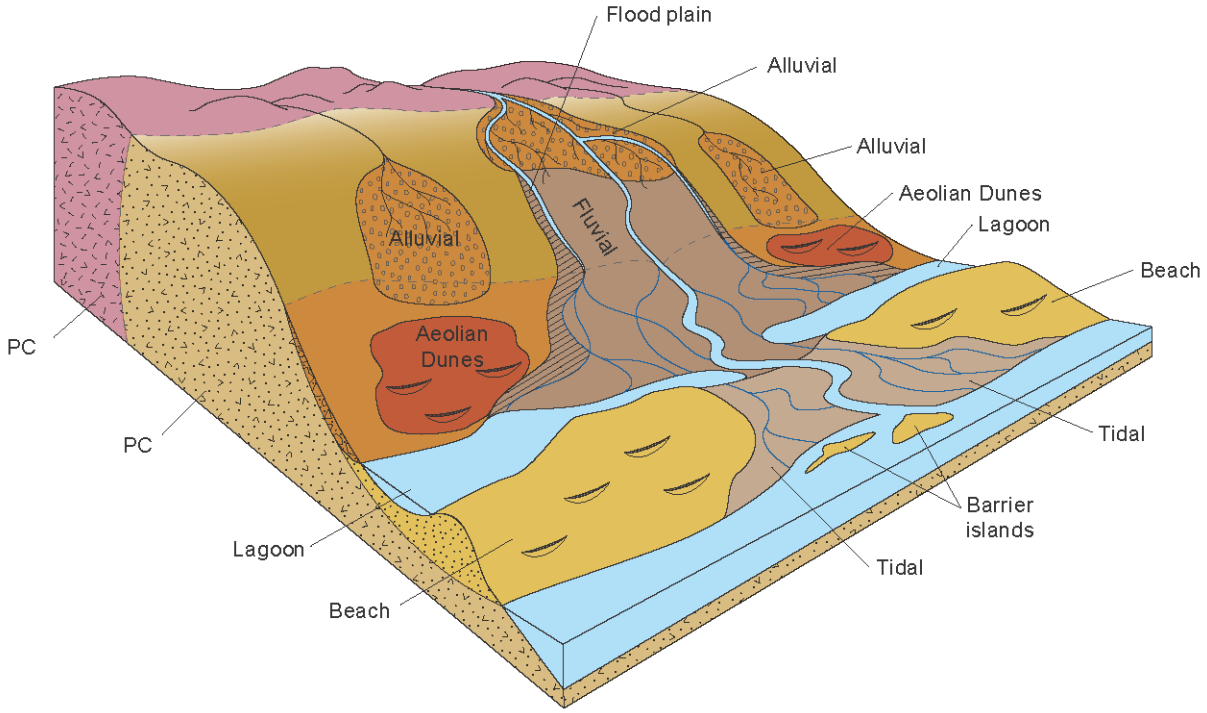

Figure 5. Depositional model reflecting all units of the Mt. Simon Sandstone. The Mt. Simon is deposited on a heterogeneous Precambrian basement (PC).

Reservoir Properties

The Mt. Simon at the IBDP is unique with respect to reservoir properties in that the greatest porosity is near the base of the formation (Figures 3 and 6). This is indicative of diagenetic heterogeneity throughout the formation, likely the result of a dynamic environment of depositional and variable sediment source-controlled regional tectonics. Both the depositional environment and the sediment source are controlling factors in the grain size, sorting, and mineralogy (Table 1), which varies throughout each unit of the Mt. Simon. Because of this lithologic and facies variation throughout the Mt. Simon, units can present variable diagenesis (i.e., compaction, cementation; Figure 7) in similar geologic settings (i.e., sediment burial and regional fluid migration events). Thus, each unit of the Mt. Simon is unique and has different reservoir properties (Table 2, Figure 6).

The upper Mt. Simon follows a regional trend of decreasing porosity with depth (Figure 6) but has a wide range of porosity and permeability. In the upper Mt. Simon, channel sandstones within the tidal flat have the best reservoir properties, whereas interbedded shale facies have the poorest. The middle Mt. Simon generally follows the trend of decreasing porosity but is much more variable in unit C, where numerous conglomerates have higher porosity than the interbedded finer grained sandstone (Figure 3). At the IBDP site, the middle Mt. Simon has the poorest reservoir properties compared with the rest of the Mt. Simon. The lower Mt. Simon is anomalous compared with the upper and middle in that it does not follow the trend of decreasing porosity with depth; rather, it generally increases with depth and typically has >10% porosity throughout the entire unit (Figure 6). At the IBDP, the porosity and permeability are highly variable but can have up to 30% porosity and 1 D of permeability. The Argenta is similar to the middle Mt. Simon, with low porosity (generally less than 10%) and permeability (generally less than 1 mD). It generally follows the upper and middle Mt. Simon depth trend by having some of the overall lowest porosities.

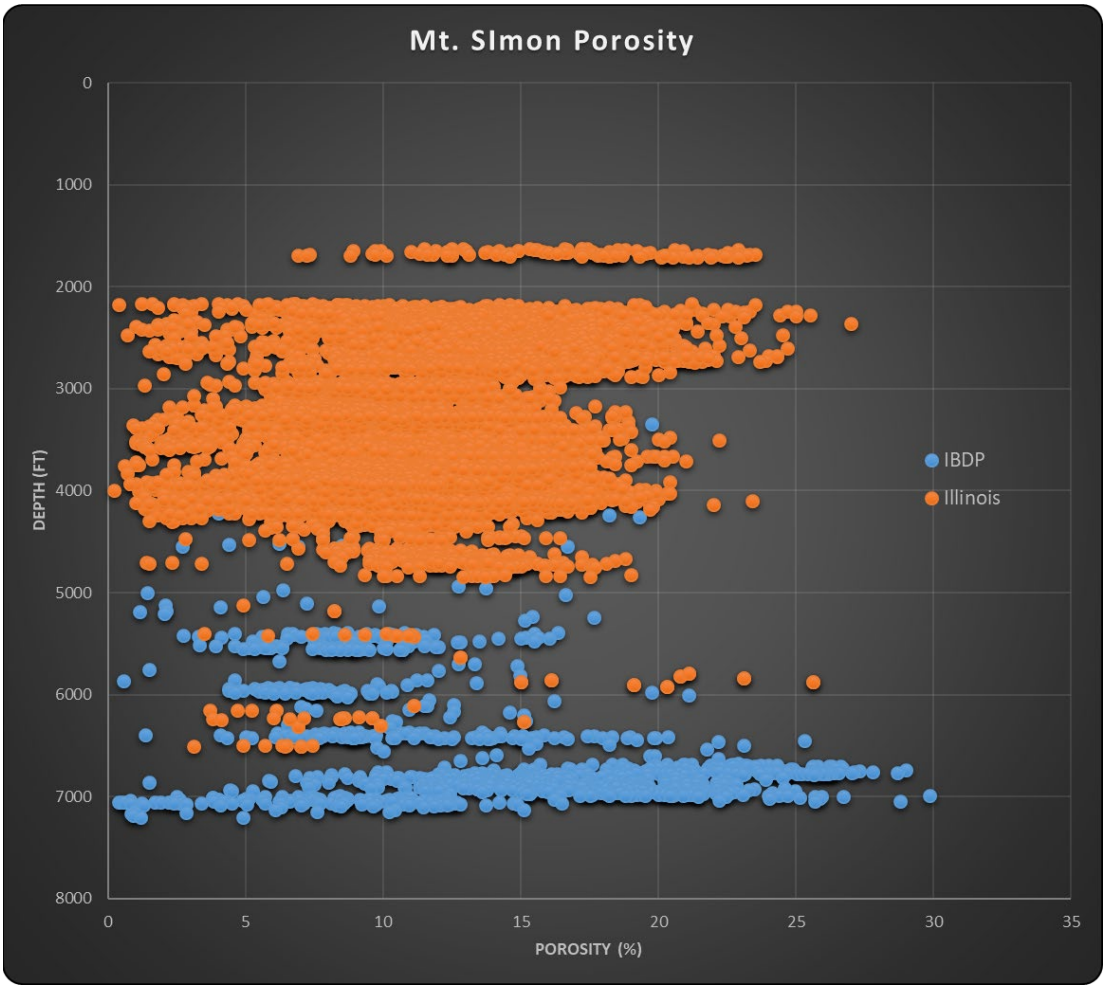

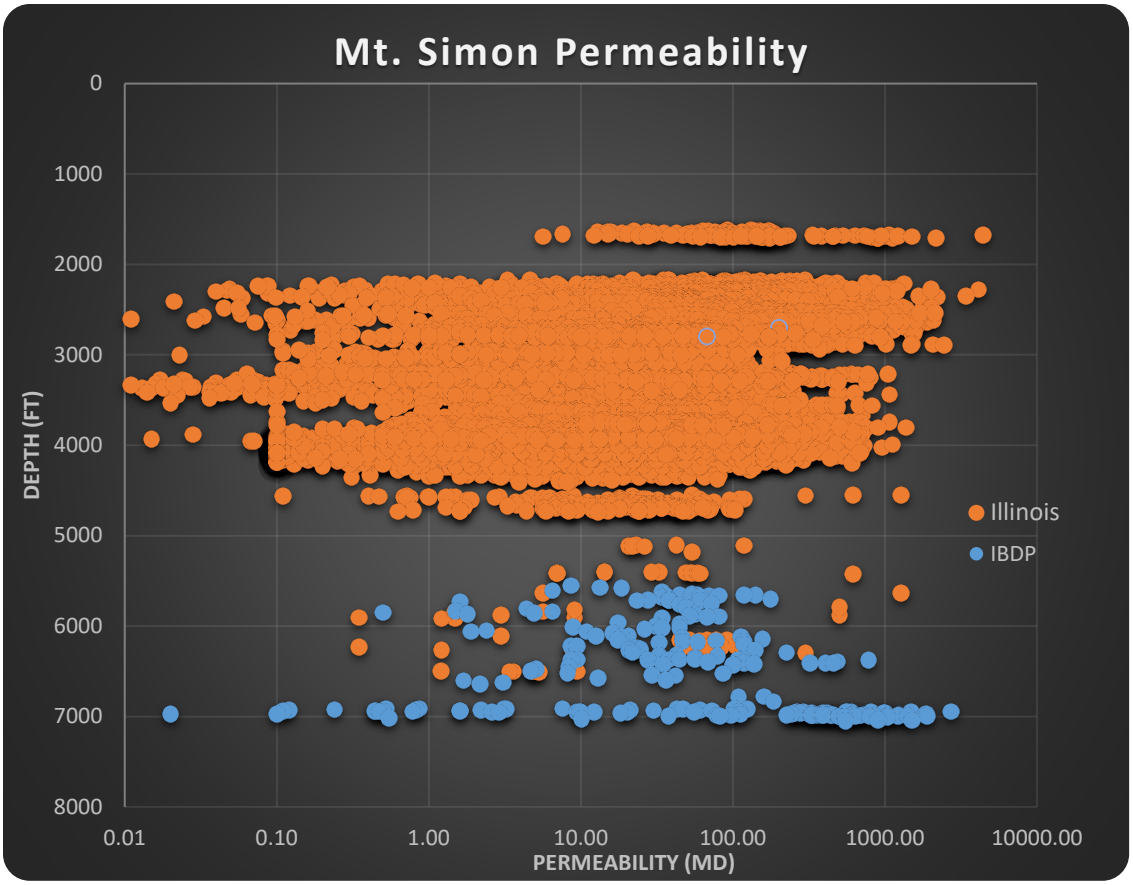

Figure 6. Porosity–depth and permeability–depth relationships of the Mt. Simon throughout Illinois. The majority of well data in Illinois are in the upper Mt. Simon (orange). Data from the Illinois Basin – Decatur Project (IBDP, blue) include the upper, middle, and lower Mt. Simon and the Argenta formation. The porosity–depth trend generally shows a porosity decrease with depth throughout Illinois. Porosity generally increases with depth at the IBDP, with porosities in the lowermost Mt. Simon similar in value to the highest values at the shallowest depths throughout Illinois. Porosity drops off in the Argenta at the IBDP and follows the general trend of decreasing porosity with depth. Permeability generally follows a similar trend, with the highest values in the lower Mt. Simon.

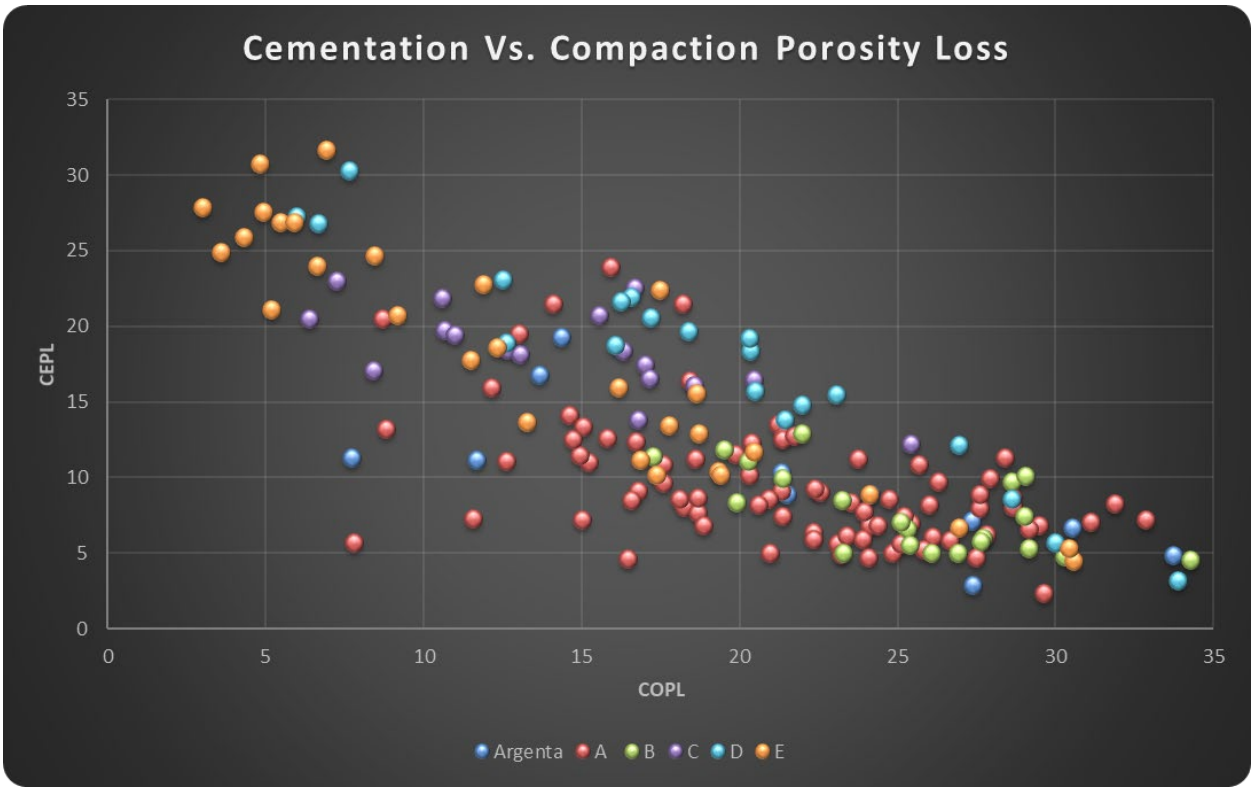

Figure 7. Cementation porosity loss (CEPL) versus compaction porosity loss (COPL) of all the Mt. Simon units and the Argenta at the Illinois Basin – Decatur Project. Note the high CEPL in units E, D, and C compared with units B, A, and the Argenta, which have lower CEPL and higher COPL values. Data from Freiburg et al. (2016).

Mineralogy and Texture

All formations described herein are heterogeneous with respect to depositional facies and diagenesis and thus can have highly variable mineralogy (Table 1). A generalized mineralogy for each formation is described below, including all the Mt. Simon units and the Argenta, based on the analytical data in Freiburg et al. (2014, 2016).

New Albany

The thickest member of the New Albany is the Grassy Creek, which is a black shale dominated by clay minerals. The primary clay mineral is illite, with lesser amounts of chlorite and mixed-layered illite–smectite. Other major detrital constituents include quartz, feldspar, and pyrite, with minor dolomite and calcite. Although not a mineral, the high total organic carbon content in the New Albany is important to note. The New Albany has the highest organic carbon content of all the shales in the Illinois Basin.

Maquoketa

The lowermost formation within the Maquoketa Group is the Scales Shale. With respect to mineralogy, it can be considered a clayey or argillaceous dolomite. Although clay minerals are a minor component, illite and mixed-layer illite–smectite is pervasive throughout. Major components include dolomite and quartz, with minor feldspar, pyrite, and siderite.

Eau Claire

The lowermost lithofacies of the Eau Claire Formation is composed of dark gray shale that is dominated by the clay minerals illite and mixed-layer illite–smectite, with minor chlorite. Potassium-feldspar, quartz, and mica detritus are abundant in the clay matrix, along with minor pyrite, apatite, and calcite.

Mt. Simon

Upper

The upper Mt. Simon is composed of relatively thick pink-maroon to white channel sandstone beds with thin interbedded dark maroon shales (Figure 8). The sandstone is subarkosic (generally >25% but <10% total K-feldspar) to

arenitic, with abundant bimodal, well-rounded, medium- to fine-grained quartz grains. Authigenic quartz and feldspar are common. Interbedded dark gray shale and dark maroon mudstone are dominated by illite with illite–smectite and by chlorite. Shale and mudstone facies often include abundant feldspar silt dominated by K-feldspar, with minor plagioclase.

Middle

The middle Mt. Simon Sandstone is composed of two units (Figure 3), of which the lower unit C was sampled for this study. It is composed of maroon to tan sandstone that is subarkosic to arenitic with fine- to pebble-grained sediment that is often well rounded and moderately to poorly sorted. Abundant K-feldspar grains are observed in coarser grained facies. Hematite is common throughout as Liesegang banding but overall is a minor component. Pore-filling clay is common and includes illite, illite–smectite, and kaolinite.

Lower

The lower Mt. Simon is composed of two units (Figure 3), and the lower unit A was sampled for this study. It is composed of a tan to light maroon-pink sandstone that is mostly subarkosic, with fine- to pebble-grained sediment that is often well rounded and moderately to well sorted. It is dominated by quartz, K-feldspar, and plagioclase. Clay is a minor constituent throughout and is primarily composed of illite. Pore-lining clay is common, and pore-filling clay is less common. Rare dark maroon mudstones dominated by the clay mineral illite are interbedded in the sandstone, with rare subarkosic siltstones associated with the mudstone facies.

Argenta

The Argenta is a tan-gray to maroon sandstone to conglomerate that is subarkosic to sublithic, with very fine to very coarse sediment that is subangular to subrounded. It is predominantly composed of quartz, K-feldspar, and clay minerals. Clay minerals are an abundant component compared with other sandstones of the Mt. Simon, and the Argenta notably contains significant amounts of pore-filling and grain-replacing kaolinite. Kaolinite may be partially altered to dickite. Pore-filling illite is also abundant, with minor chlorite throughout.

Table 1. Representative mineralogy of the Argenta, Mt. Simon sections, and overlying shale seals based on the single-sample X-ray diffraction analysis by Freiburg et al. (2014, 2016)

Formation Name	Lithology	Quartz	K-feldspar	Plagioclase	Calcite	Siderite	Dolomite	Pyrite	Hematite	Total non clay	Total Clay	Smectite	Illite-Smectite	Illite-Mica	Kaolinite	Chlorite	Organic Carbon
New Albany	Shale	33	5	7	1	0	2	3	0	51	49	0	10	28	1	10	8
Maquoketa	Clayey Dolomite	31	2	4	1	5	47	5	0	95	5	0	20	59	5	16	na
Eau Claire	Shale	9	10	0	5	1	0	3	0	28	72	0	25	66	0	8	<1
Upper Mt. Simon	Sandstone/shale	33	42	10	1	2	1	0	1	90	10	0	16	62	0	22	0
Middle Mt. Simon	Sandstone	88	2	2	0	0	1	0	0	93	7	0	45	45	5	5	0
Lower Mt. Simon	Sandstone	73	13	7	0	1	0	1	0	96	4	0	0	100	0	0	0
Argenta	Sandstone	69	6	0	1	0	2	1	1	80	20	0	0	42	43	15	0

Methodology

Representative samples from each of the seals as well as all units of the Mt. Simon were carefully selected for grain size separation, X-ray diffraction (XRD), and K-Ar dating of illite separated from samples (Table 2, Figure 8). All core samples used in this study were from the IBDP verification well 1 (API 121152346000), except for the Maquoketa sample, which was from the geophysical monitoring 2 well (API 121152359400), and the middle Mt. Simon sample, which was from the carbon capture and storage 1 well (API 121152341500). Four samples from the lower Mt. Simon, two from the Argenta, and one from all the other units were selected for analyses. More samples were selected from the lower Mt. Simon to represent the heterogeneity of the unit because that is the target storage reservoir. Thin

sections were prepared from each sample for petrographic characterization. The remaining sample was crushed for grain size separation. The grain fraction <2.0 µm was separated by using the principle of Stokes' law for the gravitational settling of particles in water. Twenty grams of sample was used for the sandstones and 10 g was used for the shales. It was assumed that after 60 min of settling, the uppermost centimeter of the fluid column would contain grain sizes <2.0 µm. From this separated <2.0-µm fraction, smaller fractions were separated by centrifuge. Parameters for centrifugation were <2.0–0.6 µm at 1,500 rpm, 20 °C, 11 min, maximum acceleration, and no brake, and <0.6–0.2 µm and <0.2 µm at 2,500 rpm, 20 °C, 35 min, maximum acceleration, and no brake. Before centrifugation, samples were homogenized with an ultrasonic homogenizer for 20 s at 20% power with constant amplitude. Samples were further processed for K-Ar age dating. Samples were prepared for random powder XRD and oriented powder. Both air-dried and glycolated oriented samples were prepared and analyzed with a Bruker D8 XRD instrument with a cobalt tube and Lynx Eye detector. Measurements were made at a 4° to 80° angle at a scan speed of 0.5°/min with a 0.5 fixed divergence slit. After XRD analysis, dialysis was performed on the samples for 48 h in deionized water to remove any salts remaining after grain size separation and subsequent evaporation. Water was exchanged twice a day and silver nitrate ($AgNO_3$) was used for testing the abundance of chloride ions in the water.

The intensity ratio (IR) and full width half maximum (FWHM) were calculated from illite peak reflections obtained from air-dried and glycolated oriented preparations (Henkel 2017). The IR is used to estimate the presence of smectite, and the FWHM aids in understanding the degree of diagenesis, such as the illitization of smectite. To quantify the illite polytypes in the grain size fractions 2.0–0.6 µm, 0.6–0.2 µm, and <0.2 µm, the peak area method (Grathoff and Moore 1996) and an XY plot for using pure polytype end-member standards and polytype mixtures (Haines and van der Pluijm 2008). Authigenic illite (1M polytype) is generally more abundant in fine-grain-size fractions, whereas illite samples commonly contain a mixture of both authigenic (1M) and detrital (2M) illite polytypes. Thus, illite age analysis (Pevear 1999) was completed to extrapolate the age based on the quantity of each polytype.

Details of the K and Ar analyses conducted at the University of Göttingen laboratory are detailed in Wemmer (1991). The K-Ar ages were calculated based on the ^{40}K abundance and decay constants recommended by the International Union of Geological Sciences as quoted in Steiger and Jaeger (1977). The analytical error for K-Ar age calculations is given at a 95% confidence level (2σ).





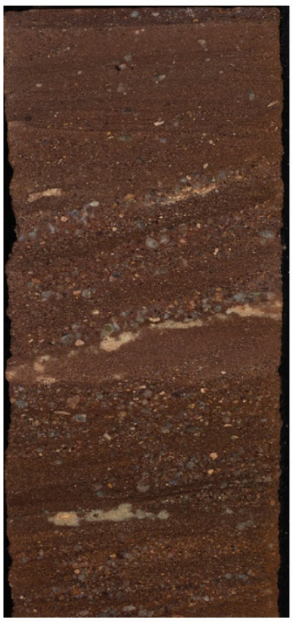






Figure 8. Slabbed core samples (4 in., 10 cm) used in this study. Samples are shown from the top, left to right, and ordered by depth: New Albany (2,157 ft, 657 m), Maquoketa (2,816 ft, 858 m), Eau Claire (5,465 ft, 1,666 m), upper Mt. Simon (5,546 ft, 1,690 m), middle Mt. Simon (6,426 ft, 1,959 m), lower Mt. Simon (6,741 ft, 2,055 m), lower Mt. Simon (6,863 ft, 2,092 m), lower Mt. Simon (6,889 ft, 2,100 m), lower Mt. Simon (6,980 ft, 2,128 m), lower Mt. Simon (6,986 ft, 2,129 m), Argenta (7,016 ft, 2,138 m), Argenta (7,025 ft, 2,141 m).

Results

Petrography

Petrographic analysis of all samples showed mineralogical, textural, and diagenetic variation among all the samples. All the samples analyzed indicated a heavy presence of clay, particularly illite. All three shales examined, including a mudstone from the Mt. Simon, contained abundant clay minerals (Figures 9 and 10). The New Albany shale, the Eau Claire shale, and the Mt. Simon mudstone were predominantly composed of an illite matrix (Figure 9). The New Albany and the Eau Claire were tightly compacted, with partly sutured quartz and K-feldspar grains, muscovite laths, and organics (New Albany). The Mt. Simon mudstone showed less compaction overall and had a coarser mineral grain content than the shales. The Maquoketa had the greatest mineralogical differences among all the seals. It was carbonate rich and primarily dolomite, with intercrystalline clay. With crystalline dolomite predominantly constituting the matrix, the Maquoketa could be considered a crystalline carbonate lithology rather than a shale. Where clay minerals occluded the pore space in the Maquoketa, minor porosity was observed between dolomite crystals. Most of this pore space was nearly to completely occluded with clay, with little interconnectivity. The paragenesis of the sealing units was beyond the scope of this research, and instead, the age of illite in each unit was obtained to interpret major diagenetic events.

All units of the Mt. Simon, including the Argenta, are highly heterogeneous and vary in the degree of diagenetic events observed. Compaction and cementation vary among units and partly relate to their stratigraphic position (Figure 7). To understand the major controls on reservoir properties and assist in the interpretation of diagenetic illite age dates, diagenetic events are described and compared in a temporal framework (Figure 11). The upper Mt. Simon sample was located near the top of the Mt. Simon, close to the Eau Claire contact (Figure 3). It included a bimodal fine- to very coarse-grained sandstone with interbedded mudstone with abundant suspended quartz and K-feldspar silt (Figures 8 and 10). Mudstone and shale often contained fluid escape structures filled with sandstone injectites. The sandstone had localized beds that were arkosic and beds that were quartz arenite (both observed in the sample studied; Figure 8). Both contained well-rounded grains with abundant cements. The arkosic sandstone was notably pink in color (Figure 8), likely a result of the abundant euhedral K-feldspar overgrowths that coated nearly every detrital feldspar grain (Figure 10). Pink sandstone beds were often located between thin laminae of maroon mudstone (Figure 8). Authigenic quartz overgrowths were abundant in both the arenites and arkose. Authigenic K-feldspar was observed as an earlier event than authigenic quartz where authigenic K-feldspar was observed growing up to the margin of a detrital quartz grain. Nowhere was authigenic quartz observed growing up against detrital K-feldspar grains without authigenic K-feldspar overgrowths. Authigenic quartz was, however, thought to be relatively cogenetic with early K-feldspar overgrowths because it appeared to predate major compaction that might otherwise have destroyed the primary porosity observed in the upper Mt. Simon. Partial dissolution of K-feldspar overgrowths was often observed as contributing to minor secondary porosity. Mudstone laminae exhibited abundant compaction, with highly sutured quartz grains at the mudstone–sandstone contact. Interlaminated clay appeared to increase suturing between the quartz grains (Figure 10). Authigenic overgrowths (i.e., quartz and K-feldspar) were absent where suspected intergranular clay occurred near mudstone laminae.

The middle Mt. Simon sample was located near the base of the middle Mt. Simon unit just above the lower Mt. Simon contact (Figure 3). The sample was a quartz arenite with nearly enough K-feldspar to be considered a subarkose. The sample contained rounded to well-rounded medium-sized grains that were moderately well sorted. Iron oxide coatings were common around nearly every detrital grain to some degree. Minor bleaching or iron oxide reduction occurred throughout. Where bleaching occurred, authigenic quartz appeared to be more common. Occasionally, bleach spots were centered around a specific detrital grain, which was typically dissolved out. In the pore space where the detrital grain once was, authigenic titanium minerals were observed as radial crystals growing in toward the center of the pore space. Early minor authigenic quartz crystals were found nucleated onto detrital quartz grains where iron oxide coats were thin or nearly absent. Later, coarse authigenic quartz crystals nucleated onto minor crystals and overgrew the detrital quartz grains with iron coating where the pore space was open. Authigenic quartz was the most abundant

cement in the sample. It commonly isolated pore space and impeded connectivity. Pore space that was not occluded by authigenic quartz was partly occluded by illite and kaolinite. Detrital quartz grains that did not have an authigenic quartz overgrowth often had a hairy illite coating over a suspected iron oxide coating. Kaolinite cements occurred as pore filling and often had fine illite between plates or booklets (Figure 10). In areas of the sample where quartz cements were low, detrital grains were more consolidated and partly compacted. Clay cements were higher in these intervals. Overall, the sample had low porosity as a result of abundant diagenetic cements, including quartz, illite, and kaolinite.

The lower Mt. Simon Sandstone samples represented the most porous and permeable unit examined (Table 2, Figure 3). Sandstone samples included a fine- to medium-grained sandstone (6,741 ft, 2,054.7 m), a coarse- to very coarse-grained sandstone (6,889 ft, or 2099.8 m), and a medium-grained sandstone (6,986 ft, 2,129.3 m; Figure 8). All the samples were described as subarkose, with a moderate amount of detrital K-feldspar. The coarsest sample commonly contained very coarse to granule-size igneous basement clasts. All the samples had varying degrees of iron oxide cements, with the uppermost sample having the most. Iron oxides primarily occurred as an early cement coating the detrital grains. In the basal two samples, trace hematite speckles occurred around grain boundaries and partly in pore spaces. Illitic clay coatings overgrew thin hematite coatings on detrital grains in all the samples. Early authigenic quartz occurred as minor euhedral crystal overgrowths where iron and illite coatings were minor or absent on detrital quartz grains. Minor authigenic feldspar partly overgrew detrital feldspar grains. Authigenic quartz and feldspar were the most common in the coarsest samples. Hairy illite was observed as a partial coating over authigenic cement overgrowths. Illite commonly partially filled pore spaces. Porosity was both primary and secondary. Primary porosity was intergranular framework porosity and was commonly lined with illite. Secondary porosity was largely grain dissolution, with K-feldspar grains partially to completely dissolved. Complete dissolution was evident, with hematite and clay casts of the dissolved feldspar grain intact. Feldspar grains often exhibited some crushing, and fractured grains with partial clay fill showed secondary porosity. Compaction was evident throughout, with concave grain boundaries at the grain-on-grain contact. Major dissolution of K-feldspars likely occurred after major grain compaction, leaving evidence of shaped or sutured grains around dissolved K-feldspar grains.

The Argenta is a tight unit underlying the lower Mt. Simon. The samples examined represented the overall poor reservoir properties of the unit, which had low porosity and moderate to low permeability (Table 2). The Argenta is a subarkose to sublithic sandstone that is often moderately sorted very fine sandstone to pebble conglomerate. The samples examined were a granule–pebble conglomerate and a coarse-grained sandstone with abundant granules and pebbles. Authigenic cements were abundant in both samples. Early hematite dusting over detrital grains was common, and partial coatings that formed over grains were apparent in some beds but not as apparent in others. Early clays occurred as pore fillings and partial coatings over grains. Authigenic quartz overgrowths were abundant throughout the overgrowing minor hematite dustings and clean detrital quartz grain surfaces. Authigenic quartz was absent where early pore-filling clay contacted the detrital grain surface. Pore-filling and grain-replacing kaolinite was abundant throughout the samples and was the most notable mineralogical difference from the overlying Mt. Simon units. Pore-filling kaolinite likely formed preauthigenic quartz but continued to develop cogenetically or after quartz cementation. This was suggested by the intergrown kaolinite in authigenic quartz cements. The crystallinity of the kaolinite varied in size throughout the samples. Sizes ranged from very fine crystals to coarse books and sometimes blocky-looking crystals. Some of the kaolinite may have been partially altered to dickite, based on the blocky nature of the crystals. A late-stage dissolution event was one of the latest events observed in the Argenta. Partial to complete dissolution of feldspars was observed. Feldspars appeared to be more prone to dissolution than rhyolitic basement lithics. Most of the porosity observed in the Argenta was the result of this dissolution event. Illite was often observed partly infilling dissolved grain spaces or between kaolinite booklets. Illite and kaolinite often filled the space surrounding secondary pore spaces of dissolved grains, isolating the pore space and resulting in low permeability throughout the sample. Compaction of grains was common and abundant throughout the sample where quartz cements were low. Grain boundaries were often sutured with early clay or stylolite between grain boundaries. Some grains that were completely replaced by kaolinite appeared to have undergone compaction before complete kaolinization. This was indicated by sutured grain boundaries along the quartz grains and feldspar grains that had been completely altered to kaolinite (Figure 10).

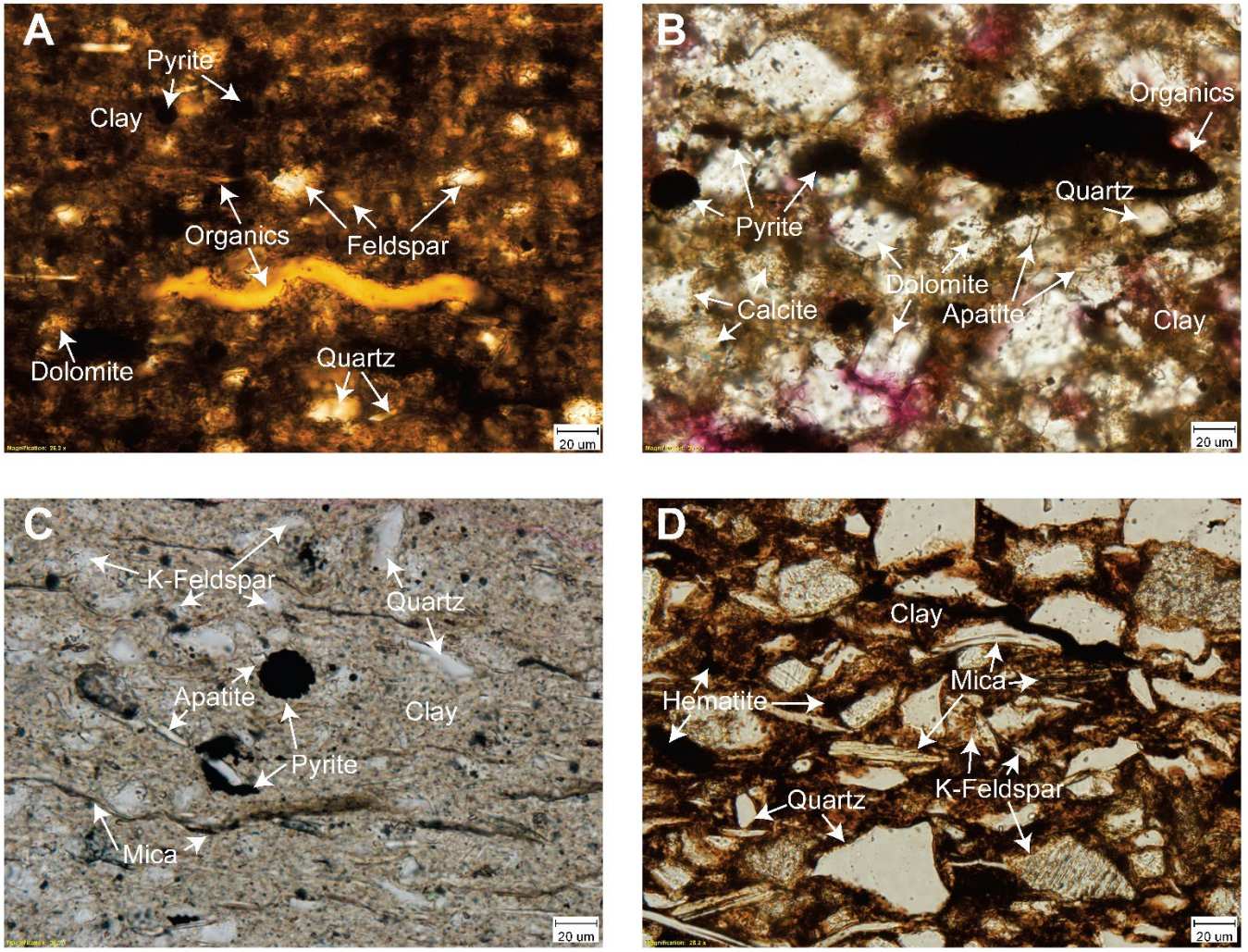

Figure 9. Thin-section photomicrographs of prominent sealing and baffle units at the Illinois Basin – Decatur Project. (A) Lower Mt. Simon mudstone (depth 6,860 ft). Subangular quartz grains, subangular to subrounded K-feldspar grains, and muscovite mica laths are in a clay matrix with minor hematite. (B) Eau Claire shale (depth 5,465 ft) with a dominant clay matrix and minor rounded quartz and K-feldspar grains, pyrite framboids, muscovite mica laths, and apatite grains. (C) Maquoketa shale predominantly composed of euhedral dolomite crystals and clay, with minor calcite, quartz, apatite, pyrite, and organics. Pore spaces (pink) were observed between dolomite crystals and were largely occluded with clay. (D) New Albany shale was primarily composed of clay with common organics (*Tasmanites*) and minor quartz, dolomite, K-feldspar, and pyrite.

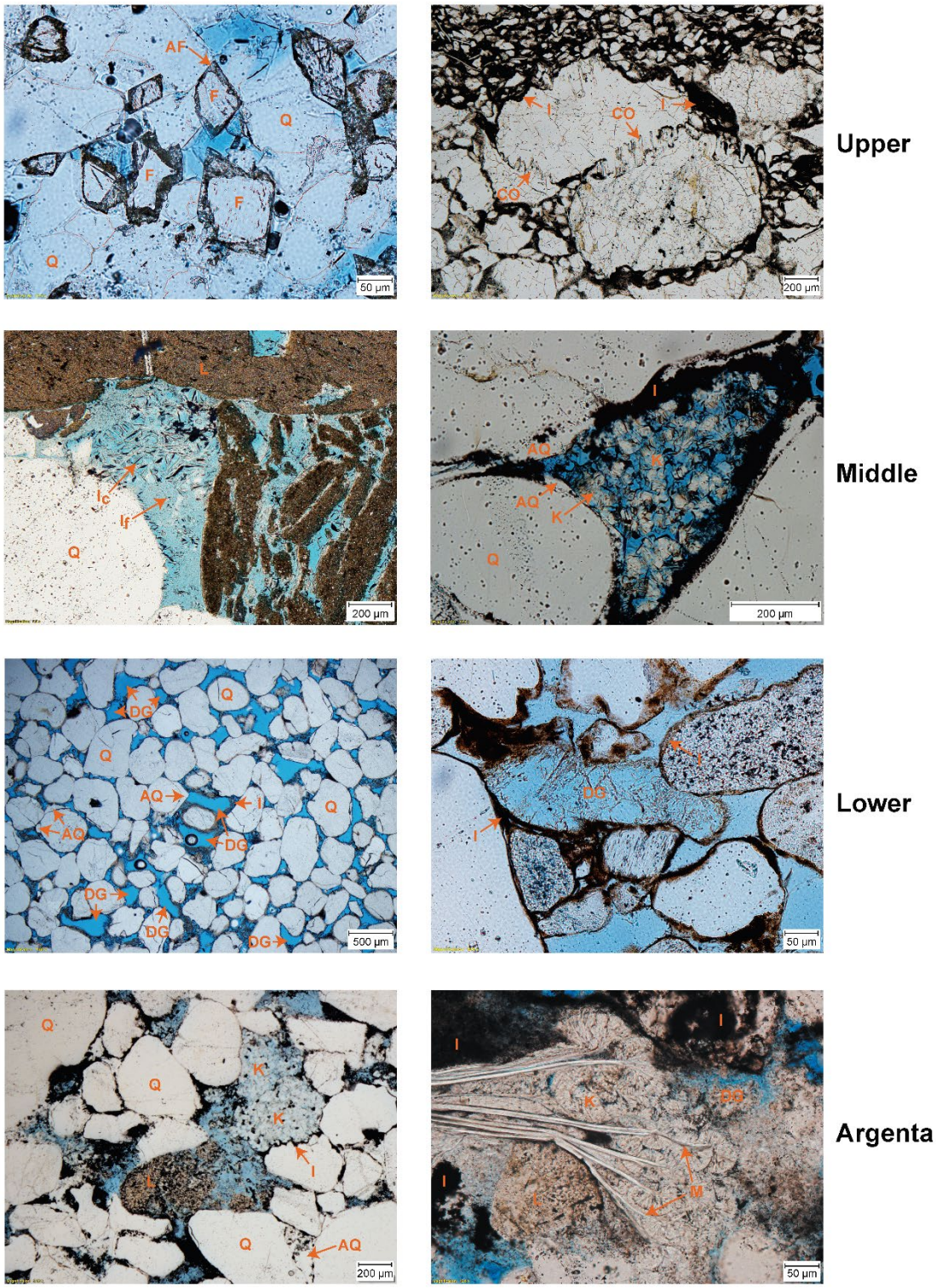

Figure 10. Thin-section photomicrographs through the Illinois Basin – Decatur Project Mt. Simon sections and Argenta sections showing important diagenetic events and depositional fabrics. AF, authigenic feldspar; F, feldspar; Q, quartz; CO, suture; I, illite; L, lithics; I_c, illite coarse; I_f, illite fine; AQ, authigenic quartz; K, kaolinite; DG, dissolved grain; M, mica.

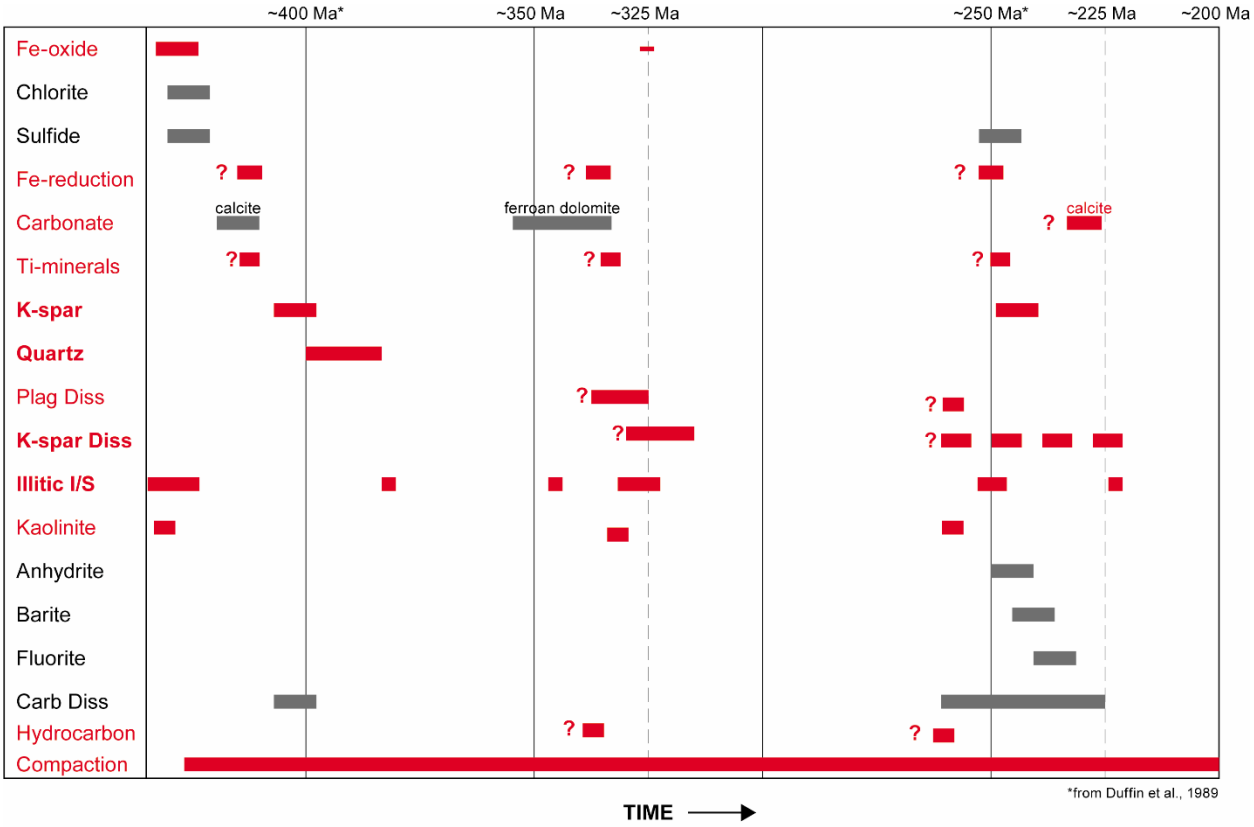

Figure 11. Generalized paragenetic sequence for the Mt. Simon Sandstone. Diagenetic events at the Illinois Basin – Decatur Project are highlighted in red. Question marks indicate that the occurrence of the event or the timing of the event is unclear. Diss, dissolution. After Fishman (1997). AAPG ©1997, reprinted by permission of the AAPG, whose permission is required for further use.

Illite

To understand the purity and diagenetic history of the illite, the IR and FWHM were calculated (Table 2). All samples had an IR >1.00, indicating the presence of smectite despite XRD results indicating a lack of smectite (Table 1). The lower Mt. Simon samples, on average, had the highest IR values, with samples at 69,80 ft (2,128 m) and 6,986 ft (2,129 m) having the highest IR values at 1.91. Within the Mt. Simon, the upper Mt. Simon sample had the lowest IR value at 1.14, followed by the middle Mt. Simon sample at 1.17. Of the seals, the New Albany and Maquoketa both had the lowest IR values at 1.12. In addition, both of these samples had the lowest FWHM at 0.36. The Eau Claire sample had the highest FWHM at 1.10. Of the Mt. Simon samples, including the Argenta, FWHM values from highest to lowest were the lower Mt. Simon, upper Mt. Simon, Argenta, and middle Mt. Simon (Table 2). All samples analyzed by XRD contained illite. Sample size fractions were analyzed to determine the purity of the samples (Table 3, Figure 12).

Illite quantification indicated that the lower and middle Mt. Simon were composed entirely of 1M and $1M_d$ illite (Table 4). Thus, the illite age analysis method (Pevear 1999) could not be used to determine the age of the end members; instead, the bulk age of the smallest size fraction was interpreted to be diagenetic. With the absence of $2M_1$ in all the <0.2-µm size fraction samples, all illite was interpreted to be diagenetic (Table 4). The presence of $2M_1$ illite in the 0.6- to 0.2-µm and 0.6- to 2.0-µm samples suggested that age dates in these samples might represent a mixture of detrital and diagenetic illite (Table 4). All samples were predominantly composed of $1M_d$ illite.

K-Ar Age Dating

Potassium–argon dating was performed on three grain size fractions (coarse 2.0–0.6 µm, medium 0.6–0.2 µm, and fine <0.2 µm) of each sample (Table 2, Figure 8). Illite was detected in all grain size fractions except the finest fraction of the New Albany and Maquoketa shale samples (Table 3). The oldest K-Ar ages were identified in the coarse size fraction of the Eau Claire (658.3 Ma) and the upper Mt. Simon (598.6 Ma). Both ages represented samples with $2M_1$ illite (Table 4). The youngest K-Ar ages were identified in three units: the Argenta fine size fraction (218.4 and 251.5 Ma) and medium size fraction (234.1 Ma), the middle Mt. Simon fine size fraction (251.9 Ma) and medium size fraction (238.3 Ma), and the Eau Claire fine size fraction (246.0 Ma). Of the sandstones, the Argenta and middle Mt. Simon had the lowest reservoir properties while recording the youngest age dates in the Mt. Simon (Table 2, Figure 3). The lower Mt. Simon had the highest reservoir properties and recorded illite older than the underlying Argenta and overlying the middle Mt. Simon, both of which have low reservoir properties (Table 2, Figure 3). All lower Mt. Simon illite was considered diagenetic (Table 4) and ranged in age from 287.3 to 375.5 Ma. The majority of ages in the lower Mt. Simon ranged from 321.1 to 347.8 Ma. One sample (6,889 ft) in the finest size fraction was dated at 287.8 Ma. Two samples (6,980 and 6,889 ft) recorded the oldest dates, 375.5 and 378.0 Ma. Numerous samples in the Mt. Simon contained K-feldspar, particularly in the coarse and medium size fractions. Of the shales, only the Eau Claire contained K-feldspar. Numerous samples in the Mt. Simon contained halite, particularly the coarse and fine size fractions (Table 3). The occurrence of these minerals in the samples affected the confidence of the K-Ar age dates. However, halite and K-feldspar were absent from numerous samples, and these samples yielded dates similar to samples in which halite and K-feldspar were detected, suggesting these minerals had little effect on the K-Ar date of the illite.

Table 2. Potassium–argon age dates of three size fractions of illite isolated from samples and the corresponding reservoir properties (from Freiburg et al. 2014), intensity ratio (IR), and full width half maximum (FWHM)[1]

Formation	Period	Depth (ft)	Depth (m)	Reservoir Rock Properties			Illite Size Fraction Age [Ma]						IR	FWHM
				Porosity (%)	Permeability (mD)	Classification	0.6-2µm	Error	0.2-0.6µm	Error	<0.2µm	Error		
New Albany	Devonian	2157	657.5	3.9	<0.01	Seal	402.2	5.0	391.0	4.0	347.3	7.1	1.12	0.36
Maquoketa	Ordovician	2816	858.3	4.7	<0.01	Seal	484.1	6.8	453.0	5.4	402.6	6.0	1.12	0.36
Eau Claire	Cambrian	5465	1665.7	1.9	<0.01	Seal	658.3	9.0	398.8	4.9	246.0	4.8	1.37	1.10
upper Mt. Simon	Cambrian	5546	1690.4	9.3	0.74	Seal	598.6	8.6	365.2	5.9	362.1	5.3	1.14	0.73
middle Mt. Simon	Cambrian	6426	1958.6	15.4	5.45	Seal	307.3	6.6	238.3	3.4	251.9	2.6	1.17	0.39
lower Mt. Simon	Cambrian	6741	2054.7	22.0	134.71	Reservoir	343.9	4.3	324.1	6.4	343.9	4.3	1.50	0.84
lower Mt. Simon	Cambrian	6889	2099.8	16.7	85.89	Reservoir	378.0	3.9	321.1	3.6	287.3	5.2	1.34	0.78
lower Mt. Simon	Cambrian	6980	2127.5	20.2	98.73	Reservoir	375.5	7.5	335.0	3.5	329.4	6.5	1.91	0.88
lower Mt. Simon	Cambrian	6986	2129.3	20.5	151.31	Reservoir	347.8	3.7	331.3	3.4	324.6	3.4	1.91	0.90
Argenta	Cambrian	7016	2138.5	8.7	49.54	Seal	304.4	3.4	274.1	3.9	251.5	3.2	1.27	0.51
Argenta	Cambrian	7025	2141.2	10.8	1.13	Seal	246.0	4.8	234.1	3.3	218.4	2.8	1.23	0.52

[1]The IR and FWHM results are from Henkel (2017), who reported oriented, air-dried, and glycolated X-ray diffraction sample results.

Table 3. Random powder X-ray diffraction of grain size fractions 2.0–0.6 µm (c), 0.6–0.2 µm (m), and <0.2 µm (f)

			Illite			Chlorite			Kaolinite			Quartz			K-feldspar			Hematite			Gypsum			Halite		
Unit	Depth (ft)	Depth (m)	c	m	f	c	m	f	c	m	f	c	m	f	c	m	f	c	m	f	c	m	f	c	m	f
New Albany	2157	657.5	x	x		x	x	x				x		x								x	x			
Maquoketa	2816	858.3	x	x		x	x	x				x		x									x			
Eau Claire	5465	1665.7	x	x	x	x	x	x				x			x	x										x
upper Mt. Simon	5546	1690.4	x	x	x	x	x	x				x		x	x	x		x	x					x		x
middle Mt. Simon	6426	1958.6	x	x	x							x	x	x	x	x		x	x			x	x	x		x
lower Mt. Simon	6741	2054.7	x	x	x							x	x	x	x	x		x	x				x	x		x
lower Mt. Simon	6889	2099.8	x	x	x							x	x	x	x	x		x	x				x	x		x
lower Mt. Simon	6980	2127.5	x	x	x							x	x	x	x	x		x	x			x	x	x	x	x
lower Mt. Simon	6986	2129.3	x	x	x							x	x	x	x	x		x	x				x	x		x
Argenta	7016	2138.5		x	x				x			x	x	x					x				x			x
Argenta	7025	2141.2		x	x				x	x	x	x	x	x					x				x			x

Table 4. Illite polytype quantification results for samples with identifiable $2M_1$ illite

			0.6-2µm			0.2-0.6µm			<0.2µm		
Unit	Depth (ft)	Depth (m)	$2M_1$	1M	$1M_d$	$2M_1$	1M	$1M_d$	$2M_1$	1M	$1M_d$
New Albany	2157	657.5	24%	6%	70%	14%	6%	80%	0%	-	-
Maquoketa	2816	858.3	9%	8%	83%	9%	8%	83%	0%	-	-
Eau Claire	5465	1665.7	<5%	6%	89%	0%	-	-	0%	-	-
upper Mt. Simon	5546	1690.4	<5%	7%	88%	0%	-	-	0%	-	-
Argenta	7016	2138.5	<5%	7%	88%	0%	-	-	0%	-	-

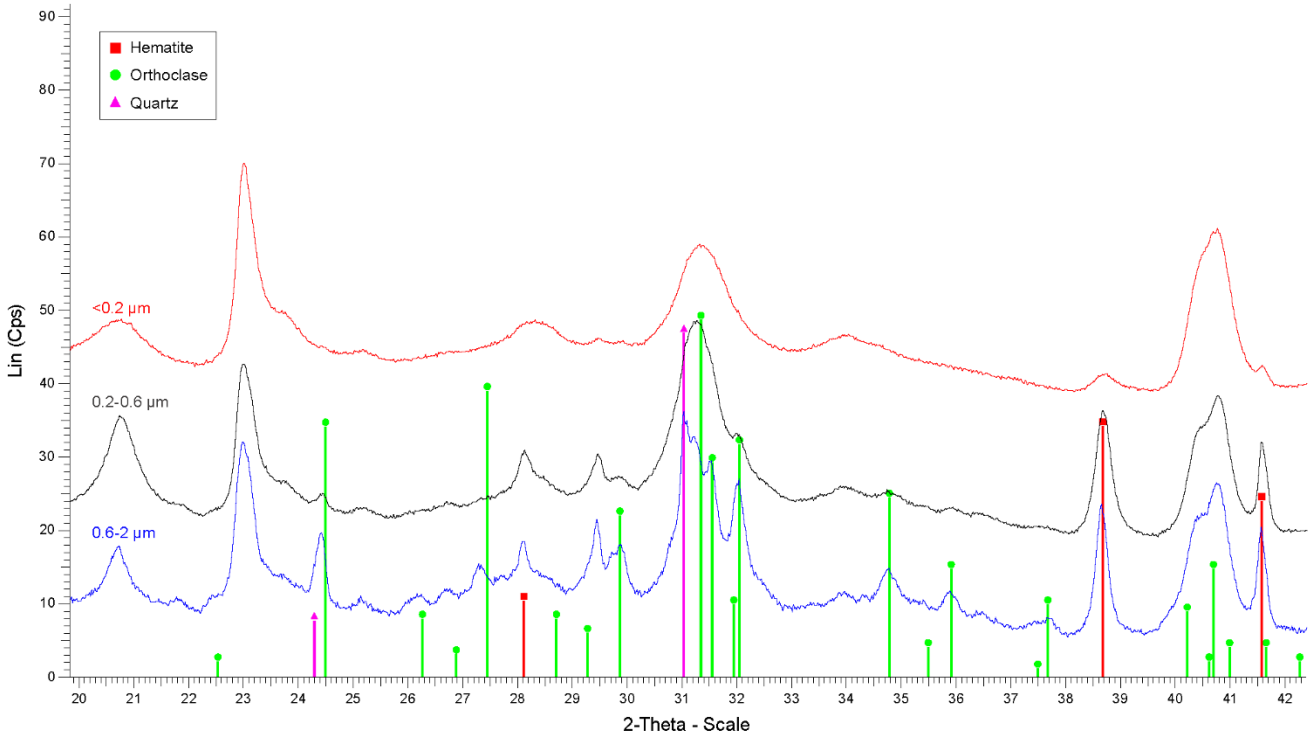

Figure 12. Diffractogram of the different size fractions of illite from the upper Mt. Simon. Size fractions included 2.0–0.6 µm (blue), 0.6–0.2 µm (black), and <0.2 µm (red). Spectral peaks identifying the mineral

peaks hematite (red), orthoclase (green), and quartz (magenta) show major differences across sample spectra. Note the complete lack of contamination of minerals in the <0.2-µm (red) illite sample.

Discussion

The Mt. Simon Sandstone in the Illinois Basin has experienced a complex history of diagenesis, including burial, numerous events of authigenic cement precipitation, and dissolution. This paragenetic history (Figure 11) suggests numerous events of tectonically controlled fluid migration and burial. The age of diagenetic illite from the Mt. Simon Sandstone and overlying major Paleozoic shales, including the Eau Claire, Maquoketa, and New Albany (Figure 13), offers insights into the timing of these tectonic events influencing the overall diagenetic overprint observed in the rocks of the Illinois Basin. The K-Ar dates of diagenetic illite extracted from these rocks suggest a complex history of burial and fluid migration through the Illinois Basin. Despite the absence of wells with samples from the Argenta and lower Mt. Simon in other studies, a strikingly similar diagenesis has been observed in the Mt. Simon throughout the entirety of the Illinois Basin (Hoholick et al. 1984; Fishman 1997; Bowen et al. 2011), with a similar timing of events (Hay et al. 1988; Duffin et al. 1989; Grathoff et al. 2001).

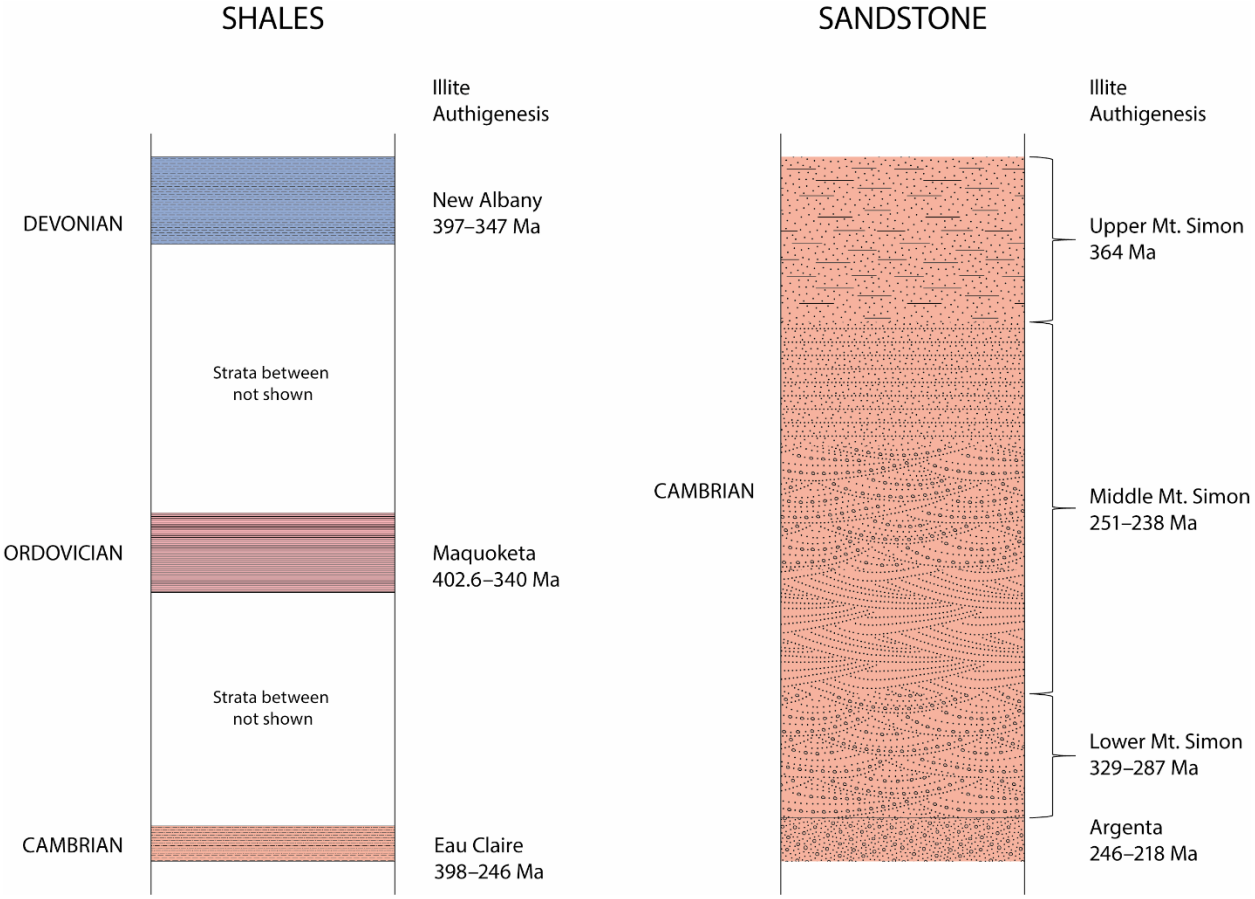

Figure 13. Generalized stratigraphic column of the three major sealing shales and the Mt. Simon Sandstone, including the Argenta, with the range in K-Ar age dates of diagenetic illite in each sampled unit.

Timing of Illitization

Similar events of illitization in Paleozoic rocks in and around the Illinois Basin have been observed previously. Three major episodes have been identified (Grathoff et al. 2001) and were first reported for the Upper Mississippi Valley (Lee and Aronson 1991): 360–340 Ma, 310–250 Ma, and 230–

215 Ma. The oldest episode is mid-Paleozoic and has been observed only within the Maquoketa shale of the Illinois Basin (Grathoff et al. 2001), the Upper Mississippi Valley (Hay et al. 1988; Lee and Aronson 1991), and the Michigan Basin (Girard and Barnes 1995).

The second episode is late Paleozoic and has been observed throughout a much wider area from the Appalachian Basin (Elliott and Aronson, 1987), throughout the Illinois Basin (Duffin et al. 1989; Lee and Aronson 1991; Grathoff et al. 2001), northeastern Missouri (Hay et al. 1988), and the Forrest City Basin in Iowa (Duffin 1990). The timing of Mississippi Valley-type ore deposits on the flanks of the Illinois Basin falls within this episode of illitization.

The third and youngest episode has been observed only in northwestern Illinois near the Upper Mississippi Valley ore deposits. Duffin et al. (1989) reported three dates of illite in the Mt. Simon Sandstone, 217, 254, and 271 Ma, and concluded that illitization and authigenic K-feldspar formed in multiple episodes of potassium metasomatism. Grathoff et al. (2001) proposed that the 254 Ma sample showed approximately 11% $2M_1$ illite and that the age should be adjusted for the presence of detrital illite. The adjusted age they proposed is as young as 214 Ma and thus falls into the youngest episode. With this correction, only two illitization episodes have been reported for the Mt. Simon Sandstone, rather than the three reported by Duffin et al. (1989).

The Mt. Simon and Paleozoic shales of the Illinois Basin of this study show dates of illitization similar to those reported by others (Elliott and Aronson 1987; Hay et al. 1988; Duffin et al. 1989; Duffin 1990; Lee and Aronson 1991; Girard and Barnes 1995; Grathoff et al. 2001), with the addition of a slightly older illitization event recorded in the shales (Figure 13). The older illitization event may be the result of detrital $2M_1$ illite in the samples (Table 4). However, samples containing solely diagenetic illite still record an older event in the Maquoketa (402.6 Ma), Eau Claire (398.8 Ma), and Mt. Simon, with dates ranging from 380 to 360 Ma. These older dates coincide with authigenic K-feldspar dates in the upper Mt. Simon (Duffin et al. 1989) and in the Precambrian basement in Wisconsin (Liu et al. 2003). Authigenic feldspar is prevalent in the Mt. Simon, especially the upper Mt. Simon (Duffin et al. 1989; Fishman 1997) and the underlying Precambrian igneous basement (Duffin 1989; Liu et al. 2003), and it likely accounts for the high percentage of feldspar in the Eau Claire (Palkovic 2015). Duffin et al. (1989) reported a K-Ar age of 396.6 Ma for authigenic feldspar in the upper Mt. Simon on a single sample, whereas Liu et al. (2003) reported Ar-Ar ages from 446 to 359 Ma for authigenic feldspar in the Precambrian alteration profile beneath the Mt. Simon in Wisconsin. They also identified a Late Devonian–Early Mississippian authigenic feldspar event that overlaps the first and second illite events identified by others, implying that the early diagenetic illite and authigenic K-feldspar are likely cogenetic. On the basis of fluid inclusion homogenization temperatures and stable isotopic analysis, authigenic feldspar is interpreted to have originated from hydrothermal basinal brines during the Acadian Orogeny (Figure 14; Liu et al. 2003), much like the Mississippi Valley-type (MVT) deposits of the central Tennessee lead–zinc (Pb-Zn) district (Nakai et al. 1990). Significant areas of new and reactivated deformation occurred in the Illinois Basin concurrent with, or perhaps in response to, the Acadian Orogeny, including the Rough Creek–Shawneetown Fault System, Waterloo–Dupo Anticline, Pennyrile Fault System, Ste. Genevieve Fault System, Lincoln Anticline, Cap au Gres Faulted Flexture, Media Anticline (Kolata and Nelson 1990; Nelson and Marshak 1996), and Reelfoot Rift (Bradbury and Baxter 1992). In addition to this tectonic deformation, igneous activity such as the Avon Diatremes (Shavers et al. 2016) occurred near the Ste. Genevieve Fault System.

Later illitization events observed by others overlap numerous mineralization events throughout the midcontinent. Authigenic feldspar in the central and southern Appalachians that is similar to the authigenic feldspar observed with the late illitization event gave late Paleozoic ages of 322–278 Ma (Hearn et al. 1987) and is likely associated with the Alleghenian Orogeny. Evidence suggests that the MVT ore deposits of the Upper Mississippi Valley Zn-Pb district in northwestern Illinois and southwestern Wisconsin that formed as a result of hydrothermal brine migration during the late

Paleozoic were related to the Alleghenian Orogeny and Ouachita Orogeny (Bethke 1986; Leach and Rowan 1986). Sphalerite deposits of the Upper Mississippi Valley Zn-Pb deposits were dated at 270 ± 5 Ma (Brannon et al. 1992). The Illinois-Kentucky Fluorspar District located on the southern Illinois Basin flank was dated at 277 ± 16 Ma (Chesley et al. 1994), and the nearby Hicks Dome carbonatite was dated at 270 Ma (Zartman et al. 1967; Snee and Hayes 1992). Calcite associated with MVT ore deposits on the flanks of the Illinois and Michigan Basins has been found to date at early Mesozoic (Rasbury and Luczaj 2017). The latest illitization events recorded in the Mt. Simon overlap these late Paleozoic and early Mesozoic mineralization events, which are thought to be associated with tectonically driven hydrothermal brines (Bethke and Marshak, 1990), possibly in response to the Alleghenian Orogeny, the Ouachita Orogeny, the ancestral Rocky Mountain Orogeny (Kluth 1986; McBride and Nelson 1999), and the formation and breakup of Pangea (Figure 14).

Overall, the K-Ar results of this study are interpreted to represent two major events of illitization in the Mt. Simon Sandstone: (1) an early event from approximately 360 to 315 Ma predominantly affecting the lower and upper Mt. Simon sections, and (2) a late event from approximately 250 to 220 Ma affecting the Argenta and middle Mt. Simon. The shales generally show evidence of both events (i.e., New Albany, 347.3 Ma; Eau Claire, 246.0 Ma). These two illitization events roughly correlate with the tectonic deformation observed throughout the Illinois Basin from the Middle Devonian through Early Mississippian and the Early Mississippian to late Permian (Kolata and Nelson 2010), perhaps in response to the orogenic compression identified above. Within the sandstones, the lithostratigraphic differentiation appears to exert a control on selective illitization and may explain younger illite events in older stratigraphic units and the interlayering of events (Figure 13). For example, illite extracted from the Argenta dates primarily to the younger illitization event, whereas the overlying lower Mt. Simon Sandstone illite dates primarily to the older illitization event (Figure 13).

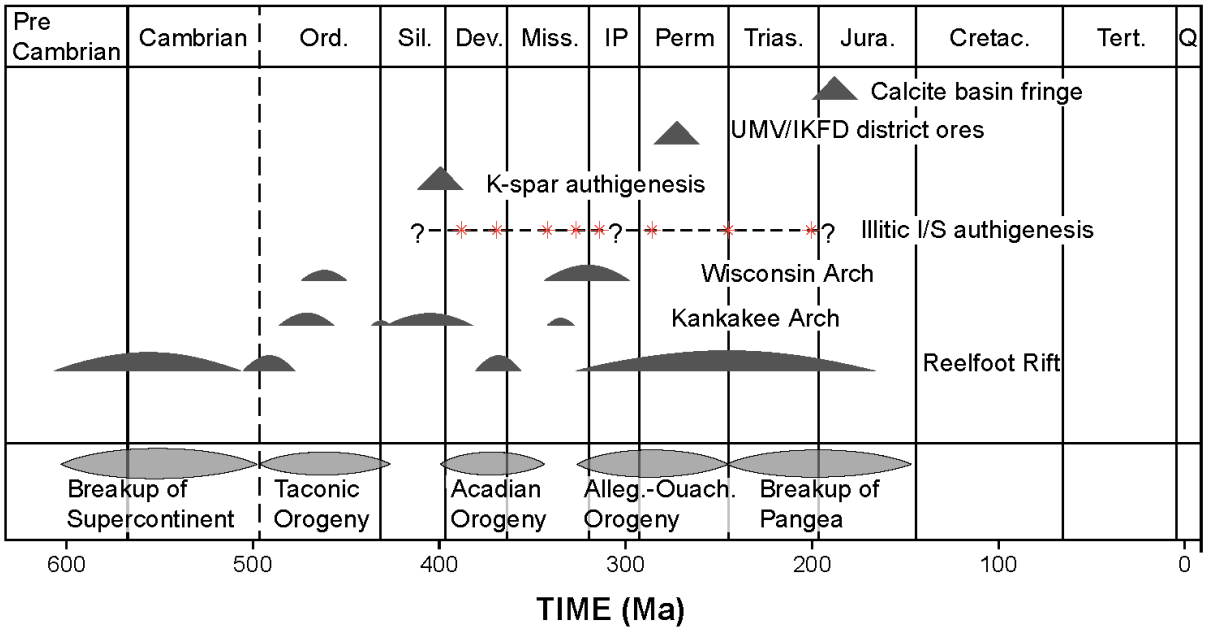

Figure 14. Diagram showing the timing of major structural, tectonic, and diagenetic events in Illinois. UMV/IKFD, Upper Mississippi Valley/Illinois-Kentucky Fluorspar District; I/S (Illite-Smectite). Modified from Fishman (1997), after Kolata and Nelson (1990). AAPG ©1997, reprinted by permission of the AAPG, whose permission is required for further use.

Controls on Illitization

The lithostratigraphy in each section of the Mt. Simon, including the Argenta, is controlled by the depositional variation and detrital source, which controls the variation observed in mineralogy, grain size, grain sorting, and ultimately the diagenetic events (i.e., clay cementation) in each section (Freiburg et al. 2016). This sedimentological and diagenetic variation results in variable reservoir properties within each section (Figure 3). The lower Mt. Simon and the upper Mt. Simon have the best reservoir properties (Figures 3 and 16A,B). Nearly the entire lower Mt. Simon exhibits porosity >10% and up to almost 30%, apart from minor interbedded lagoonal mudstones (Figure 8). The lower Mt. Simon has abundant clay coatings over most detrital grains, which prevent the nucleation of primary pores from occluding authigenic quartz. At least two generations of grain-coating illite have been observed in the lower Mt. Simon (Freiburg et al. 2016). Others have noted pore-filling illite as well as grain-coating illite in the Mt. Simon, with both proposed to be diagenetic (Fishman 1997). Our results confirm that with the absence of $2M_1$, all illite in the lower Mt. Simon is diagenetic (Table 4). The upper Mt. Simon exhibits more segregated reservoir rock with high porosity. The upper Mt. Simon has abundant intertidal shales and lagoonal mudstones interlaminated between high-porosity sandstones (Figure 8). Clay minerals are largely isolated to the shale and mudstone laminae in the upper Mt. Simon, and the interbedded sandstone is commonly well sorted and likely clean of clays from wave action. Detrital clay is preserved in these shales and mudstones in the coarsest clay size fraction (Table 2). With the lack of early pore-filling clays or grain-coating clays in the sandstone, authigenic quartz and feldspar overgrowths are common and abundant (Figure 10). Authigenic feldspar can contaminate the samples, but the XRD data indicated the absence of feldspar in the finest size fraction, with dates similar to those of the medium size fraction and lower Mt. Simon samples (Tables 2 and 3).

Unlike the mostly higher quality lower and upper Mt. Simon reservoirs, which exhibited the older illitization event, the poorer quality middle Mt. Simon and Argenta reservoirs showed a dominant younger event (Figures 3 and 16A,B). Although the reservoir properties of the samples in this study are similar, such as for the middle and lower samples, the overall reservoir properties of the units are starkly different (Figure 3). Nearly the entire Argenta and middle Mt. Simon have porosities of <10%, with overall much lower permeabilities than the lower and upper Mt. Simon (Figure 3; Freiburg et al. 2014, 2016). The Argenta and middle Mt. Simon have textural similarities as well with common poorly sorted coarse-grained facies interbedded with fine-grained facies and abundant pore-filling clays. Pore-filling clays include illite and, most notably, kaolinite. Kaolinite is both pore filling and a detrital mineral or grain replacement. Illite occurs as grain or pore lining and pore filling intermingled with kaolinite where kaolinite occurs.

One explanation for the interlayering of differently aged illite throughout the Argenta and Mt. Simon is the possibility of illite recrystallization and age resetting. In this scenario, the older illite observed in the upper and lower Mt. Simon would have occurred throughout the entire Mt. Simon and Argenta. This older illite would then have been selectively reset with recrystallization of illite solely in the middle Mt. Simon and Argenta during a younger event of illitization. This scenario is unlikely because observed coarser fractions (i.e., the middle Mt. Simon 0.6- to 2.0-µm size fraction) are older and would likely have been reset during this recrystallization event. It is also difficult to explain the stratigraphic isolation of this event with this younger illite solely observed in the tight Argenta and middle Mt. Simon. Both burial temperature and hydrologic (open-system) conditions would be expected to exert a control on the entire Mt. Simon rather than on interlayered stratigraphic units. In addition, the resetting temperature of illite is at least 250 °C (Hunziker et al. 1986; Wemmer and Ahrendt 1997), and the maximum temperatures that the Mt. Simon sediments experienced is significantly lower (Grathoff et al. 2001). The possible occurrence of dickite in the Argenta (Henkel 2017) suggests that temperatures may have exceeded previous model temperatures, although still not nearly high enough to reset illite.

Another possible and more likely explanation for the varied ages in the sandstone units is the change in mineralogy within each unit and the source of $SiO_{2(aq)}$, Al^{+3}, K^{+}, and H^{+}, all necessary components for illite nucleation and growth (Bjorkum and Gjelsvik 1988; Aagaard et al. 1992; Bjørlykke et al. 1995; Lander and Bonnell 2010). The active formation of illite is likely controlled by mineral buffers present within the sandstone (Berger et al. 1997). In formation waters that exceed 100 °C (212 °F), $SiO_{2(aq)}$ concentrations tend to be at or near equilibrium values for quartz (Kharaka et al. 1985). Kaolinite acts as an Al buffer (Bazin et al. 1997a) and K-feldspar buffers K^{+} in the absence of externally derived fluids (Bazin et al. 1997b; Yuan et al. 2019), such as K-rich brines derived from deep in the Illinois Basin (Hay et al. 1988; Fishman 1997; Grathoff et al. 2001). The mineralogy is varied throughout the Mt. Simon units and Argenta (Freiburg et al. 2016), likely a result of changing depositional environments separated by hiatal surfaces (Freiburg et al. 2014) and a locally heterogeneous basement (Freiburg et al. 2019a) that supplied sediment for early depositional units (Freiburg et al. 2019b) while later units were supplied sediment from more distal sources (Lovell and Bowen 2013). Both the Argenta and the middle Mt. Simon are believed to mark important basin evolution events (Freiburg et al. 2016). The Argenta reflects the earliest Cambrian sediments, which are highly immature, poorly sorted coarse- to clay-size sediments that are proximally sourced from normal fault-controlled highs on the flank of a local rift basin (Figure 4). The Argenta is overlain by more mature sediments in the lower Mt. Simon, likely representing a slowed sedimentation rate in a partially filled rift basin. The middle Mt. Simon represents renewed accommodation space with an influx of poorly sorted coarse- to clay-sized sediments, including increased feldspar. The upper Mt. Simon, much like the lower, represents a slowed sedimentation rate with more mature sediments. A varying detrital source rock and changes in depositional environments likely played major roles in the varying authigenic minerals, such as kaolinite.

Kaolinite is abundant in the Argenta and is likely the result of low-pH groundwaters reacting with feldspars and micas during a hiatus before deposition of the lower Mt. Simon (Freiburg et al. 2014). Although kaolinite was not detected by XRD in the single sample dated from the middle Mt. Simon in this study (Tables 1 and 3), it was observed throughout the middle Mt. Simon, although not in the abundance that was observed in the Argenta (Tables 1 and 3, Figure 10). Groundwater recharge in the middle Mt. Simon was likely common in the predominantly terrestrial deposits before marine incursion in the upper Mt. Simon. Kaolinite is largely absent in the lower and upper Mt. Simon. Kaolinite may have supplied Al in the Argenta and middle Mt. Simon for continued illite growth during a late K-rich brine migration event. The finely crystalline hairy illite intergrown within pore-filling kaolinite is evidence that kaolinite factored into the nucleation of the youngest dated illite (Figure 10). It also implies that the geochemistry involved in the nucleation of the oldest illite event differed from that of the younger event.

The abundant illite in the lower Mt. Simon is proposed to be the result of feldspar alteration and dissolution (Freiburg et al. 2014, 2016), where K and Al are derived from K-feldspar. Most feldspars in the lower Mt. Simon are partially to nearly completely dissolved, leaving abundant secondary porosity. Feldspar dissolution may have been caused by leaching of meteoric water (Emery et al. 1990), hydrothermal fluids (Taylor and Land 1996), or organic processes producing CO_2 and organic acids originating from kerogen maturation and hydrocarbon degradation (Yuan et al. 2019) producing C. Feldspar dissolution appears to be one of the latest diagenetic events (Figure 11), as evidenced by the abundant feldspar casts in the lower Mt. Simon (Figure 10). Compaction processes during burial would be expected to destroy casts formed during early dissolution events. However, the preservation of the feldspar casts may be the result of the early iron oxide coatings described by Bowen et al. (2011). When K-feldspar is dissolved, K^{+}, $SiO_{2(aq)}$, and Al^{+3} are released into solution (Yuan et al. 2019). Diagenetic illite will not nucleate directly from these ions; rather, these ions react with minerals, causing illitization. A common reactant is kaolinite (Lander and Bonnell 2010). With the near to complete lack of kaolinite in the lower Mt. Simon and lack of evidence for the complete illitization of kaolinite, smectite is the

favored reactant for alteration to illite. Thick smectite coatings over detrital grains are common in a dominantly braided river environment (Worden and Morad 2003), the predominant depositional setting of the lower Mt. Simon (Freiburg et al. 2014; Leetaru and Freiburg 2014). During illitization of detrital smectite, relatively little K^+ is consumed, leading to a high concentration of K^+ in the pore water (Thyne 2001). Because interbedded mudstones generally contain lower percentages of feldspar and high percentages of detrital clay, illitization reactions can consume large amounts of K^+, with diffusion transfer from the K^+-saturated pore waters of the sandstone to the K^+-undersaturated pore waters of the mudstone (Yuan et al. 2019). Both the lower and upper Mt. Simon contain interbedded mudstone (Figure 8). Mudstone in the lower Mt. Simon is rarer and more isolated but is common in the upper Mt. Simon. Mixed-layered illite–smectite remaining in the upper Mt. Simon (Table 1) is likely the result of partial illitization of mudstones. The lower Mt. Simon is void of smectite (Table 1). All grain-coating and pore-filling smectite is illitized, likely as a direct result of K-rich hydrothermal brine migrating through the most porous units of the Mt. Simon, during which K-feldspar is altered and dissolved. With the complete illitization of smectite and the abundant secondary porosity resulting from K-feldspar dissolution, high concentrations of K^+, $SiO_{2(aq)}$, and Al^{+3} in the pore water are likely. This may explain the common feldspar overgrowths observed in the lower and especially the upper Mt. Simon (Figure 9).

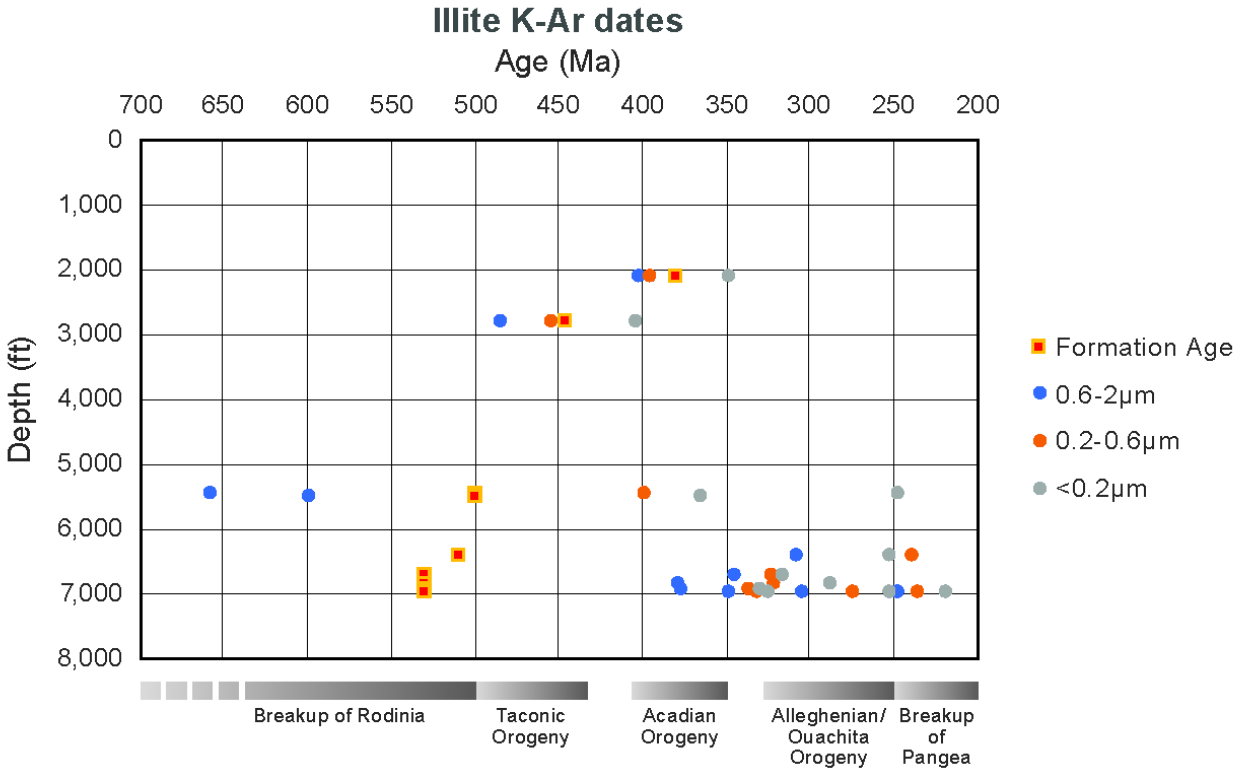

Figure 15. Plot of the sample depths, general depositional age of the sample formation, and K-Ar age date of the three illite size fractions. Identified are the approximate duration of major tectonic events during the Paleozoic and end of the Proterozoic that may have affected formation burial, fluid migration, or both in the Illinois Basin.

A

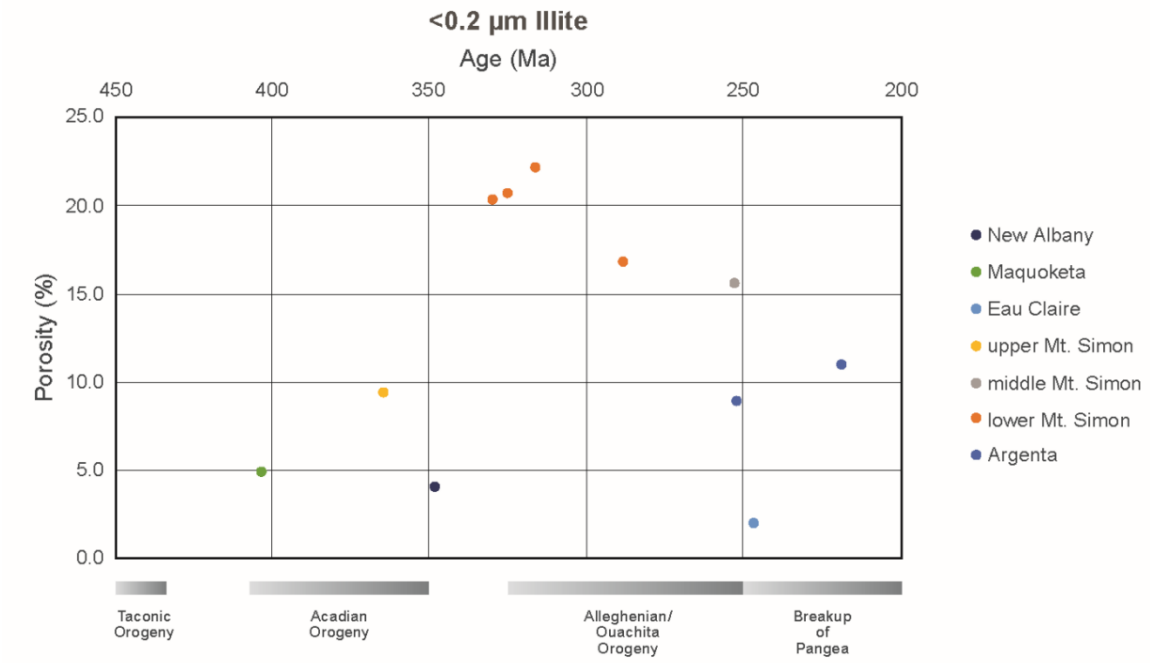

B

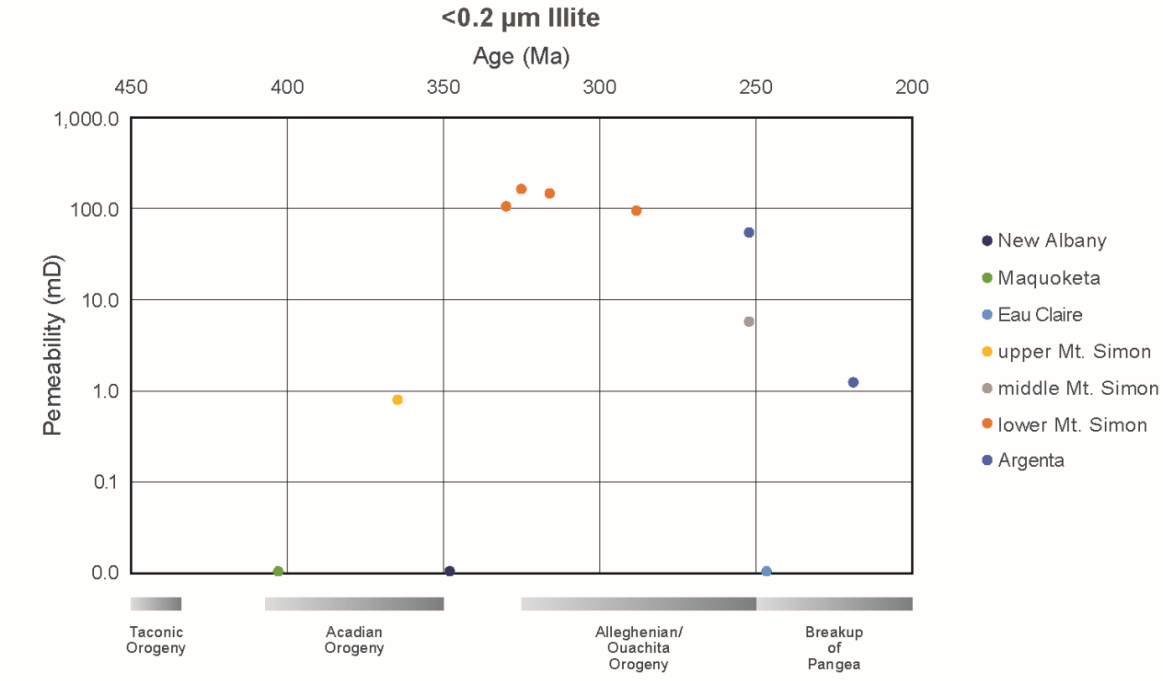

Figure 16. Plot of the sample (A) porosity and (B) permeability, and the K-Ar age date of the finest illite size fraction. Identified are the approximate durations of major tectonic events during the Paleozoic and Mesozoic that may have affected formation burial, fluid migration, or both in the Illinois Basin.

Conclusions

1. Potassium-argon dates of illite indicating two major events of illitization were identified in the Cambrian-age Mt. Simon Sandstone in central Illinois: (1) the early event formed illite from 360 to 315 Ma, predominantly in the porous lower and upper Mt. Simon sections, and (2) the late event formed illite from 250 to 220 Ma, predominantly in the tight Argenta and middle Mt. Simon.
2. Tectonic activity during the Mt. Simon deposition resulted in depositional variation, changes in the detrital source, and heterogeneity in detrital mineralogy. Detrital mineralogy exerted a major control on the diagenetic products observed throughout the Mt. Simon and resulted in the interlayering of illite events, as noted above. For example, the Argenta and middle Mt. Simon reflect units with a high sedimentation rate, immature detritus compared with other units, poorly sorted sediments, and abundant pore-filling clays. The tectonic inactivity of these units postdeposition led to slowed rates of deposition and more mature overlying sediments, an influx of meteoric waters, and early kaolinization of pore-filling clays in the Argenta and middle Mt. Simon.
3. The early and most dominant illitization event formed illite in the lower and upper Mt. Simon and likely resulted in major K-feldspar dissolution and secondary porosity enhancement in the lower Mt. Simon. This event occurred during the Late Devonian to Late Carboniferous and correlates to widespread folding, faulting, and igneous activity in and around the Illinois Basin. These deformation events are likely in response to major tectonic events, including the end of the Acadian and predominantly the Alleghenian and Ouachita Orogenies.
4. The late illitization event occurred during the Late Permian through Late Triassic and likely in response to compressional stresses during the formation of Pangea and later an episode of extension and reactivation of faults during the breakup of Pangea.
5. During early illitization, migrating brines followed the most porous pathways, illitizing all smectite, including pore-lining terrestrial smectite in the lower Mt. Simon and smectite-rich tidal shale and terrestrial mudstone in the upper Mt. Simon. Potassium feldspar was a major reactant during illitization, leading to K-feldspar dissolution and an excess source of K and resulting in the authigenic feldspar precipitation observed in the Mt. Simon, especially the upper Mt. Simon.
6. With the consumption and illitization of all smectite in the lower and upper Mt. Simon during the early event and the absence of a reactant to form illite during the late event, pore-filling kaolinite, common in the Argenta and middle Mt. Simon, reacted to form illite during the late event.

References

Aagaard, P., J.S. Jahren, and P.K. Egeberg, 1992, North Sea clastic diagenesis and formation water constraints, *in* Y.K. Kharaka and A.S, Maest, eds., Water–rock interaction: Proceedings of the 7th International Symposium on Water–Rock Interaction, volume 2: Rotterdam, Balkema, p. 1147–1152.

Bazin, B., É. Brosse, and F. Sommer, 1997a, Chemistry of oil-field brines in relation to diagenesis of reservoirs 1. Use of mineral stability fields to reconstruct in situ water composition. Example of the Mahakam Basin: Marine and Petroleum Geology, v. 14, no. 5, p. 481–495.

Bazin, B., É. Brosse, and F. Sommer, 1997b, Chemistry of oil-field brines in relation to diagenesis of reservoirs—2. Reconstruction of palaeo-water composition for modelling illite diagenesis in the Greater Alwyn area (North Sea): Marine and Petroleum Geology, v. 14, no. 5, p. 497–511.

Berger, G., J.C. Lacharpagne, B. Velde, D. Beaufort, and B. Lanson, 1997, Kinetic constraints on illitization reactions and the effects of organic diagenesis in sandstone/shale sequences: Applied Geochemistry, v. 12, no. 1, p. 23–35.

Bethke, C.M., 1986, Hydrologic constraints on the genesis of the Upper Mississippi Valley mineral district from Illinois Basin brines: Economic Geology, v. 81, no. 2, p. 233–249.

Bethke, C.M., and S. Marshak, 1990, Brine migrations across North America—The plate tectonics of groundwater: Annual Review of Earth and Planetary Sciences, v. 18, no. 1, p. 287–315.

Bickford, M.E., W.R. Van, and I. Zietz, 1986, Proterozoic history of the midcontinent region of North America: Geology, v. 14, no. 6, p. 492–496.

Bickford, M.E., W.R. Van Schmus, K.E. Karlstrom, P.A. Mueller, G.D. Kamenov, 2015, Mesoproterozoic-trans-Laurentian magmatism: A synthesis of continent-wide age distributions, new SIMS U-Pb ages, zircon saturation temperatures, and Hf and Nd isotopic compositions: Precambrian Research, 265, pp. 286-312

Bjorkum, P.A., and N. Gjelsvik, 1988, An isochemical model for formation of authigenic kaolinite, K-feldspar and illite in sediments: Journal of Sedimentary Research, v. 58, no. 3, p. 506–511.

Bjørlykke, K., P. Aagaard, P.K. Egeberg, and S.P. Simmons, 1995, Geochemical constraints from formation water analyses from the North Sea and the Gulf Coast Basins on quartz, feldspar and illite precipitation in reservoir rocks: Geological Society of London, Special Publications 86, p. 33–50.

Bowen, B.B., R.I. Ochoa, N.D. Wilkens, J. Brophy, T.R. Lovell, N. Fischietto, C.R. Medina, and J.A. Rupp, 2011, Depositional and diagenetic variability within the Cambrian Mount Simon Sandstone: Implications for carbon dioxide sequestration: Environmental Geosciences, v. 18, no. 2, p. 69–89.

Bradbury, J.C., and J.W. Baxter, 1992, Intrusive breccias at Hicks Dome, Hardin County, Illinois: Illinois State Geological Survey, Circular 550, 23 p.

Braile, L.W., W.J. Hinze, G.R. Keller, E.G. Lidiak, J.L. Sexton, 1986, Intrusive breccias at Hicks Dome, Hardin County, Illinois: Illinois State Geological Survey, Circular 550, 23 p.

Brannon, J.C., F.A. Podosek, and R.K. McLimans, 1992, Alleghenian age of the Upper Mississippi Valley zinc–lead deposit determined by Rb-Sr dating of sphalerite: Nature, v. 356, p. 509–511.

Chesley, J.T., A.N. Halliday, T.K. Kyser, and P.G. Spry, 1994, Direct dating of Mississippi valley-type mineralization; use of Sm-Nd in fluorite: Economic Geology, v. 89, no. 5, p. 1192–1199.

Collinson, C., M.L. Sargent, and J.R. Jennings, 1988, Illinois Basin region, *in* L.L. Sloss, ed., Sedimentary cover—North American craton: U.S., *in* The geology of North America, volume D-2: Boulder, Colorado, Geological Society of America, p. 383–426.

Duffin, M.E., 1989, Nature and origin of authigenic K-feldspar in Precambrian basement rocks of the North American midcontinent: Geology, v. 17. no. 8, p. 765–768.

Duffin, M.E., 1990, Potassic alteration of Cambrian-Ordovician sandstones and Precambrian basement rocks of the North American midcontinent: University of Illinois at Urbana-Champaign, PhD dissertation, 121 p.

Duffin, M.E., M. Lee, G.D. Klein, and R.L. Hay, 1989, Potassic diagenesis of Cambrian sandstones and Precambrian granitic basement in UPH-3 deep hole, Upper Mississippi Valley, USA: Journal of Sedimentary Research, v. 59, no. 5, p. 848–861.

Elliott, W.C., and J.L. Aronson, 1987, Alleghenian episode of K-bentonite illitization in the southern Appalachian Basin: Geology, v. 15, no. 8, p. 735–739.

Emery, D., K.J. Myers, R. Young, 1990, Ancient subaerial exposure and freshwater leaching in sandstones: Geology, v. 18, no. 12, p. 1178–1181.

Fishman, N.S., 1997, Basin-wide fluid movement in a Cambrian paleoaquifer: Evidence from the Mt. Simon Sandstone, Illinois and Indiana, *in* I.P. Montanez, J.M. Gregg, and K.L. Shelton, eds., Basin-wide diagenetic patterns: Integrated petrologic, geochemical, and hydrologic considerations: SEPM Special Publication 57, p. 221–234.

Freiburg, J.T., J.H. McBride, D.H. Malone, and H.E. Leetaru, 2019a, Petrology, geochronology, and geophysical characterization of Mesoproterozoic rocks in central Illinois, USA: Geoscience Frontiers (in press), https://doi.org/10.1016/j.gsf.2019.07.004.

Freiburg, J.T., D.H. Malone, and A. Beckett, 2019b, Basement crust age and Rodinian rifting in the Illinois Basin: Detrital zircon geochronology of basal Cambrian strata: GSA Abstracts with Programs, session no. 125-1.

Freiburg, J.T., D.H. Malone, S.J. Malone, and M.E. Holland, 2020, Detrital zircon geochronology of basal Cambrian strata in the deep Illinois Basin, USA: Evidence for Mesoproterozoic-Cambrian tectonic and sedimentary evolution of central Laurentia: Journal of Geology (submitted).

Freiburg, J.T., D.G. Morse, H.E. Leetaru, R.P. Hoss, and Q. Yan, 2014, A depositional and diagenetic characterization of the Mt. Simon Sandstone at the Illinois Basin – Decatur Project carbon capture and storage site, Decatur, Illinois, USA: Illinois State Geological Survey, Circular 583, 62 p.

Freiburg, J.T., R.W. Ritzi, and K.S. Kehoe, 2016, Depositional and diagenetic controls on anomalously high porosity within a deeply buried CO_2 storage reservoir—The Cambrian Mt. Simon Sandstone, Illinois Basin, USA: International Journal of Greenhouse Gas Control, v. 55, p. 42–54.

Girard, J.P., and D.A. Barnes, 1995, Illitization and paleothermal regimes in the Middle Ordovician St. Peter Sandstone, central Michigan basin: K-Ar, oxygen isotope, and fluid inclusion data: AAPG Bulletin, v. 79, no. 1, p. 49–69.

Grathoff, G.H., and D.M. Moore, 1996, Illite polytype quantification using Wildfire© calculated X-ray diffraction patterns: Clays and Clay Minerals, v. 44, no. 6, p. 835–842.

Grathoff, G.H., D.M. Moore, R.L. Hay, and K. Wemmer, 2001, Origin of illite in the lower Paleozoic of the Illinois Basin: Evidence for brine migrations: Geological Society of America Bulletin, v. 113, no. 8, p. 1092–1104.

Hay, R.L., M. Lee, D.R. Kolata, J.C. Matthews, and J.P. Morton, 1988, Episodic potassic diagenesis of Ordovician tuffs in the Mississippi Valley area: Geology, v. 16, no. 8, p. 743–747.

Haines, S.H., and B.A. van der Pluijm, 2008, Clay quantification and Ar–Ar dating of synthetic and natural gouge: Application to the Miocene Sierra Mazatán detachment fault, Sonora, Mexico: Journal of Structural Geology, v. 30, no.4, p. 525–538.

Hearn Jr, P.P., J.F. Sutter, and H.E. Belkin, 1987, Evidence for late-Paleozoic brine migration in Cambrian carbonate rocks of the central and southern Appalachians: Implications for Mississippi Valley-type sulfide mineralization: Geochemica et Cosmochimica Acta, 51(5), pp. 1323-1334

Henkel, K., 2017, Clay mineral diagenesis in the Paleozoic reservoir and seals of the Illinois Basin – Decatur Project, USA: Implications to carbon dioxide storage: Ernst-Moritz-Arndt-University Greifswald, master's thesis.

Hoholick, J.D., T. Metarko, and P.E. Potter, 1984, Regional variations of porosity and cement: St. Peter and Mount Simon sandstones in Illinois Basin: AAPG Bulletin, v. 68, no. 6, p. 753–764.

Hunziker, J.C., M. Frey, N. Clauer, R.D. Dallmeyer, H. Friedrichsen, W. Flehmig, K. Hochstrasser, P.T. Roggwiler, and H. Schwander, 1986, The evolution of illite to muscovite: Mineralogical and isotopic data from the Glarus Alps, Switzerland: Contributions to Mineralogy and Petrology, v. 92, no. 2, p. 157–180.

Kharaka, Y.K., R.W. Hull, and W.W. Carothers, 1985, Water–rock interactions in sedimentary basins.

Kluth, C.F., 1986, Plate tectonics of the ancestral Rocky Mountains: Part III. Middle Rocky Mountains, *in* J.A. Peterson, ed., Paleotectonics and sedimentation in the Rocky Mountain region, United States: American Association of Petroleum Geologists Memoir 41, p. 353–369.

Kolata, D.R., 2010, Cambrian and Ordovician Systems (Sauk Sequence and Tippecanoe I Subsequence), *in* D.R. Kolata and C.K. Nimz, eds., Geology of Illinois: Champaign, Illinois State Geological Survey, p. 136–157.

Kolata, D.R., and W.J. Nelson, 1990, Tectonic history of the Illinois Basin, *in* Part I. Illinois Basin: Evolution, *in* M.W. Leighton, D.R. Kolata, D.F. Oltz, and J.J. Eidel, eds., Interior cratonic basins: American Association of Petroleum Geologists Memoir 51, p. 263–285.

Kolata, D.R. and Nelson, W.J., 1997. Role of the Reelfoot rift/Rough Creek graben in the evolution of the Illinois basin. Geological Society of America Special Papers, *312*, pp.287-298

Kolata, D.R., and W.J. Nelson, 2010, Tectonic history, *in* D.R. Kolata and C.K. Nimz, Geology of Illinois: Champaign, Illinois State Geological Survey, p. 77–89.

Lander, R.H., and L.M. Bonnell, 2010, A model for fibrous illite nucleation and growth in sandstones: AAPG Bulletin, v. 94, no. 8, p. 1161–1187.

Leach, D.L., and E.L. Rowan, 1986, Genetic link between Ouachita foldbelt tectonism and the Mississippi Valley–type lead–zinc deposits of the Ozarks: Geology, v. 14, no. 11, p. 931–935.

Lee, M., and J.L. Aronson, 1991, Repetitive occurrence of potassic diagenesis in the region of the Upper Mississippi Valley (UMV) mineral district: Implications for a persistent paleo-hydrological setting favorable for diagenesis, *in* Program and Abstracts for Clay Minerals Society 28th Annual Meeting, Houston, Texas: Boulder, Colorado, Clay Minerals Society, p. 98–100.

Leetaru, H.E., and J.T. Freiburg, 2014, Litho-facies and reservoir characterization of the Mt. Simon Sandstone at the Illinois Basin – Decatur Project: Greenhouse Gases: Science and Technology, v. 4, no. 5, p. 580–595.

Leetaru, H.E., and J.H. McBride, 2009, Reservoir uncertainty, Precambrian topography, an carbon sequestration in the Mt. Simon Sandstone, Illinois Basin: Environmental Geosciences, 16(4), pp.235-243

Liu, J., R.L. Hay, A. Deino, and T.K. Kyser, 2003, Age and origin of authigenic K-feldspar in uppermost Precambrian rocks in the North American Midcontinent: GSA Bulletin, v. 115, no. 4, p. 422–433.

Lovell, T.R., and B.B. Bowen, 2013, Fluctuations in sedimentary provenance of the Upper Cambrian Mount Simon Sandstone, Illinois Basin, United States: The Journal of Geology, v. 121, no. 2, p. 129–154.

McBride, J.H., and W.J. Nelson, 1999, Style and origin of mid-Carboniferous deformation in the Illinois Basin, USA—Ancestral Rockies deformation? Tectonophysics, v. 305, nos. 1–3, p. 249–273.

McBride, J.H., and D.R. Kolata, 1999, Upper crust beneath the central Illinois Basin, USA: Geological Society of America Bulletin, 111(3), pp.375-394.

Monson, C.C., J.R. Damico, and N. Grigsby, 2020, A regional-scale model of the Mt. Simon Sandstone in the Illinois Basin, Part 1: Conceptual model: Illinois State Geological Survey Circular.

Nakai, S.I., A.N. Halliday, S.E. Kesler, and H.D. Jones, 1990, Rb–Sr dating of sphalerites from Tennessee and the genesis of Mississippi Valley type ore deposits: Nature, v. 346, p. 354–357.

Nelson, W.J., and S. Marshak, 1996, Devonian tectonism of the Illinois Basin region, US continental interior, in B.A. van der Pluijm and P.A. Catacosinos, eds., Basement and basins of eastern North America: Geological Society of America Special Paper 308, p. 169–180.

Palkovic, M.J., 2015, Depositional characterization of the Eau Claire Formation at the Illinois Basin – Decatur Project: Facies, mineralogy and geochemistry: University of Illinois at Urbana-Champaign, MS thesis.

Pevear, D.R., 1999, Illite and hydrocarbon exploration: Proceedings of the National Academy of Sciences, v. 96, no. 7, p. 3440–3446.

Pollington, A.D., R. Kozdon, and J.W. Valley, 2011, Evolution of quartz cementation during burial of the Cambrian Mount Simon Sandstone, Illinois Basin: In situ microanalysis of $\delta^{18}O$: Geology, v. 39, no. 12, p. 1119–1122.

Rasbury, T., and J. Luczaj, 2017, U-Pb dating of calcite to constrain basinal brine flux events: An example from the Upper Midwest USA: American Geophysical Union Fall Meeting, New Orleans, December 11–15, abstract EP12A-05.

Reesink, A.J.H, J.L. Best, J.T. Freiburg, N.D. Webb, C.C.Monson, R.W. Ritzi, 2020, Interpreting pre-vegetation landscape dynamics: the Cambrian lower Mount Simon Sandstone, Illinois, USA. Journal of Sedimentary Research

Shavers, E.J., A. Ghulam, J. Encarnacion, D.L. Bridges, and P.B. Luetkemeyer, 2016, Carbonatite associated with ultramafic diatremes in the Avon Volcanic District, Missouri, USA: Field, petrographic, and geochemical constraints: Lithos, v. 248, p. 506–516.

Snee, L.W., and T.S. Hayes, 1992, $^{40}Ar/^{39}Ar$ geochronology of intrusive rocks and Mississippi-Valley-type mineralization and alteration from the Illinois/Kentucky fluorspar district, *in* M.B. Goldhaber and J.J. Eidel, eds., Mineral resources in the Illinois Basin in the context of basin evolution: Program and abstracts: US Geological Survey Open-File Report 92-1, p. 59–60.

Steiger, R.H., and E. Jaeger, 1977, Subcommission on Geochronology: Convention on the use of decay constants in geo-and cosmochronology: Earth and Planetary Science Letters, v. 36, no. 3, p. 359–362.

Sverjensky, D.A., 1986, Genesis of Mississippi Valley-type lead-zinc deposits: Annual Review of Earth and Planetary Sciences, v. 14, no. 1, p. 177–199.

Taylor, T.R. and L.S. Land, 1996, Association of allochthonous waters and reservoir anhancement in deeply buried Miocene sandstones: Picaroon field, Corsair trend, offshore Texas: SEMP Special Publication No. 55

Thyne, G., 2001, A model for diagenetic mass transfer between adjacent sandstone and shale: Marine and Petroleum Geology, v. 18, no. 6, p. 743–755.

Wemmer, K., 1991, K/Ar-Altersdatierungsmöglichkeiten für retrograde Deformationsprozesse im spröden und duktilen Bereich—Beispiele aus der KTB-Vorbohrung (Oberpfalz) und dem Bereish der Insubrischen Linie (N-Italien): Göttingen, Im Selbstverlag der Geologischen Institute der Georg-August-Universität Göttingen, No. 51, 61 p.

Wemmer, K., and H. Ahrendt, 1997, Comparative K-Ar and Rb-Sr age determinations of retrograde processes on rocks from the KTB deep drilling project: Geologische Rundschau, v. 86, no. 1, p. S272–S285.

Worden, R.H., and S. Morad, 2003, Clay minerals in sandstones: Controls on formation, distribution and evolution, *in* R.H. Worden, and S. Morad, eds., Clay mineral cements in sandstones: International Association of Sedimentologists Special Publication 34, p. 3–42.

Yuan, G., Y. Cao, H.-M. Schulz, F. Hao, J. Gluyas, K. Liu, T. Yang, Y. Wang, K. Xi, and F. Li, 2019, A review of feldspar alteration and its geological significance in sedimentary basins: From shallow aquifers to deep hydrocarbon reservoirs: Earth-Science Reviews, v. 191, p. 114–140.

Zartman, R.E., M.R. Brock, A.V. Heyl, and H.H. Thomas, 1967, K-Ar and Rb-Sr ages of some alkalic intrusive rocks from central and eastern United States: American Journal of Science, v. 265, no. 10, p. 848–870.

Chapter vi Manuscript

High-resolution pore space imaging, mineralogical characterization, and sealing capacity estimates of caprock at the Illinois Basin – Decatur Project, USA

High-resolution pore space imaging, mineralogical characterization, and sealing capacity estimates of caprock at the Illinois Basin–Decatur Project, USA

Jared T. Freiburg[1, 2*], Markus Peltz[2], Donna C. Willette[1], Georg H. Grathoff[2]

*corresponding author: freiburg@illinois.edu

[1]*Illinois State Geological Survey, Prairie Research Institute, University of Illinois at Urbana-Champaign, 615 E. Peabody Drive, Champaign, IL 61820, USA*

[2]*Department of Geography and Geology, University of Greifswald, Greifswald, 17489, Germany*

Abstract

At the Illinois Basin–Decatur Project, a large-scale CO_2 capture and geologic storage project in the saline Mt. Simon Sandstone in central Illinois, three overlying and laterally continuous shale formations (the Eau Claire, Maquoketa, and New Albany) are considered confining units or caprock overlying the sandstone reservoir. The reservoir contains internal baffles that will influence CO_2 migration pathways and future interaction with caprock. Understanding sealing properties of caprocks and baffles is vital to the project and future commercialization of geologic carbon storage. In this paper, nanoscale-resolution focused ion beam (FIB) scanning electron microscopy (SEM), mercury injection capillary pressure (MICP), X-ray diffraction (XRD) spectroscopy, and quantitative evaluation of minerals by scanning electron microscopy (QEMSCAN) were used to characterize the controls on the sealing integrity of these caprocks and reservoir baffles. Results show that porosity and pore size generally decrease with depth, except for the carbonate-rich Maquoketa Shale. The Maquoketa contains the highest pore volume owing to dolomite as a significant portion of the mineral matrix when compared with the other mudstone and shale intervals, which are clay-rich. The shallowest caprock sample, the organic-rich New Albany Shale, has the highest frequency of the smallest pore throat size and is most comparable, with respect to pore sizes and entry pressures, to the deepest black shale and primary reservoir seal, the Eau Claire. Point specific MICP threshold pressure results, theoretical calculations based upon a range of permeabilities, and column height calculations indicate that the Mt. Simon mudstone and Eau Claire Shale are effective seals to CO_2 in the Mt. Simon reservoir.

Keywords:

caprock, shale, mudstone, porosity, permeability, FIB-SEM, seal capacity, Illinois Basin, carbon storage

Introduction

Research on subsurface CO_2 storage in geological formations has been a recent global focus to mitigate the rise of anthropogenic CO_2 emissions into the atmosphere, which is believed to be a major contributing factor to global climate change (Martin-Robertse t al., 2021). Geologic carbon storage has been comprehensively researched with preferred storage in highly saline reservoirs with overlying caprocks such as shale and mudstone providing effective sealing capacity (Koide et al., 1992; Holloway, 2001; Pacala and Socolow 2004; Bachu et al. 2007; Friedmann, 2007; Benson and Cole, 2008; Oelkers and Cole 2008; Lackner and Brennan, 2009; Rackley, 2017). A caprock is an essential component of a geologic carbon capture and storage (CCS) system. A sealing interval or caprock critically depends on the pore systems since they may provide a pathway for fluid flow. In sedimentary basins, shale and its non-fissile equivalent mudstone and their horizontal and vertical distribution and continuity are major controls of localized and regional fluid flow (Hildenbrand et al., 2002), acting as barriers to vertical flow preventing upward or downward leakage.

Besides being a seal or aquitard for aquifers, petroleum systems, or in this case a CCS system, shale may also act as a source rock and reservoir in petroleum systems. Pore connectivity, natural or induced, is crucial to produce hydrocarbons and inversely critical to contain fluid migration. In order to understand the controls on the sealing properties of the rock as a CCS reservoir caprock, the extent and connectivity of pore space must be measured and quantitatively described. To understand the controls on pore and pore network development mineralogy must be evaluated.

The Illinois Basin–Decatur Project (IBDP) in Decatur, Illinois, is a large-scale demonstration of deep saline geological storage of 1 million metric tons of CO_2 injected, stored, and actively monitored in the lower most unit of the Cambrian-age Mt. Simon Sandstone at a depth of approximately 2100 m (Figure 1). The Mt. Simon is highly heterogeneous with the injection unit comprised dominantly of fluvial and eolian

63 deposited sandstones (Freiburg et al., 2014; Reesink et al., 2020). Within and overlying the injection
64 unit, numerous well-cemented sandstones and mudstones occur that act as localized baffles to vertical
65 fluid migration. The Mt. Simon is overlain by three marine deposited shales: the Eau Claire; Maquoketa,
66 and New Albany which are considered the caprocks at the IBDP site (Finley, 2014). These three shale
67 units are relatively continuous, thick, geographically extensive, and predictable with respect to
68 mineralogy and tectonics. A variety of studies have analyzed the lithology, mineralogy, petrophysics,
69 pore size distribution and capillary entry pressure, fluid-fracture pressure, CO_2-brine-rock interaction on
70 shales throughout the Illinois Basin (Carroll et al., 2012; Liu et al., 2012; Neufelder et al., 2012; Lahann
71 et al., 2013; Mastalerz et al., 2013; Yoksoulian et al., 2013; Lahann et al., 2014; Mozley et al., 2016;
72 Medina et al., 2020), but no study has evaluated the mineralogy, pore space, and seal capacity of all
73 major caprocks at a single CCS demonstration project in the Illinois Basin such as the IBDP. This
74 evaluation is supported by using ultrahigh-resolution focused ion beam (FIB) scanning electron
75 microscopy (SEM) and mercury injection capillary pressure (MICP) analysis coupled with petrographic,
76 quantitative evaluation of minerals by scanning electron microscopy (QEMSCAN), and X-ray diffraction
77 (XRD). This research attempts to provide awareness of the nature and variability in the pore structure
78 and mineralogy in caprocks at the IBDP. It aims to characterize the pore space and mineralogy of sealing
79 rocks at this CCS project, both of which are contributing factors in the quality of a caprock and it's
80 sealing capacity. More extensive and broader studies will be needed as Illinois Basin CCS projects are
81 scaled up in the future.

82

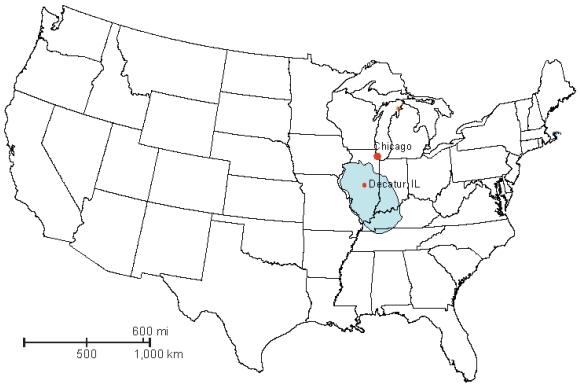

STRATIGRAPHIC COLUMN OF THE ILLINOIS BASIN

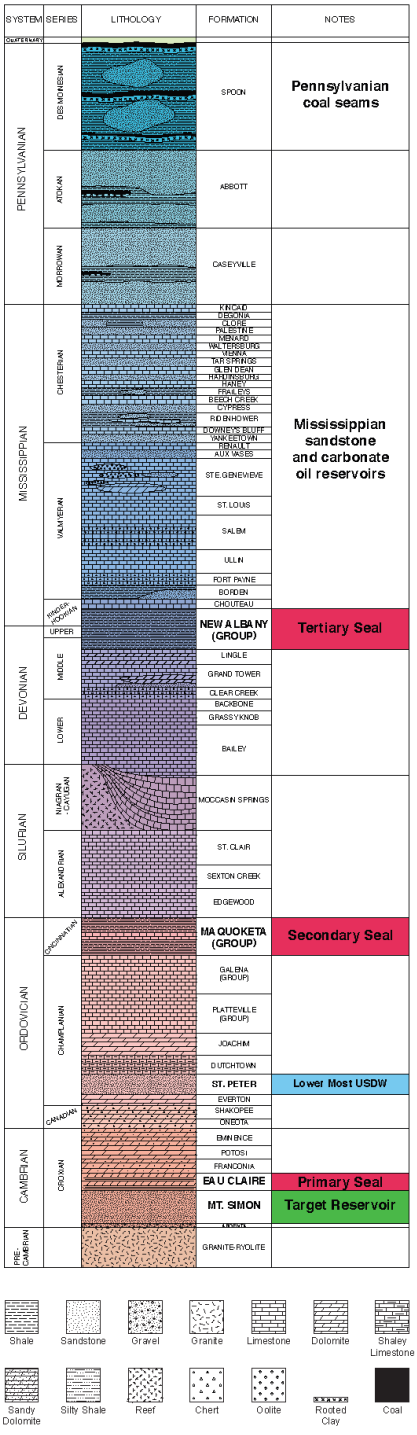

Figure 1) Location of the Illinois Basin–Decatur Project in Decatur, Illinois, USA and generalized stratigraphic column at the Illinois Basin–Decatur Project with target reservoir and major sealing units identified.

Geologic Background of IBDP Caprock

The Illinois Basin is an intracratonic basin filled with Paleozoic sedimentary rocks that cover most of Illinois, southwestern Indiana, western Kentucky, and small areas of Missouri and Tennessee. Precambrian basement rocks underlying the Paleozoic strata of the Illinois Basin are dominantly comprised of igneous felsic rocks of the Mesoproterozoic 1.48-1.38 billion year (Ga) old Eastern-Granite-Rhyolite Province (EGRP; Bickford et al., 1986) emplaced onto older crust (Freiburg et al., 2020a). Unconformably separated from and directly overlying the Precambrian basement is the lower most Paleozoic formation; the Cambrian-age Mt. Simon Sandstone (Wilman et al., 1975). Overlying the Mt. Simon are three major shales (Figure 1) that persist as laterally extensive units throughout the basin including the Eau Claire (Cambrian), Maquoketa (Ordovician), and the New Albany (Upper Devonian-lower Mississippian). The Eau Claire directly overlies the Mt. Simon whereas the Maquoketa and New Albany overly but are positioned between numerous other carbonate and siliciclastic formations. In terms of thermal maturity of the shale samples at the well site location, the New Albany is considered immature to early mature (Lewan et al., 2002) while the Maquoketa and Eau Claire were heated as a result of burial to the low end of the oil window (Grathoff et al., 2001; Schieber, 2010).

The Mt. Simon Sandstone

The Early to Middle Cambrian Mt. Simon Sandstone can be divided into three major sections, the upper, middle, and lower, and further into five distinct units based on changes in the depositional environment and sedimentological variability (Freiburg et al., 2014; Freiburg et al., 2016; Freiburg et al., 2020b). The lower Mt. Simon, comprised largely of a sub-arkosic sandstone, has the best reservoir properties as a result of primary porosity preservation and secondary porosity development (Freiburg et al., 2016) and is the IBDP reservoir. The lower Mt. Simon depositional facies are highly heterogeneous and reflect a subtle marine incursion into an alluvial/fluvial environment that regresses upward into an eolian environment. Mudstones were deposited on floodplains in a braided river system. Thus, due to the anastomosing nature of the river channels, mudstones are laterally discontinuous as observed on geophysical logs from four wells that penetrate the section within approximately 1700 m (Freiburg et al., 2014; Freiburg et al., 2016). However, locally, mudstones represent low permeability reservoir baffles overlying the CO_2 injection zone. This mudstone has been referred to as a pressure baffle as a result of pressure monitoring above and below the mudstone during CO_2 injection and the lack of pressure signals travelling vertically though this tight section (Senel et al., 2014). Despite the apparent lateral variability of this mudstone as a major shortcoming for sealing capacity of large-scale CO_2 plume containment, it has high quality caprock properties and is characterized herein.

The Eau Claire Formation

The Eau Claire Formation is considered the primary seal of the CCS reservoir for the IBDP (Finley, 2014) and functions as a regional aquitard that impedes the exchange of groundwater or mineralizing fluids between the Mt. Simon and overlying aquifers in part of Illinois, Wisconsin, Indiana, and Ohio (Leetaru et al., 2005; Benson and Cole, 2008; Neufelder et al., 2012). The Eau Claire is interpreted to have been deposited in the Middle to Late Cambrian (Palmer, 1982) and based on the fossil record is considered

Dresbachian in age; part of the Sauk II Sequence. The Eau Claire directly overlies and is conformable with the underlying Mt. Simon Sandstone. It is overlain by the Galesville Sandstone, part of Knox Megagroup. The Eau Claire is laterally extensive underlying all of Illinois and ranges from less than 100 feet (61 m) in western Illinois (Willman et al., 1975) to more than 1200 feet (370 m) in southern Illinois (Sargent, 1991). The Eau Claire is described as a heterolithic, shallow marine succession, dominated by interbedded shale, siltstone, sandstone, and dolomite (Aswasereelert et al., 2008; Yawar and Schieber, 2008; Neufelder et al., 2012; Lahann et al., 2014; Palkovic, 2015). Lithoifacies vary widely across the basin and must be reviewed for projects considering the use of the Eau Claire as a confining unit (Lahann et al., 2014). In northwestern Illinois, the Eau Claire is dominantly comprised of sandstone. In north-central Illinois, the Eau Claire is siltier and shaley. In southern to southwestern Illinois, the Eau Claire is predominantly dolomite and limestone and commonly referred to as the Bonneterre Formation, named for the town in southeastern Missouri. At the IBDP site, the basal unit of the Eau Claire is dominantly composed of silty and sandy shale to clean shale and is approximately 50 ft (15 m) thick (Lahann et al., 2014; Palkovic, 2015)..

The Maquoketa Shale Group

The Maquoketa is considered a secondary sealing unit at the IBDP part of the Tippecanoe Sequence and forms the upper section of the Ordovician System. It is widespread across the U.S. Midcontinent spanning about 680 miles (1,100 km) wide (Kolata and Graese, 1983). The Maquoketa is disconformable with the underlying limestones and dolomites of the Galena Group and overlain by limestones of the Silurian System. In Illinois, the Maquoketa is divided into several formations, from the base to top: Scales Shale, Fort Atkinson Limestone, Brainard Shale, and Neda Formation (Kolata and Graese, 1983). Although the Scales Shale contains less clay and is the more carbonate-rich facies among the two Maquoketa Shale formations, it is the basal most formation and would be the first to act as a caprock for underlying CO_2 storage reservoirs. Thus, the Scales Shale is the focus of this study and simply referred to

as the Maquoketa Shale. It ranges from 50 to 150 feet (15 to 45 m) thick across Illinois (Wilman et al., 1975). The Scales consists primarily of light gray and olive gray shale with minor amounts of olive black, brownish gray, and brownish black shale (Kolata and Graese, 1983). The Maquoketa overlies formations of the Knox Super Group and the Ancell Group, which have been proposed as prospective CCS reservoirs (Leetaru et al., 2012; Leetaru, 2014; Damiani, 2020) and have been utilized for industrial wastewater storage for decades (Freiburg and Leetaru, 2012) of which the Maquoketa is the primary shale seal. At the IBDP, the Maquoketa is considered a secondary seal (Freiburg et al., 2014)

The New Albany Shale Group

The New Albany Shale Group is part of the Kaskaskia Sequence and forms an essentially continuous body of shale that is mostly Upper Devonian in age with the sequence beginning in Mid-Devonian and ending in the lower Mississippian. It consists of laterally extensive, organic-rich shales with consistent organo-facies containing total organic carbon (TOC) values which can reach up to 13% across Illinois, western and central Kentucky and Indiana with highly variable maturity (Mastalerz et al., 2013). More than 140.4 billion barrels of oil has been generated from the New Albany Shale in thermally mature portions of the basin (Higley et al., 2003). The New Albany has a maximum thickness of 400 feet (121 m) but is eroded in northern Illinois and exposed in parts of western and southern Illinois. In Illinois, the New Albany is divided into several major shale formations, from base to top: Blocher, Sweetland Creek, Grassy Creek, Saverton, and Hannibal (Cluff et al., 1981). The New Albany also includes a thin sandstone (Sylamore) and a limestone (Louisiana) unit. This study focuses on the Grassy Creek Shale which has the highest concentration of organic carbon of any member of the New Albany Shale (Cluff et al., 1981). Natural gas has been produced from the New Albany over the past century until the present (Partin, 2004). In addition to its gas potential (Strapoc et al., 2010), the New Albany is of interest for CO_2 sequestration (Nutall et al., 2009) and is considered a secondary seal for the IBDP (Freiburg et al., 2014).

Porosity and the influence of CO_2 on the New Albany has previously been investigated on various samples across the Illinois Basin (Partin, 2004; Lahann et al., 2011)

Methods

Three representative samples of shale from the major sealing units for the IBDP were selected for analyses, including the Eau Claire Formation (depth 5465 ft; 1666 m), the Maquoketa Shale (depth 2816 ft; 858 m), and the New Albany Shale (depth 2157 ft; 657 m; Figure 2). A fourth sample, a Mt. Simon mudstone (depth 6863 ft; 2092 m), was selected as it represents a major baffle internal to the reservoir that may control CO_2 migration pathways (Figure 2). These samples were selected to be representative of potential sealing facies within each caprock interval based upon lithology and relative position within the formations. Samples were cut from 10 cm core from the Verification Well #1 and the Geophysical Monitoring Well #2 located at the IBDP site and housed at the Illinois State Geological Survey samples library (Figure 2; see Couëslan et al., 2014 for well locations). Petrographic, mineralogical, and routine petrophysical properties analyses described below were completed on all four samples. Samples were equally divided up for each separate analysis.

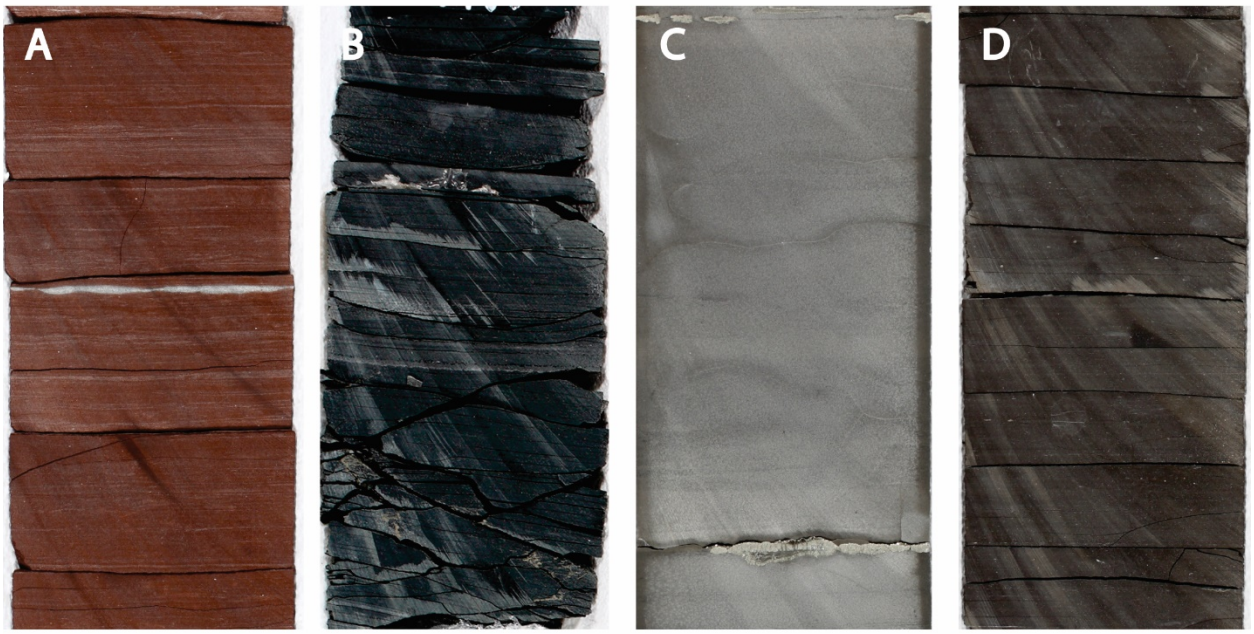

Figure 2) Sampled cores (4 inch in diameter; 10 cm) from the Illinois Basin–Decatur Project. A) Mudstone sample (depth 6863 ft; 2092 m) interbedded within the Mt. Simon Sandstone; B) Eau Claire Formation sample (depth 5465 ft; 1666 m); C) Maquoketa Shale Group sample (2816 ft; 858 m); D) New Albany Shale Group sample (depth 2157 ft; 657 m)

Thin sections of each sample were analyzed and described under plane and cross-polarized light (Figure 3). Quantitative electron mineralogy analysis by QEMSCAN was completed by SGS Laboratory in Vancouver, Canada. This included quantitative mineralogy, mineralogical distribution mapping, and particle size analysis. For this study, QEMSCAN mapping is utilized for contextual mineral distribution and not for mineral identification or quantification. Rather, X-ray diffraction (XRD) analyses were used for mineral identification, quantitative mineralogy, and clay fraction analysis (<2 μm).

Samples for XRD were analyzed with a Bruker D8 Advance instrument of Bragg-Brentano Theta-Theta geometry equipped with a Lynxeye 1D stripe detector. Step-scanned data was collected at 30 mA and 40 kV from 3° to 40° 2θ (orientated preparations) and 4° to 80° 2θ (random powders) with a fixed rate of 2° per minute and a step size of 0.02°2θ for each sample. Quantitative Rietveld refinements were realized using the BGMN / Profex software (Doebelin and Kleeberg, 2015).

Focused ion beam - scanning electron microscopy (FIB-SEM) with energy dispersive spectroscopy (EDS) was completed on a Zeiss Auriga equipped with Oxford Instruments XMAX 80 EDS detector and FE-cathode. Secondary electron (SE2) and energy selective back scattered electron (BSE) image stacks were collected at 1kV in order to minimize charging artefacts near edges and organic matter. Image resolution was 1024x768 in x- and y-direction. During the serial sectioning a beam current of 500 pA was used for cutting of about 25 nm thick slices. SE and BSE image stacks allowed to differentiate between mineral phases. As gray level normalization was performed on the polished surfaces before starting the serial sectioning process, the ability to differentiate between distinct phases depends strongly on the range of gray levels of each individual sample. Therefore, for some samples it was possible to distinguish between quartz grains and clay mineral matrix, whereas this was not possible for samples containing organic matter as well as dense metal oxides. Differences in mineral quantities between the FIB-SEM and the XRD/QEMSCAN analyses will results from the size of samples analyzed and FIB-SEM approach to specifically analyze the intergranular clay matrix. FIB-SEM area of analysis is generally 10x10x10 µm. Detrital grains such as quartz and feldspar coarser than clay-size are generally highly underestimated in FIB-SEM due to the size of the FIB-SEM area of investigation. Coarse-grained particles are avoided when selecting the area of investigation to avoid a single grain filling the entire area of investigation. Silty laminae, such as that observed in QEMSCAN (Figure 4) were avoided for FIB-SEM analysis.

226 The identification of the minerals during FIB-SEM was based on EDS mappings collected before and after
227 the serial sectioning process. Images were analyzed using Avizo 9.3 and ImageJ. After aligning the image
228 stack, filters were applied to enhance the image quality for segmentations. The filters used for image
229 analysis included an FFT filter to remove curtaining artefacts, shading and background correction, as
230 well as a Non-local-means filter to remove noise. Segmentations were done by using thresholds on grey
231 values and improved by hand using the Avizo Segmentation Editor. Pore space was binarized and
232 qualitatively and quantitatively analyzed. All objects <5 voxels were considered noise and thus removed
233 from the binary image. Image based pore size distributions (PSD) were calculated based on the
234 continuous PSD (cPSD) approach (Muench and Holzer, 2008). Porosity was further measured by mercury
235 injection capillary pressure analysis (MICP) using a Micromeritics AutoPore IV 9520 mercury porosimeter
236 at Schlumberger Reservoir Laboratories in Houston, Texas. Samples were subjected to drainage only
237 mercury injection to measure routine properties and pore throat size distribution. Total organic carbon
238 data were available for two of the samples and included with the XRD data.
239
240 A first approximation of the sealing capacity (column height of $scCO_2$ that the caprocks can retain before
241 leakage occurs) of the samples is evaluated using permeability estimates, which span the range of values
242 calculated from petrophysical analyses. This evaluation is determined from previous experimental
243 research in which statistically significant relationships between air permeability (md) and air threshold
244 pressure (psi) are evident (Li, et al., 2005; Dewhurst et al., 2002).
245 The correlation between supercritical (sc) CO_2 threshold pressure (psi) and N_2 threshold pressure (psi) is
246 key to approximating the sealing capacity to $scCO_2$. Mean pressure given in relation to $scCO_2$ is 42.7% of
247 that measured in relation to air or N_2. Using Equation (1), the relation is:
248 (1) $P_{tscCO2} = [(0.427 \times (e^{3.02} \times k_{seal}^{-0.434})]$

where P_{tscCO2} is the threshold pressure in psi and k_{seal} is permeability in millidarcys (md)

Substitution of Equation (1) into the standard evaluation of column height (2), or the height of a hydrocarbon or $scCO_2$ column the seal can hold before breakthrough, is as follows (Daniel and Kaldi, 2008):

(2) $$h_{scCO2}\ \text{max} = \frac{[0.427 \times (e^{3.02} \times k_{seal}^{-0.434})] - [(e^{3.02} \times k_{res}^{-0.434})]}{[(\rho_f - \rho_{scCO2}) \times 0.433] \times 0.3048}$$

where k_{seal} is seal permeability (md) and k_{res} is reservoir permeability (md) and ρ_f is density of the reservoir brine and ρ_{scCO2} is density of $scCO_2$ at reservoir temperature and pressure

A range of permeability values for each sample interval was calculated using temperature, pressure, and density values determined from the IBDP well data. Comparison of the New Albany Shale is not possible using this formulation as at formation temperature and pressures, CO_2 is in gas phase, not supercritical. A rigorous evaluation of threshold pressures using detailed MICP data created a range of minimum to maximum $scCO_2$ column heights based upon a range of CO_2 contact angles and Hg/air threshold pressures. This provides additional insight into seal capacity and leakage potential. Generally, prior to 2006, $scCO_2$/water/rock interfaces in the sub-surface, were assumed to have a contact angle (θ) of 0^o, as water was thought to be the wetting phase (Daniel and Kaldi, 2008). More recent experimental studies using quartz, mica, and clay substrates and $scCO_2$ immersed in brine indicate that these substrates become less water-wet in the presence of $scCO_2$, i.e. contact angles varying from 0^o to 40^o (Sarmadivaleh, et al., 2015). An increase in contact angle becomes more pronounced at higher pressures up to 20mPa, ranging from 30^o to 60^o. For the purposes of this study, a range of column heights was calculated using a contact angle of 0^o, 20^o, 40^o, 60^o to bracket the wettability uncertainty.

In addition, based upon the sample MICP entry pressure (Hg/air), the threshold pressure of the CO_2/brine system was modified by 20% (either low or high) to capture some of the variability in pore volume and permeability of changing caprock composition and resultant diagenesis. This allowed a maximum/minimum comparison of column heights relative to the data derived from the sample. Variability of capillary pressure using a range of contact angles follows the wettability transformation from an air/mercury system to brine equation (after Schowalter 1979):

(3) $P_{b/CO2} = P_{a/m} (\sigma_{b/CO2} \cos\theta_{b/CO2}) / (\sigma_{a/m} \cos\theta_{a/m})$

Where $P_{b/CO2}$ is the capillary pressure in the brine/CO_2 system, $P_{a/m}$ is the capillary pressure in the air/mercury system, $\sigma_{b/CO2}$ and $\sigma_{a/m}$ are the interfacial tensions of the brine/CO_2 and the air mercury systems respectively, $\theta_{b/CO2}$ and $\theta_{a/m}$ are the contact angles of the brine/CO_2/substrate and air/mercury/substrate systems respectively.

Calculation of the column height uses the standard equation:

(4) $h_{scCO2}\ max = (Pth_s - Pth_r) / (\rho_f - \rho_{scCO2})^*0.433$

where Pth_s is the entry pressure of the seal in the scCO$_2$/brine system, Pth_r is the entry pressure of the reservoir in the scCO$_2$/brine system, $\rho_f - \rho_{scCO2}$ is the density difference of the brine and scCO$_2$, and 0.433 the normal hydrostatic gradient of water in psi/ft, and h_{scCO2} max is the maximum column height or caprock capacity (Daniel and Kaldi, 2008)

The interfacial tension (IFT) used in the Hg/air to brine/CO_2 conversion for each sample is based upon studies indicating that it typically ranges between 21 – 27 dynes/cm under scCO$_2$ conditions (Espinoza, et al., 2010).

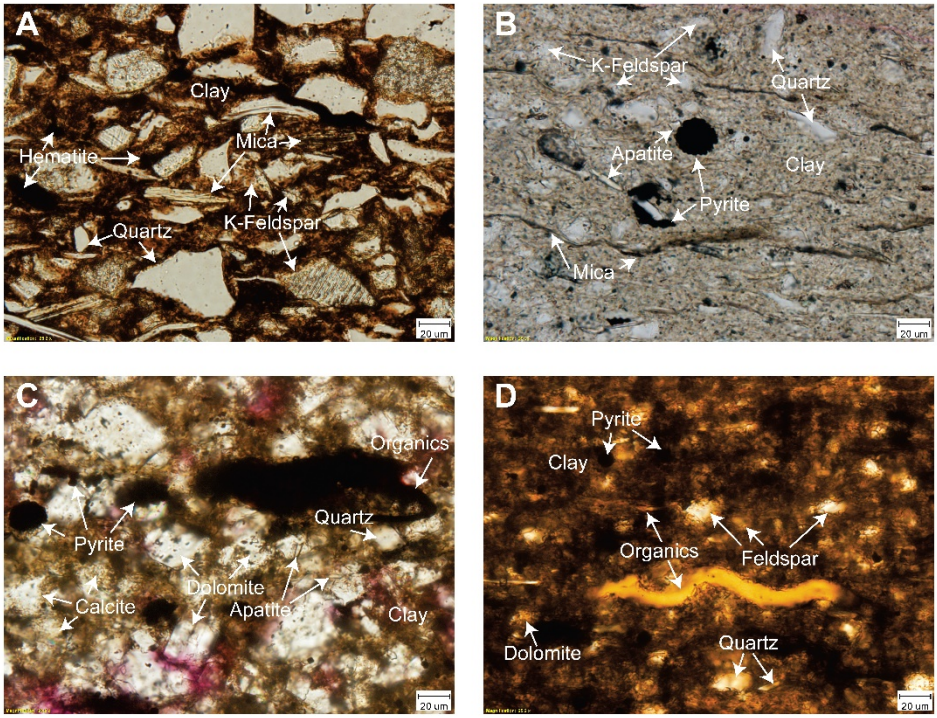

Figure 3) Thin section photomicrographs from the core samples (Figure 2). A) Mt. Simon mudstone with a hematite and illitic clay matrix hosting abundant quartz, K-feldspar, and mica. B) Shale from the Eau Claire Formation with an illitic clay matrix hosting mica, quartz, K-feldspar, apatite, and pyrite. C) Argillaceous dolomite from the Maquoketa Shale Group with dolomite, calcite and illitic clay matrix with minor pyrite, quartz, apatite, and organics. D) Shale from the New Albany Shale Group with an illitic clay rich matrix hosting minor quartz, feldspar, pyrite, dolomite, and organics.

Results and Discussion

Integration of mineralogical and pore size characterization analytical methods of samples in this study give diverse results that offer important 2-dimensional (2D) and 3-dimensional (3D) data critical to

evaluation of the sealing properties of the caprocks. For example, X-ray diffraction offers the most accurate whole-rock mineralogy of the samples in this study (Table 1). QEMSCAN results give a 2D semi-quantitative evaluation of the mineralogy of a single surface of the sample (Table 2). An important aspect of this evaluation is obtaining a spatial distribution of minerals in the scanned surface which may play an important role in pore space distribution. This spatial distribution assists in understanding detrital and diagenetic relationships to pore space development and assists in mapping the 3D mineral framework and pore space network. The qualitative mineralogical data from FIB-SEM was obtained through EDS analysis using major grayscale grouping on electron images (Table 3). Grayscales represent dominant minerals and groups of minerals that have similar back scattered signature.

Table 1) X-Ray Diffraction and total organic carbon analysis results (%) of the IBDP seals

Formation	Lithology	Quartz	K-feldspar	Plagioclase	Calcite	Siderite	Dolomite	Pyrite	Apatite	Hematite	Smectite	Illite-Smectite	Illite-Mica	Kaolinite	Chlorite	Total non-clay	Total Clay	Organic Carbon
Mt. Simon	Mudstone	30	14	0	1	0	0	0	0	4	0	2	49	0	0	49	51	na
Eau Claire	Shale	11	15	5	3	0	1	1	0	0	0	33	26	1	5	35	65	0.2
Maquoketa	Shale	31	2	4	1	5	47	5	0	0	31	0	23	35	12	95	5	na
New Albany	Shale	33	5	7	1	0	2	3	0	0	0	10	28	1	10	51	49	8.3

Table 2) QEMSCAN area % results

Formation Name	Lithology	Quartz & Silica	K Feldspar	Alkali Feldspar	Plagioclase	Calcite	Dolomite	Ferroan Dolomite	Fe Oxide & siderite	Pyrite	Barite	Rutile & Ti Silicates	Ilemenite	Apatite	Zircon	Tourmaline	Halite	Anhydrite	Muscovite	Biotite	Serecite	Illite & Illite-smectite	Fe-Illite & illite-smectite	Kaolinite	Chlorite	Total
Mt. Simon	Mudstone	40.51	22.82	0.01	0.01	0.01	0.00	0.00	0.15	0.00	0.00	0.30	0.06	0.11	0.05	0.02	0.01	0.00	0.89	0.89	5.92	9.82	18.24	0.04	0.15	100.00
Eau Claire	Shale	22.22	43.24	0.00	0.41	0.02	0.03	0.34	0.01	0.58	0.00	0.15	0.00	0.95	0.03	0.00	0.00	0.00	0.50	4.81	0.00	7.62	18.74	0.04	0.33	100.00
Maquoketa	Shale	5.57	2.67	0.00	0.07	60.12	2.55	0.79	0.00	0.76	0.00	0.06	0.01	1.45	0.01	0.00	0.00	0.05	0.82	0.33	0.00	23.44	0.00	0.50	0.80	100.00
New Albany	Shale	22.10	6.54	0.00	2.57	0.02	0.49	0.14	0.01	5.62	0.00	0.21	0.00	0.05	0.01	0.00	0.00	0.00	1.12	5.60	0.00	31.97	22.29	0.26	0.99	100.00

Table 3) Porosity and pore data from mercury intrusion capillary pressure and focused ion beam-scanning electron microscopy.

Formation	Lithology	Hg Injection Effective Porosity (%)	Median Pore Throat (nm)	Hg/Air Entry Pressure (psi)	Air/Brine Entry Pressure (psi)	Swanson Permeability (mD)	FIB-SEM Sample Volume (nm^3)	FIB-SEM Pore Volume (nm^3)	FIB-SEM Pore Fraction (%)	FIB-SEM Pores (n)
Mt. Simon	Mudstone	0.005	7.5	7180	1658	<0.01	1347.59	0.13	0.01	113
Eau Claire	Shale	0.019	13.7	617	120	<0.01	3398.97	3.66	0.11	1165
Maquoketa	Shale	0.047	9.1	435	84	<0.01	2327.38	25	1.07	8947
New Albany	Shale	0.039	8.9	694	135	<0.01	2356.9	1.73	0.07	743

Mt. Simon (Mudstone)

The mudstone is made up of silt-size particles comprised of angular to sub-rounded grains of quartz, K-feldspar, hematite, and sheets of muscovite suspended in a clay matrix (Figure 4). XRD indicates approximately half of the sample is composed of clay minerals with the other half being non-clay minerals. The clay-rich matrix is comprised of 1M_d illite with negligible amounts of well crystalline 1M illite and minor amounts of kaolinite. XRD and the 2D QEMSCAN are relatively consistent except for a likely underestimated iron oxide in the QEMSCAN due to its nm-sized grains. XRD analyses records approximately 4% hematite. Rather than iron oxides, iron is accounted for as an iron-rich illite or Fe-illite in the QEMSCAN (Table 2). Iron oxides are observed as clay-size detritus in thin section and difficult to differentiate them from the clay mineral-rich matrix. The FIB-SEM results show an anomalously high amount of iron oxides compared to the XRD, QEMSCAN, and petrographic results (Figure 6). Iron-oxides occur largely as clusters of nano- to micron-size prismatic crystals. These iron-oxides are widely distributed throughout the clay-rich matrix of the sample sectioned from FIB-SEM (Figure 5) and account for a large fraction of the sampled volume (Figure 6). The high amount of hematite is likely accurate in

the sectioned matrix-dominated area of the sample as the hematite is easily identified due to the high backscatter intensity although some overestimation may occur due to charging artifacts. Feldspars are included in the undifferentiated matrix in the FIB-SEM results.

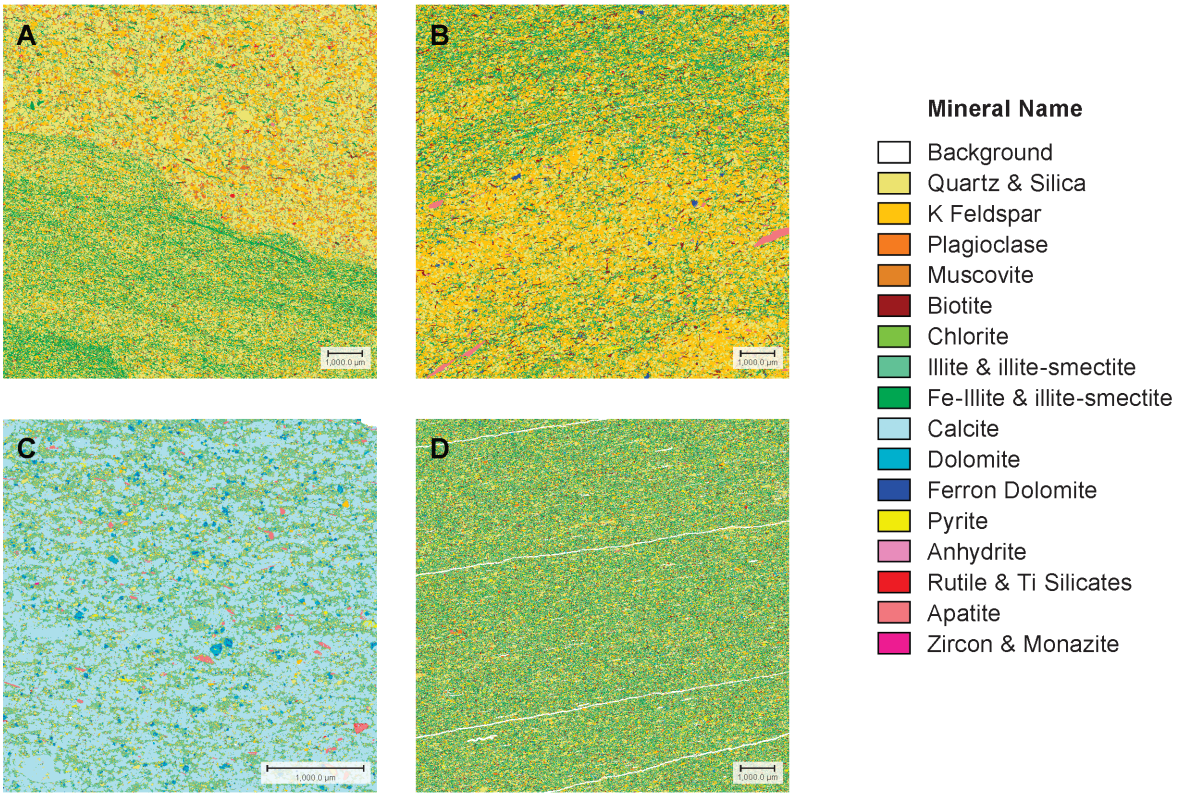

Figure 4) QEMSCAN (Quantitative Evaluation of Minerals by Scanning Electron Microscopy) mineral phase assemblage maps of selected samples. A) Mt. Simon mudstone with abundant quartz, K-feldspar, and illite; B) Eau Claire Shale with abundant K-feldspar, quartz, and illite, and illite-smectite; C) Maquoketa argillaceous dolomite showing abundant calcite and minor dolomite and illite; D) New Albany shale with abundant quartz, illite, and illite-smectite.

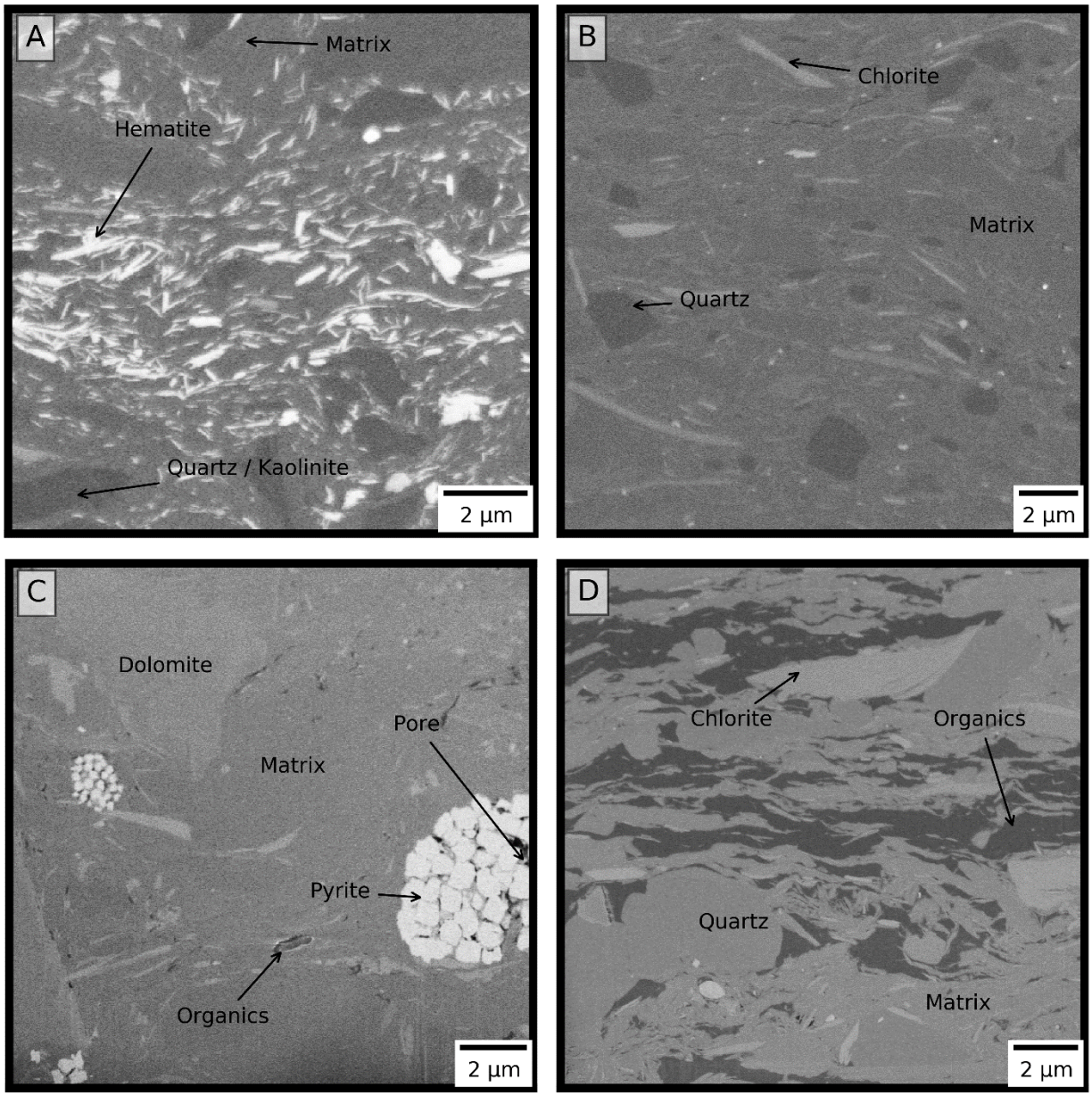

352

353 Figure 5) Select back-scattered electron images of ion-polished surfaces and segmented volume
354 fractions. A) Mt. Simon sample shows intergranular matrix with varied mineralogy. Bright laths of
355 hematite are abundant throughout much of the sample. B) Eau Claire sample showing platy chlorites in
356 lighter colors and sub-rounded quartz grains within the dense indistinguishable clay matrix. C)
357 Maquoketa sample with highest pore space volume. Largest pore clusters are concentrated in
358 framboidal pyrite. Matrix is composed of illitic clay minerals and platy chlorites in between abundant

359 angular dolomite grains. D) New Albany sample showing abundant organic material. Pore space is often

360 located in and around organic matter and oriented along the bedding plane.

361

362

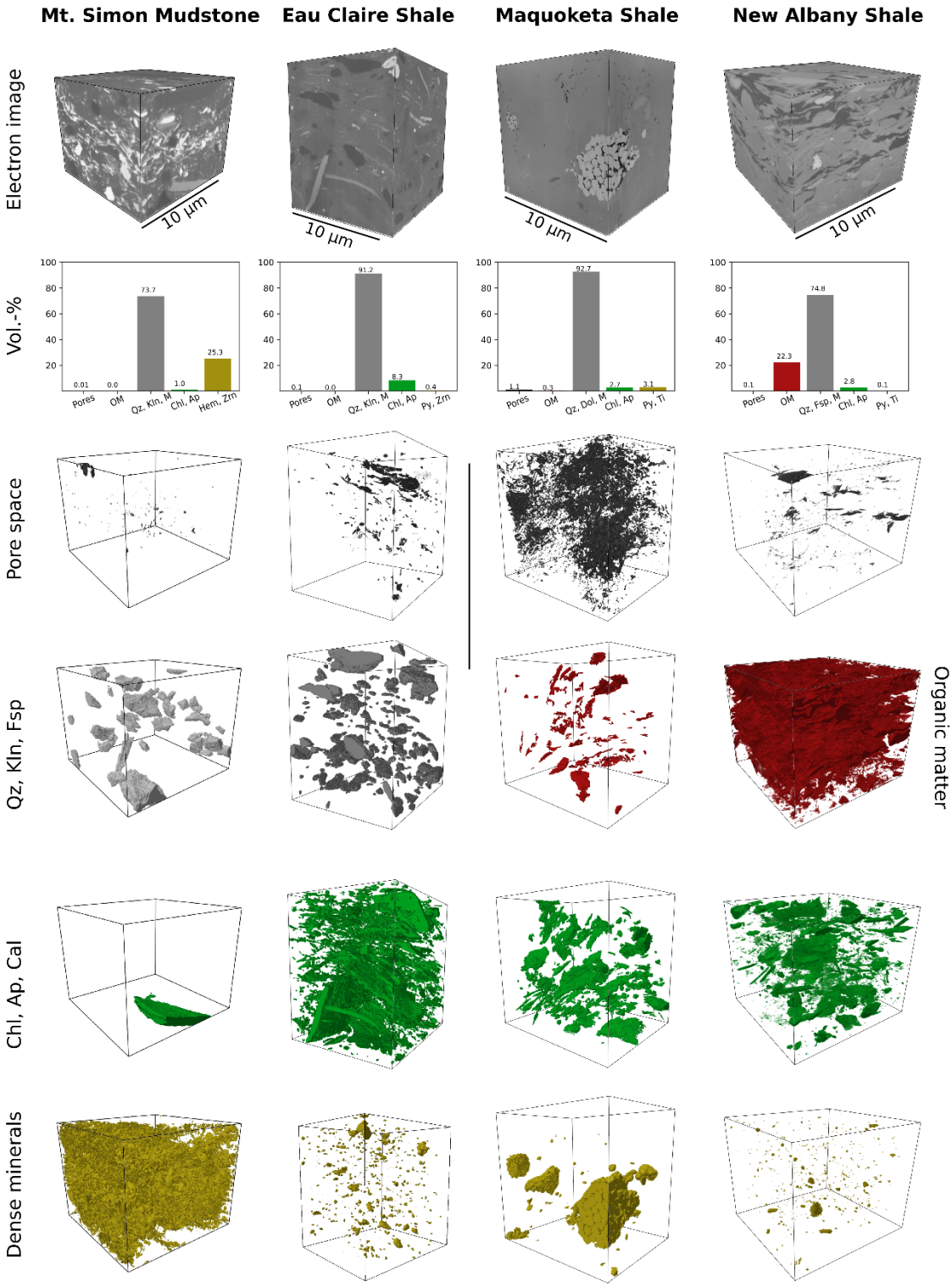

363

364 Figure 6) 3-dimensional focused ion beam-scanning electron microscopy segmentation of the four

365 samples analyzed. Segmentation and isolation of mineral phases is controlled by back scattered

366 electron contrast. Minerals such as quartz (Qz), kaolinite (Kln), feldspar (Fsp), and dolomite (Dol) are
367 isolated and segmented when BSE is sufficient. In organic-rich samples, BSE is insufficient, and these
368 minerals are not isolated and segmented. Chl – chlorite, Ap – apatite, Cal – calcite, Py – pyrite, Hem –
369 hematite, Rut – rutile, Ant – anatase, Zrn – zircon. M – indistinguishable mineral matrix. Mineral
370 abbreviations after Warr (2021).

371

372 FIB-SEM images (Figure 6) indicate minimal porosity within the mudstone, at approximately 0.01% of
373 the sample volume (Table 3). Pores are almost exclusively interparticle pores. One slit shaped pore is
374 observed and likely the result of clay desiccation during sample drying. All other pores are more
375 irregular to spherical and most common in clay matrix where hematite crystals are absent and may
376 occur as intraparticle pore space from partial dissolution in detrital grains such as feldspar (Figure 6).
377 MICP analyses confirms negligible porosity at 0.005% effective porosity. A median pore throat of 7.5 nm
378 is observed with MICP (Table 3) which is below the resolution limits of the FIB-SEM (Figure 8). The
379 calculated cPSD shows the narrowest range of pore sizes and the smallest number of pres. Of all the
380 samples observed, the Mt. Simon mudstone has an exponentially higher entry pressure than all the
381 shales (Table 3) and the lowest observed porosity, thus making it the best immediate seal or baffle
382 relative to CO_2 migration.

383

384 ## Eau Claire

385 The Eau Claire sample is a shale made up of clay-size grains of angular to sub-rounded quartz,
386 K-feldspar, and minor plagioclase, pyrite, calcite, biotite, and dolomite suspended in a dominantly clay
387 matrix (Table 1). Mica's are generally the coarsest particles, forming fine platelets elongated parallel to
388 bedding in the clay matrix. Apatite is observed in thin section (Figure 3) and QEMSCAN (Figure 4) but

was not detected in XRD. Most of the sample is comprised of clay with the greatest total percentage of clay minerals relative to all other samples analyzed. The clay is a mixture of 1*M* illite and illite-rich mixed layered illite-smectite with minor percentages of chlorite detected (Table 1). Minor amounts of organic carbon were detected in the sample. Contrary to the XRD results, QEMSCAN detected an elevated K-feldspar content at over 40% of the scanned thin section. Much less clay is detected, relative to XRD results, implying clay minerals may be counted as K-feldspar in the QEMSCAN. The high clay content is supported by FIB-SEM with nearly all the sample analyzed as undifferentiated clay matrix (Figure 6) and classifying the sample as a clean shale.

Pore space in the Eau Claire Shale sample is minimal indicated by approximately 0.11% of the total FIB-SEM sample volume. MICP analyses detected 0.019% pore volume. Reconstructed pore space in the FIB-SEM model suggests pores are largely associated with the coarse detritus, implying desiccation of the sample at clay-grain interfaces may play a role in porosity observed in sample. Disconnected spherical pores are common in the Eau Claire. The median pore throat diameter detected with MICP is 13.7 nm. Entry pressure of brine/air is considerably lower at 120 psi compared to the mercury/air entry pressure (Table 3). Despite the higher effective porosity then the internal Mt. Simon mudstone sample, the Eau Claire has the lowest effective porosity among all the major seal intervals analyzed.

Maquoketa

The results of this study indicate that the Maquoketa sample analyzed may be considered an argillaceous dolomite to dolomitic marl based on its dominant mineral composition of dolomite (Table 1). The dolomite is clay size (<63µm) and is the dominant mineral along with clay comprising the matrix of the sample (Figure 3). Subhedral dolomite is commonly associated with anhedral crystals of calcite. QEMSCAN suggests that the dominant mineral is calcite which contradicts XRD results. Data from XRD

analyses is supported by petrographic examination (Figure 3). Clay minerals appear to be common in thin section (Figure 3) and confirmed by QEMSCAN as illite and mixed layered illite-smectite (Figure 4; Table 2). XRD results show a total clay content of 28% with about 21% 1M_d illite, 5% chlorite and minor amounts of detrital 2*M* muscovite (Table 1). No kaolinite was observed in the thin section and XRD. Besides dominant percentages of dolomite, the Maquoketa sample includes minor quartz, K-feldspar, pyrite, and apatite as observed in thin section and QEMSCAN. FIB-SEM supports the predominance of dolomite within the sample with minor framboidal pyrite, clay, and trace organics (Figure 6). Trace organic material is observed in electron imaging (Figure 5) as well as in thin section (Figure 3). Within the area of FIB-SEM observation, large clusters of framboidal pyrite comprise large areas of the samples section (Figures 5 and 6). Pore space is abundant between individual crystals in the framboids (Figure 6).

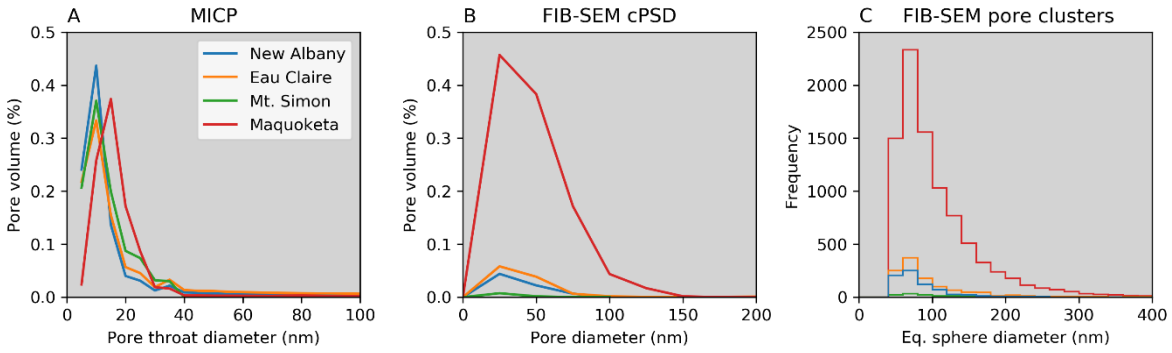

Figure 7) A) Graph of MICP data showing volume (%) of pore throat diameter. The New Albany sample has the most abundant pore throats in the finest size range (0-5 nm). The Maquoketa sample has more abundant large pore throats than any of the other samples. B) Continuous pore size distribution calculated form binarized electron image stacks. The highest porosity and largest pore radii are observed in the Maquoketa sample. C) Frequency distribution of the volume of individual pore clusters measured from binarized FIB-SEM image stacks. Most and largest pore clusters are observed in the Maquoketa

sample. Lowest number of pores and the narrowest range of pore sizes is found in the Mt. Simon sample. New Albany and Eau Claire show similar pore and cluster size distributions.

Out of all the samples analyzed the Maquoketa has the highest observable and measurable pore space (Figures 6 and 8; Table 4). The highest concentration of pore space occurs within the pyrite framboids. Other pore space is attributed to space between intercrystalline dolomite (Figure 6). FIB-SEM indicates that the Maquoketa has the highest median pore radii of all samples (Table 3) and occurs in higher frequency relative to the other samples (Figure 7). MICP analyses indicate that the median pore throat of 9.1 nm is relatively comparable to the other samples and even smaller than the deeper Eau Claire sample (Figure 7; Table 3). The Maquoketa has the lowest threshold entry pressures relative to the other major seal intervals which is attributed to the abundant and widely distributed pore space. Pore radii across the sample show the broadest distribution (Figure 8B) despite the lack of connectivity and large group of individual pore networks in the sample (Figure 8A). Pore size and connectivity is directly related to the pore host mineral. For example, pyrite framboids host the largest and most connected pore clusters (Figure 8C) where smaller pores with low connectivity are related to clay minerals and dolomite. The overall homogenous and broad distribution of pores in the FIB-SEM models indicates a widespread connectivity of pores with pore throat sizes slightly below the applied resolution as confirmed by MICP.

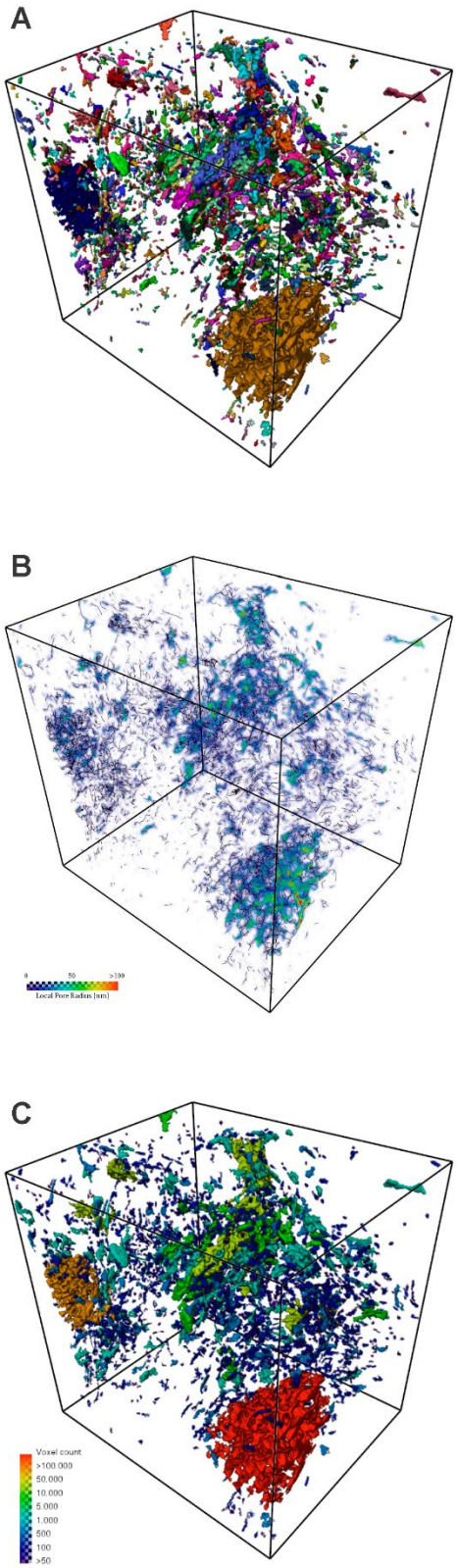

Figure 8) Images of Maquoketa pore space segmentations obtained from focused ion beam-scanning electron microscopy. A) Pore clusters individually colored to show connectivity of face, side, or edge (pores <50 voxels are not shown); B) Pore space colored to represent individual pore radius (all voxels are shown, with smallest radii shown as slightly translucent); C) Pores colored to show quantity of voxels in connected pore networks.

New Albany

The New Albany is a black to dark gray shale with a clay rich matrix hosting clay-size quartz, K-feldspar, plagioclase, and mica detritus as well as common organic material (Figure 3). Micas are preferentially aligned parallel to lamination and are dominated by muscovite that may be locally altered to chlorite. The matrix is largely comprised of 1M_d illite with minor 1M illite and chlorite (Figure 4; Table 1). Minor dolomite and trace pyrite are observed throughout (Table 2) and may be of diagenetic origin. Pyrite occurs as single crystals, framboids, and aggregates of the two (Figure 6). Dolomite cements and single crystals are observed in FIB-SEM slices with multiple generations observed in single crystals. Of all samples observed, the New Albany has the highest organic content (Figure 6; Table 1).

The FIB-SEM observed pore volume in the New Albany is the second lowest just above the Mt. Simon mudstone (Table 3). Effective porosity in the New Albany, however, is the second highest, just below the Maquoketa. The MICP measured median pore throat is 8.9 nm (Table 3). The MICP measured threshold entry pressure is comparable to the Eau Claire (Table 3). Much of the pore space in the New Albany is observed to be within close proximity to or inside of organic material (Figure 6) forming predominantly slit shaped pores. At the IBDP site location, the New Albany calculated organic matter transformation ratio (TR) is approximately 0.60-0.65 TR. This indicates that some oil and gas generation has occurred as noted by one of our coauthors (Willette, D.C.) Thus, porosity generation in the New Albany is likely related to shrinkage of organic material during oil/gas generation. Pore space is dominantly elongated linear space parallel and directly adjacent to organic material further suggesting pore space generated during organic matter volume shrinkage. The elevated total organic content throughout the sample and the direct relationship of organic material and pore space result in the high effective porosity or pore connectivity observed in the sample (Table 3).

Seal Capacity

Internal mudstones within the Mt. Simon as well as the Eau Claire Shale, Maquoketa Shale, and New Albany Shale are considered baffles and caprocks to vertical CO_2 migration from the Mt. Simon storage reservoir at the Illinois Basin–Decatur Project. As is the case with sandstones, the mineralogy and diagenetic alteration of shales can vary both vertically and horizontally within a few feet in the subsurface. This will induce rock properties such as porosity and permeability to fluctuate, sometimes by a couple of orders of magnitude. This will also affect the interpretation of MICP analytical results, as in the case of VW#1, where one sample was selected as representative from each potential sealing formation.

A range of permeability values for each caprock interval was calculated using temperature, pressure, and density values determined from the VW#1 well data. Table 4 lists the calculated brine density (ρ_f) and $scCO_2$ density (ρ_{scCO2}): Mt. Simon mudstone (ρ_f = 1.15 g/cc and ρ_{scCO2} = 0.78 g/cc); Eau Claire Shale (ρ_f = 1.10 g/cc and ρ_{scCO2} = 0.74 g/cc); and Maquoketa Shale (ρ_f = 1.10 g/cc and ρ_{scCO2} = 0.64 g/cc). Comparison of the New Albany Shale is not possible using this formulation as at formation temperature and pressures due to CO_2 being in gas phase, not supercritical.

506 Table 4). Rock and fluid properties for caprock samples taken at VW#1-IBDP. Includes pressure, temperature, and salinity data for the selected
507 samples, threshold pressures measured from MICP analyses, and calculated brine and CO2 densities. Also lists interfacial tension and contact
508 angles used in seal capacity calculations.

Formation Name (sample)	Depth of sample (m) TVDSS	Pressure at sample depth (psi) (mPa)	Temp. at sample depth (°F) (°C)	Salinity at sample depth (ppm) (mg/l)	CO_2 density (g/cm^3)	Brine density (g/cm^3)	Interfacial tension (mN/m or dynes/cm)	Contact angle (°)	Seal threshold pressure (air-Hg) psia	Reservoir threshold Pressure (air-Hg) psia
Mt. Simon mudstone	2091.7	2753.10 18.98	120.23 49.02	202900	0.78	1.145	27	0- 60	7180	10
Eau Claire shale	1666.0	2064.27 14.23	111.26 44.03	145500	0.744	1.10	26	0 - 60	617	10
Maquoketa	858.0	1219.0 8.40	91.38 32.99	140000	0.64	1.10	24	0 - 60	435	10
New Albany Shale	658.0	934.8 6.45	84.29 29.05	135000	0.21	1.10	43	0- 60	694	10

509

Theoretical $scCO_2$ column heights across a range of permeabilities were determined for the Mt. Simon mudstone and Eau Claire Shale (Figure 10). An almost identical correspondence of values was calculated between the two intervals with deviations of column heights ranging between 20 – 200 ft (6 – 61 m). However, estimates derived for the Maquoketa indicate column heights ranging between 100 – 800 ft. (30.5 – 244 m) lower than the other two shale intervals. This is due to the lower $scCO_2$ density at the Maquoketa interface and lower threshold pressures. In addition, the FIB-SEM and MICP data indicate that the Maquoketa contains the largest pore volume and lowest air/brine threshold pressure relative to the other two intervals. Therefore, the sealing capacity to CO_2 migration, while still possible, is less than the Mt. Simon mudstone and Eau Claire Shale.

Theoretical sealing capacity estimates shown on Figure 10 indicate that the Mt. Simon mudstone and Eau Claire Shale will hold $scCO_2$ column heights at least one to two orders of magnitude in excess of reservoir thickness. Caprock permeabilities between 0.02 – 0.0001 md may hold a $scCO_2$ column between approximately 1,000 to 10,000 ft (305 – 3048 m). In contrast, the Maquoketa Shale (for a similar range of permeabilities) may hold between 750 to 8000 ft (229 – 2438 m) of $scCO_2$. These are theoretical estimates that will be compared to point-source MICP analyses. It is important to note that MICP analytical results only constrain a snapshot of a limited petrophysical representation of the caprock interval.

Column height calculations from point specific MICP calculations are at least an order of magnitude less than the theoretical calculations spanning ranges of permeability values. Table 6 lists the ranges for column heights calculated for all caprock samples in which MICP analyses were run. Similar to the first approximation results, the seal capacity of the Mt. Simon mudstone and Eau Claire Shale caprocks support the largest columns relative to the other shale intervals. The Mt. Simon mudstone may support

columns ranging between 2587 – 3883 ft (788 – 1183 m) using a contact angle of 0°, which is approximately one order of magnitude larger than column heights calculated for the Eau Claire Shale. As the table indicates, larger contact angles of the $scCO_2$/water/rock interface result in diminished caprock column capacity. In general, as the contact angle increases to 60°, the amount of column the caprock can seal before breakthrough is reduced by approximately one-half. Since the pressure at sample depths for the Mt. Simon and Eau Claire range between 14 -19 mPa (2064 - 2753 psi), it is likely that a contact angle between 20°– 40° is reasonable. Therefore, the calculated minimum seal capacity could range between 1982 – 2431 ft (604 – 741 m) for the Mt Simon mudstone and 168 – 206 ft (51 – 63 m) for the Eau Claire Shale. These estimates of seal capacity exceed total reservoir interval thicknesses within the Mt. Simon.

Formation	CO_2 Column Height ft. (m) @ CA 0°	CO_2 Column Height ft. (m) @ CA 20°	CO_2 Column Height ft. (m) @ CA 40°	CO_2 Column Height ft. (m) @ CA 60°
	min – sample - max	min – sample - max	min – sample - max	min – sample - max
Mt. Simon mudstone	**2587**(788) - **3235** (986) - **3883** (1183)	**2431** (741) - **3040** (927) - **3649** (1112)	**1982**(604) - **2478** (755) - **2974**(906)	**1294**(394) - **1617**(493) - **1941**(592)
Eau Claire Shale	**219** (67) – **275** (84) – **331** (101)	**206** (63) – **258** (79) – **311** (95)	**168** (51) – **211** (64) – **253** (77)	**110** (34) – **138** (42) – **165** (50)
Maquoketa Shale	**110** (34) – **139** (42) – **167** (51)	**104** (32) – **130** (40) – **157** (48)	**85** (26) – **106**(32) – **128** (39)	**55** (17) – **69** (21) – **84** (26)
New Albany Shale^	**166** (51) – **209** (64) – **251** (77)	**156** (48) – **196** (60) – **236** (72)	**127** (39) – **160** (49) – **192** (59)	**83** (25) – **104** (32) – **125** (38)

^ column heights for the New Albany Shale (NAS) are an approximation. At formation temperature and pressure, CO_2 will be in vapor phase.

Table 5). Calculated minimum, sample value, and maximum $scCO_2$ column heights relative to caprock capacity based upon MICP analyses of one sample from the Mt. Simon mudstone, Eau Claire Shale, Maquoketa Shale, and the New Albany Shale. The variability of the column heights was calculated using a range of contact angles (CA) and threshold pressures (20% variability relative to sample value).

Of the sampled intervals, the Maquoketa Shale calculates the lowest seal capacity relative to $scCO_2$ (Table 5). This is also the case using the theoretical calculations depicted in Figure 10. Based upon the mineral characterization and pore network modeling described previously, this result is consistent with the caprock providing a lower seal capacity relative to $scCO_2$. It should be noted that the Maquoketa Shale (and New Albany Shale) are considered non-primary caprocks and there are no reservoirs of note (rocks with elevated porosity and permeability) directly beneath the seals. In the case of the New Albany Shale, due to formation pressures and temperatures, any CO_2 present would be in vapor phase. For these reasons, column heights calculated for these intervals are approximations and should be considered preliminary.

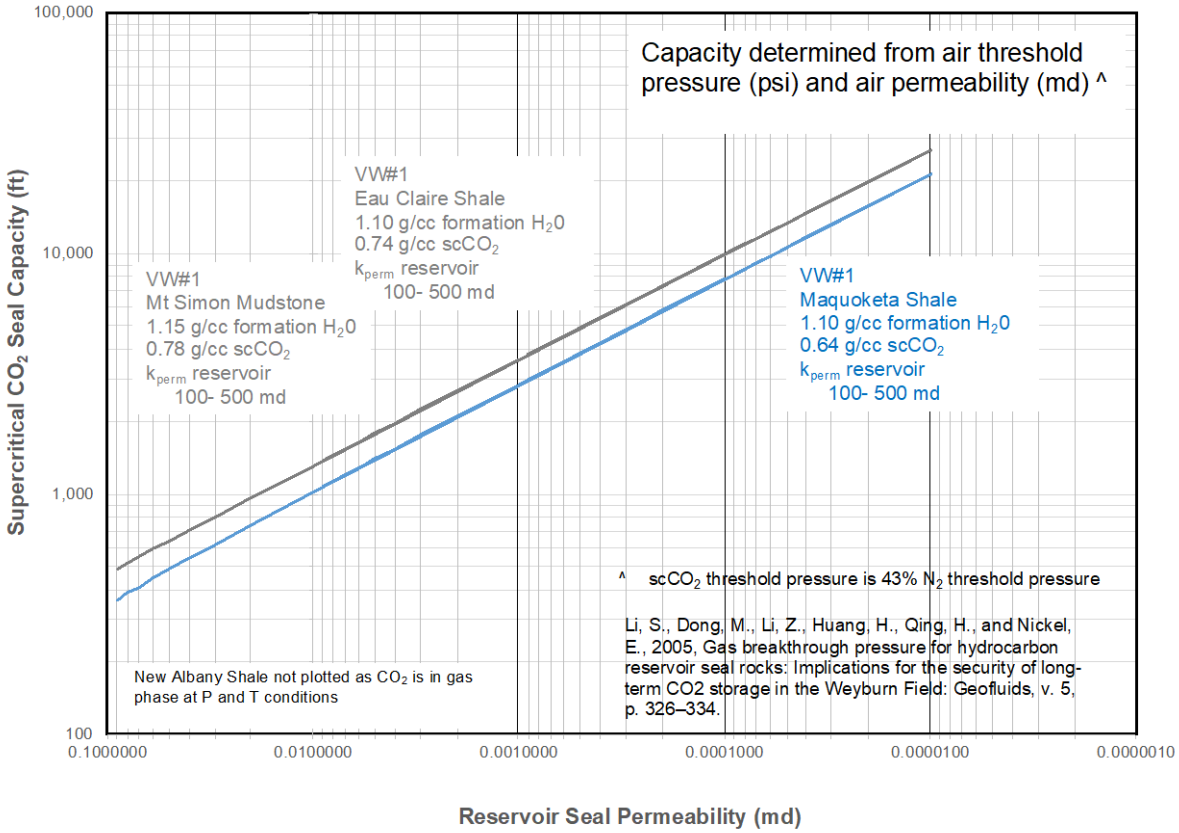

Figure 9). An approximation of seal capacity for the Mt. Simon Mudstone, Eau Claire Shale, and Maquoketa Shale using permeability as the major variable (after Li, et al., 2005).

Conclusion

The three major seals overlying the Mt. Simon reservoir as well as one major baffle internal to the reservoir are highly heterogenous with respect to mineralogy and thus have very different pore networks and varied permeabilities. MICP threshold pressure results, theoretical calculations based upon a range of permeabilities, and column height calculation confirm this observation and indicate that all samples analyzed will provide a seal with variable sealing capacity to an underlying reservoir:

1) The Eau Claire sample provides the overall best seal. The Eau Claire has the lowest effective porosity despite the higher median pore throat and lower fluid/gas entry pressure than the New Albany. This slightly lower entry pressure may be the result of more abundant pore volume than the New Albany.
2) The New Albany sample is the second-best seal. It has the second highest effective porosity and the highest fluid/gas entry pressure. It has the smallest reported median pore throat size (MICP), the lowest shale porosity according to FIB-SEM analysis, and the smallest overall pore volume. It is considered a secondary caprock at the IBDP location due to its vertical distance from the primary CO_2 reservoir.
3) The Maquoketa sample is ranked last out of the three sample. It has the highest effective porosity and the lowest fluid/gas entry pressure. The Maquoketa has the second largest pore throat size and the broadest range of pore sizes. Analyses indicate that the Maquoketa has the highest pore connectivity out of all samples analyzed (FIB-SEM), largely a result of connected pore throats in framboidal and perhaps to a lesser extent the abundance of rigid carbonate grains within the sample preserving the pore volume.

4) The mudstone internal to the Mt. Simon reservoir exhibits the best sealing properties relative to all samples analyzed. However, the interval is not ranked or considered a major seal due to its lack of lateral continuity. Despite this, the mudstone is an excellent baffle and should prevent any localized vertical CO_2/fluid migration. The mudstone has an exponentially lower effective porosity (MICP) as well as entry pressure relative to the other samples. Although the FIB-SEM porosity is similar to the Eau Claire and New Albany, the median pore range is smaller than all samples. The mudstone also exhibits the smallest pore volume out of all samples analyzed.
5) Point specific MICP threshold pressure results, theoretical calculations based upon a range of permeabilities, and column height calculations indicate that the Mt. Simon mudstones and Eau Claire Shale are effective seals to $scCO_2$ in the Mt. Simon reservoir. As the mudstones are laterally discontinuous, they should be considered as baffles (where present) to $scCO_2$ migration. The Maquoketa Shale and New Albany Shale caprocks are considered non-primary seals and will provide additional sealing capacity. However, column height calculations are considered approximations since a porous reservoir for CO_2 migration is absent beneath the formations.

Acknowledgments

This research was supported by the Midwest Geological Sequestration Consortium (MGSC), which is funded by the U.S. Department of Energy through the National Energy Technology Laboratory (NETL) via the Regional Carbon Sequestration Partnership Program (contract number DE-FC26-05NT42588) and by a cost share agreement with the Illinois Department of Commerce and Economic opportunity, Office of Coal Development through the Illinois Clean Coal Institute.

References

Aswasereelert, W., Simo, J.A. and LePain, D.L., 2008. Deposition of the Cambrian Eau Claire Formation, Wisconsin: Hydrostratigraphic implications of fine-grained cratonic sandstones. *Geoscience Wisconsin*, *19*(1), pp.1-21.

Bachu, S., Bonijoly, D., Bradshaw, J., Burruss, R., Holloway, S., Christensen, N.P. and Mathiassen, O.M., 2007. CO2 storage capacity estimation: Methodology and gaps. *International journal of greenhouse gas control*, *1*(4), pp.430-443.

Benson, S.M. and Cole, D.R., 2008. CO2 sequestration in deep sedimentary formations. *Elements*, *4*(5), pp.325-331.

Bickford, M.E., Van, W.R. and Zietz, I., 1986. Proterozoic history of the midcontinent region of North America. *Geology*, *14*(6), pp.492-496.

Carroll, S. A., McNab, W. W., Dai, Z., & Torres, S. C. (2012). Reactivity of Mount Simon sandstone and the Eau Claire shale under CO2 storage conditions. *Environmental science & technology*, *47*(1), 252-261.

Cluff, R. M., Reinbold, M. L., & Lineback, J. A. (1981). New Albany shale group of Illinois. *Ill. State Geol. Surv., Circ.; (United States)*, *518*.

Couëslan, M. L., Smith, V., El-Kaseeh, G., Gilbert, J., Preece, N., Zhang, L., & Gulati, J. (2014). Development and implementation of a seismic characterization and CO2 monitoring program for the Illinois Basin–Decatur Project. *Greenhouse Gases: Science and Technology*, *4*(5), 626-644.

Daniel, R.F., and J.G., Kaldi, 2008. Evaluating seal capacity of caprocks and intraformational barriers for the geosequestration of CO_2. Paper-PESA Eastern Australian Basin Symposium III, Sydney, 14-17 September,2008.

626 Damiani, D., 2020. *SAFE GEOLOGIC STORAGE OF CAPTURED CARBON DIOXIDE: TWO DECADES OF DOE'S*
627 *CARBON STORAGE R&D PROGRAM IN REVIEW*. US DOE Office of Fossil Energy.
628 Dewhurst, D.N., Jones, R.M., and M.D. Raven, 2002. Microstructural and petrophysical characterization
629 of Muderong Shale: Application to top seal risking: Petroleum GeoScience, 8, 371-383.
630 Doebelin, N. and Kleeberg, R., 2015. Profex: a graphical user interface for the Rietveld refinement
631 program BGMN. *Journal of applied crystallography*, *48*(5), pp.1573-1580.
632 Espinoza, D.N. and Santamarina, J.C., 2010. Water-CO2 mineral systems – Interfacial tension, contact
633 angle, and diffusion. Implications to CO2 geological storage. Water Resources Research, 46, WO7537.
634 Finley, R. J. (2014). An overview of the Illinois Basin–Decatur project. *Greenhouse Gases: Science and*
635 *Technology*, *4*(5), 571-579.
636 Friedmann, S.J., 2007. Geological carbon dioxide sequestration. *Elements*, *3*(3), pp.179-184.
637 Freiburg, J.T., McBride, J.H., Malone, D.H. and Leetaru, H.E., 2020a. Petrology, geochronology, and
638 geophysical characterization of Mesoproterozoic rocks in central Illinois, USA. *Geoscience*
639 *Frontiers*, *11*(2), pp.581-596.
640 Freiburg, J.T., Holland, M.E., Malone, D.H. and Malone, S.J., 2020b. Detrital zircon geochronology of
641 basal Cambrian strata in the deep Illinois Basin, USA: evidence for the Paleoproterozoic-Cambrian
642 tectonic and sedimentary evolution of central Laurentia. *The Journal of Geology*, *128*(3), pp.303-317.
643 Freiburg, J.T., Ritzi, R.W. and Kehoe, K.S., 2016. Depositional and diagenetic controls on anomalously
644 high porosity within a deeply buried CO2 storage reservoir—The Cambrian Mt. Simon Sandstone, Illinois
645 Basin, USA. *International Journal of Greenhouse Gas Control*, *55*, pp.42-54.
646 Freiburg, J. T., Morse, D. G., Leetaru, H. E., Hoss, R. P., & Yan, Q. (2014). A Depositional and Diagenetic
647 Characterization of the Mt. Simon Sandstone at the Illinois Basin-Decatur Project Carbon Capture and

Storage Site, Decatur, Illinois, USA. *Illinois State Geological Survey, Prairie Research Institute, University of Illinois.*

Freiburg, J. T., & Leetaru, H. E. (2012). Controls on porosity development and the potential for CO2 sequestration or wastewater disposal in the Cambrian Potosi Dolomite (Knox Group): Illinois Basin. In *41st Annual Eastern Section AAPG Meeting. Program Abstracts*.

Grathoff, G. H., Moore, D. M., Hay, R. L., & Wemmer, K. (2001). Origin of illite in the lower Paleozoic of the Illinois basin: evidence for brine migrations. *Geological Society of America Bulletin*, *113*(8), 1092-1104.

Higley, D.K., Henry, M.E., Lewan, M.D. and Pitman, J.K., 2003. *The New Albany Shale Petroleum System, Illinois Basin-Data and Map Image archive from the Material-Balance Assessment* (No. 2003-37).

Hildenbrand, A., Schlömer, S., & Krooss, B. M. (2002). Gas breakthrough experiments on fine-grained sedimentary rocks. *Geofluids*, *2*(1), 3-23.

Holloway, S., 2001. Storage of fossil fuel-derived carbon dioxide beneath the surface of the earth. *Annual Review of Energy and the Environment*, *26*(1), pp.145-166.

Koide, H., Tazaki, Y., Noguchi, Y., Nakayama, S., Iijima, M., Ito, K. and Shindo, Y., 1992. Subterranean containment and long-term storage of carbon dioxide in unused aquifers and in depleted natural gas reservoirs. *Energy Conversion and management*, *33*(5-8), pp.619-626.

Kolata, D.R. and Graese, A.M., 1983. *Lithostratigraphy and depositional environments of the Maquoketa Group (Ordovician) in northern Illinois*. Champaign, Ill.: Illinois State Geological Survey, Prairie Research Institute

Lackner, K.S. and Brennan, S., 2009. Envisioning carbon capture and storage: expanded possibilities due to air capture, leakage insurance, and C-14 monitoring. *Climatic Change*, *96*(3), pp.357-378.

Lahann, R., Mastalerz, M., Rupp, J. A., & Drobniak, A. (2013). Influence of CO 2 on New Albany Shale composition and pore structure. *International Journal of Coal Geology*, *108*, 2-9.

Lahann, R., Rupp, J. and Medina, C., 2014. An evaluation of the seal capacity and CO2 retention properties of the Eau Claire Formation (Cambrian). *Environmental Geosciences*, *21*(3), pp.83-106.

Leetaru, H.E., Morse, D.G., Bauer, R., Frailey, S., Keefer, D., Kolata, D., Korose, C., Mehnert, D.M.W., Rittenhouse, S., Drahovzal, J. and Fisher, S., 2005. Saline reservoirs as a sequestration target. *An Assessment of Geological Carbon Sequestration Options in the Illinois Basin*, pp.253-324.

Leetaru, H. (2014). *Maquoketa Shale Caprock Integrity Evaluation*. US DOE Report Number: DOE/FE002068-9

Leetaru, H., Brown, A., Lee, D., Senel, O. and Coueslan, M., 2012. *CO {sub 2} Injectivity, Storage Capacity, Plume Size, and Reservoir and Seal Integrity of the Ordovician St. Peter Sandstone and the Cambrian Potosi Formation in the Illnois Basin*. Univ. of Illinois at Urbana-Champaign, IL (United States).

Lewan, M. D., Henry, M. E., Higley, D. K., & Pitman, J. K. (2002). Material-balance assessment of the New Albany-Chesterian petroleum system of the Illinois basin. *AAPG bulletin*, *86*(5), 745-778.

Li, S., Dong, M., Li, Z., Huang, H., Qing, H., and E. Nickel, 2005. Gas break-through pressure for hydrocarbon reservoir seal rocks: Implications for the security of long-term CO_2 storage in the Weyburn Field: Geofluids, 5, 326-334.

Liu, F., Lu, P., Griffith, C., Hedges, S. W., Soong, Y., Hellevang, H., & Zhu, C., (2012). CO_2–brine–caprock interaction: reactivity experiments on Eau Claire shale and a review of relevant literature. *International Journal of Greenhouse Gas Control*, *7*, 153-167.

691 Martin-Roberts, E., Scott, V., Flude, S., Johnson, G., Haszeldine, R.S. and Gilfillan, S., 2021. Carbon
692 capture and storage at the end of a lost decade. *One Earth*, *4*(11), pp.1569-1584.

693 Mastalerz, M., Schimmelmann, A., Drobniak, A. and Chen, Y., 2013. Porosity of Devonian and
694 Mississippian New Albany Shale across a maturation gradient: Insights from organic petrology, gas
695 adsorption, and mercury intrusionGeohorizon. *AAPG bulletin*, *97*(10), pp.1621-1643.

696 Medina, C.R., Mastalerz, M., Lahann, R.W. and Rupp, J.A., 2020. A novel multi-technique approach used
697 in the petrophysical characterization of the Maquoketa Group (Ordovician) in the southeastern portion
698 of the Illinois Basin: Implications for seal efficiency for the geologic sequestration of CO2. *International*
699 *Journal of Greenhouse Gas Control*, *93*, p.102883.

700 Mozley, P.S., Heath, J.E., Dewers, T.A. and Bauer, S.J., 2016. Origin and heterogeneity of pore sizes in the
701 Mount Simon Sandstone and Eau Claire Formation: Implications for multiphase fluid
702 flow. *Geosphere*, *12*(4), pp.1341-1361.Münch, B. and Holzer, L., 2008. Contradicting geometrical
703 concepts in pore size analysis attained with electron microscopy and mercury intrusion. *Journal of the*
704 *American Ceramic Society*, *91*(12), pp.4059-4067.

705 Neufelder, R.J., Bowen, B.B., Lahann, R.W. and Rupp, J.A., 2012. Lithologic, mineralogical, and
706 petrophysical characteristics of the Eau Claire Formation: Complexities of a carbon storage system
707 seal. *Environmental Geosciences*, *19*(3), pp.81-104.

708 Nuttall, B. C., Drahovzal, J. A., Eble, C. F., & Bustin, R. M., 2009. Regional assessment of suitability of
709 organic-rich gas shales for carbon sequestration: An example from the Devonian shales of the Illinois
710 and Appalachian basins, Kentucky.

711 Oelkers, E.H. and Cole, D.R., 2008. Carbon dioxide sequestration a solution to a global
712 problem. *Elements*, *4*(5), pp.305-310.

713 Pacala, S. and Socolow, R., 2004. Stabilization wedges: solving the climate problem for the next 50 years
714 with current technologies. *science*, *305*(5686), pp.968-972.

715 Partin, T., 2004. Demand for high price spurs a new era of drilling for New Albany Shale gas wells in
716 Harrison County, Indiana. In *Devonian Black Shales of the Eastern US New Insights into Sedimentology*
717 *and Stratigraphy from the Subsurface and Outcrops in the Illinois and Appalachian Basins*.

718 Rackley, S.A., 2017. *Carbon capture and storage*. Butterworth-Heinemann.

719 Reesink, A.J.H., Best, J., Freiburg, J.T., Webb, N.D., Monson, C.C. and Ritzi, R.W., 2020. Interpreting pre-
720 vegetation landscape dynamics: The Cambrian Lower Mount Simon Sandstone, Illinois, USA. *Journal of*
721 *Sedimentary Research*, *90*(11), pp.1614-1641.Sarmadivaleh, A., Al-Yaseri, Z, and Iglauer, S., 2015.
722 Influence of Temperature and Pressure on quartz=water-CO2 contact angle and CO2=water interfacial
723 tension. Journal of Colloid and Interface Science, 441, 59-64.

724 Schieber, J., 2010. Common themes in the formation and preservation of intrinsic porosity in shales and
725 mudstones-illustrated with examples across the Phanerozoic. In *SPE Unconventional Gas Conference*.
726 Society of Petroleum Engineers.

727 Schieber, J., 2013. SEM Observations on Ion-milled Samples of Devonian Black Shales from Indiana and
728 New York: The Petrographic Context of Multiple Pore Types, *In* W. Camp, E. Diaz, and B. Wawak, eds.,
729 Electron microscopy of shale hydrocarbon reservoirs: AAPG Memoir 102, p. 153-171

730 Schowalter, T.T., 1979. Mechanics of secondary hydrocarbon migration and entrapment. AAPG
731 Bulletin, 63, pp. 723-760.

732 Senel, O., Will, R., & Butsch, R. J., 2014. Integrated reservoir modeling at the Illinois Basin–Decatur
733 Project. *Greenhouse Gases: Science and Technology*, *4*(5), 662-684.

734 Strapoc, D., Mastalerz, M., Schimmelmann, A., Drobniak, A., & Hasenmueller, N. R., 2010. Geochemical
735 constraints on the origin and volume of gas in the New Albany Shale (Devonian–Mississippian), eastern
736 Illinois Basin. *AAPG bulletin*, *94*(11), 1713-1740.

737 Warr, L.N., 2021. IMA–CNMNC approved mineral symbols. *Mineralogical Magazine*, pp.1-30.

738 Willman, H.B., Atherton, E., Buschbach, T.C., Collinson, C.W., Frye, J.C., Hopkins, M.E., Lineback, J.A. and
739 Simon, J.A., 1975. Handbook of Illinois stratigraphy. *Bulletin no. 095*.

740 Yoksoulian, L. E., Freiburg, J. T., Butler, S. K., Berger, P. M., & Roy, W. R., 2013. Mineralogical alterations
741 during laboratory-scale carbon sequestration experiments for the Illinois Basin. *Energy Procedia*, *37*,
742 5601-5611.

743

Acknowledgments

I gratefully thank my advisors Dr. Georg Grathoff and Dr. Laurence Warr for granting me this opportunity to study under their guidance and welcome me to conduct my thesis with the auspices of the University of Greifswald, Germany. I would also like to thank Georg's family for the warm welcome and treating me like family. I am also very appreciative of the all the students and staff at the University of Greifswald that helped me along the way. I am more than grateful to my employer, the Illinois State Geological Survey (ISGS) at the University of Illinois. The team at ISGS worked tirelessly to successfully bring in the CCS projects and continue these exciting times of research in the Illinois Basin. I would also like to thank the crazy folks in the mineral world. You know who you are, and you helped keep my chin up along the way. And lastly, but mostly, I thank my wife and my three wild boys for keeping it real and putting me in my place. Love you!